

POLISH ACADEMY OF SCIENCES – WROCLAW BRANCH
WROCLAW UNIVERSITY OF TECHNOLOGY

ARCHIVES OF CIVIL AND MECHANICAL ENGINEERING

Quarterly
Vol. XI, No. 2

WROCLAW 2011

EDITOR IN CHIEF

ZBIGNIEW GRONOSTAJSKI

EDITORIAL LAYOUT AND PROOF-READING

WIOLETTA GÓRALCZYK

TYPESSETTING

SEBASTIAN ŁAWRUSEWICZ

SECRETARY

WIOLETTA GÓRALCZYK

Publisher: Committee of Civil and Mechanical Engineering
of Polish Academy of Sciences – Wrocław Branch,
Faculty of Civil Engineering and Faculty of Mechanical Engineering
of Wrocław University of Technology

© Copyright by Oficyna Wydawnicza Politechniki Wrocławskiej, Wrocław 2011

OFICYNA WYDAWNICZA POLITECHNIKI WROCŁAWSKIEJ

Wybrzeże Wyspiańskiego 27, 50-370 Wrocław

<http://www.oficyna.pwr.wroc.pl>

e-mail: ofiewyd@pwr.wroc.pl

ISSN 1644-9665

Drukarnia Oficyny Wydawniczej Politechniki Wrocławskiej. Zam. nr 648/2011.

Contents

P. BORKOWSKI, Hydro-jetting method of bas-relief shaping	267
F. FILUS, I. SCHINDLER, J. FIALA, S. LASEK, T. KUBINA, G. NIEWIELSKI, D. KUC, E. HADASIK, Electro-chemical monitoring of static recrystallization	277
W. GLABISZ, Cellular automata in nonlinear vibration problems of two-parameter elastic foundation	285
M. GRABA, The influence of material properties and crack length on the Q -stress value near the crack tip for elastic-plastic materials for single edge notch plate in tension...	301
A. KASPRZYCKI, L. TOMSKI, Chojen constructional solutions of the structures loading the Ekler columns In vibration and stability studies.....	321
A. KATUNIN, The conception of the fatigue model for layered composites considering thermal effects	333
A. KOPCZYŃSKI, M. PTAK, P. HARNATKIEWICZ, The influence of frontal protection system design on pedestrian passive safety	345
A. KOSIŃSKA, S. KOSIŃSKI, Love waves in initially deformed rubberlike Gent and Yeoh materials	365
S. KRAWIEC, The synergistic effect of copper powder with PTFE in a grease lubricant under mixed friction conditions	379
R. KUTYŁOWSKI, B. RASIAK, M. SZWECHŁOWICZ, Topology optimisation as a tool for obtaining a multimaterial structure	391
Z. MIRSKI, T. PIWOWARCZYK, Wettability of hardmetal surfaces prepared for brazing with various methods	411
N. SENE, P. BALLAND, R. ARRIEUX, Numerical study of the micro-formability of thin metallic materials: virtual micro-forming limit diagrams	421
J. SŁOMA, I. SZCZYGIEL, A. SACHAJDAK, Modelling of thermal phenomena In electric arc during surfacing	437
D. SZELIGA, M. PIETRZYK, R. KUZIAK, V. PIDVYSSOTSKYY, Rheological model of Cu based alloys accounting for the preheating prior to deformation	451
K. WIDANKA, Effect of Boron on the structure and mechanical properties of PM Fe-Si compacts after through vacuum carburising.....	469
P. ZAJĄC, The idea of the model of evaluation of logistics warehouse systems with taking their energy consumption under consideration.....	479

Spis treści

P. BORKOWSKI, Metoda hydrostrumieniowego kształtowania płaskorzeźb	267
F. FILUS, I. SCHINDLER, J. FIALA, S. LASEK, T. KUBINA, G. NIEWIELSKI, D. KUC, E. HADASIK, Elektrochemiczne monitorowanie przebiegu statycznej rekrytalizacji ...	277
W. GLABISZ, Automaty komórkowe w nieliniowych zagadnieniach drgań dwuparametrowego podłoża sprężystego	285
M. GRABA, Wpływ stałych materiałowych i długości pęknięcia na rozkład naprężeń Q przed wierzchołkiem pęknięcia w materiałach sprężysto-plastycznych dla płyty z jednostronną szczeliną poddanej rozciąganiu	301

A. KASPRZYCKI, L. TOMSKI, Wybrane rozwiązania konstrukcyjne struktur obciążających kolumny Eklera w badaniach drgań i stateczności	321
A. KATUNIN, Koncepcja modelu zmęczeniowego dla kompozytów warstwowych z uwzględnieniem efektów cieplnych	333
A. KOPCZYŃSKI, M. PTAK, P. HARNATKIEWICZ, Wpływ przedniego układu zabezpieczającego na bezpieczeństwo bierne pieszego	345
A. KOSIŃSKA, S. KOSIŃSKI, Fale Love'a we wstępnie odkształconych materiałach Genta i Yeoha	365
S. KRAWIEC, Efekt synergetyczny proszku miedzi i PTFE w smarze plastycznym podczas tarcia mieszanego	379
R. KUTYŁOWSKI, B. RASIAK, M. SZWECHŁOWICZ, Optymalizacja topologii narzędziem do uzyskania konstrukcji multimateriałowej	391
Z. MIRSKI, T. PIWOWARCZYK, Zwilżalność powierzchni spieków węglkowych przygotowanych różnymi metodami do lutowania twardego	411
N. SENE, P. BALLAND, R. ARRIEUX, Numeryczne badania mikro-odkształcalności materiałów metalicznych; wirtualna krzywa odkształceń granicznych dla mikroformowania	421
J. SŁOMA, I. SZCZYGIEL, A. SACHAJDAK, Modelowanie zjawisk cieplnych w łuku elektrycznym podczas napawania	437
D. SZELIGA, M. PIETRZYK, R. KUZIĄK, V. PIDVYSSOTSKYY, Model reologiczny stopu miedzi uwzględniający schemat nagrzewania wstępnego przed odkształcaniem.....	451
K. WIDANKA, Wpływ boru na strukturę i własności mechaniczne wyprasek Fe-Si nawęglanych próżniowo na wskroś.....	469
P. ZAJĄC, Koncepcja modelu oceny logistycznych systemów magazynowych z uwzględnieniem ich energochłonności.....	479



Hydro-jetting method of bas-relief shaping

P. BORKOWSKI

Koszalin University of Technology, Unconventional HydroJetting Technology Center, Raclawicka 15-17, 75-620 Koszalin, Poland.

The paper presents a novel method for the 3D shaping of different materials using a high-pressure abrasive water jet and a flat target image. For steering movement process of the jet a principle similar to raster image way of record and readout was used. However, respective colours of pixel of such a bitmap are connected with adequate jet feed rate that causes erosion of material with adequate depth. Thanks to that innovation, one can observe spatial imaging of the object. Theoretical basis of material shaping and experimental stand including steering program are presented in. There are also presented methodical and some experimental erosion results as well as practical examples of object's bas-relief made of metal.

Keywords: *abrasive water jet, bas-relief shaping*

1. Introduction

The development of high-pressure abrasive water jet (AWJ) machining method is mainly a result of tool elasticity and the fact that the technique never causes any structural changes in the substrate. Water jets were first used in the 1980s, and since then, much research has been done to optimize the technology and improve the cutting efficiency. Examination of abrasive grain interaction in the treatment zone led to an understanding of the mechanism of abrasive erosion [10], making it simpler to characterize and execute specific boring processes [9] such as slender holes [17]. Precision and quality of the treated surfaces were analyzed. Water jet techniques can be applied to ductile materials (e.g., aluminium [7] and titanium [20] alloys), and to assorted brittle materials (e.g., tool steel [18], stone [20], [12] and glass [17], [12]). A number of experiments [18], [8], [15] have clarified the mechanisms of abrasive water jet cutting that define eroded grooves shape [11], [13], process characteristics [14], as prediction of cutting parameters [19]. This knowledge led to simulations of efficiency [16] and cost [19], [21].

As a result of better understanding the cutting mechanism, techniques such as milling [9], drilling [17] and surface treatment [6] have become possible. Recently, a new method of automatic abrasive water jet sculpturing [2–3] of different materials was presented. It enables the production of a spatial shaping of an object based on a photograph [5], [1]. In order to manipulate the position of the jet, a principle similar to image rastering was employed. Here, the colour of a pixel in the image is correlated to a specific jet feed rate that induces erosion of the substrate to a particular depth [5], [4]. Thanks to this innovation, one can observe spatial imaging of the object.

2. The basics of shaping material

The concept of spatial material shaping depends on determining, from an image, the light intensity on the surface of a target object. In practice, this process controlled by a computer navigation program that reads the object's image and then steers the working heads and regulates their feed rates. Its longitudinal movement is velocity-controlled by an analogue input, which allows for continuous control of the degree of material removal caused by abrasive water jet.

By referencing the pitting pattern left in the wake of the jet, it is possible to relate the depth of a given cut to the desired pattern in the target image. The amount of time that the jet interacts with the substrate is proportional to the expected erosion depth, and this allows feed rate to be used as the governing parameter for erosion depth. In this case, the smallest treatable area is determined by the diameter of the jet. The combination of different jet interactions with the substrate allows a spatial bas-relief of the real object to be constructed.

Taking the above conditions into consideration, one can calculate the required interaction time as

$$\Delta t_i = \frac{d_m}{V_i}, \quad (1)$$

where:

d_m – focusing nozzle diameter;

V_i – velocity of the jet movement above chosen elementary cell (i) of shaped material.

The essence of this method consists of properly specifying the erosion depth and working head positions in relation to the minimum resolution required to capture the target feature. The method relies on image rastering to address each pixel and to construct the whole image. Owing to the similarity between this method and data manipulation of rastered images, the bitmap file format was used as the standard. For such bitmaps, respective pixel colours are correlated to specific erosion depths. The essence of this method is illustrated in Figure 1.

The following steps are required for this technique:

- 1) The image, typically a photograph, is scanned in gray-scale.
- 2) The pixel values in the resulting bitmap are converted to working head feed rates that determine the jet interaction time at each location on the substrate.
- 3) The feed rates are passed to the water jets, and the image geometry is parsed into the control language of a 2-axis plotter that physically rasters the jets across the substrate.

While this approach requires only a simple 2-axis plotter, position control of the jets is crucial, and a specialized program to parse the image data in the control language of the plotter is required.

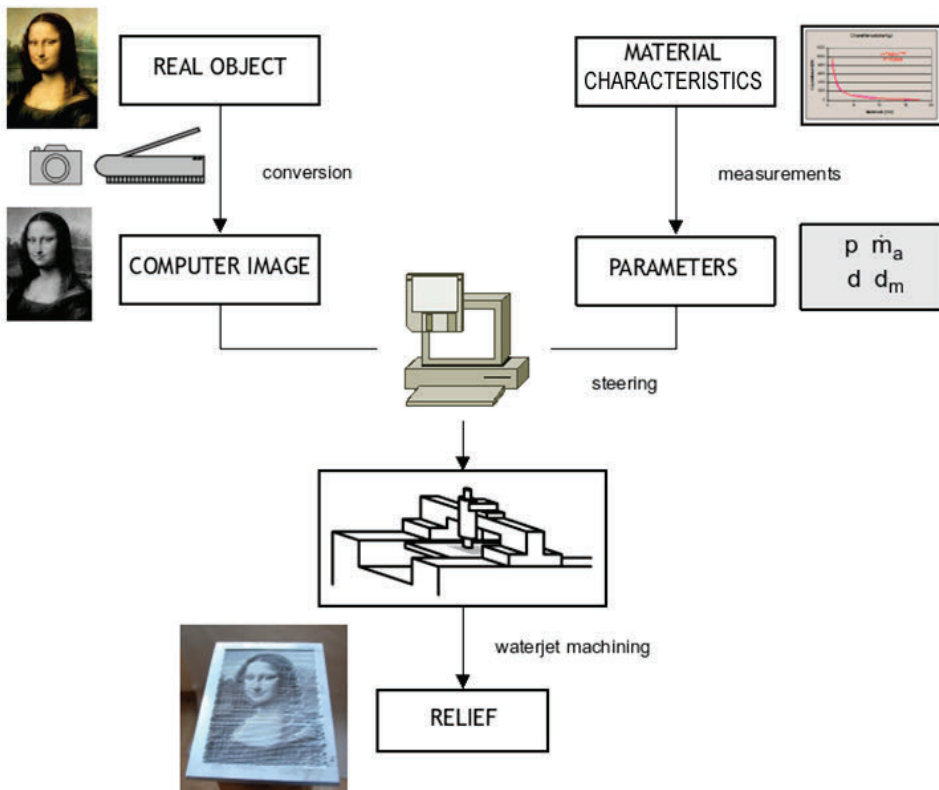


Fig. 1. 3D material forming with utilization of flat virtual object luminance

3. Experimental methodology

A special experimental stand was designed and built (Figure 2). Two stepper-driven lead screws (WX6 08500 by Isert Electronic) were used as linear actuators to control the planar position of the working head, while an additional lead screw system was affixed to these to provide a base for the working head. This gantry ensures XY positioning accuracy of ± 0.005 mm over a table area of 1 m^2 . This customized gantry supported a water supply to the working head that was pressurized up to 50 MPa, thereby ensuring constant feed rate of the abrasive material from the reservoir.

Longitudinal movements of the head were produced with stepping frequencies of $1\text{--}2400 \text{ s}^{-1}$ that taking lead screw travel in account, gives a feed rate of approximately $0.005\text{--}12 \text{ mm/s}$, allowing a wide range of different cuts to be made. The actual control of the water jet was controlled with custom-made WaterJetLab software that was written in C++. The FreeDOS platform was used to provide access to PC hardware. This system handles all of the aforementioned functions in only 5000 lines of code, has easily obtainable hardware requirements and presents a simple user interface.



Fig. 2. General view of test stand for spatial material machining with high pressure abrasive-water jet:
 1 – frame, 2 – y direction slideways, 3 – x direction slideway, 4 – abrasive-water jet working head,
 5 – abrasive feed container, 6 – steering PC computer, 7 – high-pressure water pump type As500/15A

All actions related to process configuration are performed by the user according to a strict procedure [20]. Once prepared, the software records the settings and initializes the appropriate modules. Image processing can be performed by using a filter that transforms bitmaps into 256 step gray scale images based on calculating the luminance from an RGB image according to [17].

$$\text{Grey depth} = 0.3 \cdot \text{Red} + 0.59 \cdot \text{Green} + 0.11 \cdot \text{Blue}. \quad (2)$$

Basing on that procedure it was possible to realize experiments on ceramics, glasses, plastics and other popular materials. Aluminium alloy, 5 mm thick AlMg1SiMn, was used most commonly. Depending upon the shape of the object to be reproduced, the maximum erosion depth defined in the WaterJetLab program was set to values ranging from 1.5 mm to 2.5 mm. A water nozzle of 0.7 mm diameter and focus nozzle of 2.5 mm diameter was installed in work head, while a standoff distance was set at 5 mm.

Experiments were conducted with a water pressure range of 10–50 MPa, while garnet #80 was used as the abrasive material and was set to output at 0.9 g/s. For such conditions, the dimensions of a mapped gray scale element on sample surface were set to 2×2 mm. Calibration of the material's erosive properties was then conducted. Surface morphology was characterized using a laser gauge (TalySurf CLI 2000 by Taylor Hobson).

4. Abrasive-water jet sculpturing effects

Basing on this prototype jet-machine, a wide array of different uses for abrasive water jets was considered. The process needs neither complicated process control nor complex position control. Adequate software of such jet machining processes need only ensure the possibility for proper “relocation” between sample material features and abrasive-water jet erosiveness and working head feed rate that is finally responsible for material spatial sculpturing basing on the photo.

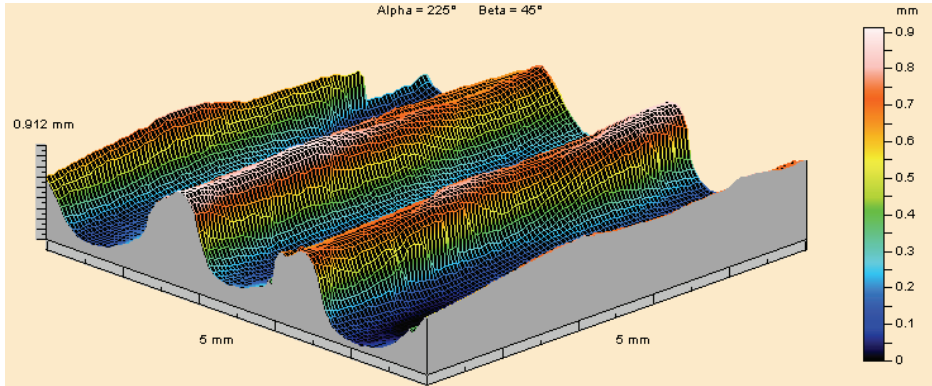


Fig. 3. Shape regularity and edge height of respective jet paths after AWJ treating of AlMg1SiMn for $p = 50$ MPa, $m_a = 0.90$ g/s

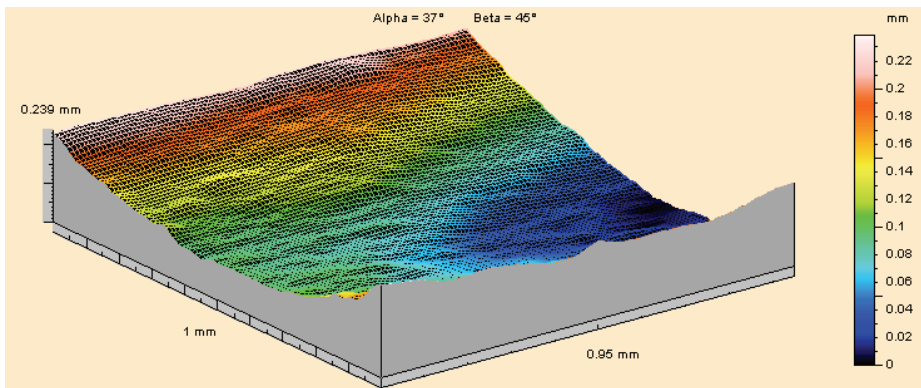


Fig. 4. Typical shape of the bottom of eroded region for AWJ treating of AlMg1SiMn ($p = 40$ MPa, $m_a = 0.56$ g/s)

One should have in mind that during such abrasive water jet spraying, the upper surface of the sample becomes slightly tarnished based on the roughness parameters. Moreover, between the jet paths and at the bottom of the eroded regions are small regions that do not erode. Depending on the erosion parameters, the shape of these re-

gions can form regular edges, as presented in Figure 3. The shape of these furrows is fairly regular (Figure 4), and their surface roughness is similar to that which occurs during the grinding process.

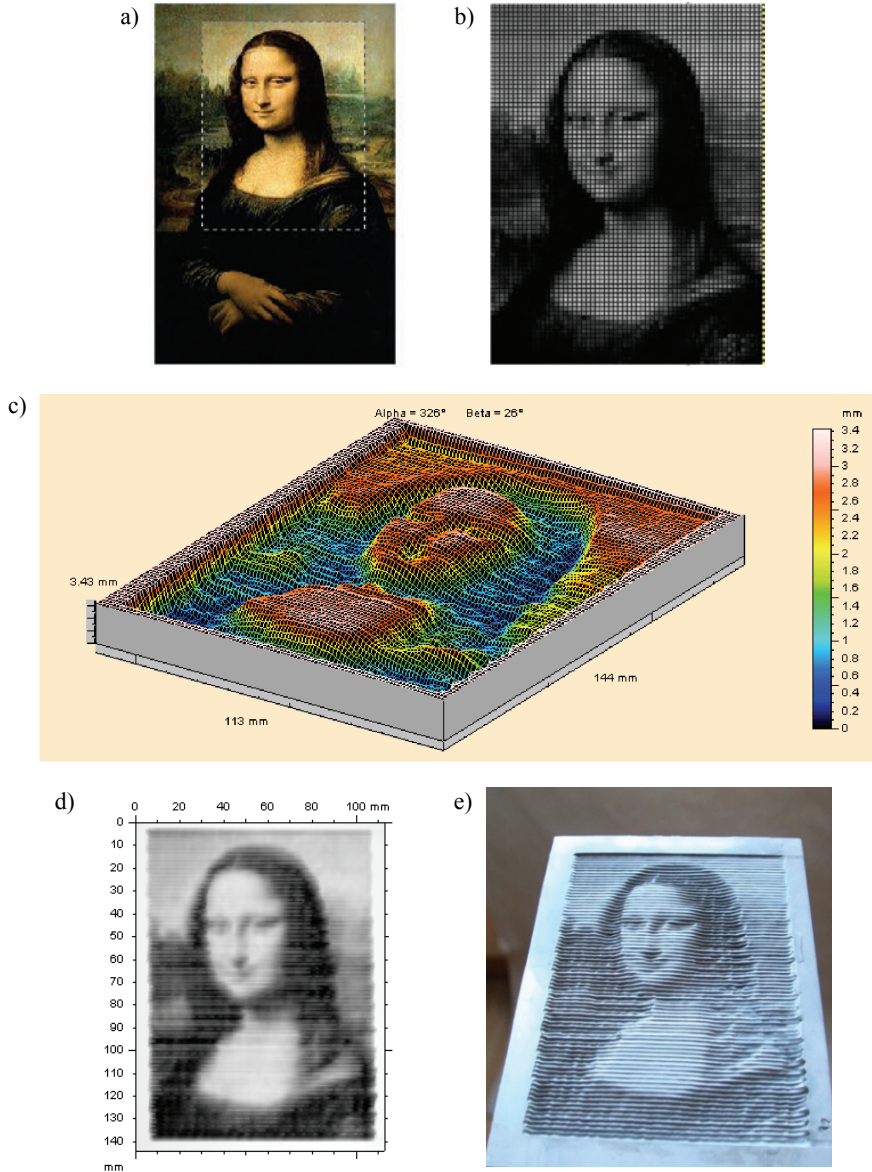


Fig. 5. Images showing important phases of spatial object (Mona Lisa) sculpturing basing on its photocopy: a) picture, b) virtual 2D matrix, c) perspective scanned view showing depth analysis, d) image scanned from the relief, e) photo of 3D bas-relief cut in AlMg1SiMn plate

Examinations of the effect of material on the ability to produce a particular shape with a high-pressure abrasive-water jet led to the collection of interesting data. Specifically, it was determined that erosion depth can be verified and that spatial objects can be produced based on flat image templates. Common results from such work can be seen in the following pictures.

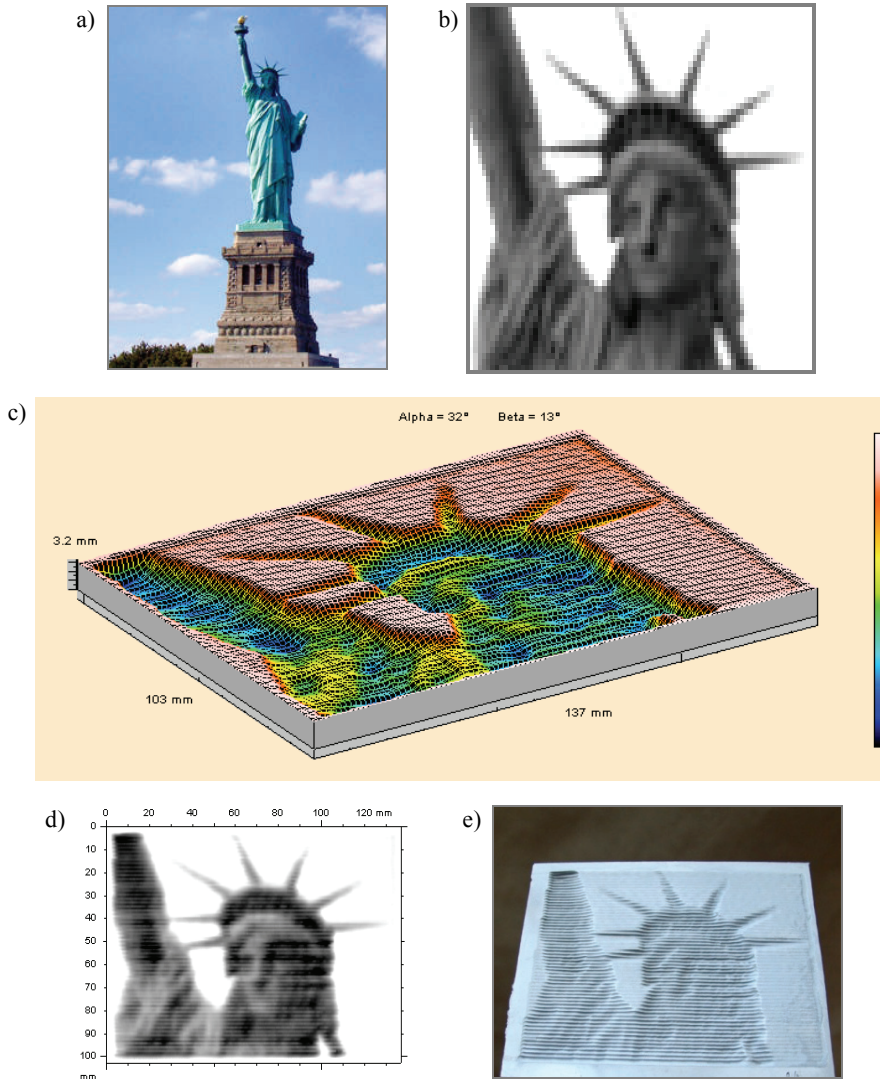


Fig. 6. Images showing important phases of spatial object (Statue of Liberty) sculpturing basing on its photocopy: a) picture, b) virtual 2D matrix, c) perspective scanned view showing depth analysis, d) image scanned from the relief, e) photo of 3D bas-relief cut in AlMg1SiMn plate

Figure 5 presents a photocopy of a well known painting and includes a set of illustrations showing the important phases of its reproduction in a metal plate. The presented images show the phases of converting a real object (Figure a) into a virtual 2D matrix (Figure b) with the resolution reduced to a level that is reproducible with an abrasive water working head in 3D bass-relief (Figure c), scanned that way image (Figure d) and its perspective view showing out its real resolution (Figure e).

An important effect related to contrast is presented in Figure 6. While there is enormous advantage in the automated water jet cutting technique presented, inaccuracy was noted in the form of incomplete reproduction of the erosion depth in regions of high contrast compared to the surroundings. It was observed that proper erosion depth can be achieved only when consecutive pixels in a rastered line share fairly similar gray scale values. Moreover, the quality needs to be improved with respect to the boundary levelling that occurs between individual lines.

It can be claimed that, despite the relatively low matrix resolution, the quality of the reproduced image in metal plates is satisfactory. Further, it should be noted that characteristics of the target object are preserved. A particular example of this may be seen in still recognizable subtle smile of La Gioconda presented in Figure 5. Despite the problem discussed earlier, these results suggest a good future for this technology.

5. Conclusions

The abrasive water jet based material shaping technique presented here confirms assumptions about water jet machining and presents a software based procedure for controlling the position of the work head. Based on the presented data, one can generally admit that, despite low matrix resolution, images given in the form of bitmaps were reconstructed relatively well in metal samples. Therefore, the presented method gives satisfactory results.

References

- [1] Borkowski P., Szpakowicz A.: *Abrasive-water jet shaping of bas-relief*, WJTA American Waterjet Conference, August 18–20, 2009, Houston, Texas, Paper No. 3-A.
- [2] Borkowski P., Szpakowicz A.: *Hydro-jetting shaping of bas-relief*, Journal of Machine Engineering, Vol. 13, No. 1–2, 2008, pp. 81–89.
- [3] Borkowski P., Żukociński T.: *Basis of three dimensional material forming using high-pressure abrasive-water jet controlled by virtual image luminance*, Advances in Manufacturing Science and Technology, Vol. 30, No. 1, 2006, pp. 53–62.
- [4] Borkowski P., Żukociński T.: *Three dimensional method of material forming using high-pressure abrasive-water jet controlled by flat image luminance*, 18th Int. Conf. Jetting Technology, Gdańsk, 2006, pp. 265–274.
- [5] Borkowski P.: *Creation of bas-relief basing on photography using high-pressure abrasive-water jet*, Journal of Machine Engineering, Vol. 8, No. 2, 2008, pp. 43–51.

- [6] Borkowski P.: *Theoretical and experimental basis of hydro-jet surface treatment* (in Polish), ISSN 0239-7129, Koszalin, 2004.
- [7] Chung Y., Geskin E.S., Singh P.J.: *Prediction of the geometry of the kerf created in the course of abrasive waterjet machining of ductile materials*, 11th Int. Conf. on Jet Cutting Technology, St. Andrews, Scotland, 1992, pp. 525–541.
- [8] Groppetti R., Gutema T., Di Lucchio A.: *A Contribution to the analysis of some kerf quality attributes for precision abrasive water jet cutting*, 14th Int. Conf. on Jetting Technology, Brugge, 1998, pp. 253–269.
- [9] Hashish M.: *An investigation of milling with abrasive-waterjets*, Trans. ASME, Journal of Engineering for Industry, Vol. 111, No. 2, 1989, pp. 158–166.
- [10] Hashish M.: *On the modelling of abrasive-waterjet cutting*, 7th Int. Symposium on Jet Cutting Technology, Ottawa, Canada, 1984, pp. 249–265.
- [11] Henning A., Westkamper E.: *Modelling of contour generation in abrasive waterjet cutting*, 15th Int. Conf. on Jetting Technology, Ronneby, 2000, pp. 309–320.
- [12] Lauand V.H., Hennies W.T., Stellin A. Jr.: *Glass and marble (Cachoeiro de Itapemirim) milling with abrasive water jetting*, 19th Int. Conference Water Jetting, BHR Group, Nottingham, 2008, pp. 121–139.
- [13] Laurinat A., Louis H., Meier-Wiechert G.: *A model for milling with abrasive water jets*, 7th American Water Jet Conf. Seattle, Washington, 1993, pp. 119–139.
- [14] Momber A.W.: *A generalized abrasive water jet model*, 8th American Water Jet Conf. Houston, Texas, 1995, pp. 359–376.
- [15] Tan D.K.M.: *A model for the surface finish in abrasive-waterjet cutting*, 8th Int. Symposium on Jet Cutting Technology, Durham, England, 1986, Vol. 31, pp. 309–313.
- [16] Yong Z., Kovacevic R.: *3D simulation of macro and micro characteristics for AWJ machining*, 9th American Water Jet Conf. Dearborn, Michigan, 1997, pp. 133–144.
- [16] Yong Z., Kovacevic R.: *Modelling of jetflow drilling with consideration of the chaotic erosion histories of particles*, Wear, No. 209, 1997, pp. 284–291.
- [17] Zeng J., Kim T.J.: *Development of an abrasive waterjet kerf cutting model for brittle materials*, 11th Int. Conf. on Jet Cutting Technology, St. Andrews, Scotland, 1992, pp. 483–501.
- [18] Zeng J., Kim T.J.: *Parameter prediction and cost analysis in abrasive waterjet cutting operations*, 7th American Water Jet Conf. Seattle, Washington, 1993, pp. 175–189.
- [19] Zhang S., Galecki G., Summers D.A., Swallow C.: *Use of pre-profiling a milled pocket as a means of improving machining and lowering energy costs*, WJTA Conference and Expo, Houston, Texas, 2007, Paper 3-H.
- [20] Zhang S., Shepherd J.D., Summers D.A.: *Experimental investigation of rectangular pocket milling with abrasive water jet using specially designed tool*, 17th International Conference on Water Jetting, BHR Group, Mainz, Germany, 2004, pp. 435–447.

Metoda hydrostrumieniowego kształtowania płaskorzeźb

Artykuł prezentuje nową metodę przestrzennego kształtowania powierzchni różnych materiałów przy użyciu wysokociśnieniowej strugi wodno-ściernej na podstawie obrazu rzeźbionego obiektu. Ogólna koncepcja tej metody polega na wierszującym skanowaniu materiału przez głowicę roboczą wytwarzającą strugę wodno-ścierną. Sterowanie czasem oddziaływania

strugi na materiał obrabiany, decydujące o głębokości erozji, polega na selektywnym wyborze pozycjonowania głowicy roboczej, w którym wykorzystuje się zróżnicowane natężenie oświetlenia obiektu, zarejestrowane na jego fotograficznym obrazie. Dzięki takiej procedurze z poszczególnych wierszy umieszczonych obok siebie w obrabianym materiale powstaje płaskorzeźba wyjściowego obrazu. Oprócz wyjaśnienia istoty takiej metody wykonywania płaskorzeźb w artykule tym omówiono zastosowane stanowisko badawcze oraz metodykę i warunki przestrzennego kształtowania materiałów. Zaprezentowano także rezultaty przeprowadzonych badań wraz z analizą jakości wytwarzanych powierzchni oraz przykłady obiektów wyrzeźbionych tą metodą w próbkach materiałów metalowych.

Electro-chemical monitoring of static recrystallization

F. FILUS, I. SCHINDLER, J. FIALA, S. LASEK, T. KUBINA

VSB – Technical University of Ostrava, Faculty of Metallurgy and Materials Engineering,
17. listopadu 15, 708 33 Ostrava, Czech Republic.

G. NIEWIELSKI, D. KUC, E. HADASIK

Silesian University of Technology, Faculty of Materials Engineering and Metallurgy,
ul. Krasińskiego 8, 40-019 Katowice, Poland.

The electro-chemical potentiokinetic method has proved to be a sensitive technique for monitoring of static recrystallization in austenitic steel AISI 304 after its cold forming and annealing. Results obtained in this manner are in very good conformity with the results of metallographic and X-ray analysis, as well as with the measured values of hardness. Corrosion current density appeared to be a suitable criterion for evaluation of development of relaxation processes.

Keywords: *static recrystallization; corrosion; stainless steels; x-ray diffraction; hardness*

1. Introduction

Recrystallization is a relaxation process, the result of which is generally non-equilibrium, non-ergodic state of material. As the individual structural characteristics develop in the course of recrystallization in different manner, the description of the state achieved at certain time often differs depending on the laboratory technique used for investigation of this phenomenon and subsequent evaluation of the course of recrystallization made on this basis [6] and [9]. Investigation of properties of austenitic stainless steel AISI 304 after its cold forming and high temperature annealing revealed very close correlation between the development of static recrystallization and results of electro-chemical measurements, which gives possibility of monitoring of relaxation processes by unconventional procedure.

2. Experimental

The steel AISI 304 with chemical composition as follows was investigated: 0.06 C – 1.71 Mn – 0.35 Si – 0.032 P – 0.025 S – 9.1 Ni – 18.3 Cr (in wt. %). Rolled flat bar with dimensions of cross-section thickness 4.23 x width 40 mm was characterised by fully recrystallized austenitic structure with minority occurrence of ferrite elongated in direction of rolling – Figure 1.

Total height reduction of 30.5% to the final thickness 2.94 mm was achieved by multi-pass laboratory rolling at room temperature. Then individual samples for subse-

quent investigation were prepared by annealing in electric resistance furnace – Table 1 gives their list.

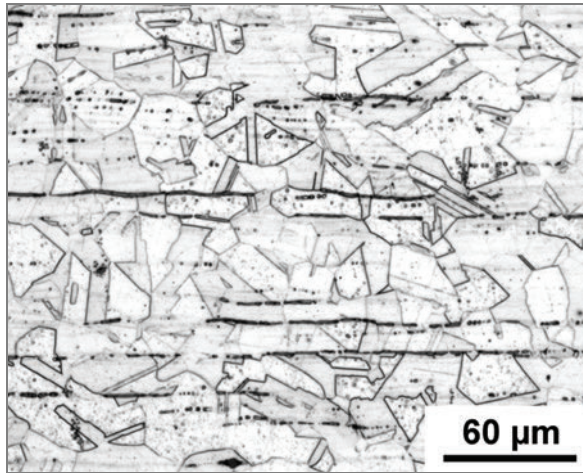


Fig. 1. Microstructure of investigated material in initial state

Table 1. Parameters of preparation of individual samples

Sample	Processing history
CR	cold rolled with total height reduction of 30.5 %
A1	subjected to recrystallization annealing after rolling – furnace 1000 °C/30 min./air
A2	subjected to recrystallization annealing after rolling – furnace 1000 °C/60 min./air
A3	subjected to recrystallization annealing after rolling – furnace 1050 °C/60 min./air

Basic description of the samples microstructure of was made using of optical microscopy (metallography) and it was completed by measurement of hardness HV5. X-ray evaluation of structure relates to magnitude of mosaic blocks (coherent diffraction regions) of austenite crystals [2–5]. Each mosaic block with due orientation gives rise to a diffraction spot – reflexion – on registration film. The basic form of Bragg's condition is

$$\lambda = 2d \sin \vartheta, \quad (1)$$

where:

λ – wavelength of the radiation used,

d – interplanar distance of diffracting lattice family,

ϑ – angle of incidence of the primary X-ray beam on the diffracting lattice family.

If mosaic blocks are larger than 10 μm , only few of them are present in diffracting volume and their reflexions are well discernable; on the basis of the number and size of discerned reflexions it is then possible to determine dimensions of large mosaic

blocks. If mosaic blocks are smaller than 10 μm , the diffracting volume contains many of them and their reflexions overlap; they create then on the film a continuous background under solitary reflexions of coarse-grained structural component. On the basis of relation of intensity of this background to the intensity of solitary reflexions it is then possible to calculate share of fine-grained component (i.e. of mosaic blocks smaller than 10 μm).

Additional information was obtained by electro-chemical potentiokinetic reactivation (EPR) method [1] and [7]. This is usually applied as rapid non-destructive method for evaluation of susceptibility of stainless steel to inter-crystalline corrosion. Principle of the method consists in creation of certain electro-chemical instability between metal and electrolyte, which has direct relation to anodic dissolution of metal – corrosion process. The sample is first polarised into passive area and at polarisation from this area re-activation is observed, which is dependent particularly on difference in contents of alloying elements (namely chromium) in solid solution and in depleted areas. Sensitised grain boundaries are as a result of chromium depletion below the limit of passivation covered by imperfect or defective passive film, which means that at re-activation the grain boundaries are dissolved preferentially and current density increases, while remaining part of surface, which has sufficient content of chromium and resistant passive film, corrodes only slightly and its changes be manifested by small difference of values on polarisation curve. This method is also suitable for testing of other types of corrosion related to local changes or re-distribution of content of elements, influencing passive state, since resistance and stability may be less dependent on other factors (e.g. deformation of crystal lattice by dislocations).

Surface of investigated samples from the steel AISI 304 was adjusted by fine wet grinding by SiC papers with granularity Nos. 400, 800 and 1500. Eating away of surface layer then occurred during repeated polarisation measurements. All the samples were right before testing cleaned by alcohol and rinsed by de-mineralised water. Tests of susceptibility of the sample to inter-crystalline corrosion were performed by DL-EPR method in accordance with the standard ISO 12732 [7], during which polarisation curves were measured and values of corrosion parameters were determined [8]. A three-electrode connection was used during testing: working electrode = sample; reference electrode = saturated calomel electrode (SCE); auxiliary electrode = platinum wire. Tests were realised in special vessels with solution of 0.5 M H_2SO_4 + 0.01 M KSCN at the temperature of 23 $^\circ\text{C}$, without mixing and with free access of air. Polarisation of the samples were made within an interval from -500 mV to $+300$ mV in respect to SCE and back at the rate of $100 \text{ mV}\cdot\text{min}^{-1}$ in both directions and with recording of polarisation curves (i.e. dependencies of current on potential).

3. Results and discussion

From the results of metallographic examination it follows that cold forming lead to creation of strongly anisotropic structure with deformation bands and with grains

elongated in the direction of rolling (Figure 2a). Austenitic grains recrystallized at high temperature annealing and they got coarser with increasing temperature (Figures 2b and 2c).

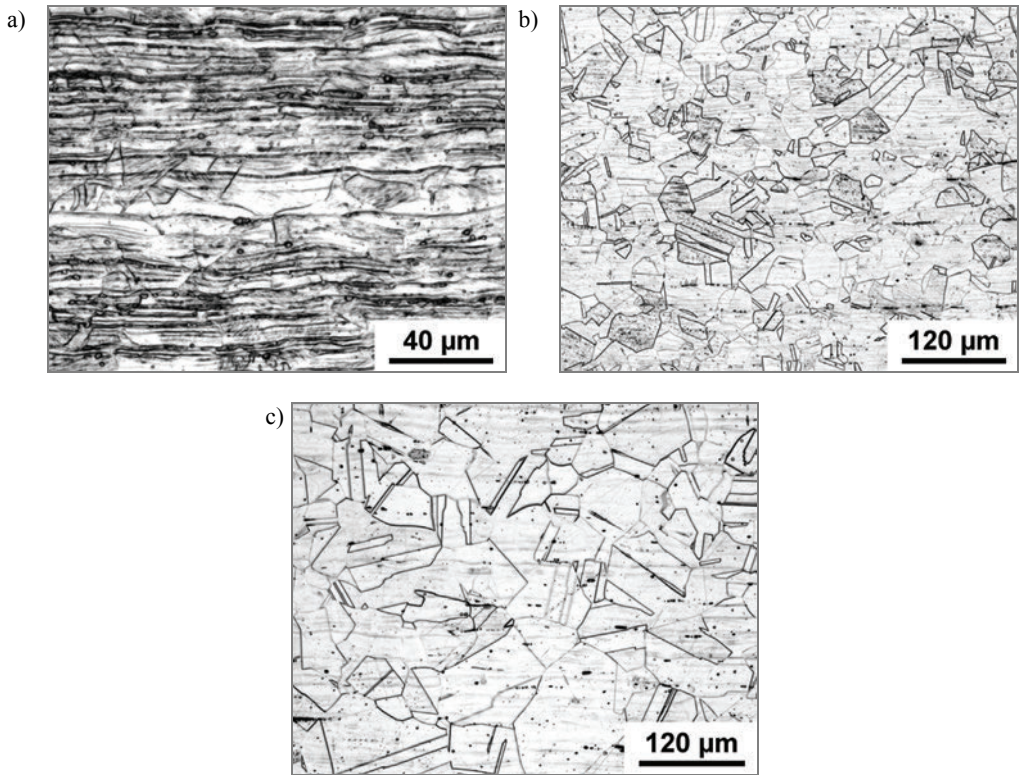


Fig. 2. Microstructure of selected samples: a) sample CR – after cold forming, b) sample A1 – after annealing 1000 °C/30 min, c) sample A3 – after annealing 1050 °C/60 min

Results of X-ray diffraction are documented in Figure 3. All the mosaic blocks in the cold rolled sample CR are smaller than 10 μm. When recrystallization is initiated by annealing, larger blocks begin to grow at the expense of smaller blocks, the number of which gradually decreases. Reflexions become sharper with increasing temperature and duration of annealing. This is caused by relaxation of curvature of slip planes, which occurs at plastic deformation. This curvature leads to “blurring” of diffraction traces, which are created by reflexion of X-radiation on deformed mosaic blocks as on curved mirrors. Magnified detail of X-ray diffraction pattern of the sample A3 shows that “blurring” of diffraction traces as a result of curvature of slip planes was not perfectly relaxed even after long term annealing.

The following parameters were determined by electro-chemical measurements: critical passivation current density, re-activation current density and corresponding

charges, and also corrosion potential, corrosion current density, average rate of corrosion and polarisation resistance of individual samples. It was established by regression and correlation analysis that:

- strong dependence exists between hardness of the sample HV5 and corresponding corrosion current density J_{cor} [$\mu\text{A}\cdot\text{cm}^{-2}$] (determined as share of corrosion current and exposed area with use of polarisation curve according to the Stern's method – see for example [7]);
- corrosion current density and corresponding average rate of corrosion or polarisation resistance are not mutually independent variables, since very unequivocal relations exist between them [1] and [8], and for this reason the results are further related only to the quantity J_{cor} .

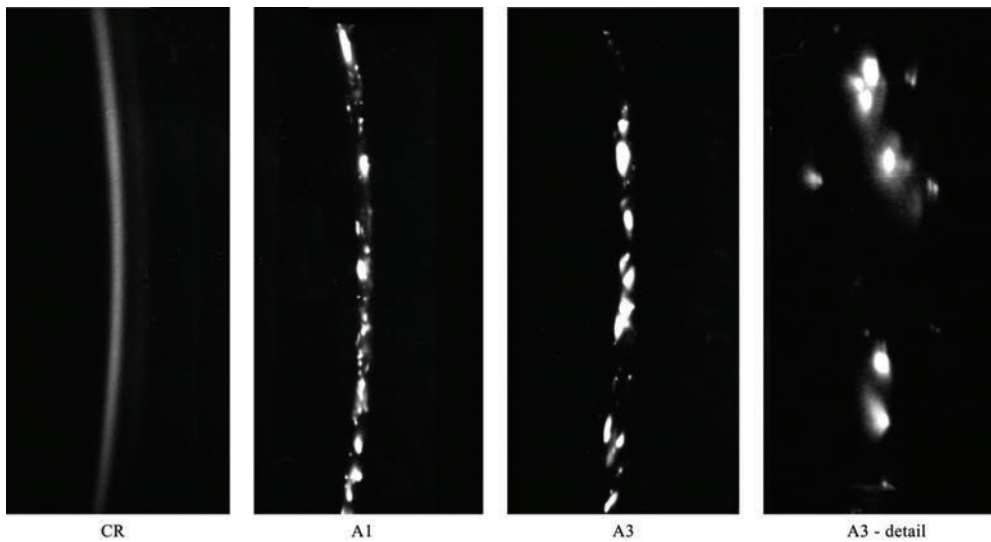


Fig. 3. Examples of obtained X-ray diffraction patterns

Table 2 summarises and compares the obtained values.

Table 2. Values of selected quantities measured on individual samples.

M – share of fine-grained component, D – size of mosaic blocks of coarse-grained component

Sample	HV5	J_{cor} [$\mu\text{A}\cdot\text{cm}^{-2}$]	X-ray diffraction	
			M [%]	D [μm]
CR	308	32.8	100	–
A1	166	18.4	10	53
A2	130	11.4	0	51
A3	126	8.7	0	60

It was determined that corrosion current density is a sensitive characteristic of processes, which occur in investigated material by static recrystallization after cold rolling. The values J_{cor} are determined by thermo-dynamic potential, which is significantly influenced by forming and subsequent annealing of material. The biggest corrosion current density shows material, the thermo-dynamic potential of which was increased by cold rolling. Annealing initiated recrystallization; energy input into material by rolling relaxes more intensively with increasing temperature of annealing and with longer duration of annealing. Material as a result of this becomes less reactive and corrosion current density decreases. This corresponds to drop of the measured hardness and to information obtained by evaluation of X-ray diffraction patterns. The relation $J_{\text{cor}} = f(\text{HV5})$ can be in the investigated case described with high precision by quadratic equation (see Figure 4).

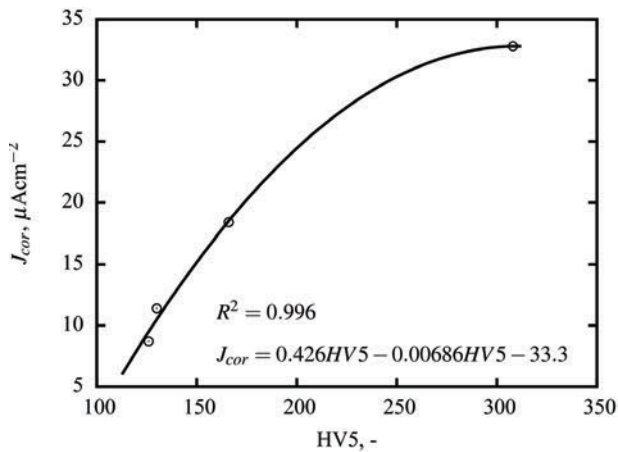


Fig. 4. Relation between the measured values of corrosion current density and hardness

The detail of the diffraction pattern of the sample A3 in Figure 3 confirms, that „blurring” of diffraction spots as a result of curvatures of slip planes did not relax completely even after one-hour annealing at the temperature of 1050 °C. This explains why corrosion current density after this annealing ($J_{\text{cor}} = 8.7 \mu\text{A}\cdot\text{cm}^{-2}$) is still higher than in initial state (before cold rolling $J_{\text{cor}} = 5.4 \mu\text{A}\cdot\text{cm}^{-2}$). It demonstrates at the same time the required sensitivity of the described electro-chemical technique for monitoring of recrystallization process [8].

4. Conclusion

The described electro-chemical potentiokinetic method has proved to be a sensitive technique for monitoring of static recrystallization processes in austenitic stainless steel AISI 304 after its cold forming and high temperature annealing. Results obtained in this manner are in very good conformity with the results of metallographic and X-ray

analysis, as well as with the measured values of hardness. Corrosion current density, or average corrosion rate related to it, appeared to be a suitable criterion for evaluation of development of relaxation processes.

Acknowledgement

This work was realized in the framework of solution of the project MSM 6198910015 (Ministry of Education of the Czech Republic).

References

- [1] ASTM G-102: *Calculations of corrosion rates and related information from electrochemical measurements*, 1999.
- [2] Fewster P.J., Andrew N.L.: *Reciprocal space mapping and ultra-high resolution diffraction of polycrystalline materials*, in: *Defect and microstructure analysis by diffraction*, Eds. R.L. Snyder, J. Fiala, H.-J. Bunge, Oxford University Press Inc., New York, 1999.
- [3] Fiala J., Kolega M.: *Applications of two-dimensional detectors in X-ray diffraction materials structure analysis*, Particle and Particle Systems Characterization, Vol. 22, No. 6, 2006, pp. 397–400.
- [4] Fiala J., Němeček S.: *X-ray diffraction imaging as a tool of mesostructure analysis*, Advances in X ray Analysis, Vol. 44, 2001, pp. 24–31.
- [5] Fiala J., Němeček S.: *XRD analysis of coarse crystalline materials*, in: *Applied crystallography*, Eds. H. Morawiec, D. Stróż, World Scientific, Singapore, 2001.
- [6] Himmel J. (ed.): *Recovery and recrystallization of metals*, American Institute of Mining, Metallurgical, and Petroleum Engineers, John Wiley and Sons, New York, 1963.
- [7] ISO 17475: *Corrosion of metals and alloys. Electrochemical test methods. Guidelines for conducting potentiostatic and potentiodynamic polarization measurements*, 2005.
- [8] Landolt D.: *Corrosion et chimie de surfaces des métaux*, Presse polytechniques et Universitaires Romandes, Lausanne, 1993.
- [9] Sakai T.T., Suzuki H.G. (eds.): *Recrystallization and related phenomena*, The Japan Institute of Metals, Sendai, 1999.

Elektrochemiczne monitorowanie przebiegu statycznej rekrytalizacji

W pracy zbadano możliwość elektrochemicznego monitorowania statycznej rekrytalizacji przy zastosowaniu metody potencjokinetycznej w austenitycznej stali AISI 304 po odkształceniu plastycznym na zimno i wyżarzaniu. Otrzymane wyniki wskazują na bardzo dobrą zgodność z wynikami badań metalograficznych i analizy rentgenowskiej oraz pomiarami twardości. Zmiany natężenia prądu korozyjnego mogą stanowić wygodne kryterium oceny przebiegu procesów relaksacyjnych.

Cellular automata in nonlinear vibration problems of two-parameter elastic foundation

W. GLABISZ

Wrocław University of Technology, Wybrzeże Wyspiańskiego 27 50-370 Wrocław, Poland.

Cellular automata procedure for the analysis of nonlinear viscously damped transverse vibrations of two-parameter elastic foundation was defined. Parameters were obtained by comparing the cellular automata defining rules with relations resulting from the discrete form of the mathematical description of the string modelling the foundation's surface layer. A series of numerical analysis of a foundation under arbitrary static or dynamic load, including moving forces and the simulation of the behaviour of rigid structures on a foundation were done. Numerical results demonstrate that cellular automata can constitute a simple and effective tool for the analysis of two-parameter elastic foundation complex problems which have not been analyzed in this way before.

Keywords: *cellular automata, two-parameter elastic foundation, nonlinear vibration, dynamic loading, moving forces*

1. Introduction

When describing reality, researchers naturally tend to include its complexity in the description, which leads to complicated mathematical models, usually in the form of ordinary differential equations, partial equations, differential-integral equation or integral equations. Depending on the complexity of the described phenomenon, the equations are solved by numerical methods or sometimes (for a narrow class of problems) by analytical methods.

Recently, instead of complex equations, simple mathematical models, called cellular automata (CA), have been increasingly used to describe physical phenomena. Cellular automata can be regarded as discrete dynamic systems whose evolution is described by simple local rules. Using cellular automata one can represent an investigated phenomenon as the synchronous mutual interaction of a space-time discrete set of cells. The behaviour of a cell depends on its state and the states of the cells in its nearest neighbourhood. One can say that cellular automata allow one to effectively describe global phenomena through local rules of the evolution of their discrete representation.

The idea and mathematical foundations of cellular automata were formed by von Neuman and Ulam in the 1940s [37]. Although CA became the subject of interest to researchers, it was as late as in the 1970s, when John Conway proposed the now famous game of life [21], that this interest rapidly grew and resulted in a great number

of research works on the theory and application of cellular automata. A broad survey of literature dealing with the description and use of CA can be found in, e.g., [46], [43], [35], [38], [39], [26]. Wolfram [49] contributed greatly to the theory of cellular automata and their possible use. He summarized his achievements in extensive monograph.

In recent years cellular automata have been effectively applied in: traffic flow problems [34], the simulation of brain tumour growth dynamics [25], biochemical phenomena [30], fluid and gas dynamics and particle transport [15], [7], ecological modelling [24], biological modelling [4], vegetation dynamics [3], migration problems [40], the modelling of reaction-diffusion systems [47], the modelling of water release and absorption in soils [45], soil erosion by water [2], the modelling of epidemics [48], forest fire modelling [5], the design of variable-stiffness composite layers [41] and in many other areas. Cellular automata have proved to be an effective tool in data compression and encryption [32], the generation of high-quality random numbers [44], cryptographic procedures [17] and in the analysis of partial differential Equations [42], [18]. In mechanics, CA have been used to describe the deformations of an elastic body and the frictionless contact between the body and a rigid foundation [1], and in non-linear string vibration problems [27–28] and [22]. In [22] an alternative formulation of the CA model of damped nonlinear transverse string vibrations was presented and it was shown that CA can be a simple and effective tool for the analysis of several complex problems previously not analyzed in this way.

One of the major mechanics problems is the analysis of structures resting on an elastic foundation and the analysis of the foundation's behaviour. The simplest one-parameter foundation model is the Winkler foundation, i.e. a system of densely spaced independent linear springs with specific spring stiffness [29]. The reaction of the Winkler foundation is proportional to displacements and arises in exclusively the nonzero displacement zone, which leads to discontinuities on the boundaries of the areas subjected and not subjected to load. The discontinuities are due to the lack of interaction between the springs of the Winkler foundation. Two-parameter foundations [50], in which interaction between the springs modelling the Winkler foundation was introduced in different ways, do not suffer from this drawback. Such a model can be perceived as a liquid with a tensed surface layer resting on densely spaced springs. Two-parameter foundation models make it possible to transfer shearing forces from areas under load to adjacent areas not subjected to load. Two-parameter models have an identical mathematical representation and differ in only their definitions of the foundation parameters. These elastic foundation models have been applied to several technical problems, assuming that the foundations react in both compressed and tensioned areas. Tensionless elastic foundations, whose reaction decays in the tensioned areas, make up another class of models. Foundations of this type have been used in many papers dealing with beams, rings and plates on one-parameter foundations [12–14], [23] and two-parameter foundations [10–11], [16], [19–20].

Problems relating to the behaviour of an elastic foundation and the structure resting on it are solved mainly by numerical methods based on local (differential) or global (integral) problem formulations.

The aim of this paper is to formulate a CA model of the two-parameter nonlinear elastic foundation and to apply it to:

- an analysis of a foundation under arbitrary static or dynamic load, including moving load;
- the simulation of the behaviour of rigid structures on a foundation, whose motion can be caused by any dynamic force load or any kinematic load.

In section 2, a CA formulation for nonlinear problems relating to the viscously damped transverse vibration of the two-parameter elastic foundation is presented. In section 3, test solutions are provided and the proposed approach is used to analyze the nonlinear vibration of a foundation under an arbitrary dynamic load and to analyze rigid structures whose motion can be caused by loads simulating earthquakes or crump in underground drifts. The results are summarized in section 4.

2. Cellular automata model of elastic foundation

The CA model which describes the nonlinear vibration of the two-parameter foundation is a modification of the CA model of nonlinear string vibrations. The modification consists in the incorporation of the Winkler foundation into the string model whereby a model of the two-parameter foundation (in which one of the parameter is the initial tension of the surface layer and the second is Winkler parameter) consistent with its physical interpretation presented in the introduction is obtained.

Let us assume that the model of the elastic foundation’s surface layer is a chain of evenly distributed point masses (cells) connected by elastic massless elements of a string whose fragment is shown in Figure 1.

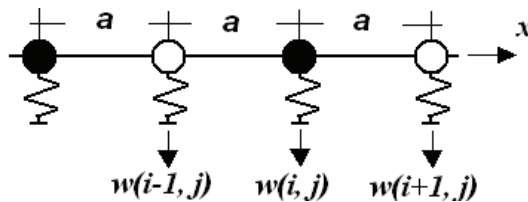


Fig. 1. Model of elastic foundation’s surface layer

The transverse displacement of the i -th mass of the foundation’s surface layer in the j -th time, called a cell state, is denoted as $w(i, j)$. As it is defined in the papers by Kawamura et al. [27–28], the evolution of the state of a string (which here models the foundation’s surface layer) can be divided into two stages identical in their description. For example, in the first stage the white balls in Figure 1 undergo displacement

while the black balls remain stationary, whereas in the second stage the opposite happens. Physically, this way of analyzing should be interpreted as the propagation of a transverse disturbance which in a given time interval covers exactly distance a (resulting from the adopted uniform division of the surface layer into n elements) between neighbouring balls, each of which can be a source of transverse vibration. State $(w(i, j))$ of a black ball after time Δt ($w(i, j+1)$), during which the transverse disturbance reaches the neighbouring balls and the black ball undergoes undamped free vibration not constrained by the reaction of the Winkler foundation, can be obtained from the relation

$$w(i, j+1) = w(i, j) + 2w_0, \quad (1)$$

where:

$$w_0 = 1/2[w(i-1, j) + w(i+1, j)] - w(i, j). \quad (2)$$

The relations are graphically interpreted in Figure 2.

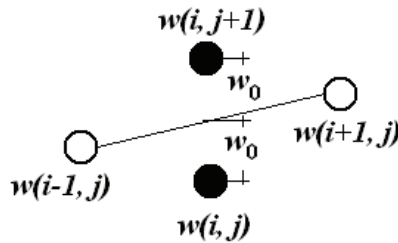


Fig. 2. Graphic interpretation of cell state update

If one takes into account the influence of the distributed (transverse to axis x of the surface layer) Winkler foundation reactions $-k(x)w(x, t)$ (where stiffness $k(x)$ is a Winkler foundation parameter), exciting forces $(q(x, t))$ and viscous damping $(C(x, t))$ on cell state $w(i, j+1)$, then one gets

$$w(i, j+1) = \delta[2w_0 + \chi f(i, j+1)] + w(i, j), \quad (3)$$

where parameters δ and χ (undetermined yet) are responsible for respectively vibration damping and the effect of current transverse load $f(i, j+1)$ (being the resultant of the load and the foundation reaction) on displacement state $w(i, j+1)$. It should be noted that the current (at instant $j+1$) state of transverse load is included in relation (3), whereby the convergence of the algorithm significantly improves in the case of non-linear vibrations.

Taking relation (2) into account one can write relation (3) in the following form

$$w(i, j + 1) = \delta[w(i - 1, j) + w(i + 1, j)] + (1 - 2\delta)w(i, j) + \delta \chi f(i, j + 1), \tag{4}$$

which represents the state of the i -th cell in time $j + 1$ (a procedure for the evolution of the cell state) as a function of: its previous state $w(i, j)$ (before time Δt passes), states ($w(i - 1, j)$, $w(i + 1, j)$) of the neighbouring cells, the current values of the Winkler foundation's reactions, transverse load and damping.

The nonlinear model of the transverse vibration of the string (here modelling the foundation's tensed surface layer) was first formulated by Kirchhoff [31], and Carrier [8–9] included the longitudinal displacement of the string in its nonlinear vibration. The theoretical formulation presented in the above works was further developed in numerous publications. A survey of this literature with regard to theoretical formulations, numerical methods and experimental investigations can be found in [33], [6] and [36].

The mathematical Kirchhoff model [31] of the transverse nonlinear vibrations of the string modelling the foundation's surface layer, neglecting displacements along the string's axis, averaging tension (N) over its length (l) and taking into account the effect of the linear reaction of the Winkler foundation, can be derived (in an elementary way) from Newton's second law and written as

$$\rho A \frac{\partial^2 w(x, t)}{\partial t^2} + C \frac{\partial w(x, t)}{\partial t} - \left(N_0 + \frac{EA}{2l} \int_0^l \left(\frac{\partial w(x, t)}{\partial x} \right)^2 dx \right) \frac{\partial^2 w(x, t)}{\partial x^2} + k(x)w(x, t) = q(x, t), \tag{5}$$

where: ρ , E , C , N_0 , $k(x)$ and $q(x, t)$ are respectively: the density of the surface layer material, Young's modulus, the foundation's viscous damping parameter, the initial tension of the surface layer, a parameter characterizing the reaction of the Winkler foundation, and the intensity of transverse load.

Applying difference approximation (central difference for the second derivatives and $\partial w / \partial t = (w(x, t + \Delta t) - w(x, t)) / \Delta t$) to $\partial^2 w / \partial t^2$, $\partial^2 w / \partial x^2$ and $\partial w / \partial t$ one can write Equation (5) (after elementary transformations and taking into account the current (in time $t + \Delta t$) transverse loads) in the form presented in papers by Kawamura et al. [27–28] and Glabisz [22], which is here completed with the current reaction of the Winkler foundation

$$w(x, t + \Delta t) = \frac{1}{\gamma + 1} [w(x + \Delta x, t) + w(x - \Delta x, t)] + \frac{\gamma - 1}{\gamma + 1} w(x, t) + \frac{1}{\gamma + 1} \frac{(\Delta t)^2}{\rho A} [q(x, t + \Delta t) - k(x)w(x, t + \Delta t)], \tag{6}$$

where:

$$\gamma = C\Delta t / \rho A,$$

$$1/(\gamma + 1) * (\Delta t)^2 / \rho A = (\Delta t)^2 / (C\Delta t + \rho A).$$

Relation (6) includes the previously described procedure for the two-stage updating of the surface layer state, according to which the cell state updated in time t ($w(x, t)$) was not updated in the previous step $t - \Delta t$ and so ($w(x, t - \Delta t) = w(x, t)$).

By comparing relations (4) and (6) one can easily determine the so far unknown parameters δ and χ of the cellular automaton.

$$\delta = \frac{1}{\lambda + 1} = \frac{\rho A}{c\Delta t + \rho A} \quad (7)$$

$$\chi = \frac{\Delta t}{\rho A}.$$

For relations (7) one can show that $(1 - 2\delta) = (\gamma - 1)/(\gamma + 1)$, which fully agrees with the relations proposed by Kawamura et al. [28].

Considering that the work of load $q(x, t)$ and Winkler foundation reaction $-k(x)w(x, t)$ for the displacements shown in Figure 2 is a linear displacement function and the energy dissipation function is a homogenous quadratic velocity function, the current load in relation (4) is $f(i, j + 1) = q(i, j + 1) - k(i)w(i, j + 1)$ and the damping per unit string length parameter in relation is (7) $c = \frac{2}{3}C$, which is due to the zero velocities of the balls directly neighbouring the ball moving in one of the stages of string evolution [22].

Because of the dependence of $f(i, j + 1)$ on $w(i, j + 1)$, after an elementary transformation Equation (4) can be written as follows

$$w(i, j + 1) = \frac{1}{1 + \delta \chi k(x)} \{ \delta [w(i - 1, j) + w(i + 1, j)] + (1 - 2\delta)w(i, j) + \delta \chi q(i, j + 1) \}. \quad (8)$$

The equation together with (7) and definition c explicitly define the cellular automaton evolution law for the nonlinear transverse vibration of the two-parameter elastic foundation in which one of the parameter is the initial tension of the surface layer N_0 and the second is Winkler foundation parameter $k(x)$.

Velocity v with which the wave of surface layer transverse disturbances propagates is defined as $v = \sqrt{N / \rho A}$ and so in the nonlinear equation analyzed here it is

$$v(t) = \sqrt{\frac{1}{\rho A} \left(N_0 + \frac{EA}{2l} \int_0^l \left(\frac{\partial w(x, t)}{\partial x} \right)^2 dx \right)}. \quad (9)$$

According to the proposal by Kawamura et al. [28], time-variable velocity $v(t)$ is the basis for the use of evolution-variable time increment Δt (changing the values of parameters δ and χ) so matched that the disturbance wave front covers exactly distance $a = l/n$ (constant throughout the entire analysis) during this time.

3. Numerical analysis

A numerical analysis of the behaviour of an exemplary two-parameter nonlinear elastic foundation with length $l = 80.0$ m and a width of 1.0 m is carried out here for several test problems whose schemes are shown in Figure 3.

In all the problems the foundation is divided into 100 equal segments (cells), each with length $a = l/n = 0.8$ m. By properly matching tension N_0 of the surface layer, its density ρ and cross-sectional surface area A one can freely shape initial velocity v_0 of the propagation of the transverse wave in the foundation. Surface area A should be understood as a conventional part of the foundation's cross section, which undergoes transverse vibration. By matching Young's modulus, the value of foundation parameter $k(x)$ and surface layer tension N_0 one can model (consistently with site surveys) the transverse displacements of the foundation and the shape of the depression in the surface of the ground.

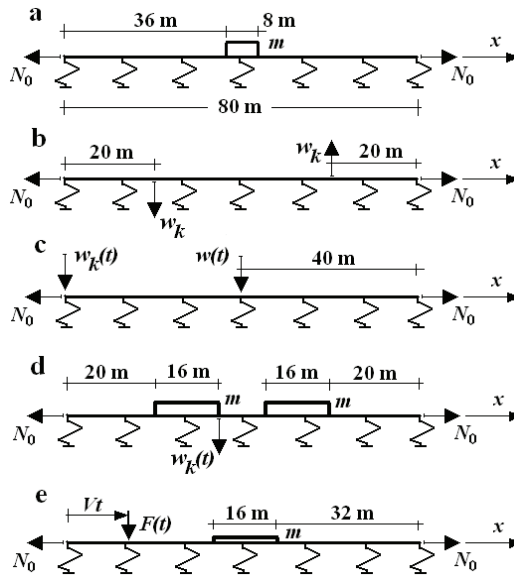


Fig. 3. Schemes of test problems

In the problems analyzed below it was assumed that $E = 20.0$ MPa, $\rho = 2.0 \times 10^3$ kg/m³, $A = 2.0$ m², viscous damping parameter $C = 2.0 \times 10^6$ Ns/m² and gravitational acceleration $g = 10.0$ m/s². Figure 4 shows exemplary displacement states of the

elastic foundation surface under a rigid slab having the same width as the analyzed foundation band, a length of 8.0 m and mass $m = 20000.0 \text{ kg/m}$ (Figure 3a). The parameter characterizing the Winkler foundation was $k(x) = 10^3 \text{ kN/m}^3$ and $k(x) = 10^4 \text{ kN/m}^3$ for respectively low-bearing soil (Figure 4a) and high-bearing soil (Figure 4b). The depressions in the foundation surface at $N_0 = 10^5 \text{ N}$ and $N_0 = 5.0 \times 10^6 \text{ N}$ are represented by respectively a solid line and a dashed line.

As it can be easily verified, the elementary condition that the load (the weight of the slab) and the reaction of the elastic foundation are equal and the relative error for adopted division $n = 100$ does not exceed 0.5% and decreases with increasing n is satisfied in the considered problems.

The velocities of transverse wave propagation in soil are: $v_0 = \sqrt{N_0 / \rho A} = 5.0 \text{ m/s}$ at $N_0 = 10^5 \text{ N}$ and $v_0 = 35.36 \text{ m/s}$ at $N_0 = 5.0 \times 10^6 \text{ N}$ and according to formula (9) they change with the deformation of the surface layer.

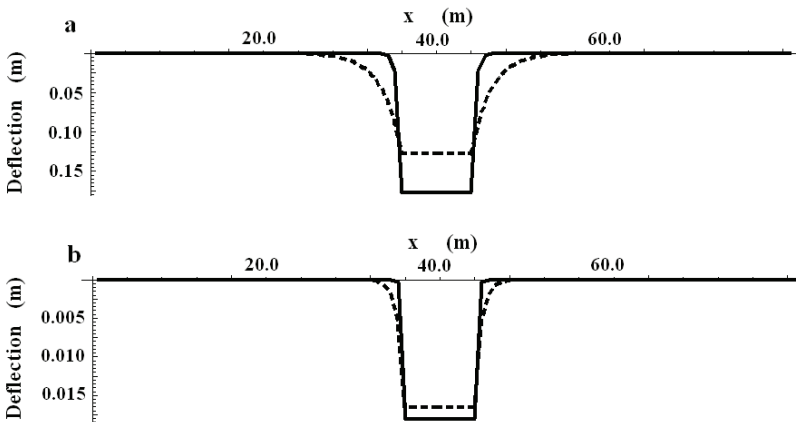


Fig. 4. Depression in foundation surface at: $k(x) = 10^3 \text{ kN/m}^3$ a) $k(x) = 10^4 \text{ kN/m}^3$, b) two tension forces: $N_0 = 10^5 \text{ N}$ (solid line) and $N_0 = 5.0 \times 10^6 \text{ N}$ (dashed line)

After simple modifications the CA algorithm for a foundation having the same characteristic $k(x)$ under both compression and tension can be applied to a foundation whose characteristic under tension ($p \times k(x)$), regulated by parameter p , is different than the one adopted for compression. Figure 5 shows the states of displacement of the foundation surface layer ($k(x) = 10^2 \text{ kN/m}^3$) under static kinetic excitation w_k at $1/4$ of span l ($w_k = 0.9 \text{ m}$) and $3/4l$ ($w_k = -0.9 \text{ m}$) (Figure 3b) for $p = 1$ (solid line) and against the background of this solution (dashed line) for $p < 1$. It was assumed that $N_0 = 10^5 \text{ N}$ and $p = 0.4$ (Figure 5a) and $N_0 = 5.0 \times 10^6 \text{ N}$ and $p = 0.05$ (Figure 5b). Tests of this kind allow one to select model parameters which satisfactorily describe the analyzed reality.

Under assigned dynamic kinetic excitation $w_k(t) = 2.0 \times \cos(0.1 \times t)$ of the left extreme point of the foundation with $k(x) = 10 \text{ kN/m}^3$ and $C = 2.0 \times 10^2 \text{ Ns/m}^2$ (Figure 3c), the point's state of displacement $w(t)$ in the middle of the foundation's span is

shown in Figure 6a while Figure 6b shows a ratio ($\beta = v/v_0$) of the elastic wave velocity (v) under current tension $N(t)$ to the elastic wave velocity (v_0) under initial tension $N_0 = 10^5$ N.

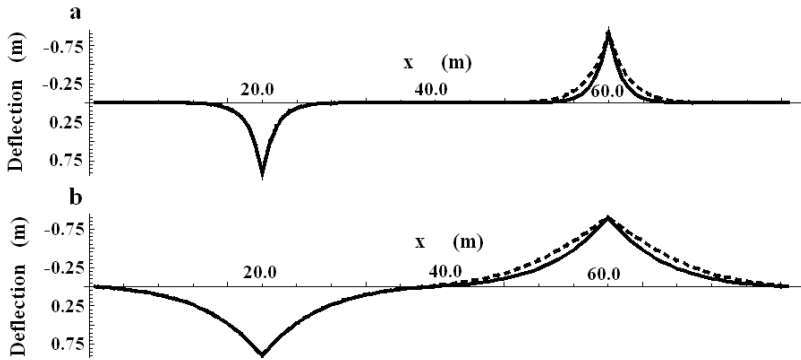


Fig. 5. Excited kinetic foundation displacements under different tension forces at a) $p = 1$ (solid lines) and $p = 0.4$ (dashed line), b) at $p = 0.05$ (dashed line)

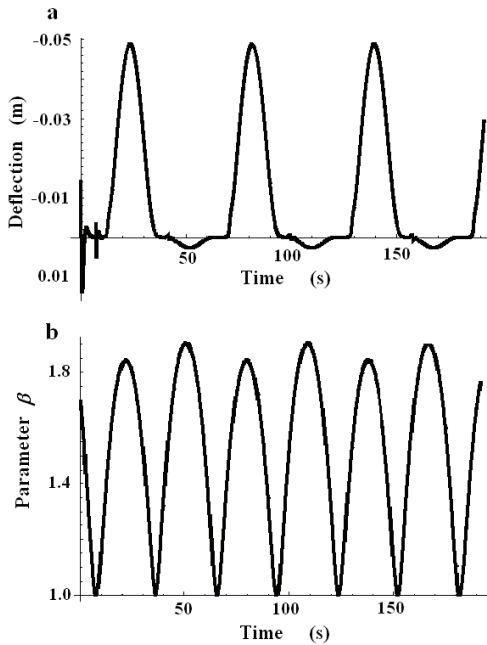


Fig. 6. a) Foundation midpoint displacement $w(t)$, b) parameter β versus time t

Parameter β can be regarded as a measure of problem nonlinearity. In the case of large displacements causing a significant change in the tension force, parameter β can assume values much higher than the ones shown in Figure 6b. One should bear in

mind that force $N(t)$ in a given instant of time is constant along the length of the foundation whose surface layer undergoes exclusively transverse vibration.

The states of displacement of the elastic foundation loaded with the weight of two rigid bodies of buildings, each with mass $m = 5000.0$ kg/m (Figure 3d), at $k(x) = 10^3$ kN/m³, $N_0 = 5.0 \times 10^6$ N, $C = 2.0 \times 10^6$ Ns/m² and $p = 0.5$ are shown in Figures 7 and 8. Figures 7a and 7b show the displacement of the foundation's surface layer at respectively $w_k(t) = 0.0$ m and $w_k(t) = 0.3$ m, which may model the state of the buildings before and after a local crump. The states of displacement of the system in selected instants t after sudden dynamic kinematic excitation $w_k(t) = 0.3 + 0.3 \times \cos(0.1t)$ are shown in Figure 8. The analyses whose results are presented in Figures 7 and 8 were carried out in two stages. In the first stage the state of the foundation under the weight of the buildings was generated and in the second stage it was disturbed with prescribed kinetic excitations.

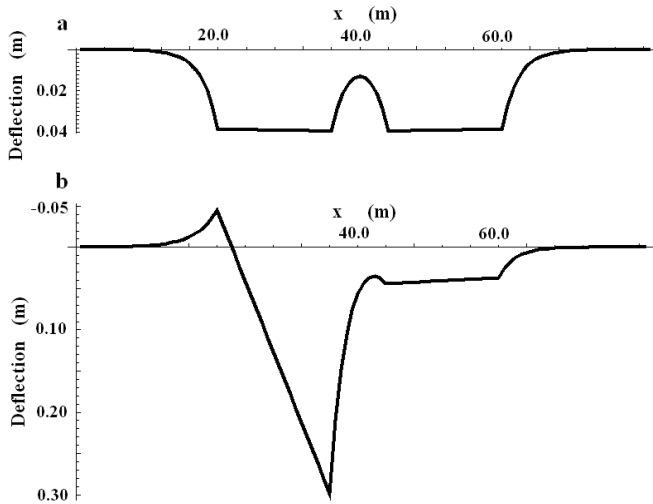


Fig. 7. a) Displacements of foundation under weight of buildings before and, b) after local crump $w_k(t) = 0.3$ m

The effectiveness of the CA algorithm was also tested for moving point load. Figure 9 shows displacement states in different instants t , starting from the appearance of point force $F(t) = 10^5$ N moving in uniform motion with velocity $V = 2.0$ m/s. The force moved on a foundation having parameters as shown in Figures 7 and 8 and additionally loaded (in its centre) with the weight of a rigid slab with mass $m = 5000.0$ kg/m and a span of 16.0 m (Figure 3e). In problems of this type the choice of a proper value of damping parameter C significantly affects the solution.

The CA model presented in section 2 was effectively applied also to problems with: a dynamically changing moving force, time-variable tension of the surface layer and variable foundation characteristic $k(x)$.

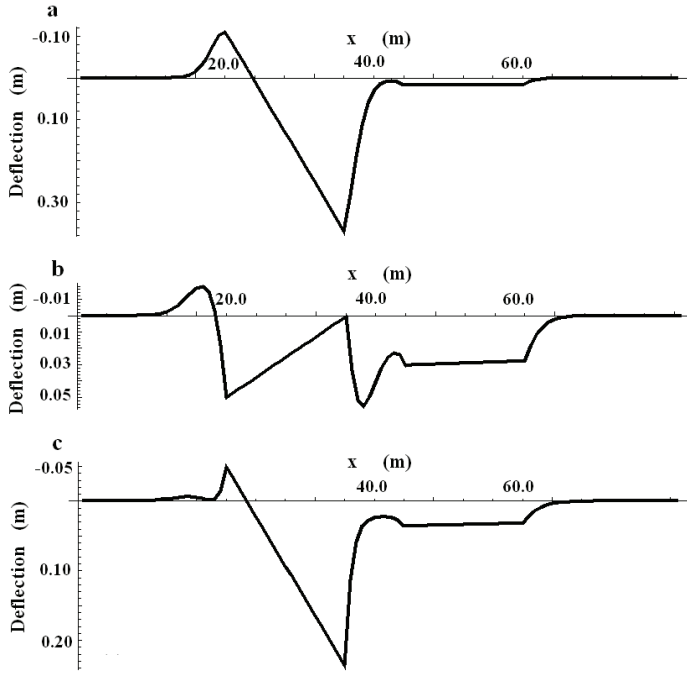


Fig. 8. Foundation displacements caused by dynamic kinetic load $w_k(t)$ in time a) $t = 6.74$ s, b) $t = 15.77$ s, c) $t = 22.56$ s

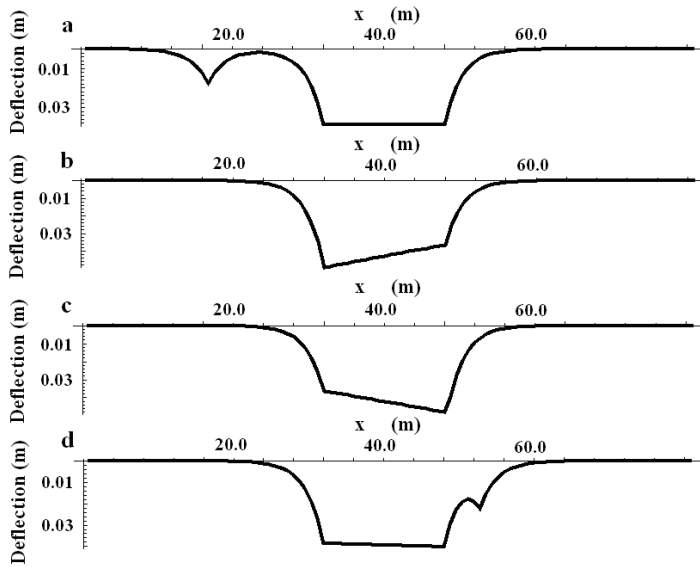


Fig. 9. Foundation displacements caused by moving force $F(t)$ in time a) $t = 8.0$ s, b) $t = 16.0$ s, c) $t = 24.0$ s, d) $t = 28.0$ s

4. Recapitulation and conclusions

Cellular automata can be an effective alternative to complex mathematical descriptions of many physical phenomena. For this purpose simple repeatable rules describing the evolution of CA, operating in discrete representations of the phenomena, are used. A major aspect decisive for the effectiveness of the use of CA models is parameter calibration.

In this paper, a CA procedure suitable for the analysis of the nonlinear viscously damped transverse vibration of the two-parameter elastic foundation was defined. CA parameters were obtained by comparing the CA evolution defining rules with the relations stemming from the discrete form of the mathematical description of the transverse foundation surface layer vibration model. Several numerical tests were carried out and their results were found to qualitatively and quantitatively agree with those of the solutions reported in the literature. On this basis one can say that:

- cellular automata are simple and effective tools for the analysis of the linear and nonlinear vibrations of the two-parameter elastic foundation,
- cellular automata procedure may be very useful in numerical solutions of many difficult dynamic problems of an elastic foundation e.g.: moving forces with arbitrary acceleration, vibration of stiff block under kinetic excitation, earthquake modelling and so on,
- the CA algorithm can be easily modified whereby different complex problems can be analyzed (this usually requires simple changes in the algorithm's structure, e.g. when unilateral Winkler foundation is introduced, Winkler parameters are described by any function or any local constraints are introduced).

References

- [1] Abdellaoui M., El Jai A., Shillor M.: *Cellular automata model for contact problem*, Mathematical and Computer Modelling, Vol. 36, 2002, pp. 1099–1114.
- [2] Ambrosi D.D., Di Gregorio S., Gabriele S., Gaudio R.: *A cellular automata model for soil erosion by water*, Phys. Chem. Earth (B), Vol. 26, 2001, pp. 33–39.
- [3] Balzter H., Braun P.W., Kohler W.: *Cellular automata models for vegetation dynamics*, Ecological Modelling, Vol. 107, 1998, pp. 113–125.
- [4] Bard G., Edelstein-Keshet L.: *Cellular automata approaches to biological modelling*, J. Theor. Biol., Vol. 160, 1993, pp. 97–133.
- [5] Barros F.J., Mendes M.T.: *Forest fire modelling and simulation in DELTA environment*, Simulation Practice and Theory, Vol. 5, 1997, pp. 185–197.
- [6] Bilbao S.: *Conservative numerical methods for nonlinear strings*, J. Acoust. Soc. Am., Vol. 118, 2005, pp. 3316–3327.
- [7] Boghosian B.M.: *Lattice gases and cellular automata*, Future Generation Computer Systems, Vol. 16, 1999, pp. 171–185.
- [8] Carrier G.F.: *A note on the vibrating string*, Q. J. Appl. Math., Vol. 7, 1949, pp. 97–101.

- [9] Carrier G.F.: *On the nonlinear vibration problem of the elastic string*, Q. J. Appl. Math., Vol. 3, 1945, pp. 157–165.
- [10] Celep Z., Demir F.: *Circular rigid beam on a tensionless two-parameter elastic foundation*, Z. Angew. Math. Mech., Vol. 85, 2005, pp. 431–439.
- [11] Celep Z.: *Dynamic response of a beam on elastic foundation*, Z. Angew. Math. Mech., Vol. 64, 1984, pp. 279–286.
- [12] Celep Z., Gençoğlu M.: *Forced vibrations of rigid circular plate on a tensionless Winkler edge support*, Journal of Sound and Vibration, Vol. 263, 2003, pp. 945–953.
- [13] Celep Z.: *In-plane vibrations of circular rings on a tensionless foundation*, Journal of Sound and Vibration, Vol. 143, 1990, pp. 461–471.
- [14] Celep Z., Malaika A., Anu-Hussein M.: *Forced vibrations of a beam on a tensionless elastic*, Journal of Sound and Vibration, Vol. 128, 1989, pp. 235–246.
- [15] Chopard B., Masselot A.: *Cellular automata and lattice Boltzmann methods: a new approach to computational fluid dynamics and particle transport*, Future Generation Computer Systems, Vol. 16, 1999, pp. 249–257.
- [16] De Rosa M.A., Maurizi M.J.: *The influence of concentrated masses and Pasternak soil on the free vibrations of Euler beams – exact solution*, Journal of Sound and Vibration, Vol. 212, 1998, pp. 573–581.
- [17] Del Rey A.M., Mateus J.P., Sanches G.R.: *A secret sharing scheme based on cellular automata*, Applied Mathematics and Computation, Vol. 170, 2005, pp. 1356–1364.
- [18] Doeschl A., Davison M., Rasmussen H., Reid G.: *Assessing cellular automata based models using partial differential equations*, Mathematical and Computer Modelling, Vol. 40, 2004, pp. 977–994.
- [19] Filipich C.P., Rosales M.B.: *A further study about the behaviour of foundation piles and beams in a Winkler–Pasternak soil*, Int. J. Mech. Sci., Vol. 44, 2002, pp. 21–36.
- [20] Filipich C.P., Rosales M.B.: *A variant of Rayleigh's method applied to Timoshenko beams embedded in a Winkler-Pasternak medium*, Journal of Sound and Vibration, Vol. 124, 1988, pp. 443–451.
- [21] Gardner M.: *The fantastic combinations of John Conway's new solitaire game "Life"*, Sci. Am., Vol. 223, 1970, pp. 120–123.
- [22] Glabisz W.: *Cellular automata in nonlinear string vibration*, Archives of Civil and Mechanical Engineering, Vol. 10, 2010, pp. 27–41.
- [23] Guler K., Celep Z.: *Static and dynamic responses of a circular plate on a tensionless elastic foundation*, Journal of Sound and Vibration, Vol. 183, 1995, pp. 185–195.
- [24] Hogeweg P.: *Cellular automata as a paradigm for ecological modelling*, Applied Mathematics and Computation, Vol. 27, 1988, pp. 81–100.
- [25] Kansal A.R., Torqato S., Harsh IV G.R., Chiocca E.A., Deisboeck T.S.: *Simulated brain tumour growth dynamics using a tree-dimensional cellular automata*, J. Theor. Biol., Vol. 203, 2000, pp. 367–382.
- [26] Kari J.: *Thory of cellular automata: a survey*, Theoretical Computer Science, Vol. 334, 2005, pp. 3–33.
- [27] Kawamura S., Shirashige M., Iwatsubo T.: *Simulation of the nonlinear vibration of a string using the cellular automation method*, Applied Acoustics, Vol. 66, 2005, pp. 77–87.
- [28] Kawamura S., Yoshida T., Minamoto H., Hossain Z.: *Simulation of the nonlinear vibration of a string using cellular automata based on the reflection rule*, Applied Acoustics, Vol. 67, 2006, pp. 93–105.

- [29] Kerr A.D.: *Elastic and viscoelastic foundation models*, J. Appl. Mech., Vol. 31, 1964, pp. 491–498.
- [30] Kier L.B., Chao-Kun Cheng, Testa B.: *Cellular automata models of biochemical phenomena*, Future Generation Computer Systems, Vol. 16, 1999, pp. 273–289.
- [31] Kirchhoff G.: *Vorlesungen über Mathematische Physik: Mechanik*, Leipzig, Druck und Verlag von B.G. Teubner, 1867.
- [32] Lafe O.: *Data compression and encryption using cellular automata transforms*, Engng Applic. Artif. Intell., Vol. 10, 1997, pp. 581–591.
- [33] Li-Quen Chen, Hu Ding: *Two nonlinear models of a transversely vibrating string*, Arch. Appl. Mech., Vol. 78, 2008, pp. 321–328.
- [34] Maerivoet S., De Moor B.: *Cellular automata of road traffic*, Physics Reports, Vol. 419, 2005, pp. 1–64.
- [35] Mitchell M., Crutchfield J., Das R.: *Evolving cellular automata with genetic algorithms: a review of recent work*, First International Conference on Evolutionary Computation and its Applications, 1996.
- [36] Molteno T.C., Tuffillaro N.B.: *An experimental investigation into the dynamics of a string*, Am. J. Phys., Vol. 72, 2004, pp. 1157–1169.
- [37] Neumann J.V.: *The theory of self-reproducing automata*, Burks A.W. (ed). Urbana and London, Univ. of Illinois Press, 1966.
- [38] Pal Chaudhuri P., Chowdhury A.R., Nandi S., Chatterjee S.: *Additive cellular automata – theory and applications*, USA, IEEE Computer Society Press, Vol. 1, 1997.
- [39] Sarkar P.: *A brief history of cellular automata*, ACM Computing Systems, Vol. 32, 2000, pp. 80–107.
- [40] Schonfisch B., Lacoursiere C.: *Migration in cellular automata*, Physica D, Vol. 103, 1997, pp. 537–553.
- [41] Setoodeh S., Gurdal Z., Watson L.T.: *Design of variable-stiffness composite layers using cellular automata*, Comput. Methods Appl. Mech. Engrg., Vol. 195, 2006, pp. 836–851.
- [42] Toffoli T.: *Cellular automata as an alternative to (rather than an approximation of) differential equations in modelling physics*, Physica 10D, 1984, pp. 117–127.
- [43] Toffoli T., Margolus N.: *Invertible cellular automata: a review*, Physica D, Vol. 66, 1994, pp. 1–24.
- [44] Tomassini M., Sipper M., Zolla M., Perrenoud M.: *Generating high-quality random numbers in parallel by cellular automata*, Future Generation Computer Systems, Vol. 16, 1999, pp. 291–305.
- [45] Townend J.: *Modelling water release and absorption in soils using cellular automata*, Journal of Hydrology, Vol. 220, 1999, pp. 104–112.
- [46] Vollmar T.: *Cellular space and parallel algorithms: an introductory survey. Parallel computation-parallel mathematics*, Feilmeier M. (ed), North Holland Publishing Co, 1977, pp. 49–58.
- [47] Weimar J.R.: *Cellular automata for reaction-diffusion systems*, Parallel Computing, Vol. 23, 1997, pp. 1699–1715.
- [48] White S.H., Del Rey A.M., Sanches G.R.: *Modelling epidemics using cellular automata*, Applied Mathematics and Computation, Vol. 186, 2007, pp. 193–202.
- [49] Wolfram S.: *A new kind of science*, Champaign, Wolfram Media Inc., 2002.
- [50] Zhang Y.: *Tensionless contact of a finite beam resting on Reissner foundation*, Int. J. Mech. Sci., Vol. 50, 2008, pp. 1035–1041.

Automaty komórkowe w nieliniowych zagadnieniach drgań dwuparametrowego podłoża sprężystego

W artykule zdefiniowano procedurę automatów komórkowych, którą przystosowano do analizy nieliniowych, wiskotycznie tłumionych drgań poprzecznych dwuparametrowego podłoża sprężystego. Parametry automatów komórkowych otrzymano porównując reguły definiujące ewolucję CA ze związkami wprost wynikającymi z dyskretnej postaci matematycznego opisu drgań struny modelującej warstwę wierzchnią podłoża. Przeprowadzono szereg analiz numerycznych zachowania się podłoża sprężystego pod działaniem obciążeń statycznych i dynamicznych, obciążeń ruchomych i obciążeń sztywnymi blokami. Wykonane testy numeryczne pokazują, że automaty komórkowe mogą być prostym i skutecznym narzędziem analizy szeregu złożonych zagadnień zachowania się dwuparametrowego podłoża sprężystego dotychczas tym sposobem nie analizowanych.

The influence of material properties and crack length on the Q -stress value near the crack tip for elastic-plastic materials for single edge notch plate in tension

M. GRABA

Kielce University of Technology, Faculty of Mechatronics and Machine Design,
Chair of Fundamentals of Machine Design, Al. 1000-lecia PP 7, 25-314 Kielce, Poland.

In the paper the values of the Q -stress determined for various elastic-plastic materials for single edge notched plates in tension (SEN(T)) presented. Used in the paper specimens, are the basic structural elements, which can be used to idealizing real construction, based on FITNET procedure. The influence of the yield strength, the work-hardening exponent and the crack length on the Q -parameter was tested. The numerical results were approximated by the closed form formulas. All obtained results may be a handy catalogue of the J - Q curves, which may be useful in engineering practice.

Keywords: *fracture mechanics, cracks, Q -stress, stress fields, HRR solution, FEM, J -integral*

1. Theoretical backgrounds for elastic-plastic fracture mechanics

In 1968 J.W. Hutchinson [9] published the fundamental paper, which characterized stress fields in front of a crack for Ramberg-Osgood (R-O) material in the form:

$$\sigma_{ij} = \sigma_0 \left(\frac{J}{\alpha \sigma_0 \varepsilon_0 I_n r} \right)^{\frac{1}{1+n}} \tilde{\sigma}_{ij}(\theta, n), \quad (1)$$

where:

r and θ – polar coordinates of the coordinate system located at the crack tip,

σ_{ij} – the components of the stress tensor,

J – the J -integral,

n – R-O exponent,

α – R-O constant,

σ_0 – yield stress,

ε_0 – strain related to σ_0 through $\varepsilon_0 = \sigma_0/E$.

Functions $\tilde{\sigma}_{ij}(n, \theta)$, $I_n(n)$ must be found by solving the fourth order non-linear homogenous differential equation independently for plane stress and plane strain [9]. Full algorithm and the computer program for evaluation these function are presented in [5]. Equation (1) is commonly called the “HRR solution”.

The HRR solution includes the first term of the infinite series only. The numerical analysis shown, that results obtained using the HRR solution are different from the results obtained using the finite element method (FEM). To eliminate this difference, it's necessary to use more terms in the HRR solution.

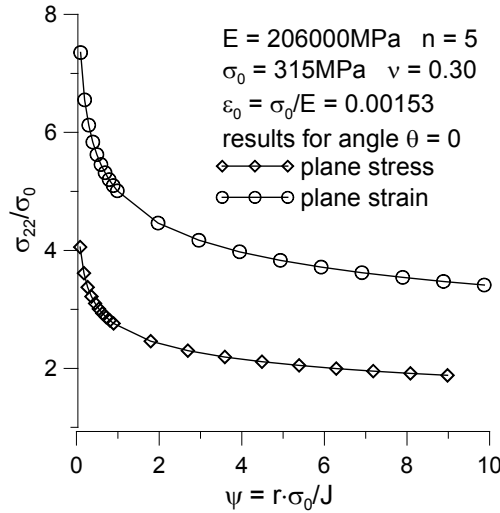


Fig. 1. The crack opening stress distribution for elastic-plastic materials, obtained using the HRR solution

In 1985 Li and Wang [12] using two terms in the Airy function, obtained the second term of the asymptotic expansion for the two materials described by $n = 3$ and $n = 10$. Next, they compared their results with the HRR fields and FEM results. Their analysis shown, that using the two term solution to describe the stress field near the crack tip, brings closer analytical results to FEM results. Two term solution much better describes the stress field near the crack tip, and the value of the second term, which may not to be negligible, depends on the material properties and the geometry specimen.

In 1993 Yang, Chao and Sutton [18] using the Airy function with the separate variables in the infinite series form, proposed, that stress field near the crack tip may be described by the Equation (2) in the infinite series form:

$$\frac{\sigma_{ij}}{\sigma_0} = \sum_{k=1}^{+\infty} A_k \bar{r}^{\gamma_k} \tilde{\sigma}_{ij}^{(k)}(\theta), \tag{2}$$

where:

- k – the number of the series terms,
- A_k – the amplitude for the k series term,
- \bar{r} – the normalized distance from the crack tip,

s_k – power exponent for the k series term,
 $\tilde{\sigma}_{ij}^{(k)}$ – “stress” function.

When limited to only three terms, Equation (2) may be written in the following form:

$$\frac{\sigma_{ij}}{\sigma_0} = A_1 \bar{r}^s \tilde{\sigma}_{ij}^{(1)}(\theta) + A_2 \bar{r}^t \tilde{\sigma}_{ij}^{(2)}(\theta) + \frac{A_2^2}{A_1} \bar{r}^{2t-s} \tilde{\sigma}_{ij}^{(3)}(\theta), \tag{3}$$

where:

$\tilde{\sigma}_{ij}^{(k)}$ – functions, which must be found by solving the fourth order non-linear homogenous differential equation independently for plane stress and plane strain [18],

s – the power exponent, which is identical to the one in the HRR solution (s may be calculated as $s = -1/(n+1)$),

t – the power exponent for the second term of the asymptotic expansion, which must be found numerically by solving the fourth order non-linear homogenous differential equation independently for plane stress and plane strain [18],

\bar{r} – normalized distance from the crack tip calculated as $\bar{r} = r/(J/\sigma_0)$,

A_1 – the amplitude of the first term of the infinite series evaluated as $A_1 = (\alpha \varepsilon_0 I_n)^{-1/(n+1)}$,

A_2 – the amplitude of the second term, which is calculated by fitting the Equation (3) to the numerical results of the stress fields close to crack tip.

In 1993 Shih, O’Dowd and Kirk [16] proposed simplified solution. They assumed that the FEM results are exact and computed the difference between the numerical and HRR results. They proposed, that the stress field near the crack tip may be described by following equation:

$$\frac{\sigma_{ij}}{\sigma_0} = \left(\frac{J}{\alpha \varepsilon_0 \sigma_0 I_n r} \right)^{1/(n+1)} \tilde{\sigma}_{ij}(\theta; n) + Q \left(\frac{r}{J/\sigma_0} \right)^q \hat{\sigma}_{ij}(\theta; n), \tag{4}$$

where:

$\hat{\sigma}_{ij}(\theta; n)$ – functions evaluated numerically,

q – the power exponent, which value changes in the range (0; 0.071),

Q – the parameter, which is the amplitude of the second term asymptotic solution.

O’Dowd and Shih [14–15] tested the Q -parameter in the range $J/\sigma_0 < r < 5J/\sigma_0$ near the crack tip. They showed, that the Q -parameter weakly depend on crack tip distance in the range of the $\pm\pi/2$ angle. O’Dowd and Shih proposed only two terms to describe the stress field near the crack tip:

$$\sigma_{ij} = (\sigma_{ij})_{HRR} + Q \sigma_0 \hat{\sigma}_{ij}(\theta). \tag{5}$$

To avoid the ambiguity during the calculation of the Q -stress, O’Dowd and Shih [14–15] have suggested, where the Q -stress may be evaluated. It was assumed that the

Q -stress should be computed at $r = 2J/\sigma_0$ for $\theta = 0$ direction. O'Dowd and Shih postulated, that for $\theta = 0$ the function $\hat{\sigma}_{\theta\theta}(\theta=0)$ is equal to 1. That's why the Q -stress may be calculated from following relationship:

$$Q = \frac{(\sigma_{\theta\theta})_{\text{FEM}} - (\sigma_{\theta\theta})_{\text{HRR}}}{\sigma_0} \text{ for } \theta = 0 \text{ and } \frac{r\sigma_0}{J} = 2, \quad (6)$$

where:

$(\sigma_{\theta\theta})_{\text{FEM}}$ – the stress value calculated using FEM,

$(\sigma_{\theta\theta})_{\text{HRR}}$ – stress value evaluated from HRR solution.

During analysis, O'Dowd and Shih shown, that in the range of $\theta = \pm\pi/4$, the following relationships take place: $Q\hat{\sigma}_{\theta\theta} \approx Q\hat{\sigma}_{rr}$, $\hat{\sigma}_{\theta\theta}/\hat{\sigma}_{rr} \approx 1$ and $Q\hat{\sigma}_{r\theta} \approx 0$ (because $Q\hat{\sigma}_{r\theta} \ll Q\hat{\sigma}_{\theta\theta}$). Thus, the Q -stress value determines the level of the hydrostatic stress. For plane stress, the Q -parameter is equal to zero, but for plane strain, the Q -parameter is in the most cases smaller than zero.

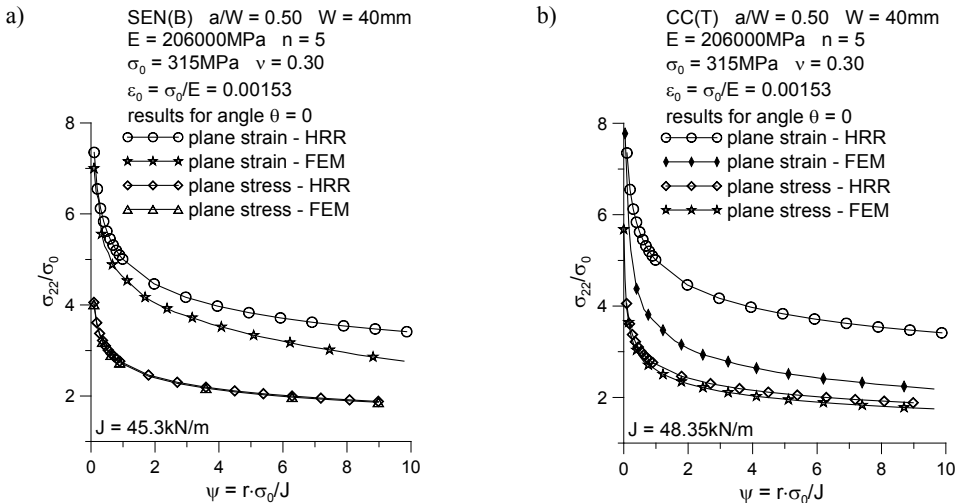


Fig. 2. Comparison the FEM results and HRR solution for plane stress and plane strain for: a) single edge notched specimen in bending (SEN(B)); b) centre cracked plate in tension (CC(T))

2. The engineering aspects of the J - Q theory

To describe the stress field near the crack tip for elastic-plastic materials, the HRR solution is most often used (Equation 1). However the results obtained are usually overestimated and analysis is conservative. The HRR solution includes the first term of the infinite series only. The numerical analysis shown, that results obtained using the HRR solution are different from the results obtained using the finite element

method (FEM). To eliminate this difference, it's necessary to use more terms in the HRR solution, for example the J - A_2 theory suggested by Yang, Chao and Sutton [18], or the O'Dowd and Shih approach - the J - Q theory [14–15].

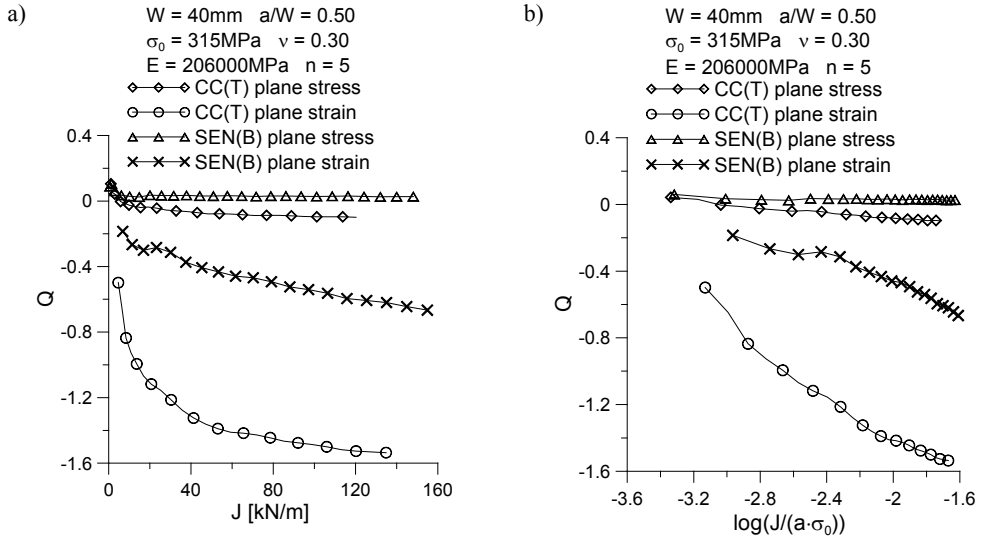


Fig. 3. a) The comparison of the J - Q trajectories and
 b) $Q = f(\log(J/(a \times \sigma_0)))$ trajectories for CC(T) and SEN(B) specimen

For using the O'Dowd approach, engineer needs only the Q -stress (which calculated numerically). That's why O'Dowd approach is easier and pleasanter in use in contrast to J - A_2 theory. Using the J - A_2 theory, first engineer must to solve fourth order nonlinear differential equation to determine the $\tilde{\sigma}_{ij}^{(k)}$ function and the t power exponent. Next engineer using FEM results calculated the A_2 amplitude by fitting the Equation 3 to numerical results.

The J - Q theory found application in European Engineering Programs, like SINTAP [17] or FITNET [10]. The Q -stress is applied under construction the fracture criterion and to assessment the fracture toughness of the structural component. Thus O'Dowd theory has practical application in engineering issues.

Sometimes using the J - Q theory may be limited, because there is no value of the Q -stress for given material and specimen. Using any fracture criterion, for example proposed by O'Dowd in [13], or another criterion [10, 17], engineer can estimate fracture toughness quit fast, if the Q -stress are known. Literature doesn't announce the Q -stress catalogue and Q -stress value as function of external load, material properties or geometry of the specimen. In some articles, engineer may found the J - Q graphs for certain group of material. The best solution will be, origin the catalogue of the J - Q graphs for materials characterized by various yield strength, different work-hardening

exponent. Such catalogue should take into consideration the influence of the external load, kind of the specimen (SEN(B) specimen – bending, SEN(T) specimen – tension) and geometry of the specimen, too. For SEN(B) specimens, such catalogue was presented in [6–8].

In the next parts of the paper, the values of the Q -stress will be determined for various elastic-plastic materials for single edge notched specimens in tension (SEN(T)). The SEN(T) specimen is the basic structural element, which is used in the FITNET procedures [9] to modelling real constructions. All results will be presented in the graphic form – the $Q = f(J)$ graphs. Next, the numerical results will be approximated by the closed form formulas.

3. Details of numerical analysis

In the numerical analysis, the single edge notched specimens in tension (SEN(T)) were used (Figure 4). Dimensions of the specimens satisfy the standard requirement which is set up in FEM calculation – $L \geq 2W$, where W is the width of the specimen and L is the measuring length of the specimen. Computations were performed for plane strain using small strain option. The relative crack length was: $a/W = \{0.05, 0.20, 0.50, 0.70\}$ where a is a crack length and the width of specimens W was equal to 40 mm (for this case, the measuring length $L \geq 80$ mm). All geometrical dimension of the SEN(T) specimen were presented in the Table 1.

Table 1. The geometrical dimension of the SEN(T) specimen used in numerical analysis

Width, W [mm]	Measuring length, $4W$ [mm]	Total length $2L$ [mm]	Relative crack length, a/W	Crack length, a [mm]	Length of the non-cracked section of the specimen $b = (W - a)$ [mm]
40	160	176	0.05	2	38
			0.20	8	32
			0.50	20	20
			0.70	28	12

The choice of the SEN(T) specimen was intentional, because the SEN(T) specimens are used in the FITNET procedures [10] to modelling real structural elements. Also in FITNET procedures, the limit load and stress intensity factors solutions for SEN(T) specimens are presented. However in the EPRI procedures [11], the hybrid method for calculation the J -integral, crack opening displacement (COD) or crack opening displacement (CTOD) are given. Also some laboratory test in order to determine the critical values of the J -integral, may be done using the SEN(T) specimen. The ASTM E 1820-05 standard requirements [3] dictate, that the plane strain fracture toughness is determined using the SEN(B) specimen – single edge notch specimen in bending.

Computations were performed using ADINA SYSTEM 8.4 [1–2]. Due to the symmetry, only a half of the specimen was modelled. The finite element mesh was

filled with the 9-node plane strain elements. The size of the finite elements in the radial direction was decreasing towards the crack tip, while in the angular direction the size of each element was kept constant. The crack tip region was modelled using 36–50 semicircles. The first of them was at least 20 times smaller than the last one. It also means, that the first finite element behind to crack tip is smaller 2000 times then the width of the specimen. The crack tip was modelled as quarter of the arc which radius was equal to $r_w = (1-2.5) \times 10^{-6}$ m (it's $(0.000025-0.0000625) \times W$). The whole SEN(T) specimen was modelled using 323 finite elements and 1353 nodes. External load was applied to bottom edge of the specimen. The example finite element model for SEN(T) specimen is presented on Figure 5.

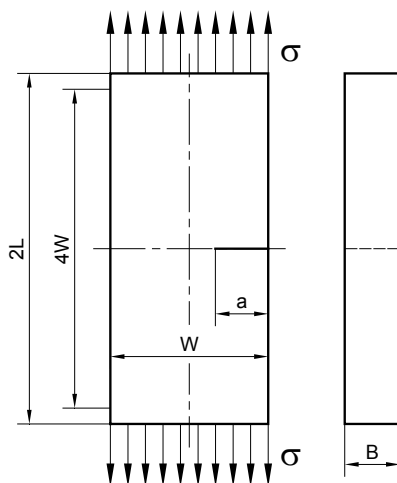


Fig. 4. The single edge notched specimen in tension SEN(T)

In the FEM simulation, the deformation theory of plasticity and the von Mises yield criterion were adopted. In the model the stress–strain curve was approximated by the relation:

$$\frac{\varepsilon}{\varepsilon_0} = \begin{cases} \sigma/\sigma_0 & \text{for } \sigma \leq \sigma_0 \\ \alpha(\sigma/\sigma_0)^n & \text{for } \sigma > \sigma_0 \end{cases}, \quad (7)$$

where $\alpha = 1$. The tensile properties for the materials which were used in the numerical analysis are presented below in the Table 2. In the FEM analysis, calculations were done for sixteen materials, which were differed by yield stress and the work hardening exponent.

The J -integral were calculated using two methods. The first method, called the “virtual shift method”, uses concept of the virtual crack growth to compute the virtual energy change. The second method is based on the J -integral definition:

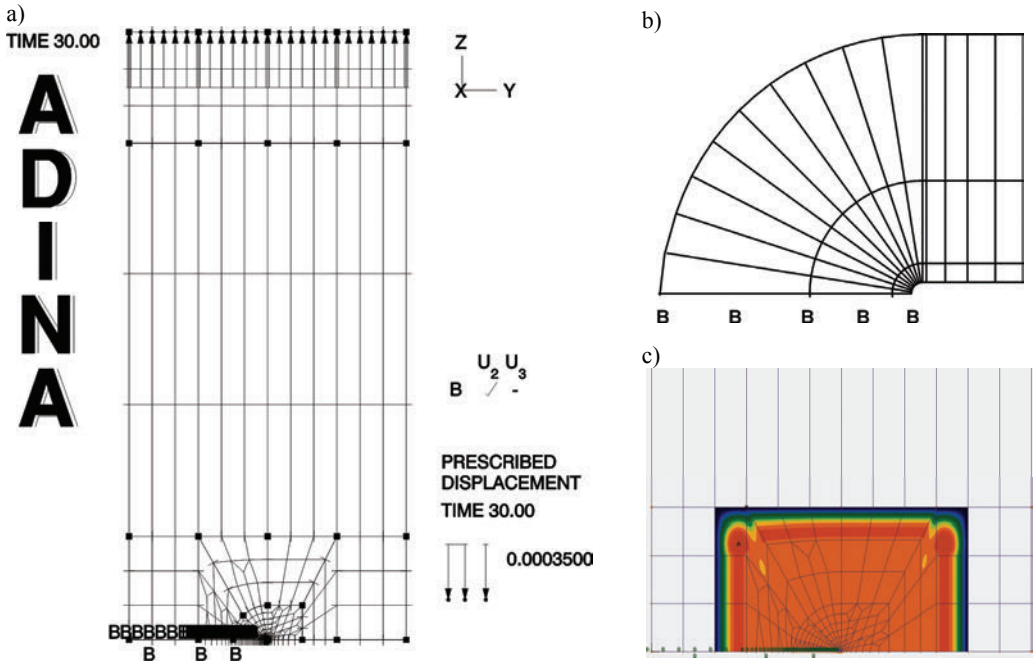


Fig. 5. a) The finite element model for SEN(T) specimen; b) The crack tip model used to modelling the SEN(T) specimen; c) The integral contour to calculation the J -integral

$$J = \int_C [w dx_2 - \mathbf{t}(\partial \mathbf{u} / \partial x_1) ds] \quad (8)$$

where:

- w – the strain energy density,
- \mathbf{t} – the stress vector acting on the contour C drawn around the crack tip,
- \mathbf{u} – denotes displacement vector,
- ds – the infinitesimal segment of contour C .

Table 2. The mechanical properties and parameter of the HRR fields for materials used in numerical analysis

σ_0 [MPa]	E [MPa]	ν	$\varepsilon_0 = \sigma_0/E$	α	n	$\tilde{\sigma}_{\theta\theta}(\theta=0)$ for plane strain	I_n for plane strain
315	206000	0.3	0.00153	1	3	1.94	5.51
500			0.00243		5	2.22	5.02
1000			0.00485		10	2.50	4.54
1500			0.00728		20	2.68	4.21

In the numerical analysis 64 SEN(T) specimens were used, which were differed by crack length (different a/W) and material properties (different ratio σ_0/E and values of the power exponent n).

4. Numerical results

The analysis of the results obtained was made in the range $J/\sigma_0 < r < 6J/\sigma_0$ near the crack tip, and it is shown, that:

- the Q -stress decrease if the distance from the crack tip increase (Figure 6);
- if the external load increases, the Q -stress decreases and the difference between Q -stress calculated in the following measurement points increase (Figure 6);

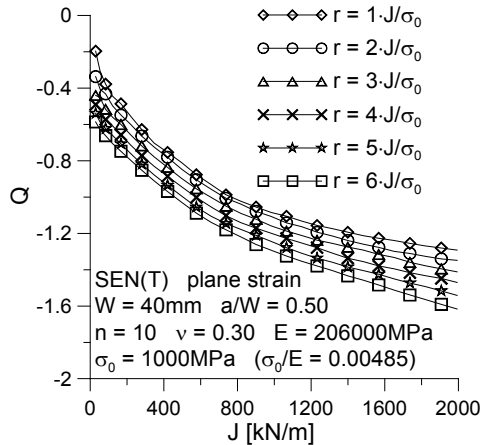


Fig. 6. “The J - Q family curves” for SEN(T) specimen calculated at six distances r

- if the crack length decreases then Q -stress reaches more negative value for the same J -integral level (Figure 7).

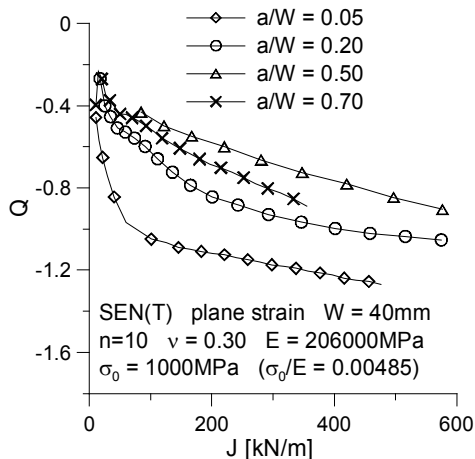


Fig. 7. The influence of the crack length on J - Q trajectories for SEN(T) specimens

For the sake of the fact, that the Q -parameter, which is used in fracture criterion is calculated at distance equal to $r = 2J/\sigma_0$, it is necessary to notice, that:

- if the yield stress increases, the Q -parameter increase too, and it reflects for all SEN(T) specimen with different crack length a/W (Figure 8a);
- for smaller yield stress the J - Q trajectories shape up well lower and it's observed faster changes of the Q -parameter if the external load is increase (Figure 8a);

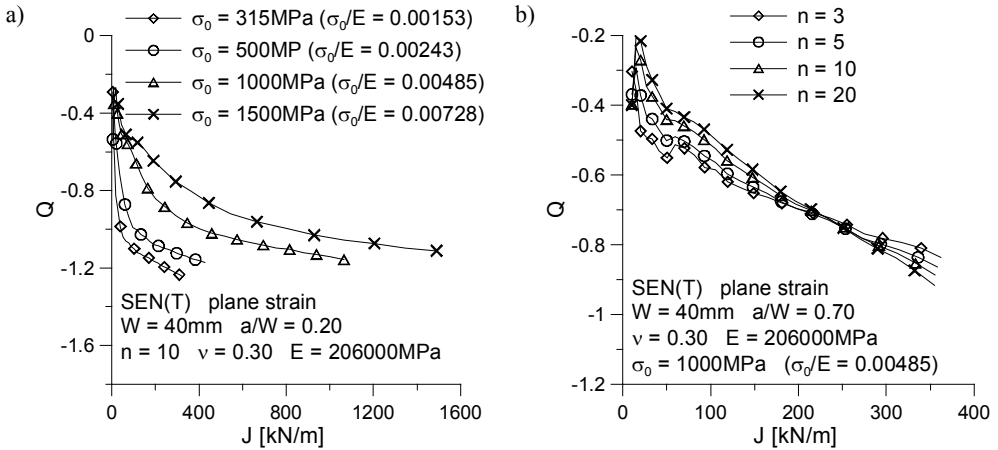


Fig. 8. a) The influence of the yield stress and b) the work hardening exponent on J - Q trajectories for SEN(T) specimens

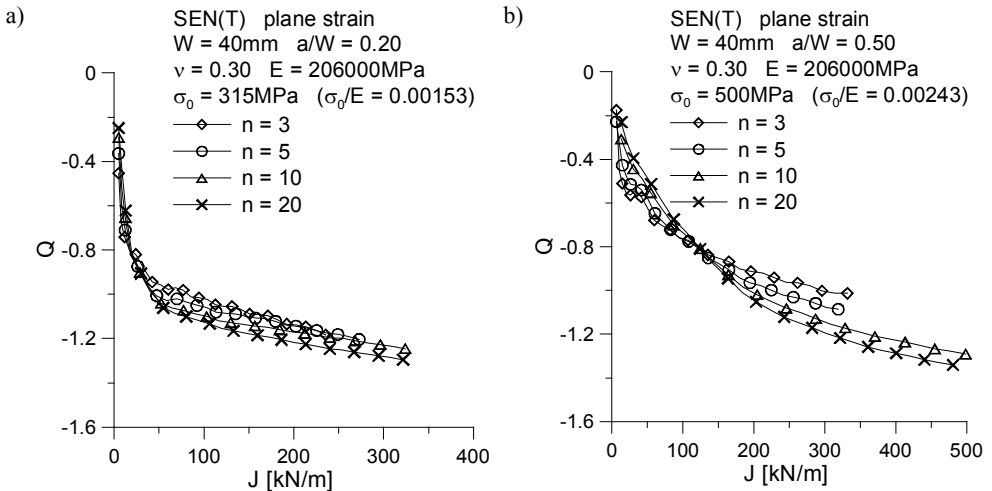


Fig. 9. The influence of the work hardening exponent (b) on J - Q trajectories for SEN(T) specimens: a) SEN(T), $a/W = 0.20$, $\sigma_0 = 315 \text{ MPa}$; b) SEN(T), $a/W = 0.50$, $\sigma_0 = 500 \text{ MPa}$

- comparing the J - Q trajectories for different values of σ_0/E , it's observed, that the biggest differences are characterized for materials with small work-hardening exponent ($n = 3$ – strongly work-hardening materials) and the smallest for materials characterized large work-hardening exponent ($n = 20$ – weakly work-hardening materials); if the crack length increase, this differences somewhat increase too;
- for SEN(T) specimens, the ambiguous behaviour of the J - Q trajectories depending of the work-hardening exponent is observed; for specimens with short cracks ($a/W \leq 0.20$) and the same yield stress, for smaller values of the work-hardening exponent n (e.g. $n \leq 5$), the Q -stress become less negative (Figure 9a); for specimens with the normative crack length ($a/W = 0.50$) or with the long cracks ($a/W = 0.70$), the cutting of the J - Q trajectories was observed (Figures 8b and 9b) – first the higher values of the Q -stress were observed for specimen characterized by strongly hardening material, but for increasing external load the reversal of the trend took place and the higher Q -stress were observed for specimens characterized by weakly hardening material;
- for short cracks the Q -stress value drops more rapidly than for long ones in the range of the small external load (Figure 7);
- for specimen with long cracks ($a/W = 0.70$), the another nature of the J - Q trajectories was observed than for specimen with relative cracks length $a/W \leq 0.50$ (Figure 7); it may be a consequence of the absence in the analysis of the stress field, the consideration of the bending stress near the crack tip, which was discussed by Chao [4].

5. Approximation of the numerical results

In the literature the mathematic formulas, to calculate the Q -stress taking into consideration the level of external load, material properties and geometry of the specimen are not known for the most of the cases. Presented in the paper numerical computations provided with the J - Q catalogue and the universal formula (9), which allows calculating the Q -stress and taking into consideration all the parameters influencing the value of the Q -stress. All results, were presented in the $Q = f(\log(J/(a \cdot \sigma_0)))$ graph forms. Next all graphs were approximated by the simple mathematical formulas, taking the material properties, external load and geometry specimen into consideration. All the approximations were made for results obtained at the distance $r = 2.0 \cdot J/\sigma_0$.

Each of the obtained trajectories $Q = f(\log(J/(a \cdot \sigma_0)))$, was approximated by the third order polynomial in the form:

$$Q(J, a, \sigma_0) = A + B \cdot \left(\log \left(\frac{J}{(a \cdot \sigma_0)} \right) \right) + C \cdot \left(\log \left(\frac{J}{(a \cdot \sigma_0)} \right) \right)^2 + D \cdot \left(\log \frac{J}{(a \cdot \sigma_0)} \right)^3, \quad (9)$$

where A, B, C, D is coefficients depend on the work-hardening exponent n , σ_0 is yield stress and a/W is crack length.

Table 3. The coefficients of Equation (9) for SEN(T) specimen with the crack length $a/W = 0.05$

$a/W = 0.05$											
$\sigma_0 = 315 \text{ MPa}$			$\sigma_0/E = 0.00153$			$\sigma_0 = 1000 \text{ MPa}$			$\sigma_0/E = 0.00485$		
n	A	B	C	D	R^2	n	A	B	C	D	R^2
3	-3.285	-4.365	-2.941	-0.681	0.992	3	-1.997	-2.145	-1.413	-0.337	0.992
5	-3.241	-4.312	-2.969	-0.695	0.995	5	-1.970	-1.859	-1.230	-0.312	0.994
10	-2.476	-2.735	-1.957	-0.490	0.997	10	-1.589	-0.742	-0.415	-0.139	0.996
20	-2.005	-1.733	-1.334	-0.371	0.998	20	-1.463	-0.247	-0.014	-0.049	0.996
$\sigma_0 = 500 \text{ MPa}$			$\sigma_0/E = 0.00243$			$\sigma_0 = 1500 \text{ MPa}$			$\sigma_0/E = 0.00728$		
n	A	B	C	D	R^2	n	A	B	C	D	R^2
3	-2.996	-4.038	-2.758	-0.649	0.992	3	-1.570	-1.328	-0.821	-0.199	0.991
5	-2.794	-3.500	-2.402	-0.570	0.998	5	-1.591	-1.043	-0.594	-0.157	0.994
10	-2.194	-2.172	-1.553	-0.403	0.999	10	-1.416	-0.301	-0.006	-0.030	0.996
20	-1.798	-1.209	-0.896	-0.268	0.999	20	-1.393	-0.002	0.274	0.037	0.997

Table 4. The coefficients of Equation (9) for SEN(T) specimen with the crack length $a/W = 0.20$

$a/W = 0.20$											
$\sigma_0 = 315 \text{ MPa}$			$\sigma_0/E = 0.00153$			$\sigma_0 = 1000 \text{ MPa}$			$\sigma_0/E = 0.00485$		
n	A	B	C	D	R^2	n	A	B	C	D	R^2
3	-2.476	-2.221	-1.165	-0.228	0.993	3	-1.875	-1.438	-0.651	-0.119	0.958
5	-2.128	-1.722	-0.999	-0.223	0.997	5	-1.198	0.007	0.217	0.037	0.990
10	-1.752	-0.991	-0.604	-0.163	0.998	10	-1.065	0.552	0.622	0.116	0.995
20	-1.677	-0.683	-0.379	-0.121	0.997	20	-1.163	0.533	0.654	0.122	0.996
$\sigma_0 = 500 \text{ MPa}$			$\sigma_0/E = 0.00243$			$\sigma_0 = 1500 \text{ MPa}$			$\sigma_0/E = 0.00728$		
n	A	B	C	D	R^2	n	A	B	C	D	R^2
3	-1.618	-0.876	-0.397	-0.087	0.986	3	-1.601	-1.099	-0.477	-0.089	0.982
5	-1.105	0.104	0.119	-0.008	0.996	5	-1.469	-0.537	-0.056	-0.002	0.990
10	-1.365	-0.139	0.029	-0.026	0.996	10	-1.401	-0.078	0.328	0.080	0.996
20	-1.465	-0.145	0.075	-0.017	0.996	20	-1.486	-0.085	0.364	0.088	0.996

Table 5. The coefficients of Equation (9) for SEN(T) specimen with the crack length $a/W = 0.50$

$a/W = 0.50$											
$\sigma_0 = 315 \text{ MPa}$			$\sigma_0/E = 0.00153$			$\sigma_0 = 1000 \text{ MPa}$			$\sigma_0/E = 0.00485$		
n	A	B	C	D	R^2	n	A	B	C	D	R^2
3	-2.743	-1.606	-0.456	-0.059	0.990	3	-4.009	-4.031	-1.629	-0.229	0.977
5	-2.909	-1.516	-0.334	-0.038	0.990	5	-2.662	-1.869	-0.545	-0.059	0.997
10	-0.621	1.913	1.291	0.205	0.996	10	-2.773	-1.760	-0.403	-0.032	0.996
20	0.238	3.364	2.03142	0.320	0.996	20	-2.971	-1.789	-0.312	-0.006	0.997
$\sigma_0 = 500 \text{ MPa}$			$\sigma_0/E = 0.00243$			$\sigma_0 = 1500 \text{ MPa}$			$\sigma_0/E = 0.00728$		
n	A	B	C	D	R^2	n	A	B	C	D	R^2
3	-3.927	-3.615	-1.435	-0.209	0.982	3	-2.612	-2.335	-0.943	-0.138	0.994
5	-3.383	-2.414	-0.728	-0.088	0.995	5	-2.505	-1.895	-0.629	-0.078	0.999
10	-2.009	-0.132	0.435	0.094	0.997	10	-2.559	-1.688	-0.420	-0.035	0.996
20	-1.810	0.450	0.811	0.160	0.997	20	-2.357	-1.041	0.048	0.059	0.997

The rank of the fitting the formula (9) to numerical results for the worst case was equal $R^2 = 0.95$. For different work hardening exponents n , yield stresses σ_0 and ratios

a/W , which were not include in the numerical analysis, the coefficients A, B, C and D may be evaluated using the linear or quadratic approximation.

Table 6. The coefficients of Equation (9) for SEN(T) specimen with the crack length $a/W = 0.70$

$a/W = 0.20$											
$\sigma_0 = 315$ MPa			$\sigma_0/E = 0.00153$			$\sigma_0 = 1000$ MPa			$\sigma_0/E = 0.00485$		
n	A	B	C	D	R^2	n	A	B	C	D	R^2
3	-6.051	-4.762	-1.512	-0.179	0.989	3	-6.703	-6.471	-2.323	-0.286	0.985
5	-3.287	-0.872	0.171	0.049	0.991	5	-7.237	-6.937	-2.456	-0.301	0.996
10	0.290	3.710	2.045	0.294	0.993	10	-7.642	-7.198	-2.481	-0.297	0.998
20	4.424	8.931	4.175	0.574	0.993	20	-8.527	-8.058	-2.747	-0.325	0.997
$\sigma_0 = 500$ MPa			$\sigma_0/E = 0.00243$			$\sigma_0 = 1500$ MPa			$\sigma_0/E = 0.00728$		
n	A	B	C	D	R^2	n	A	B	C	D	R^2
3	-8.575	-8.072	-2.818	-0.341	0.989	3	-5.580	-5.462	-2.021	-0.256	0.976
5	-10.470	-9.908	-3.417	-0.410	0.997	5	-5.819	-5.576	-2.011	-0.250	0.995
10	-11.036	-9.958	-3.227	-0.365	0.998	10	-5.990	-5.608	-1.961	-0.238	0.998
20	-0.753	2.846	1.979	0.325	0.993	20	-7.453	-7.315	-2.617	-0.322	0.999

Results of the numerical approximation (all coefficients of the approximation numerical results by Equation (9)) are presented in Tables 3–6.

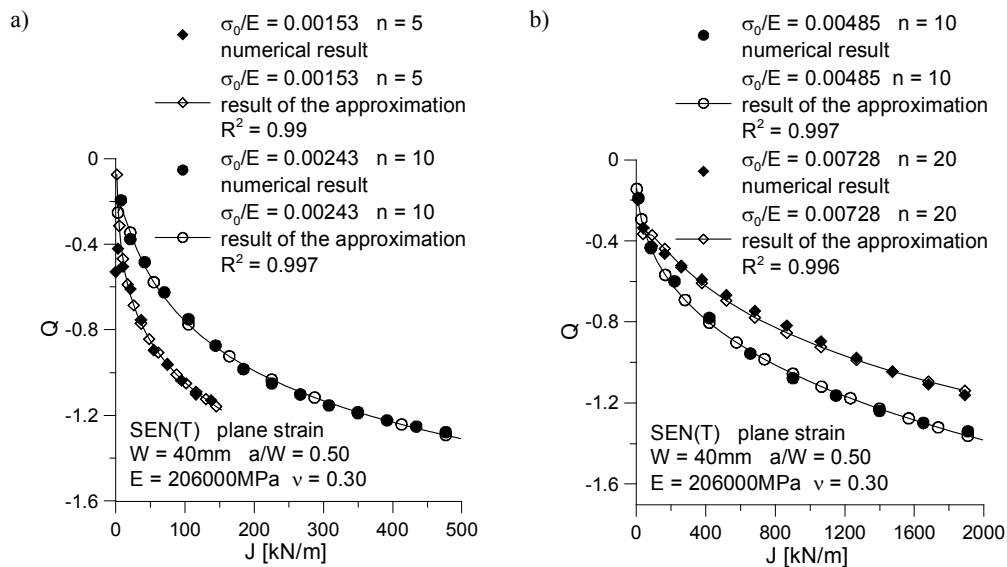


Fig. 10. Comparison of the numerical results and their approximation for J - Q trajectories for SEN(T) specimens with relative crack length $a/W = 0.50$: a) $\sigma_0 = \{315, 500\}$ MPa, $n = \{5, 10\}$; b) $\sigma_0 = \{1000, 1500\}$ MPa, $n = \{10, 20\}$

Figure 10 presents the comparison of the numerical results and their approximation for J - Q trajectories for several cases of the SEN(T) specimens. The annexes attached

to the article (Annexes A-D) presents in the graphical form (Figures 11–14), all numerical results obtained for SEN(T) specimens in plain strain. All results are presented using the J - Q trajectories for each analyzed case.

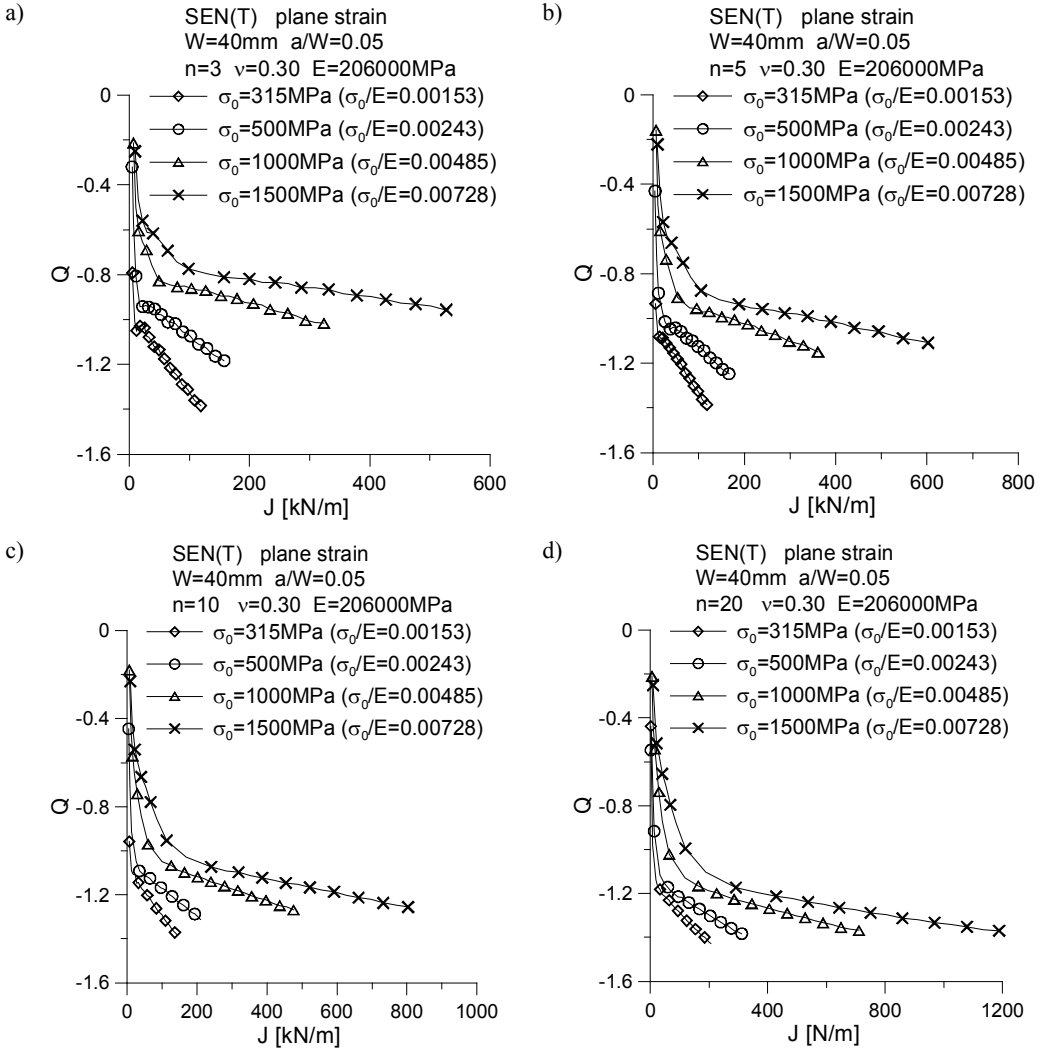


Fig. 11. The influence of the yield stress on J - Q trajectories for SEN(T) specimens with crack length $a/W = 0.05$ for different power exponents n in R-O relationship: a) $n = 3$; b) $n = 5$; c) $n = 10$; d) $n = 20$

6. Conclusions

In the paper the values of the Q -stress were determined for different mechanical properties, which can be referred to real elastic-plastic materials for single edge

notched specimens in tension (SEN(T)). The influence of the yield strength, the work-hardening exponent and the crack length on the Q -parameter was tested. All obtained results were presented in the graphical form. The numerical results were approximated by the closed form formulas. For all analyzed cases, the coefficients of the approximation were presented in the tables located in appendix.

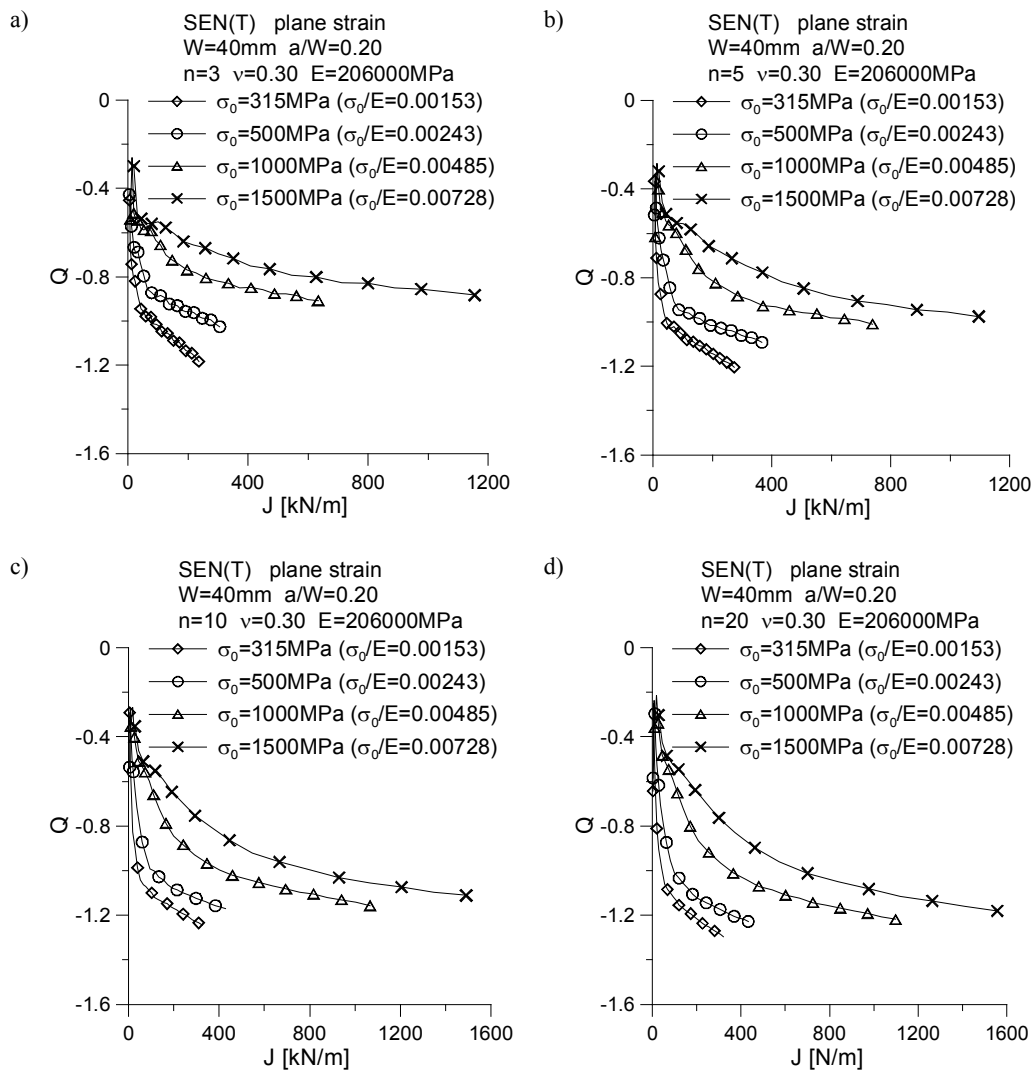


Fig. 12. The influence of the yield stress on J - Q trajectories for SEN(T) specimens with crack length $a/W = 0.20$ for different power exponents n in R-O relationship:
a) $n = 3$; b) $n = 5$; c) $n = 10$; d) $n = 20$

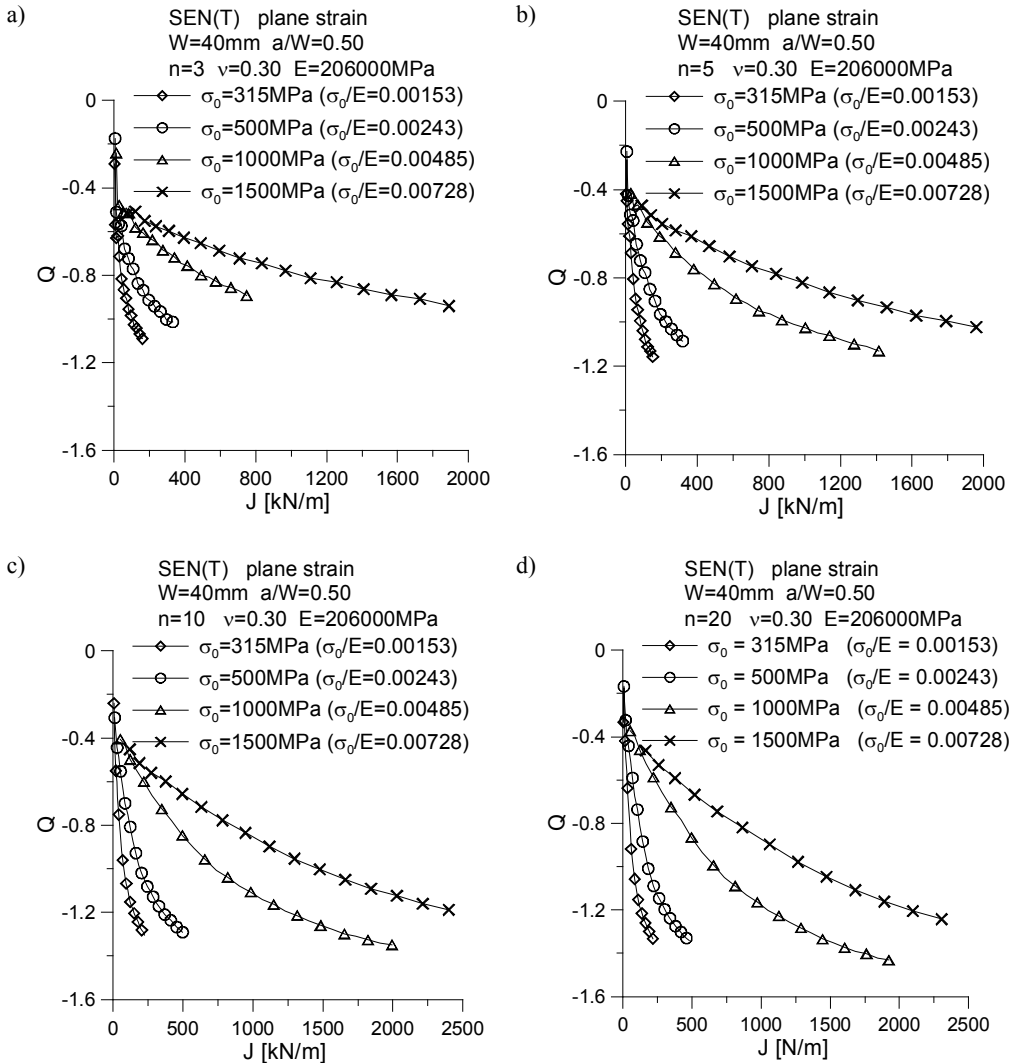


Fig. 13. The influence of the yield stress on J - Q trajectories for SEN(T) specimens with crack length $a/W = 0.50$ for different power exponents n in R-O relationship: a) $n = 3$; b) $n = 5$; c) $n = 10$; d) $n = 20$

The most important results are summarized as follows:

- the Q -stress depends on geometry and external the load; different values of the Q -stress are obtained for centre cracked plane in tension (CC(T)) and different for the SEN(T) specimen, which are characterized by the same material properties;
- the Q -parameter is a function of the material properties; its value depends on the work-hardening exponent n and the yield stress σ_0 ;

- if the crack length decreases then Q -stress reaches more negative value for the external load.

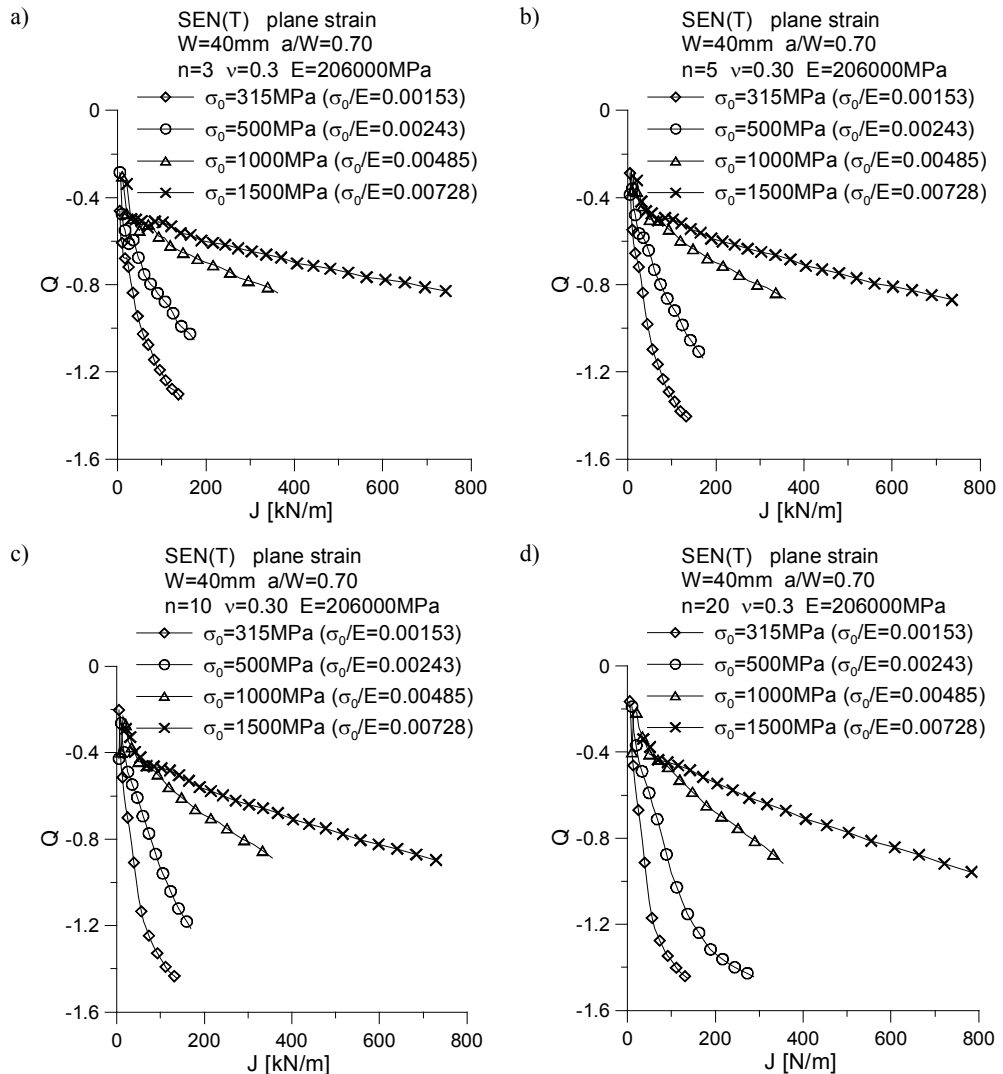


Fig. 14. The influence of the yield stress on J - Q trajectories for SEN(T) specimens with crack length $a/W = 0.70$ for different power exponents n in R-O relationship: a) $n = 3$; b) $n = 5$; c) $n = 10$; d) $n = 20$

References

- [1] ADINA 8.4.1: *User interface command reference manual – Volume I: ADINA solids & structures model definition*, Report ARD 06-2, ADINA R&D, Inc., 2006.

- [2] ADINA 8.4.1: *Theory and modelling guide – Volume I: ADINA*, Report ARD 06-7, ADINA R&D, Inc., 2006.
- [3] ASTM E 1820-05: *Standard test method for measurement of fracture toughness*, American Society for Testing and Materials, 2005.
- [4] Chao Y.J., Zhu X.K., Kim Y., Lar P.S., Pechersky M.J., Morgan M.J.: *Characterization of crack-tip field and constraint for bending specimens under large-scale yielding*, International Journal of Fracture, Vol. 127, 2004, pp. 283–302.
- [5] Gałkiewicz J., Graba M.: *Algorithm for determination of $\tilde{\sigma}_{ij}(\mathbf{n}, \theta)$, $\tilde{\varepsilon}_{ij}(\mathbf{n}, \theta)$, $\tilde{u}_i(\mathbf{n}, \theta)$, $d_n(\mathbf{n})$ and $I_n(\mathbf{n})$ functions in Hutchinson-Rice-Rosengren solution and its 3d generalization*, Journal of Theoretical and Applied Mechanics, Vol. 44, No. 1, 2006, pp. 19–30.
- [6] Graba M.: *The influence of material properties and crack length on the Q -stress value near the crack tip for elastic-plastic materials* (in Polish), IV MSMZMiK – Augustów 2007, conference proceeding, 2007, pp. 109–114.
- [7] Graba M.: *The influence of material properties on the Q -stress value near the crack tip for elastic-plastic materials*, Theoretical Backgrounds, Transcom, proceedings of the section 7 – Machines and Equipment. Applied Mechanics, 2007, pp. 53–57.
- [8] Graba M.: *The influence of material properties on the Q -stress value near the crack tip for elastic-plastic materials. Numerical results and their approximation*, Transcom, proceedings of the section 7 – Machines and Equipment. Applied Mechanics, 2007, pp. 59–63.
- [9] Hutchinson J.W.: *Singular behaviour at the end of a tensile crack in a hardening material*, Journal of the Mechanics and Physics of Solids, Vol. 16, 1968, pp. 13–31.
- [10] Kocak M., Webster S., Janosch J.J., Ainsworth R.A., Koers R.: *FITNET report, (european fitness-for-service network)*, Contract No. GIRT-CT-2001-05071, 2006.
- [11] Kumar V., German M.D., Shih C.F.: *An engineering approach for elastic-plastic fracture analysis*, EPRI Report NP-1931, Electric Power Research Institute, Palo Alto, CA., 1981.
- [12] Li Y., Wang Z.: *High-order asymptotic field of tensile plane-strain nonlinear crack problems*, Scientia Sinica (Series A), Vol. XXIX, No. 9, 1985, pp. 941–955.
- [13] O’Dowd N.P.: *Applications of two parameter approaches in elastic-plastic fracture mechanics*, Engineering Fracture Mechanics, Vol. 52, No. 3, 1995, pp. 445–465.
- [14] O’Dowd N.P., Shih C.F.: *Family of crack-tip fields characterized by a triaxiality parameter – I. Structure of fields*, J. Mech. Phys. Solids, Vol. 39, No. 8, 1991, pp. 989–1015.
- [15] O’Dowd N.P., Shih C.F.: *Family of crack-tip fields characterized by a triaxiality parameter – II. Fracture applications*, J. Mech. Phys. Solids, Vol. 40, No. 5, 1992, pp. 939–963.
- [16] Shih C.F., O’Dowd N.P., Kirk M.T.: *A framework for quantifying crack tip constraint*, Constraint effects in fracture, ASTM STP 1171, E.M. Hackett, K.-H. Schwalbe, R.H. Dodds, Eds., American Society for Testing and Materials, Philadelphia, 1993, pp. 2–20.
- [17] SINTAP Procedure: *Structural integrity assessment procedures for european industry. Final procedure*, Brite-Euram Project No BE95-1426, Rotherham: British Steel, 1999.
- [18] Yang S., Chao Y.J., Sutton M.A.: *Higher order asymptotic crack tip in a power. Law hardening material*, Engineering Fracture Mechanics, Vol. 45, No. 1, 1993, pp. 1–20.

Wpływ stałych materiałowych i długości pęknięcia na rozkład naprężeń Q przed wierzchołkiem pęknięcia w materiałach sprężysto-plastycznych dla płyty z jednostronną szczeliną poddanej rozciąganiu

W pracy przedstawione zostaną wartości naprężeń Q wyznaczone dla szeregu materiałów sprężysto-plastycznych dla płyty z jednostronną szczeliną poddanej rozciąganiu (SEN(T)). Wybrana w pracy geometria jest jednym z podstawowych elementów konstrukcyjnych zalecanych przez procedury FITNET do idealizacji złożonych, rzeczywistych konstrukcji zawierających pęknięcia. Omówiony zostanie wpływ granicy plastyczności i wykładnika umocnienia na wartość naprężeń Q , a także wpływ długości pęknięcia. Wyniki obliczeń numerycznych aproksymowano formułami analitycznymi. Rezultaty pracy stanowią podręczny katalog krzywych J - Q , możliwy do wykorzystania w praktyce inżynierskiej.

Chosen constructional solutions of the structures loading the Euler columns in vibration and stability studies

A. KASPRZYCKI, L. TOMSKI

Częstochowa University of Technology, ul. Dąbrowskiego 73, 43-201 Częstochowa, Poland.

The influence of the adapter type (rolling bearing, stiff cylindrical element) between coactive and load taking heads on stability and vibrations of Euler loaded columns has been analysed in this paper. Using a stiff cylindrical element in the load charging heads, in comparison to a rolling element, makes the rotating loop stiff between the two cooperating structure loading elements.

Keywords: *free vibration, stability, slender system, Euler load*

1. Euler loaded columns

Conservative loads may be induced by loading or supporting structure. Depending on the construction solution we can have a jointed support, stiff fix or resilient fix of the column.

1.1. Physical model

The shape of the deflected axle and a physical model of the column are shown in Figure 1.

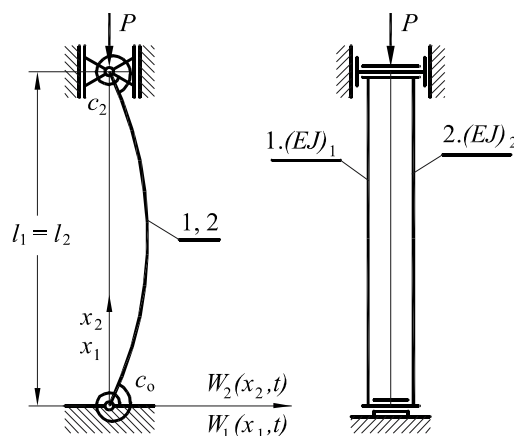


Fig. 1. Physical model of the Euler loaded column

This column is built from two rods with the symmetrical distribution of bend stiffness ($E_i J_i$) and mass per length unit ($\rho_i A_i$), while $E_1 J_1 = E_2 J_2$, $\rho_1 A_1 = \rho_2 A_2$ where E_i , J_i , A_i , ρ_i ($i = 1, 2$) are accordingly: elongated resiliency module, sectional central moment of inertia, square measure and volume weight of i - column rod. The rods are rigidly connected at both ends assuring evenness of movement and the deflection angle at the simply-supported points. Quantity c_0 , c_2 are stiffnesses of the rotational springs at the fixing points of column. In the case of a supporting column at $x = 0$ fixing stiffness $c_0 \rightarrow \infty$.

1.2. Constructional solutions

Euler loaded columns have been studied with two optional end fixing solutions. These are: jointed (both column ends were fixed to rotating loops) and supported (one column end fixed to a rotating loop and the other strengthened).

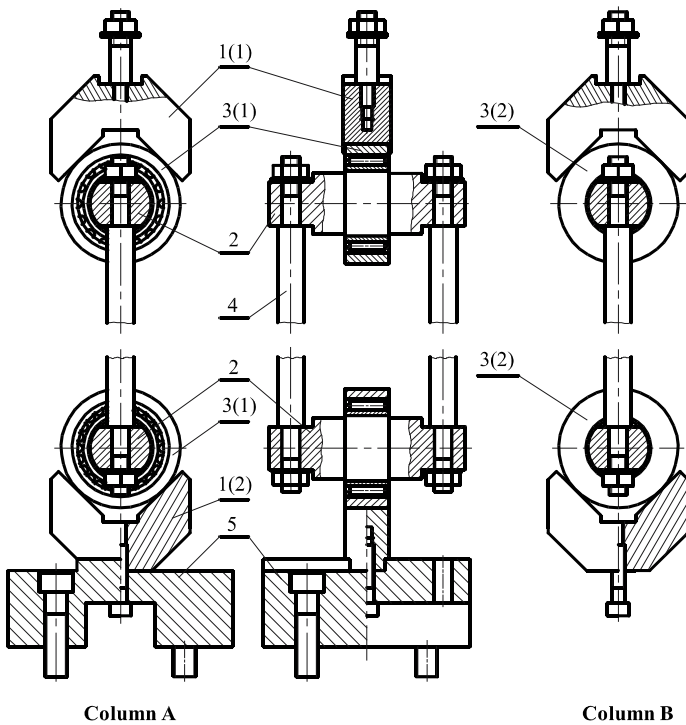


Fig. 2. The constructional solution for the jointed column structure

The constructional solution for the jointed Euler loaded column is shown in Figure 2. The active load charging head is the prism 1(1). The head taking the active or passive column 4 load is the set of shaft 2 and accordingly: needle rolling bearing 3(1) – column A – or stiff cylindrical element 3(2) – column B. The head taking the load – prism 1(2) – is fixed to base 5.

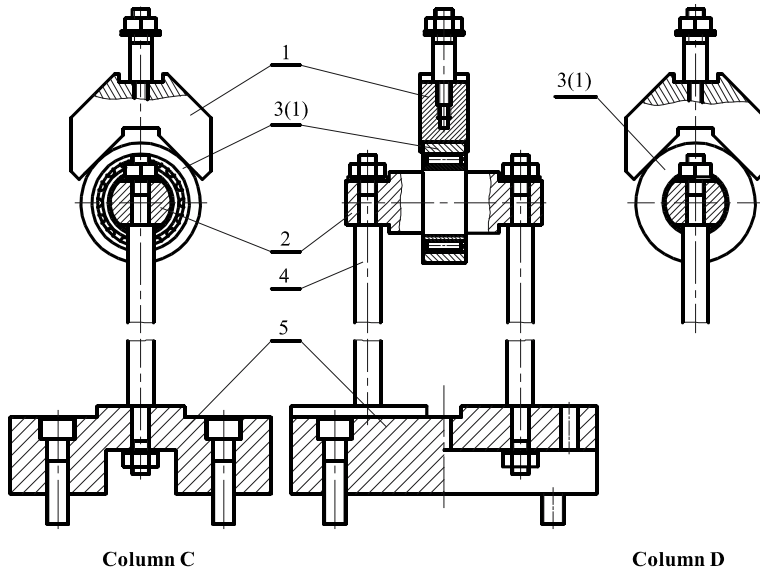


Fig. 3. The constructional solution for the supported column structure

The constructional solution for the supported Euler loaded column is shown in Figure 3. The difference between this solution and the column in Figure 2 is the direct fixing of one end of the column 4 onto base 5. The columns are labelled according to the cylindrical element in use:

- column C – rolling ball bearing 5(1),
- column D – stiff cylindrical element 5(2) with circular contour of the working area.

2. Vibration and stability of columns

A loss of stability occurs in the plane with lower bending stiffness, after exceeding a certain value of the axial force P called *critical force* P_c . The formulation of the vibration topic is based on the Hamilton rule using the Bernoulli-Euler theory. For this purpose we define the components of kinetic and potential energy of the elements of the structure, taking into account the physical model of the column (Figure 1), number of its rods ($i = 2$) and the internal forces in the rod S_i ($S_1 = S_2 = 0.5 P$).

2.1. The mechanical energy of the structure

The kinetic energy of the structure in Figure 1 is formulated:

$$T_1 = \frac{1}{2} \sum_i (\rho A)_i \int_0^{l_i} \left[\frac{\partial W_i(x_i, t)}{\partial t} \right]^2 dx_i. \quad (1)$$

Total potential energy V_1 of the column is the sum of the energy of the internal and external forces, support and fix stiffness i.e.

$$V_1 = V_{11} + V_{21} + V_{31}, \quad (2)$$

where :

- elastic strain energy

$$V_{11} = \frac{1}{2} \sum_i (EJ)_i \int_0^{l_i} \left[\frac{\partial^2 W_i(x_i, t)}{\partial x_i^2} \right]^2 dx_i, \quad (3)$$

- potential lengthwise energy S

$$V_{21} = -\frac{1}{2} \sum_{j=1}^2 S_j \int_0^{l_j} \left[\frac{\partial W_j(x_j, t)}{\partial x_j} \right]^2 dx_j, \quad (4)$$

- potential energy of support and fix resiliency

$$V_{31} = \frac{1}{2} c_0 \left[\frac{\partial W_1(x_1, t)}{\partial x_1} \Big|_{x_1=0} \right]^2 + \frac{1}{2} c_2 \left[\frac{\partial W_1(x_1, t)}{\partial x_1} \Big|_{x_1=l_1} \right]^2. \quad (5)$$

2.2. Hamilton rule, boundary conditions and movement formulas

Considering the kinetic (formula (1)) and potential energy (formulae (2–5)), the Hamilton rule is written as follows:

$$\delta \int_{t_1}^{t_2} (T_1 - V_1) dt = 0. \quad (6)$$

Computing the variation of kinetic energy T_1 , and potential energy V_1 and using a variation of integration (by time t and spatial coordinate x), and also doing integration by parts of the expressions (1–5), we obtain:

$$\int_{t_1}^{t_2} \sum_{i=1}^2 \left\{ -(EJ)_i \left[\frac{\partial^2 W_i(x_i, t)}{\partial x_i^2} \delta \frac{\partial W_i(x_i, t)}{\partial x_i} \Big|_{x_i=0}^{x_i=l_i} - \frac{\partial^3 W_i(x_i, t)}{\partial x_i^3} \delta W_i(x_i, t) \Big|_{x_i=0}^{x_i=l_i} \right] + \right.$$

$$\begin{aligned}
 & + \int_0^{l_i} \frac{\partial^4 W_i(x_i, t)}{\partial x_i^4} \delta W_i(x_i, t) dx_i \Big] + \sum_{i=1}^2 \left[\frac{1}{2} P \frac{\partial W_i(x_i, t)}{\partial x_i} \delta W_i(x_i, t) \Big|_{x_i=0}^{x_i=l_i} + \right. \\
 & - \frac{1}{2} P \int_0^{l_i} \frac{\partial^2 W_i(x_i, t)}{\partial x_i^2} \delta W_i(x_i, t) dx_i \Big] - c_0 \frac{\partial W_1(x_1, t)}{\partial x_1} \delta \frac{\partial W_1(x_1, t)}{\partial x_1} \Big|_{x_1=0} + \\
 & \left. - c_2 \frac{\partial W_1(x_1, t)}{\partial x_1} \delta \frac{\partial W_1(x_1, t)}{\partial x_1} \Big|_{x_1=l_1} - \sum_{i=1}^2 \int_0^{l_i} (\rho A)_i \frac{\partial^2 W_i(x_i, t)}{\partial t^2} \delta W_i(x_i, t) dx_i \right\} dt = 0 \tag{7}
 \end{aligned}$$

Including the geometric boundary conditions of the column in the form

$$W_1(0, t) = W_2(0, t) = 0, \tag{8}$$

$$W_1(l_1, t) = W_2(l_2, t) = 0, \tag{9}$$

$$\frac{\partial W_1(x_1, t)}{\partial x_1} \Big|_{x_1=0} = \frac{\partial W_2(x_2, t)}{\partial x_2} \Big|_{x_2=0}, \tag{10}$$

$$\frac{\partial W_1(x_1, t)}{\partial x_1} \Big|_{x_1=l_1} = \frac{\partial W_2(x_2, t)}{\partial x_2} \Big|_{x_2=l_2}, \tag{11}$$

In Equation (7) we get the natural boundary conditions necessary to solve the boundary problem:

$$(EJ)_1 \frac{\partial^2 W_1(x_1, t)}{\partial x_1^2} \Big|_{x_1=0} + (EJ)_2 \frac{\partial^2 W_2(x_2, t)}{\partial x_2^2} \Big|_{x_2=0} - c_0 \frac{\partial W_1(x_1, t)}{\partial x_1} \Big|_{x_1=0} = 0, \tag{12}$$

$$-(EJ)_1 \frac{\partial^2 W_1(x_1, t)}{\partial x_1^2} \Big|_{x_1=l_1} - (EJ)_2 \frac{\partial^2 W_2(x_2, t)}{\partial x_2^2} \Big|_{x_2=l_2} - c_2 \frac{\partial W_1(x_1, t)}{\partial x_1} \Big|_{x_1=l_1} = 0. \tag{13}$$

In the case of the supporting column (columns C, D), at $x = 0$ fixing resilience $c_0 \rightarrow \infty$, so the boundary condition, defined by Equation (12), will have the form:

$$\frac{\partial W_1(x_1, t)}{\partial x_1} \Big|_{x_1=0} = 0. \tag{14}$$

Achieving a condition for clearing all the equation elements (7) by assuming that it can accept any value leads to the differential equation of movement in a lateral direction to the column axis:

$$(EJ)_i \frac{\partial^4 W_i(x_i, t)}{\partial x_i^4} + \frac{P}{2} \frac{\partial^2 W_i(x_i, t)}{\partial x_i^2} + (\rho A)_i \frac{\partial^2 W_i(x_i, t)}{\partial t^2} = 0. \quad (15)$$

A two-rod column may vibrate if it is made of two identical rods, so: $(EJ)_1 = (EJ)_2 = EJ$ and $(\rho_0 A)_1 = (\rho_0 A)_2 = \rho_0 A$.

Further considerations are made using the dimensionless values:

$$\tau = \omega t, \quad (16)$$

$$\xi_i = \frac{x_i}{l_i}, \quad (17)$$

$$w_i(\xi_i, \tau) = \frac{W_i(x_i, t)}{l_i}, \quad (18)$$

so the geometrical and natural boundary conditions will be:

$$w_1(0, \tau) = w_2(0, \tau) = 0, \quad (19)$$

$$w_1(1, \tau) = w_2(1, \tau) = 0, \quad (20)$$

$$\left. \frac{\partial w_1(\xi, \tau)}{\partial \xi} \right|_{\xi=0} = \left. \frac{\partial w_2(\xi, \tau)}{\partial \xi} \right|_{\xi=0}, \quad (21)$$

$$\left. \frac{\partial w_1(\xi, \tau)}{\partial \xi} \right|_{\xi=1} = \left. \frac{\partial w_2(\xi, \tau)}{\partial \xi} \right|_{\xi=1}, \quad (22)$$

$$\left. \frac{\partial^2 w_1(\xi, \tau)}{\partial \xi^2} \right|_{\xi=0} + \left. \frac{\partial^2 w_2(\xi, \tau)}{\partial \xi^2} \right|_{\xi=0} - c_0^* \left. \frac{\partial w_1(\xi, \tau)}{\partial \xi} \right|_{\xi=0} = 0, \quad (23)$$

$$\left. \frac{\partial^2 w_1(\xi, \tau)}{\partial \xi^2} \right|_{\xi=1} + \left. \frac{\partial^2 w_2(\xi, \tau)}{\partial \xi^2} \right|_{\xi=1} - c_2^* \left. \frac{\partial w_1(\xi, \tau)}{\partial \xi} \right|_{\xi=1} = 0, \quad (24)$$

where:

$$c_0^* = \frac{c_0 l_1}{EJ}, \quad (25)$$

$$c_2^* = \frac{c_2 l_1}{EJ}. \quad (26)$$

The dimensionless differential equation of the lateral vibrations is as follows:

$$\frac{\partial^4 w_i(\xi_i, \tau)}{\partial \xi_i^4} + k_i^2 \frac{\partial^2 w_i(\xi_i, \tau)}{\partial \xi_i^2} + \Omega_i^2 \frac{\partial^2 w_i(\xi_i, \tau)}{\partial \tau^2} = 0, \quad (27)$$

where:

$$k_i^2 = \frac{Pl_i^2}{2EJ}, \quad (28)$$

$$\Omega_i^2 = \frac{(\rho_0 A)\omega^2 l_i^4}{EJ}. \quad (29)$$

2.3. Boundary problem solution to structural free vibration

The solution to differential Equation (27) may be found by achieving the boundary conditions and after separation of the variables towards spatial and time coordinate:

$$w_i(\xi_i, \tau) = y_i(\xi_i) \cos(\tau). \quad (30)$$

After substituting we get the movement differential equation in form:

$$\frac{d^4 y_i(\xi_i)}{d\xi_i^4} + k_i^2 \frac{d^2 y_i(\xi_i)}{d\xi_i^2} - \Omega_i^2 y_i(\xi_i) = 0, \quad (31)$$

or using derivatives

$$y_i^{IV}(\xi_i) + k_i^2 y_i''(\xi_i) - \Omega_i^2 y_i(\xi_i) = 0. \quad (32)$$

Solutions to Equation (32) are as follows:

$$y_i(\xi_i) = D_{i1} \cosh(\alpha_i \xi_i) + D_{i2} \sinh(\alpha_i \xi_i) + D_{i3} \cos(\beta_i \xi_i) + D_{i4} \sin(\beta_i \xi_i), \quad (33)$$

where:

$D_{i1}, D_{i2}, D_{i3}, D_{i4}$ – are constants of integration of each column element,

$$\alpha_i^2 = -0,5k_i^2 + \sqrt{0,25k_i^4 + \Omega_i^2}, \quad (34)$$

$$\beta_i^2 = 0,5k_i^2 + \sqrt{0,25k_i^4 + \Omega_i^2}. \quad (35)$$

Substituting solution (33) into the boundary conditions we get a set of homogeneous equations with unknowns D_{ij} ($i = 1, 2; j = 1, 2, 3, 4$), which we can write as follows

$$[b_{pg}] \text{col}\{D_{i1}, D_{i2}, D_{i3}, D_{i4}\} = 0 \quad (36)$$

where $p, g = 1, 2, \dots, 4i$.

The requirement for a nontrivial solution imposes equation:

$$\det[b_{pg}] = 0, \quad (37)$$

which leads to a transcendental equation determining the relations between the column load and its free vibrations.

3. Numerical and experimental studies

3.1. Vibration frequency in the external load function

In the scope of Euler column studies (jointed type A, B, and supported type C, D) numerical calculation of column free vibration in the external load function has been done. Experimental studies at the test bench [1] have been done as a validation. Rolling bearing (type A, C) or stiff cylindrical elements (type B, D) have been used as intermediary elements in the structural solution for the heads charging the load (Figures 2 and 3). The physical and geometrical parameters of the columns for which the numerical calculations and experimental studies have been carried out are presented in Table 1.

The course of changes in frequency in the external load function derived from the experimental studies are approximated in order to get a theoretical characteristic curve with the largest possible correlation factor (r) and the smallest possible standard deviation (S). The approximated curves of free vibration frequency are plotted along with the appropriate theoretical curves for selected columns in Figure 4.

Table 1. The physical and geometrical parameters of the given columns

Column (identification)	l [m]	$(EJ)_i$ [Nm ²]	$(\rho A)_i$ [kg/m]
A1, B1, C1, D1	0.730	76.3407	0.3155
A2, B2, C2, D2		141.4306	0.4295
A3, B3, C3, D3	0.800	76.3407	0.3155
A4, B4, C4, D4		141.4306	0.4295
A5, B5, C5, D5	0.730	104.8412	0.8641
A6, B6, C6, D6		194.2313	1.1761
A7, B7, C7, D7	0.800	104.8412	0.8641
A8, B8, C8, D8		194.2313	1.1761

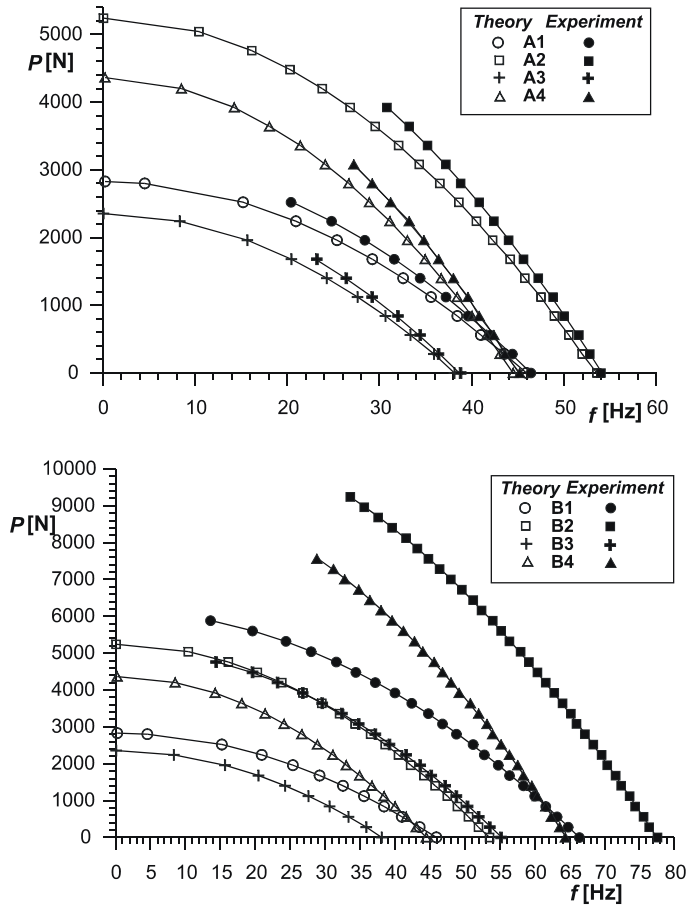


Fig. 4. Theoretical curves and experimental free vibration frequencies of columns A1–A4 and B1–B4

The characteristic curve equations together with the designated values of correlation factors and standard deviations are shown in Table 2. Only the basic free vibration frequency has been used in the experimental studies.

Table 2. Equations of approximating functions, values of correlations factors and standard deviations of columns A1–A4 and B1–B4

Column	Approximating function	r []	S []
A1	$f = 46.184227 - 0.0062235146 P - 1.519065 \cdot 10^{-6} P^2$	0.9974	0.2204
A2	$f = 54.016956 - 0.004277 P - 4.05164 \cdot 10^{-7} P^2$	0.9994	0.1871
A3	$f = 38.586071 - 0.0068908 P - 1.378 \cdot 10^{-6} P^2$	0.9951	0.0872
A4	$f = 45.003596 - 0.0043447 P - 4.609453 \cdot 10^{-7} P^2$	0.9987	0.1590
B1	$f = 66.63146 - 0.0038344 P - 7.303 \cdot 10^{-7} P^2$	0.9914	0.6063
B2	$f = 77.024688 - 0.00284587 P - 1.916915 \cdot 10^{-7} P^2$	0.9977	0.2841
B3	$f = 54.217286 - 0.004133815 P - 7.963 \cdot 10^{-7} P^2$	0.9945	0.3889
B4	$f = 64.17482 - 0.0028843 P - 2.24157 \cdot 10^{-7} P^2$	0.9980	0.2196

3.2. Torque rigidity in the external load function

In order to designate the character of the eigenvalue changes in the structures after stiffening the columns in those places where the charging heads with an intermediate element (rolling bearing or stiff cylindrical element) are acting, we modify the boundary conditions as follows

$$\sum_{i=1}^2 (EJ)_i w''(x,t) \Big|_{x=0}^{x=l} + c_T w'(x,t) \Big|_{x=0}^{x=l} = 0. \quad (38)$$

Based on the calculation programme we derive torque rigidity M , described by stiffness coefficient c_T , of the rotational spring. Value $c_T = M$ is derived based on the results of experimental studies (approximating function). Resulting curves M [Nm] in the external load changing function of the given columns are shown in Figure 5, and their equations with derived coefficients r , S are shown in Table 3.

Table 3. Equations of function $M = f(P)$, correlation coefficient and standard deviation values of columns A1–A4 and B1–B4

Column	Approximating function	r []	S []
A1	$M = 12.372909 + 0.014288961 P$	0.9985	0.0699
A2	$M = 22.984 + 0.014240816 P$	0.9984	0.1124
A3	$M = 11.265357 + 0.015626276 P$	0.9984	0.0664
A4	$M = 20.918462 + 0.015614635 P$	0.9992	0.1150
B1	$M = 762.6449 + 0.020072699 P$	0.9981	1.9732
B2	$M = 1414.8156 + 0.019461094 P$	0.9974	2.3028
B3	$M = 696.15462 + 0.021875276 P$	0.9985	1.6689
B4	$M = 1291.1764 + 0.021254643 P$	0.9969	2.0647

In reference [1] was shown that in the case of a one side fixed column which is loaded with a constant direction, the course of changes in the dimensionless free vibration frequency parameter in the dimensionless load parameter function is described by:

$$\Omega = \pi^4 \left(1 - \frac{\lambda}{\pi^2} \right), \tag{39}$$

while

$$\Omega = \frac{\rho A \omega^2 l^4}{EJ}, \tag{40}$$

$$\lambda = \frac{Pl^2}{EJ}. \tag{41}$$

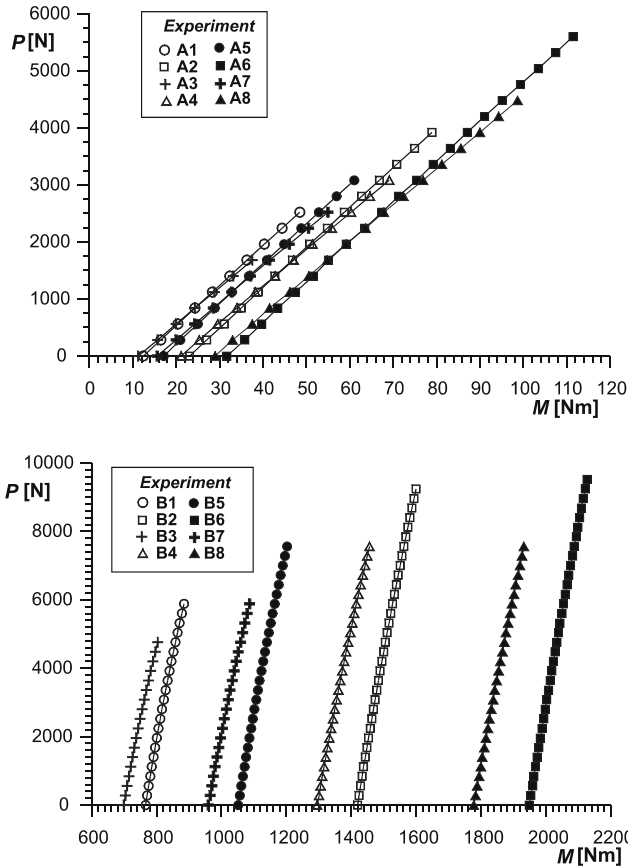


Fig. 5. The experimental curves of the torque rigidity of columns A1–A8 and B1–B8

Using the linear regression results, we derived the value of the dimensionless stiffness coefficient of the replacement rotational spring in external load parameter func-

tion, which was introduced into the boundary conditions. The resulting equations of the given structures are seen in Table 4.

Table 4. Equations of function $M^* = f(\lambda)$, for the given columns

Column	Approximating function
A1–A8	$M^* = 0.059152608 + 0.019526691 \lambda$
B1–B8	$M^* = 3.6630037 + 0.022380404 \lambda + 0.00024714467 \lambda^2$
C1–C8	$M^* = 0.089724791 + 0.024060625 \lambda + 0.00031038146 \lambda^2$
D1–D8	$M^* = 6.3205787 + 0.022411286 \lambda + 0.000929338348 \lambda^2$

It has been found that for a column loaded with a head with a rolling bearing as an intermediary element, the results of vibration frequency from experimental studies and numerical calculations are convergent (columns A and C). Using a stiff cylindrical element in loading head leads to a significant increase in the base free vibration frequency (columns B and D).

All the columns in the experimental studies are divergent type (negative slope of the characteristic curve).

Acknowledgements

The work has been done under grants BS 1-101-302/99/P and partially N N501 117236.

References

- [1] Tomski L., Kukła S., Posiadała B., Przybylski J., Podgórska-Brzdękiewicz I., Sochacki W., Szmidla J., Uzny S.: *Drgania i stateczność układów smukłych*, Praca zbiorowa pod kierunkiem naukowym i redakcją L. Tomskiego, Wydawnictwa Naukowo Techniczne, Fundacja „Książka Naukowo-Techniczna”, Warszawa, 2004.
- [2] Tomski L., Przybylski J., Podgórska-Brzdękiewicz I., Szmidla J., Uzny S., Kasprzycki A.: *Drgania swobodne i stateczność obiektów smukłych jako układów liniowych i nieliniowych*, Praca zbiorowa pod kierunkiem naukowym i redakcją L. Tomskiego, Wydawnictwa Naukowo Techniczne, Fundacja „Książka Naukowo-Techniczna”, Warszawa, 2007.

Wybrane rozwiązania konstrukcyjne struktur obciążających kolumny Eulera w badaniach drgań i stateczności

W niniejszej pracy przeanalizowano wpływ rodzaju elementu pośredniczącego (łożysko toczne, sztywny element walcowy) pomiędzy głowicą wymuszającą i przejmującą obciążenie na stateczność i drgania kolumn poddanych obciążeniu Eulera. Zastosowanie elementu sztywnego walcowego, w głowicach realizujących obciążenie w porównaniu z elementem tocznym, powoduje usztywnienie węzła obrotowego pomiędzy dwoma współdziałającymi elementami struktury obciążającej układ.



The conception of the fatigue model for layered composites considering thermal effects

A. KATUNIN

Silesian University of Technology, Department of Fundamentals of Machine Design,
ul. Konarskiego 18A, 44-100 Gliwice, Poland.

Polymer-based layered composites are widely used in many responsible applications, such as turbine blades, helicopter propellers etc. Therefore its behaviour must be predictable in different conditions and operational states. Dynamic excitation of polymer composites obliges to consider it as a viscoelastic material, which introduce additional phenomena, e.g. self-heating effect. This effect occurred into two states: steady and non-steady. The strain of the structure subjected to the self-heating could be evaluated basing of DMA measurements and using Arrhenius kinetic concept together with time-temperature superposition principle. For obtaining the fatigue model the pseudo-strain approach was used. The fatigue model was based on damage function with taking into consideration self-heating effect.

Keywords: *laminar fatigue, pseudo-strain, self-heating*

1. Introduction

The wide applicability of polymer-based layered composites in many responsible engineering solutions indicates to carry out research on its behaviour. Behaviour of the composite must be known in different loading conditions and operational states with appeared additional phenomena. If the polymer-based composite specimen is loaded cyclically, then its behaviour must be characterized as viscoelastic. Therefore, the hysteresis loop and derivative effects occurred due out-of-phase oscillation between stress and strain amplitudes. One of these effects is self-heating, which occurs in the steady and non-steady states. The occurrence of the self-heating effect is related with high stress values. The temperature evolution during the effect occurrence may differ depending on the mode of loading (constant stress or constant strain loading). In the case of constant strain loading the temperature grows rapidly to the equilibrium value between stored dissipation energy and the convection thermal boundary conditions. In the case of constant stress amplitudes the temperature rises rapidly until the breakdown of the structure. Such a phenomenon is known as thermal fracture [1, 18]. The heating up of the structure causes the stiffness degradation, which reflects in the development of microcracks in the areas of high stresses and thus the spontaneous degradation. In the practical applications the self-heating effect may occurs in two situations. In the first case the self-heating may occurs during the high stress loading even

with small excitation frequencies, which is noticed for parts of solid-propellant engines [22], gears made of plastics [17], etc. Such situation should be predictable and could be eliminated or minimized in the designing phase of the structural element. In the second case the structural element working in normal conditions (the self-heating effect does not occur) could be damaged which changes its natural frequencies of vibration. In the situation when the excitation frequency coincides with one of the resonant frequencies of vibration the spontaneous increase of the stress and strain amplitudes initiates the self-heating [8]. The effect of self-heating is not often taken into consideration but may have a great influence on the composite behaviour, e.g. fatigue and fracture processes.

The first research on the self-heating effect was introduced by Ratner and Korobov in late 60s. [19]. Their works were based on experimental determination of phase angle between stress and strain amplitudes. Then, theoretical investigations in this area were introduced by Senchenkov [21]. The authors [21] present the resulting constitutive equations in complete and approximate formulation of thermoviscoelasticity. Research of self-heating phenomenon was continued by Dinzart and Molinari [2]. They use the approximate formulation based on complex rigidity for describing steady state of temperature distribution caused by self-heating effect on viscoelastic homogeneous material. The author's research were also coincides with self-heating effect. In [10] Katunin discovered the one-dimensional model of self-heating of cantilever rectangular plate based on complex rigidity for in-plane laminate in a steady state. Then, the two-dimensional model for cases of cyclic simple bending of rectangular plates was investigated in [7].

The transient point between steady and non-steady state can be formulated as activation energy in light of the kinetic concept of fatigue. It can be obtained experimentally using dynamic mechanical analysis (DMA), but also by the Friedman method using a differential scanning calorimetry [25]. Analytically, it can be solved using Zhurkov's kinetic concept e.g. based on the logarithmic decrement of damping [16]. The logarithmic decrement of damping could be related with changes of the hysteresis loop during prolonged cyclic loading and thus with the amount of the dissipated energy occurred in this process. Having in mind an Arrhenius relation and the time-temperature superposition (TTS) principle for polymers it is possible to construct the master curves which describe the behaviour of the structure both in frequency and temperature domains [5]. Based on the loss rigidity master curve it is possible to determine the evolution of the dissipated energy in varying temperatures and frequencies.

The problem of fatigue and fracture of layered composites is a great subject of many scientific studies. There are many concepts and theories for describing the mechanisms of these phenomena. A great review of the fatigue models for composites was presented by Kamiński in [4]. The fatigue models could be classified in several groups: the models based on the estimation of the number of cycles to damage, stiffness reduction models, fatigue crack growth models and the models based on the damage

function estimation. Most of them are based on the power laws and be the most suitable for proper estimation and prediction of fatigue life of the structure.

The first research on polymers fatigue having taken into consideration self-heating were carried out by Oldyrev (see e.g. [14]). He discovered cyclically loaded FRP and their thermal response in a function of a number of cycles and presented the typical curve of self-heating temperature increase. In [15] the authors present empirical models of fatigue and fracture due to self-heating processes for FRP. Oldyrev also shows the problem of temperature non-stationarity due to the self-heating processes. The problem of self-heating effect during fatigue was reflected by the several authors, e.g. [1, 11–12], however the description of its influence was based on empirical relations and could not be generalized. The numerical studies of non-stationary temperature increase and its influence on the fatigue process were presented in [6, 9]. However, in many cases the self-heating remains in steady state and its influence on composite fatigue also must be predictable. Viscoelastic behaviour of a polymer-based laminate can be presented following the Boltzmann superposition principle. An alternative method of its behaviour can be presented by pseudo-strain approach proposed by Schapery [20] and developed by Sullivan [24]. This method allows linearization of the equation of viscoelasticity to an elastic-like equation with the introduction of pseudo variables, which could be used for constructing a fatigue model.

The main objective of this paper is to present a conception of fatigue model for polymeric composite materials subjected to prolonged cyclic loading with consideration of thermal effects. The investigated model is a rectangular plate made from layered FRP and described as a linear viscoelastic material. The viscoelasticity is presented using a pseudo-strain approach and a self-heating temperature is presented by complex rigidity based on the Boltzmann superposition principle. The acquisition of the activation energy is presented as combined experimental-theoretical approach and possibilities. Fatigue representation is based on a damage function while corresponding to a composite stiffness reduction.

2. Statement of the problem

Consider a rectangular transversal isotropic linearly viscoelastic layered thin plate subjected to the simple cyclic bending with constant strain amplitudes. The behaviour of such a plate could be described following the Boltzmann superposition principle with a given spectrum function, cf. [24]:

$$D_e \varepsilon_{ij}(t) = \sigma_{ij}(t) + \frac{n}{\pi} \int_0^t \varepsilon_{ij}(t-\tau, \theta) \psi(\tau) d\tau, \quad (1)$$

where:

D_e – the initial flexural rigidity,

ε_{ij} , σ_{ij} – the time-dependent strain and stress functions respectively,

n – the material constant [s^{-1}],
 τ – the relaxation time,
 θ – the temperature and

$$\psi(t) = \int_{n_0 t}^{\infty} \frac{\cos(z - n_0 t)}{z} dz. \quad (2)$$

The time-dependent stress $\sigma(t)$ could be presented in terms of complex rigidity [7]:

$$\sigma(t) = \varepsilon_{\max} \hat{D}(\omega, \theta_a), \quad (3)$$

where ε_{\max} is the maximum strain amplitude. The complex rigidity (4) can be expressed by the storage rigidity $D'(\omega, \theta_a)$ and the loss rigidity $D''(\omega, \theta_a)$ (5) [2]:

$$\hat{D}(\omega, \theta_a) = D'(\omega, \theta_a) + iD''(\omega, \theta_a), \quad (4)$$

$$D'(\omega, \theta_a) = \omega \int_0^{\infty} D(t, \theta_a) \sin(\omega t) dt, \quad D''(\omega, \theta_a) = \omega \int_0^{\infty} D(t, \theta_a) \cos(\omega t) dt, \quad (5)$$

and W is the deflection function for a plate with given boundary conditions [7].

Here, the complex rigidity and its parts depend on loading frequency ω and averaged temperature θ_a . The temperature dependence will be explained in Section 3.

3. The pseudo-strain method with self-heating

The viscoelasticity Equation (1) one can reduce to the form of the elastic-like equation by introducing the pseudo-strain concept, cf. [20]:

$$\varepsilon_{ij}^R(t) = \frac{1}{D^R} \int_0^t D(\omega, \theta_a, t - \tau) \dot{\varepsilon}_{ij} d\tau, \quad (6)$$

where:

D^R – the reference rigidity,

$D(\omega, \theta_a, t)$ – a frequency- and temperature-dependent complex rigidity. The stress function can be presented similarly to Hooke's law for the whole time spectrum:

$$\sigma(t) = D^R [\varepsilon^R(t) + \varepsilon^\theta(t)], \quad (7)$$

where ε^θ is the thermal stress component representing by self-heating.

Because of the steady state of self-heating we can assume that ε^θ is the time independent and expressed by (13) and D^R is the temperature independent.

$$\varepsilon^\theta = \alpha \Delta\theta, \tag{8}$$

where:

- α – the thermal expansion coefficient,
- $\Delta\theta$ – the self-heating temperature increment.

The dissipated energy can be obtained basing on hysteresis loop during cyclic loading:

$$Q_{sh} = \frac{2\pi}{\omega} \int_0^T \sigma_{ij} \dot{\varepsilon}_{ij} dt, \tag{9}$$

which can be expressed after several substitutions as [7]:

$$Q_{sh} = \frac{3}{2} \omega W^2 \varepsilon_{\max}^2 D''(\omega, \theta_a). \tag{10}$$

According to small temperature variation during one cycle the averaged form of self-heating temperature (9) will be used in further investigations [2].

$$\theta_a = \frac{2\pi}{\omega} \int_t^{t+T} \theta(t) dt, \tag{11}$$

where ω denotes the angular frequency and T denotes the cycle period.

The solution of the self-heating problem was based on the synergy between linear viscoelasticity equation and heat transfer equation. The solution was sought in the form of infinite double trigonometric series in the light of Fourier’s theorem. The two-dimensional temperature field for investigated case can be expressed as [7]:

$$\theta_a = \frac{6\omega W^2 \varepsilon_{\max}^2 D''(\omega, \theta_a)}{\lambda} \sum_{m,n=1}^{\infty} \frac{\text{sinc } \mu_m \text{ sinc } \gamma_n \cos \xi_m x \cos \xi_n y}{(1 + \text{sinc } 2\mu_m)(1 + \text{sinc } 2\gamma_n)(\xi_m^2 + \xi_n^2)} + \theta_0, \tag{12}$$

$$\mu \tan \mu = \alpha l, \quad \gamma \tan \gamma = \alpha b, \tag{13}$$

$$\xi_m = \frac{\mu_m}{l}, \quad \xi_n = \frac{\gamma_n}{b}, \tag{14}$$

where:

W – the shape function,

λ – denotes thermal conductivity,

θ_0 – an ambient temperature,

μ_m, γ_n – successive roots of Equations (13) obtained from thermal boundary conditions.

By substitution (12) to (8) we obtain thermal stress component in (7). The obtained dependence will be appropriate for steady state of self-heating of the layered composite.

4. Influence of the self-heating on the strain history

As it was mentioned before, the process of self-heating in polymer-based layered composites occurred in steady and non-steady states. During the cyclic loading with a constant strain rate the self-heating temperature increases exponentially and achieves the steady state. The temperature evolution was identified in the experiment for a cantilever FRP plate during cyclic loading using IR-camera [13]. The experiment was carried out for a plate with the following dimensions: effective length of 0.18 [m], width of 0.01 [m] and thickness of 0.0025 [m]. The plate was excited on its fundamental frequency of 262 [Hz] using the electrodynamic shaker. Typical self-heating temperature evolution obtained from the experimental data was presented in Figure 1, where the presented values are the peak temperature values of the distribution for a given time.

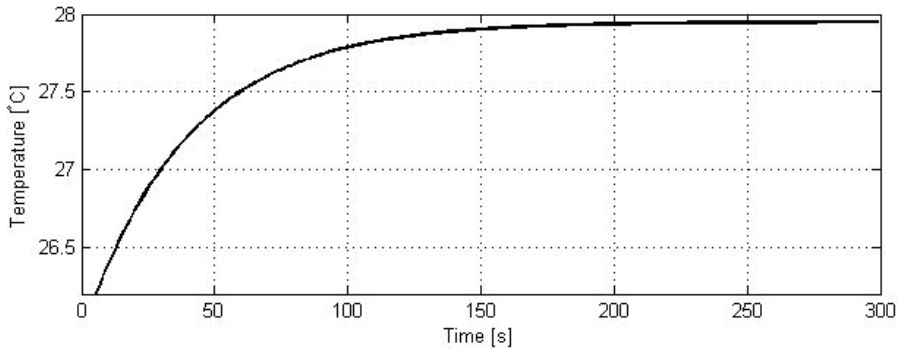


Fig. 1. Typical self-heating temperature evolution during cyclic loading with constant strain rate

The steady-state temperature distribution could be determined by the analytical model presented in [7]. According to the rapidity of the non-stationary process of the self-heating it could be assumed the steady state in whole strain history. For determining the stress function for various temperatures and excitation frequencies the complex rigidity from (6) should be achieved. The dependence of the complex rigidity from frequency and temperature could be determined using the Arrhenius relationship and TTS principle and presented in the form of a master curve. Such dependence was determined experimentally using DMA [5]. From the temperature scans with various

excitation frequencies the glass transition temperatures θ_g were determined and using Arrhenius kinetic concept (15) the activation energy E_a was calculated.

$$f = f_0 \exp\left(-\frac{E_a}{R\theta_r}\right). \tag{15}$$

Here f is an excitation frequency, $f = \omega/2\pi$, f_0 is the pre-exponential factor, R is the universal gas constant (8.314472 J/K·mol) and θ_r is the reference temperature ($\theta_r = \theta_g$).

Following the TTS principle (16) the rigidity for a given temperature and frequency equals to the rigidity for a reference temperature and frequency multiplied by the shift factor, which could be determined for the activation energy determined from (15) and for each temperature (17).

$$D(a_T f, \theta_r) = D(f, \theta), \tag{16}$$

$$\ln(a_T) = \frac{E_a}{2.303R} \left(\frac{1}{\theta} - \frac{1}{\theta_r} \right). \tag{17}$$

Based on the temperature scans and having shift factors it is possible to construct the master curve for the complex rigidity. The sequences of the complex rigidity should be presented in a frequency domain and then multiplied by the appropriate shift factor values for the translation of the sequences horizontally. The direction of shifting is determined by θ_r . The master curve of the complex rigidity allows determining the value of complex rigidity for arbitrary temperature and frequency and fulfilling the Equation (6). Having the strain history for arbitrary excitation parameters and considering self-heating effect the fatigue conception could be discussed.

5. The conception of fatigue model

Based on the kinetic concept the energy density W^R one can define as a product of the function of pseudo-strain and damage function S :

$$W^R = \frac{M(S)(\varepsilon^R + \varepsilon^\theta)^2}{2}, \tag{18}$$

where $M(S)$ is the constitutive function of damage. According to viscoelasticity $M(S)$ depends on time, because the damage function also depends on time. Finally one can write [23]:

$$\varepsilon^R(t) = \frac{D_e}{D^R} \left[\left(1 - \frac{m}{2}\right) (\varepsilon_{ij}(t) - \varepsilon_{ij}(0)) + \frac{m}{n} \int_0^t \varphi(n_0(t - \tau)) \dot{\varepsilon}_{ij} d\tau \right], \tag{19}$$

where

$$\varphi(n_0 t) = \int_{n_0 t}^{\infty} \frac{\sin(z - n_0 t)}{z} dz, \quad m = \frac{n}{n_0}.$$

For the damage function evaluation the Kachanov's damage law was applied [3]:

$$\frac{dS}{dt} = C \left(\frac{\sigma(t)}{1-S} \right)^\eta, \quad (20)$$

where C, η – empirical material constants. Assuming uniform damage growth and taking the integral from (20) we obtain:

$$S(t) = 1 - \left[1 - C(\eta + 1) \int_0^t (\sigma(t))^\eta dt \right]^{\frac{1}{\eta+1}}. \quad (21)$$

Assuming, that $S(t) = 1$, when breakdown occurs and considering (21) one can obtain the rupture time t_R :

$$t_R = [C(\eta + 1)(\sigma_0)^\eta]^{-1}. \quad (22)$$

Solving (21) for the term $C(\eta + 1)$ and taking into account (18) the damage function can be expressed as:

$$S(t) = 1 - \left\{ 1 - \frac{\int_0^t [M(t)(\varepsilon^R(t) + \varepsilon^\theta(t))]^\eta dt}{\int_0^{t_R} [M(t)(\varepsilon^R(t) + \varepsilon^\theta(t))]^\eta dt} \right\}^{\frac{1}{\eta+1}}, \quad (23)$$

where ε^θ will be time-independent only in steady state. Based on (23) the fracture model can be proposed by insertion of the faults function $S^F(t)$:

$$\bar{S}(t) = S^F(t) \left[1 - \left\{ 1 - \frac{\int_0^t [M(t)(\varepsilon^R(t) + \varepsilon^\theta(t))]^\eta dt}{\int_0^{t_R} [M(t)(\varepsilon^R(t) + \varepsilon^\theta(t))]^\eta dt} \right\}^{\frac{1}{\eta+1}} \right]. \quad (24)$$

The faults function is depended on time and has an influence on the constitutive function and thermal processes, therefore (24) must be taken as the first approximation solution.

6. Conclusions

The conception of the fatigue model considering self-heating effect for FRP composites was proposed. An applied pseudo-strain method for the viscoelasticity evaluation gives a possibility of simplifying the form of the viscoelasticity equation by taking into consideration the whole time spectrum. The thermal stress component was included into a stress function which was based on a pseudo-strain method. This component was presented as self-heating of the composite in a thermal steady state. The complex rigidity could be determined using the Arrhenius kinetic concept and TTS principle for fulfilling the frequency- and temperature-dependent strain component. Based on a pseudo-strain method the conception of a damage function was proposed: the Kachanov's damage growth law was enriched by a thermal stress component and the first approximation solution of a fracture model was discovered. In the fracture model it is necessary to evaluate the faults function based on the experiment and assume its values for different types of faults and its rate. The choice of the Kachanov's law allow to evaluate the character of the structural degradation of a composite structure precisely due to the fact that it is a power law, which coincides with several theoretical and experimental studies.

In the case of loading of the FRP structure with a constant strain rate the self-heating temperature increases rapidly and achieving the steady state, thus for a prolonged fatigue loading it could be assumed that the temperature is constant and equal to the steady-state self-heating temperature value. Proposed conception could be applied for the evaluation of loading parameters for the elements made of polymeric composites in the designing phase for neutralizing the self-heating effect during their operation. Moreover, it could be useful during the maintenance of damaged elements for the prediction of their residual life. For conducting the proposed conception the experimental study will be carried out.

Acknowledgements

Results presented in this paper have been carried out within the framework of the research grant No. N N504 282137 financed by the Polish Ministry of Science and Higher Education.

References

- [1] Bellenger V., Tcharkhtchi A., Castaing Ph.: *Thermal and mechanical fatigue of a PA66/glass fibers composite materials*, International Journal of Fatigue, Vol. 28, 2006, pp. 1348–1352.

- [2] Dinzart F., Molinari A., Herbach R.: *Thermomechanical response of viscoelastic beam under cyclic bending; self-heating and thermal failure*, Arch. Mech., Vol. 60, No. 1, 2008, pp. 59–85.
- [3] Kachanov L.M.: *On the time of failure under creep conditions*, Izv. Akad. Nauk SSR, Otdel Tekhn. Nauk, Vol. 8, 1958, pp. 26–31.
- [4] Kamiński M.: *On probabilistic fatigue models for composite materials*, International Journal of Fatigue, Vol. 24, 2002, pp. 477–492.
- [5] Katunin A., Hufenbach W., Kostka P., Holeczek K.: *Frequency dependence of the self-heating effect in polymer-based composites*, Journal of Achievements in Materials and Manufacturing Engineering, Vol. 41, No. 1–2, 2010, pp. 9–15.
- [6] Katunin A., Moczulski W.: *The conception of a methodology of degradation degree evaluation of laminates*, Eksploatacja i Niezawodność – Maintenance and Reliability, Vol. 41, No. 1, 2009, pp. 33–38.
- [7] Katunin A.: *Analytical model of the self-heating effect in polymeric laminated rectangular plates during bending harmonic loading*, Eksploatacja i Niezawodność – Maintenance and Reliability, Vol. 48, No. 4, 2010, pp. 91–101.
- [8] Katunin A.: *Influence of the steady-state self-heating on natural vibrations of GFRP laminate rectangular plates*, Proc. of 14th European Conference on Composite Materials, Budapest, No. 629, 2010, pp. 1–9.
- [9] Katunin A.: *Numerical study of the fatigue delamination growth considering thermal phenomena*, Diagnostyka, Vol. 56, No. 4, 2010, pp. 23–26.
- [10] Katunin A.: *Self-heating effect in laminate plates during harmonic forced loading*, Scientific Problems of Machine Operation and Maintenance, Vol. 44, No. 2, 2009, pp. 73–84.
- [11] Liu Y., Tian Z., Xie Z., Du X.: *Dynamic viscoelasticity of polyester/rubber composites under cyclic loading*, Journal of Materials Science and Technology, Vol. 21, No. 3, 2005, pp. 367–370.
- [12] Liu Z.Y., Beniwal S., Jenkins C.H.M., Winter R.M.: *The coupled thermal and mechanical influence on a glassy thermoplastic polyamide: Nylon 6,6 under vibro-creep*, Mechanics of Time-Dependent Materials, Vol. 8, 2004, pp. 235–253.
- [13] Moczulski W., Katunin A., Fidali M.: *Experimental study on the evolution of the self-heating temperature distributions in polymeric composites during resonant vibrations* (in Polish), Proc. 8th “Scientific and Technological Problems in Competitive Yachting Sport”, Warsaw, 2011.
- [14] Oldyrev P.P.: *Self-heating and failure of plastics under cyclic loading*, Trans. Mekhanika Polimerov, Vol. 3, No. 3, 1967, pp. 483–492.
- [15] Parfeev V.M., Oldyrev P.P., Tamuzh V.P.: *Damage summation in nonstationary cyclic loading of fiberglass-plastic*, Trans. Mekhanika Kompozitnykh Materialov, No. 1, 1979, pp. 65–72.
- [16] Porebska R.: *Selected problems of evaluation of mechanical properties of thermoplastic composites* (in Polish), PhD Thesis, Cracow Univ. of Techn., Cracow, 2008.
- [17] Ramkumar A., Kannan K., Gnanamoorthy R.: *Experimental and theoretical investigation of a polymer subjected to cyclic loading conditions*, International Journal of Engineering Science, Vol. 48, 2010, pp. 101–110.
- [18] Ratner S.B., Korobov V.I., Agamalyan S.G.: *Mechanical and thermal fracture of plastics under cyclic strains*, Trans. Fiziko-Khimicheskaya Mekhanika Polimerov, Vol. 5, No. 1, 1969, pp. 88–93.

- [19] Ratner S.B., Korobov V.I.: *Self-heating of plastics during cyclic deformation*, Trans. Mekhanika Polimerov, Vol. 1, No. 3, 1965, pp. 93–100.
- [20] Schapery R.A.: *Simplifications in the behaviour of viscoelastic composites with growing damage*, Proc. IUTAM on Inelastic DeJbrm. of Compos. Mater., Springer, New York, 1990, pp. 193–214.
- [21] Senchenkov I.K., Karnaukhov V.G., Kozlov V.I.: *Toward a theory of governing equations of thermoviscoelasticity for periodic deformation*, Trans. Prikladnaya Mekhanika, Vol. 22, No. 8, 1986, pp. 97–104.
- [22] Senchenkov I.K., Karnaukhov V.G.: *Thermomechanical behaviour of nonlinearly viscoelastic materials under harmonic loading*, International Applied Mechanics, Vol. 37, 2001, pp. 1400–1432.
- [23] Sullivan R.W.: *Development of viscoelastic continuum damage model for cyclic loading*, Mech. Time-Depend. Mater., Vol. 12, 2008, pp. 329–342.
- [24] Sullivan R.W.: *On the use of a spectrum-based model for linear viscoelastic material*, Mech. Time-Depend. Mater., Vol. 10, 2006, pp. 215–228.
- [25] Wang T., Liu R.Y., Zhu M.L., Zhang J.S.: *Activation energy of self-heating process studied by DSC. Combustion synthesis mixture of Ti-75 at% Al*, Journal of Thermal Analysis and Calorimetry, Vol. 70, 2002, pp. 507–519.

Koncepcja modelu zmęczeniowego dla kompozytów warstwowych z uwzględnieniem efektów cieplnych

Polimerowe kompozyty warstwowe są szeroko stosowane w wielu odpowiedzialnych aplikacjach takich, jak łopatki turbin, śmigła helikopterów itd. Z tego względu ich zachowanie powinno być przewidywalne w różnych warunkach i stanach operacyjnych. Dynamiczne wzbudzenie kompozytów polimerowych obliuguje do rozpatrywania ich jako materiału lepkosprężystego, co powoduje dodatkowe zjawiska, np. efekt samorozgrzania. Efekt występuje w stanie ustalonym i nieustalonym. Odkształcenia struktury pod działaniem efektu samorozgrzania mogą być określone w oparciu o pomiary DMA oraz z zastosowanie kinetycznej zasady Arrheniusa i zasady superpozycji czasowo-temperaturowej. W celu otrzymania modelu zmęczeniowego posłużono się metodą pseudo-odkształceń dla opisu lepkosprężystości. Model zmęczeniowy bazuje na funkcji zniszczenia z uwzględnieniem efektu samorozgrzania.



The influence of frontal protection system design on pedestrian passive safety

A. KOPCZYŃSKI, M. PTAK, P. HARNATKIEWICZ

Wrocław University of Technology, Faculty of Mechanical Engineering, 50-370 Wrocław, Poland
mariusz.ptak@pwr.wroc.pl

Car-to-pedestrian front impacts have been well described in the papers. However, there is still insufficient data measuring the performance of new type of Frontal Protection Systems (FPS) fitted on Sport Utility Vehicles (SUVs). Therefore, the aim of the studies was to validate the method of the FPS design, complying with the European Commission Regulations. The complete numerical model of the vehicle front with FPS was created and then subjected to a precise pedestrian impactor subtest. The physical experiment results proved good conformity with the outcomes from numerical simulations. Hence, the design of the presented FPS design was a base for legal process such as European Union homologation.

Keywords: Frontal Protection Systems (FPS), design of FPS, pedestrian impactor, pedestrian safety, experimental results, numerical simulations, European Union homologation

1. Introduction

It the late 60's, a rapid vehicle development trend made people think that 21st century cars would be more comfortable, particularly economical and, at the same time, safer. However, despite advanced research methods, aiming at reducing collisions, the statistics clearly do not agree with a forecasted safety image. In 2004, the World Health Organization stated that in 2010 the number of people killed in road accidents might reach 1/3 of overall deaths in the world [14]. Nowadays, the number of road fatalities is estimated to be 1.2 million and as many as 50 million others are injured [13].

The significant increase in the number of fatal car accidents has resulted in the development of studies aimed at reducing both the number of car-pedestrian accidents (the introduction of various early warning systems, allowing the driver to overtake the pedestrian or to suddenly stop the car) as well as the reduction of the pedestrian's injuries as a result of a collision with a vehicle (an appropriate motor-car body design).

Although car-pedestrian collisions can be reduced, they cannot be eliminated. Vehicle manufacturers have begun efforts to develop new solutions to car bonnets and bumpers. This work is mainly based on the requirements of EU directives concerning the pedestrians' safety, elaborated by the working group of EU EEVC WG 17 and the car industry experts [4]. The main objective of this research is to determine a minimum impact on lower limbs, pelvis and head injuries caused by pedestrian head-on collisions with vehicles.

The Directive 2003/102/EC of the European Parliament and of the Council of 17th November 2003 relates to the protection of pedestrians and other vulnerable road users prior to and in collisions with a motor vehicle. This Directive determines the type and form of tests necessary to obtain official certificates for new types of vehicles.

The legalization of a basic approach to pedestrian safety has resulted in alternating the motor vehicles' construction and therefore bumpers, wiper arms, door handles, hinges and headlight designs had been modified [8].

A pedestrian struck by a speeding car is particularly prone to leg and head injuries. A classical scenario of an adult being hit by a car can be described as follows. The victim's lower leg, in a car accident, is hit by the most protruding body parts of the car, such as bumpers and headlights. Secondly, the victim's body hits the engine shield as well as the intercooler which results in the victim being thrown forward on the bonnet making them hit their head on the edge of the bonnet cover, the windshield or the front pillar (Figure 1).

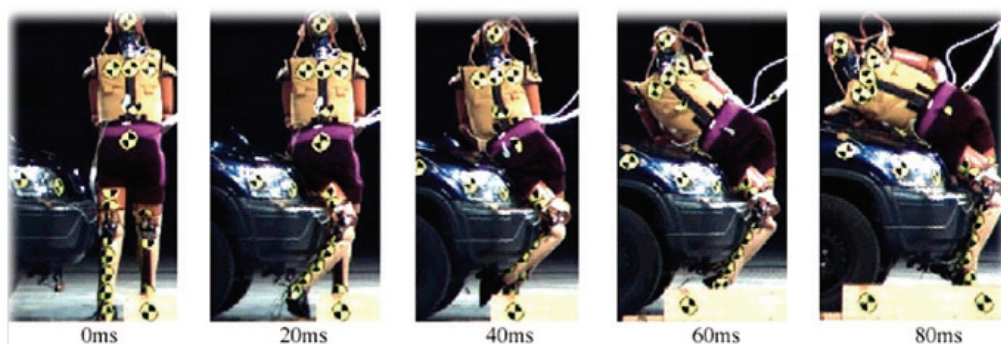


Fig. 1. The simulation of a pedestrian-SUV collision (crash test dummy) [12]

Subsequently, the body of a pedestrian is deflected behind or in front of the vehicle, resulting in the most serious injuries, very often impossible to alleviate. One way to increase pedestrian safety is the use of car high deformable bumpers [10]. At the instant of collision with a pedestrian, bumpers are prone to considerable deformations, allowing a significant absorption of impact energy. The lower a pedestrian is hit (preferably below the knees), the greater the likelihood that they will be undercut rather than thrown forward into the air – thus the greater chances of survival.

Another frequently used solution, designed to protect pedestrians, is to replace the hard surface of the bonnet, which the body of the passer-by falls on, with a more vulnerable surface, positioned at a specified distance from the engine shield.

2. Sport Utility Vehicle – SUV

SUVs (Sport Utility Vehicles) percentage in agglomerations is rapidly growing. They ensure better visibility, more spacious interiors, more luxurious, as well as more

practical compared to conventional passenger cars. However, they have drawbacks such as a larger mass (and therefore a higher fuel consumption), they are greater in height, which may result in a risk of rolling over (it is easier to master a lighter and lower regular passenger vehicle when entering a rapid turn). Yet, a very strong disadvantage of SUVs, which is rarely taken into account by consumers, is that the pedestrians' mortality rate after being run over by one is twice as high compared to accidents involving passenger cars [7].

The assumption that the sole threat caused by SUVs to pedestrians is their weight and size can be very misleading [6]. An increased mortality rate among run over pedestrians is mainly attributed by an improperly designed (in terms of pedestrian safety) geometry of the frontal part of the vehicle, which is primarily responsible for the vast injuries suffered by car accident victims [5, 9].

It is easy to introduce structural changes in passenger vehicles which aim at increasing the pedestrian's chances of survival in a crash with a speeding vehicle (the breaking/snapping of wiper blades, vulnerable bumpers, the front mask suspended on special hinges that increase their vulnerability in case of head impact). However, when it comes to off-road vehicles, or most common SUVs, in which case the front mask is usually positioned at chest level of an adult and the damper shield is positioned at the child's head level, the introduction of similar based changes would only inconsiderably increase the pedestrian's chances of survival.

The torso of a human body suffers no rotation (sliding down the mask) on impact with an SUV due to the impact being closer to the mass centre (in passenger vehicles far below), and therefore it results in the energy impact being several times more intense. For instance, raising the front bonnet of a vehicle by 600 to 850 mm results in doubling the impact on pedestrians, causing extensive damage to the head, chest and abdominal region [2].

3. Frontal Protection System – FPS

It is possible to achieve an increase in pedestrian safety, concerning off-road cars and SUVs, through the use of additional energy-absorbing components [11] mounted on the front part of the vehicle. The use of the Frontal Protection System (FPS) leads to a situation where a person colliding with a vehicle is subjected to rotation, causing the pedestrian to be jolted into the air and coincidentally falling on the mask instead of falling on the road and being pulled under the vehicle. The FPS (also known as a bull bar in some countries) is an element fitted to the front end of a car. Throughout history the aim of the FPS was the protection of the frontal mask during a collision with other vehicles, as well as animals, such as kangaroos in Australia. The European Parliament Directive 2005/66/EC regulates the requirements of bull bars to be met and therefore it is a requirement for FPS to have official certification in all the European Union countries – assembly and sale of non-certificate bull bars is illegal.

Based on EEVC WG17 directives (European Enhanced Vehicle – safety Committee) [8], the leg form test impactor and upper leg form test impactor had been elaborated, designed to investigate the frontal protection systems in motor vehicles. Verification and official certification of the frontal tubing consists of the lower leg impactor's impact velocity being 40 km/h on the absorber. During this test the following elements were measured: tibia deceleration, dynamic knee bending angle and knee joint displacement. Vehicle areas covered by the test include: the lower part of the bonnet, car grill, car grill shield, 1/3 of the mask height, called the Bonnet Leading Edge (BLE). In case of vehicle possessing front tubing as a constituent element, which is fitted to the BLE it should be subjected to the tests described in the above mentioned Directive.

4. The proposed research procedure

Directive 2005/66/EC of the European Parliament and of the Council of 26th October 2005 concerning the use of frontal protection systems in motor vehicles and amending Council Directive 70/156/EEC, is apprehensive with the use of frontal protection systems. It had been elaborated based on a report evaluated by a team of consultants entitled “European Enhanced Vehicle-safety Committee – Improved test methods to evaluate pedestrian protection afforded by passenger cars”.

The aim of the presented research results was the evaluation of a credible method of numerical simulations providing pedestrian safety and other vulnerable road users in such a way that the frontal protection system, treated as a separate technical unit designed for more than one type of vehicle, was separately certified for each vehicle type. Tests were performed according to technical requirements specified in Directive 2006/368/EC, which relates to Directive 2005/66/EC. Provisions included in the Directive contain the frontal protection system tests of the Nissan Navara, as a separate technical unit on the basis of point 2.1 2006/368/EC to Directive 2005/66/EC.

On the basis of point 2.2 of Directive 2005/66/EC 2006/368/EC, tests were performed on the numerical model of the Nissan Navara, which strictly corresponds with the basic outer dimensions of the front part of the actual vehicle, i.e. BLE. A numeric code LS-DYNA, designed for dynamic numerical calculations, had been used. Moreover, virtual leg and lower leg impactor models validated by Oasys Ltd. Company had been used in the test according to EU requirements. The impactors account for dynamic and nonlinear material and geometry – Chapter 3 and 4 of the subject norm. Numerical tests had been performed in compliance with the room temperature of 20 °C according to point 4.5 Chapter III, detailed technical provisions 2006/368/EC. The tolerance for the direction of the velocity vector in the horizontal plane and in the longitudinal plane was $\pm 2^\circ$ at the time of first contact.

The bottom of the impactor was 25 mm above ground reference level according to point 4.5 chapter III, detailed technical provisions 2006/368/EC to Directive 2005/66/EC, at initial contact of the impactor with the frontal protection system. It is shown in Figure 2.

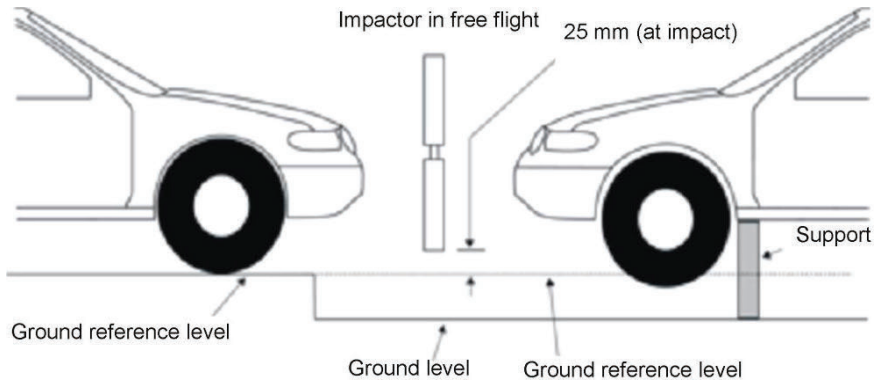


Fig. 2. Identifying impactor's ground reference level towards frontal protection system [3]

The impactor's coordinates had been positioned in such a way that the axis of the impactor was perpendicular to the horizontal plane with a tolerance of $\pm 2^\circ$ in lateral and longitudinal plane (Figure 3).

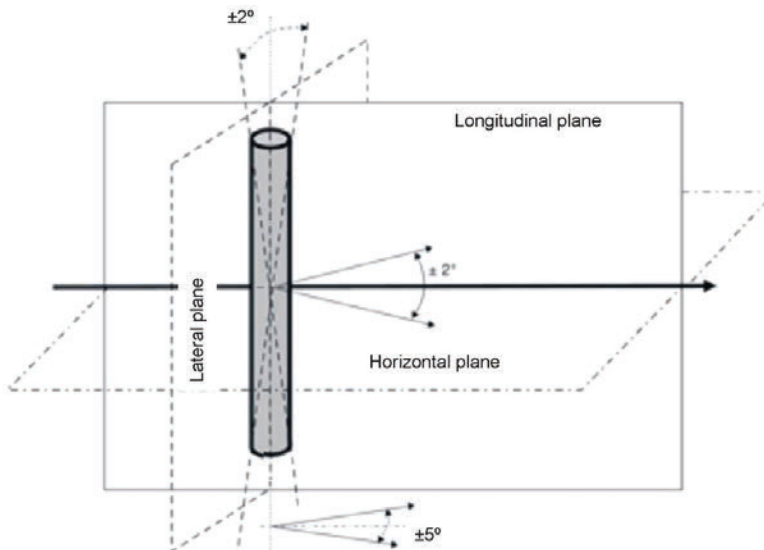


Fig. 3. Impact location [3]

On the basis of point 4.6 chapter III, detailed technical provisions 2006/368/EC to Directive 2005/66/EC a vertical axis was positioned with a tolerance of 5° for the correct operation of a knee joint. Tests had been performed assuring that the impactor had no contact with the ground or any other object after initial contact with the frontal protection system. Based on point 4.9 chapter III detailed technical provisions, the impact velocity of the impactor when striking the frontal protection system was

11.1 m/s. Tests were performed using the lower leg impactor according to point 3.1.2. and 3.1.2.2 attachment I to subject Directive as the lower part of the frontal protection system was 490 mm (Figure 4).

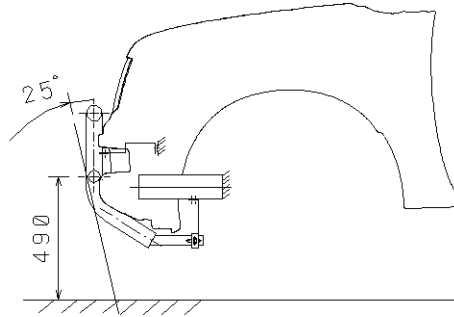


Fig. 4. The scope of application of the lower leg impactor according to point 3.1.2 attachment I to Directive 2005/66/EC

4.1. Numerical models – lower leg form model of pedestrian impactor

The lower leg impactor had been used in this test (Figure 5). The lower leg impactor, having a foam and skin layer, was suspended in a horizontal position. The impactor was suspended in such a way so that its longitudinal axis is horizontal, with a tolerance of $\pm 0.5^\circ$ and perpendicular to the direction of certified impactor with a tolerance of $\pm 2^\circ$. The impactor was properly positioned in relation to its longitudinal axis, with a tolerance of $\pm 2^\circ$ in order to provide a realistic functioning of a knee joint.

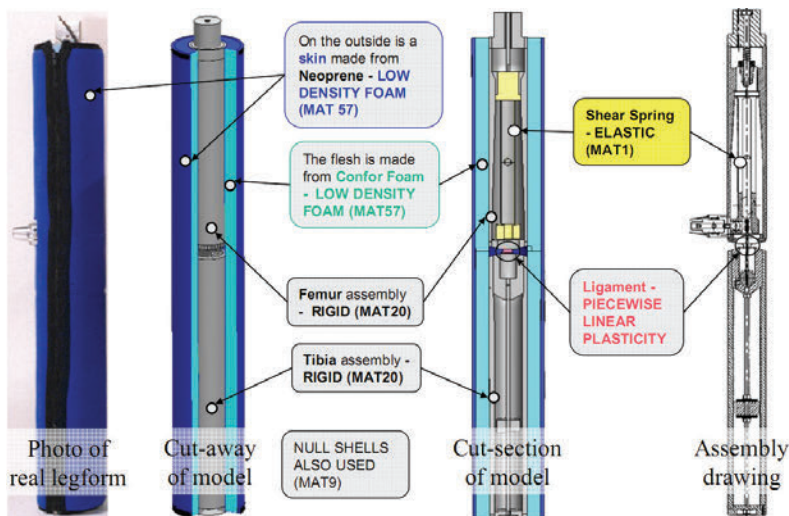


Fig. 5. The leg-form impactor covered with foam which represents skin and its numerical counterpart [1]

The numerical leg-form impactor model consists of 24 933 finite elements, 10 513 deformable elements, 16 097 nodes. Figure 6 shows description of upper impactor together with damper. The upper part of the impactor had been digitalized by the use of shell, beam and non-deformable elements of a rigid type.

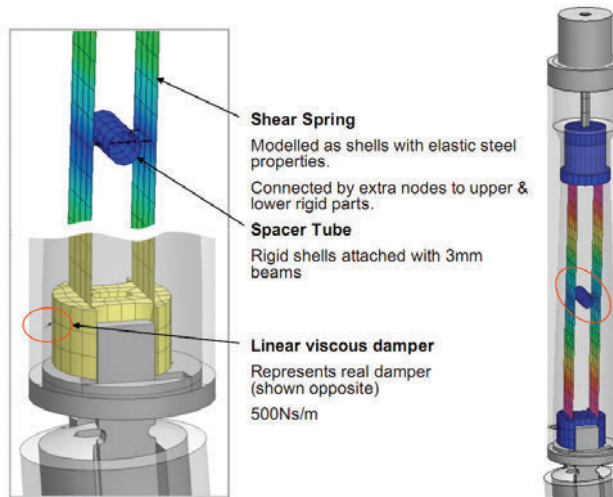


Fig. 6. Part of thigh bone together with damper [1]

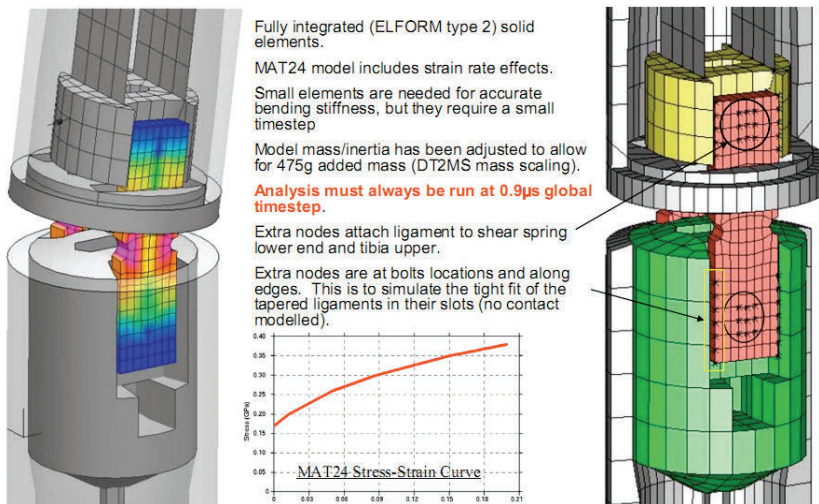


Fig. 7. Knee ligament structure [1]

The ligament had been described by the use of fully integrated shell and solid finite elements. In order to adjust the model's mass to its actual equivalent, mass elements had been used. Ligament elements are interdependent due to the definition of contact.

The impactor contains a mathematical description of the damper which is included within the shear displacement measurement system – Figure 7.

4.2. Numerical and experimental investigations

Actual tests of the frontal protection systems fitted to the Nissan Navara were performed (Figure 8) in accordance with the technical provisions of Directive 2005/66/EC of the European Parliament and of the Council on the use of the frontal protection systems on motor vehicles.



Fig. 8. The Frontal Protection System – 400 mm tubing fitted to the Nissan Navara, front view

Experimental tests were performed at the IDIADA Company in Spain, which is an approved authorized test unit on vehicles and components (Figure 9) providing design, engineering, testing and homologation services (in this case – tibia deceleration, knee bending angle and knee joint displacement were registered).



Fig. 9. The Crash test centre in IDIADA Company

Figure 10 shows tibia deceleration registered during the test in the IDIADA institution in Spain on the researched 400 mm tubing.

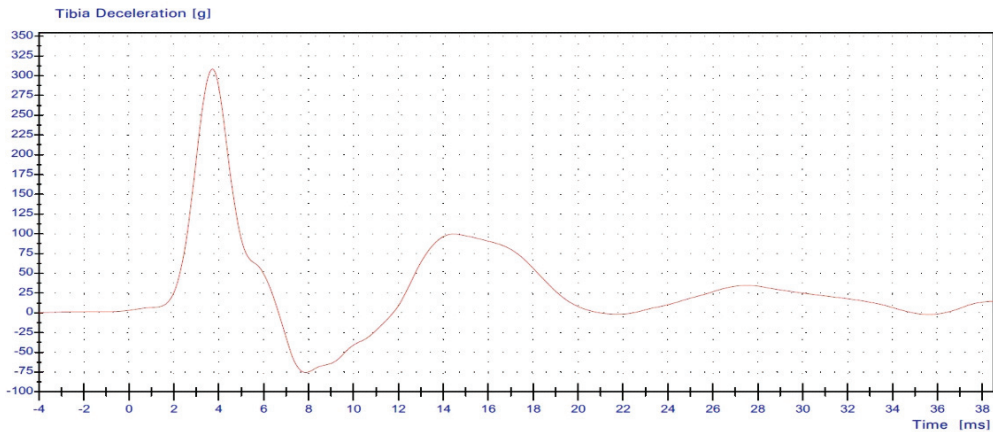


Fig. 10. Tibia deceleration registered during experimental tests in the IDIADA institution in Spain on the investigated 400 mm tubing

Numerical simulations were performed at the CAD Division, Institute of Machine Design and Operation of Wroclaw University of Technology. They were performed according to the subject Directive. During the first stage of the test, geometry of the Nissan Navara was reproduced by scanning the front part of the body of the car. In order for the numerical analyses of the pedestrian's safety to take place, body elements of the tested car had been optically scanned and reconstruction of CAD surface models was performed (reverse engineering). The obtained geometrical model of the vehicle was further equipped with the frontal protection system, basing on the precise documentation (Figure 11).

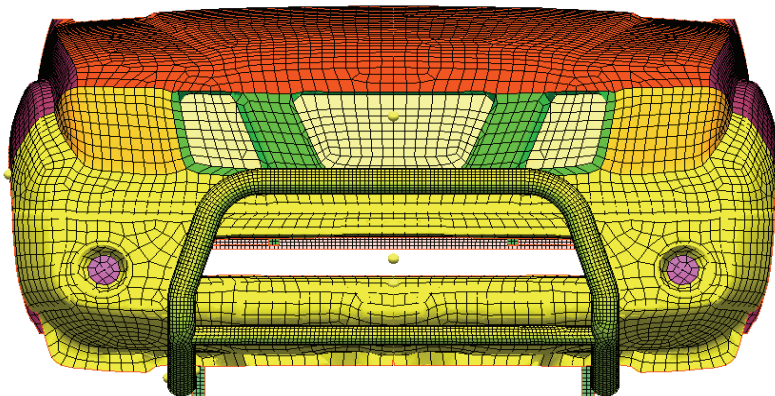


Fig. 11. Discrete model of Bonnet Leading Edge – Nissan Navara

The numerical simulations of the impact on the certified leg impactor to the bonnet leading edge were performed at the CAD Division of Wrocław University of Technology Institute of Machine Design and Operation. The tests were performed in accordance with the subject directive (2005/66/EC).

Boundary conditions of the analyzed object were specified based on Directive 2005/66/EC of the European Parliament and of the Council of 26th October 2005 concerning the use of the frontal protection systems in motor vehicles and specified technical requirements 2006/368/EC to Directive 2005/66/EC. Based on point 4.9, chapter III particular technical requirements, the impact velocity of the impactor was 11.1 m/s when striking the frontal protection system. Calculations had been made using the explicit code by the use of the LS-DYNA program.

Figures 12–14 show the results of numerical simulations and experimental tests in the form of characteristics representing the tibia deceleration, bending angle and lower leg shear displacement. Comparative analysis of the measured acceleration values from the experimental research, as well as from numerical studies led to the conclusion that the tests had been carried out correctly. Acceleration peak values were similar.

The research team evaluated the results of the tests, using finite element method [15], as satisfactory. Considering the importance of the research problem and the results obtained, it had been decided to perform a test on 565 mm tubing. The 565 mm marking refers to the distance between the axes of the lower crossbar of the Frontal Protection System to the ground. Figure 15 shows 565 mm tubing fitted to the tested Nissan Navara.

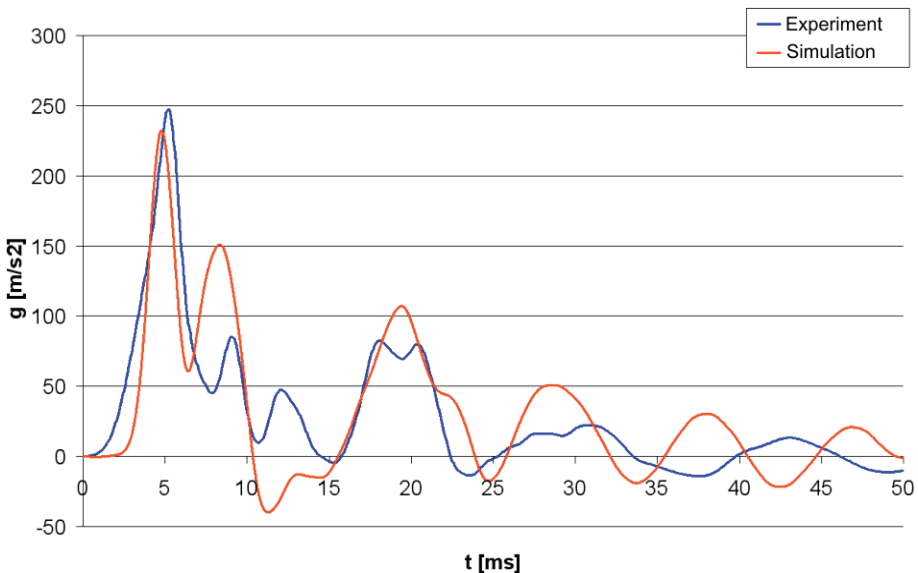


Fig. 12. The comparison of tibia deceleration results for the experimental test and numerical simulation during impact on 400 mm tubing

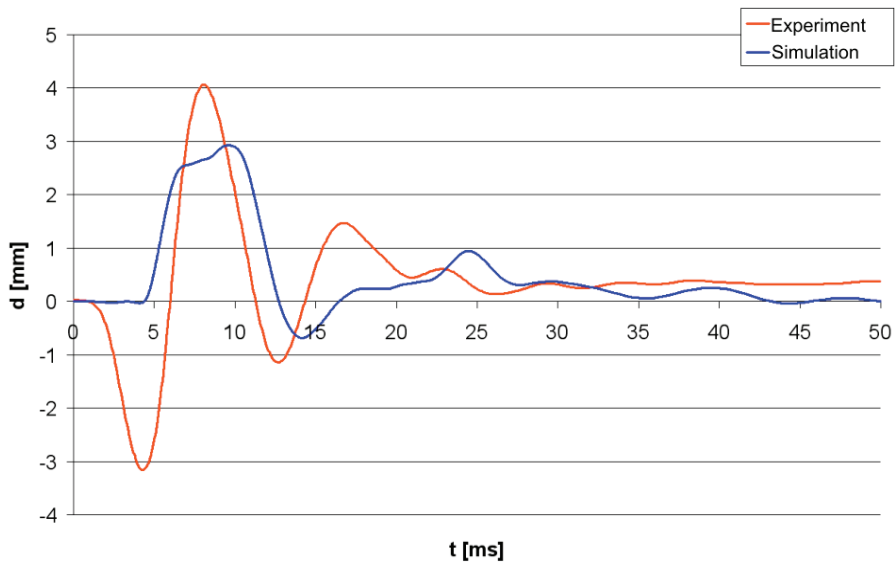


Fig. 13. The comparison of bending angle results for the test and numerical simulation during impact on 400 mm tubing

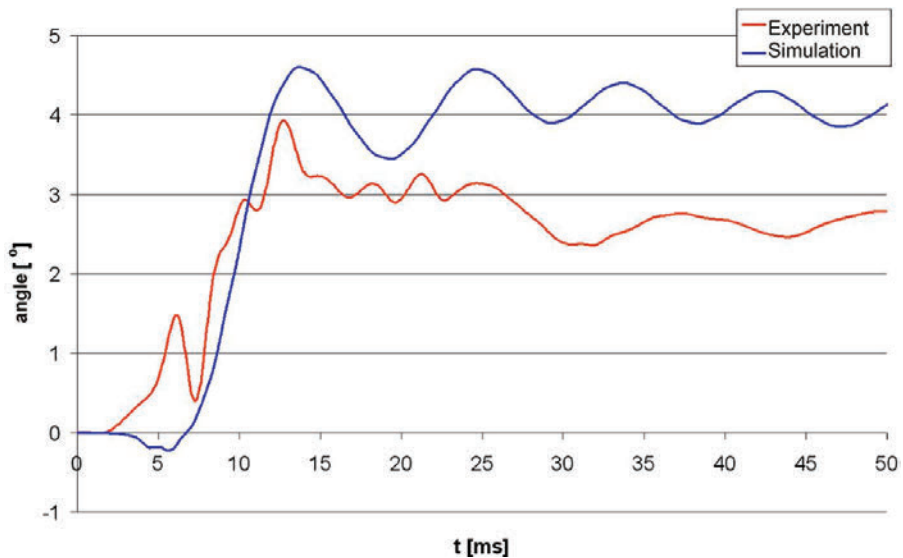


Fig. 14. The comparison of shear displacement angle results for the test and numerical simulation during impact on 400 mm tubing

Similarly to the 400 mm tubing, tests were performed on the 565 mm tubing at the IDIADA Company according to technical standards and regulations, Directive 2005/66/EC of the European Parliament and of the Council concerning the implementation

of frontal protection systems on motor vehicles and detailed technical requirements indispensable for carrying out tests specified in Directive 2006/368/EC of the European Parliament and of the Council concerning the implication of frontal protection systems on motor vehicles. Detailed conditions and regulations needed for the tests were described in Directive 2005/66/EC. Figure 16 shows the tested tubing and leg impactor at the test centre IDIADA in Spain.



Fig. 15. The frontal protection system – 565 mm tubing fitted to the Nissan Navara, a close-up was made on the points of measurement

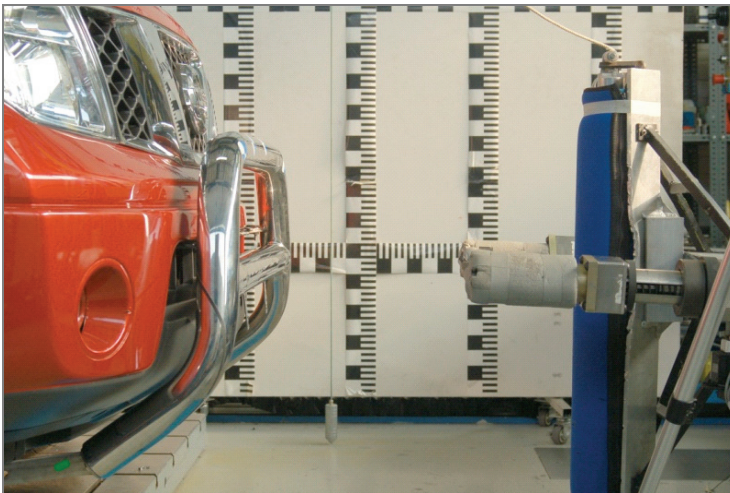


Fig. 16. Experimental test of 565 mm tubing

Figure 17 depicts the research results of the frontal protection system in the form of tibia deceleration registered during the test at the IDIADA centre, exploring the 565 mm tubing.

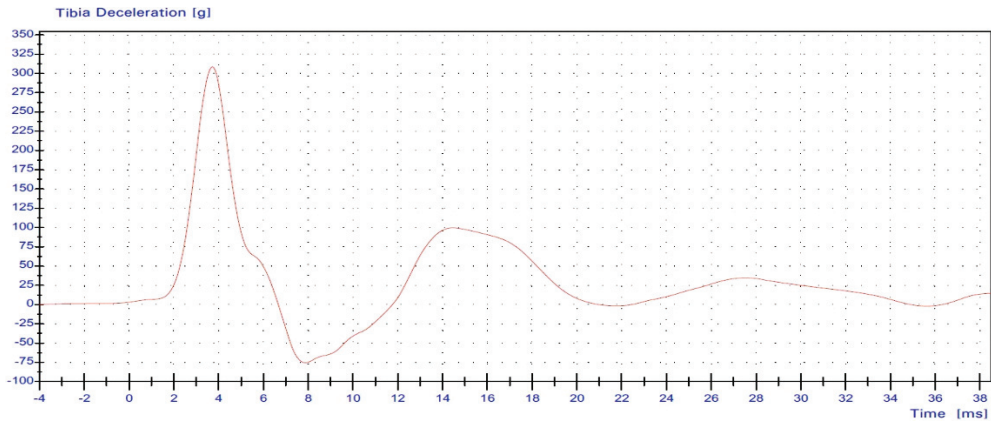


Fig. 17. The tibia deceleration registered during frontal protection system research on the Nissan Navara - 565 mm tubing was used

The numerical simulations, similarly as in the case of 400 mm tubing, had been carried out at the CAD Division of Institute of Machine Design and Operation, Wrocław University of Technology. Calculations had been done according to the subject Directive. The geometrical model of bonnet leading edge of the Nissan Navara had been used in the calculations. The geometrical model of the vehicle had been fitted with frontal protection system consisting of 565 mm tubing including the mounting. Figure 18 shows the discrete model of bonnet leading edge together with the frontal protection system – 565 mm tubing.

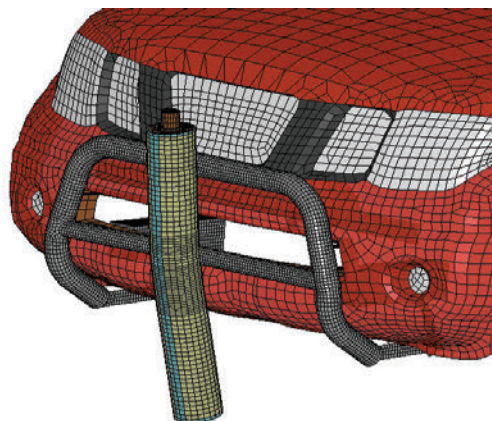


Fig. 18. Frontal Protection Systems numerical researches

Calculations had been made by the use of an explicit code using the LS-DYNA program. Figures 19–21 show the results of numerical simulations and experiments in the form of graphs representing the tibia deceleration, bending angle and lower leg shear displacement on central impact.

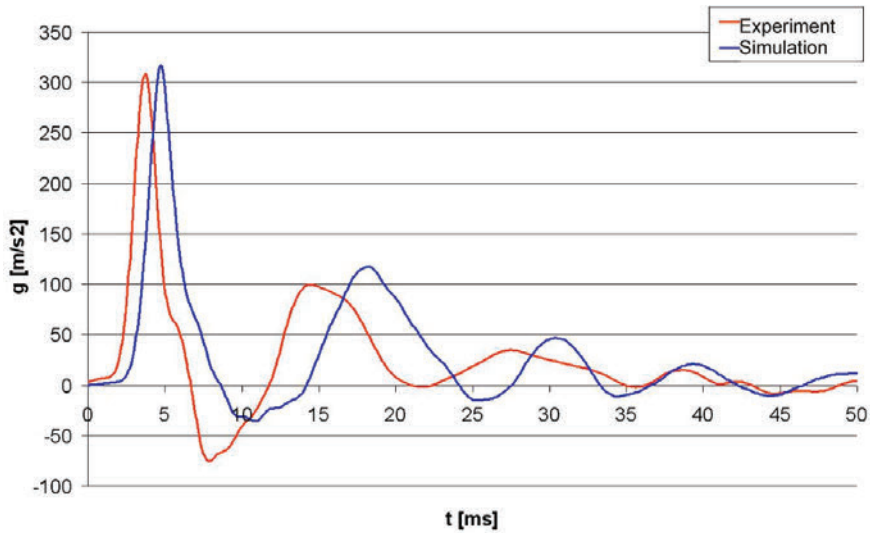


Fig. 19. The comparison of tibia deceleration results for the test and numerical simulation during impact on 565 mm tubing

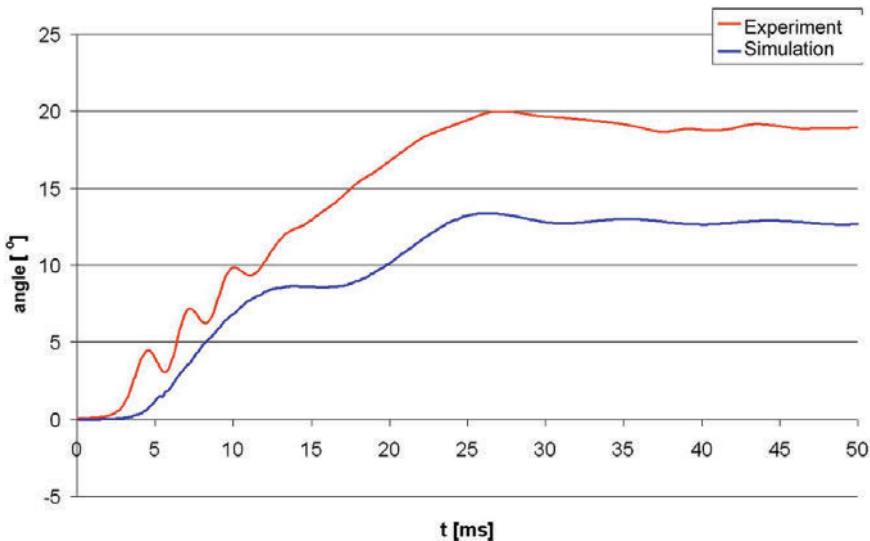


Fig. 20. The comparison of bending angle results for the test and numerical simulation during impact on 565 mm tubing

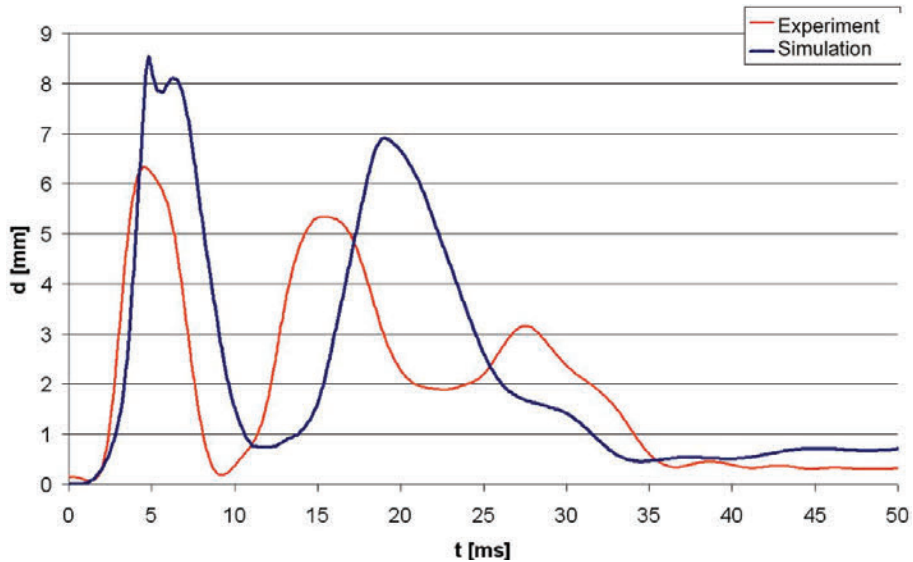


Fig. 21. The comparison of shear displacement results for the test and numerical simulation during impact on 565 mm tubing

The numerical simulations had been performed according to the subject Directive and the well-established methods for conducting numerical simulations, the evidence having similar characteristics of acceleration assessed at the point of measurement. The maximum value of the overload impact on the leg form impactor amounted to 303 g in the performed numerical simulation and 308 g in the actual test. The value defined in the Directive amounted to 250 g and shall not be exceeded – point 3.1.1.1.1. Directive 2005/66/EC. Based on the analysis of the calculation results, it had been claimed that the change in the binding thickness and shape of the 565 mm tested tubing, is not significant for the level of tibia deceleration the impactor is exposed to. Therefore, optimization of the 565 mm tubing was conducted in order to adapt its shape to the requirements of Directive 2005/66/EC.

The result of optimizing the design of 565 mm tubing was the change in diameter in the lower crossbar from 70 mm to 54 mm and its subsequent lowering to the cross-axis distance of 513 mm from the ground. Change in diameter and lowering the lower crossbar led to lowering of the bottom of the frontal protection system to the height of 490 mm from the ground. Therefore it was possible to carry out research according to Directive using the lower leg impactor – point 3.1.2 and 3.1.2.2 Attachment I to Directive 2005/66/EC. Figures 22 and 23 depict optimized frontal protection system meeting the technical requirements concerning carrying out researches on the leg impactor.

The object's discrete model was built, as previously, and the numerical calculations were carried out by the use of the LS-DYNA explicit code. Based on point 2.1., chapter III Attachment to detailed technical provisions – 2006/368/EC four types of researches were

performed on the frontal protection system impact on lower leg form impactor between upper and lower reference line of the frontal protection system. The points chosen for measurement were: $Y = 0$ mm in the centre of the bull bar; $Y = 362$ mm – offset from the car central axis. They have been described as the most injury prone places. Figures 24–29 illustrate research results of the frontal protection system according to the Directive 2005/66/EC.

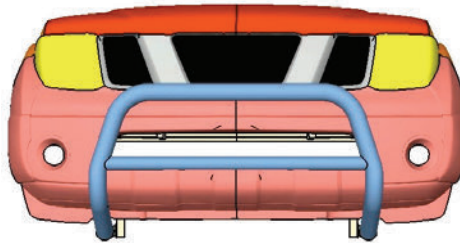


Fig. 22. Evaluated geometrical model of the frontal protection system with a lower crossbar at the height of 513 mm

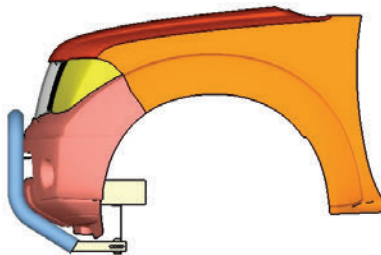


Fig. 23. Evaluated geometrical model of the frontal protection system with a lower crossbar at the height of 513 mm – side view

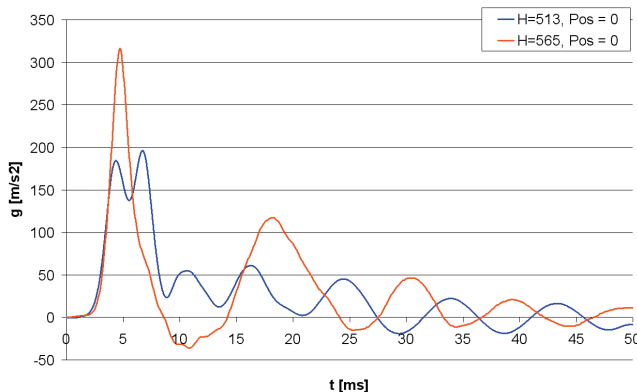


Fig. 24. The tibia deceleration results for the frontal protection systems 565 mm and 513 mm during central impact at point $Y = 0$ mm

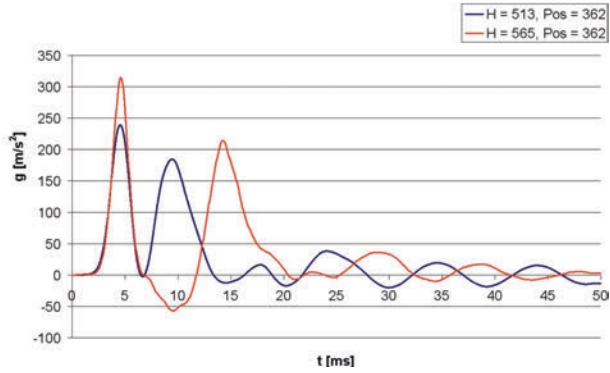


Fig. 25. The tibia deceleration results for frontal protection systems 565 mm and 513 mm during impact at offset point $Y = 362$ mm

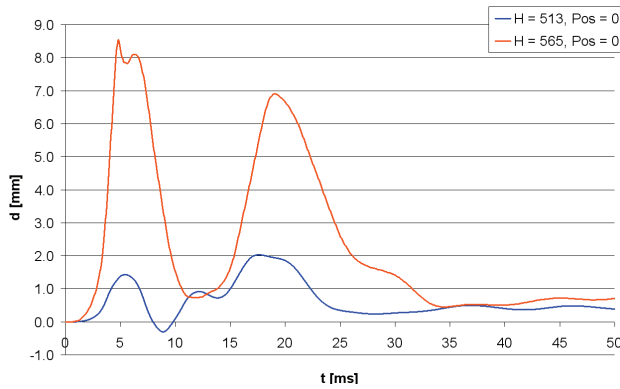


Fig. 26. The shear displacement results for the frontal protection systems 565 mm and 513 mm during central impact at point $Y = 0$ mm

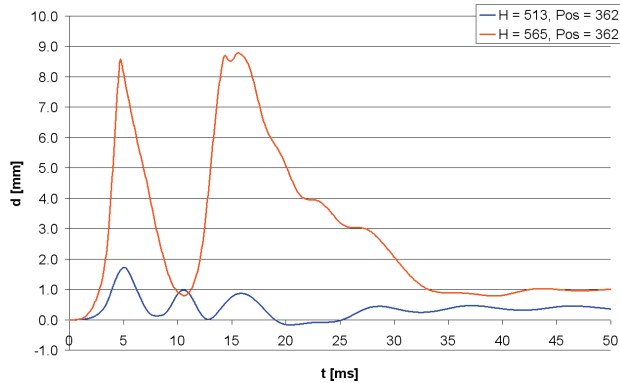


Fig. 27. The shear displacement results for the frontal protection systems 565 mm and 513 mm during impact at offset point $Y = 362$ mm

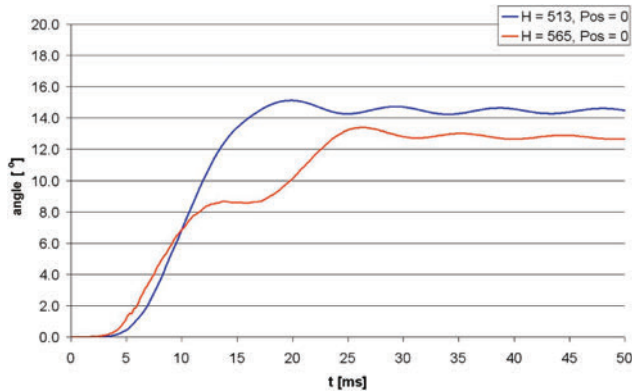


Fig. 28. Turning angle in time function for frontal protection systems 565 mm and 513 mm during central impact at point $Y = 0$ mm

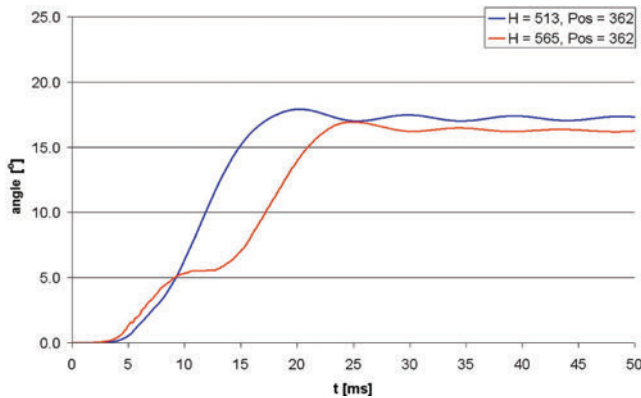


Fig. 29. Bending angle in time function for frontal protection systems 565 mm and 513 mm during impact at offset point $Y = 362$ mm

5. Conclusion

The aim of the presented results of the performed tests were to validate the methods used in the researches on the frontal protection system using finite element analysis, according to the Directive 2005/66/EC of the European Parliament and of the Council concerning the implication of frontal protection systems in motor vehicles.

The maximum overload impact on the numerical lower leg impactor amounted to 316 g whereas the value determined during the experiment was 308 g (in both cases, exceeding the limit value of 250 g as defined in Directive 2005/66/EC). The maximum value of the knee joint displacement was 8.54 mm for the numerical simulation and 6.35 mm for the test, while the maximum measured value of the bending angle was 13.39° for the numerical simulation and 19.98° for the real test.

Analysis of the tibia deceleration, the bending angle and the knee joint displacement obtained from the experimental and numerical researches proves that the tests had been performed correctly. The values gained from the numerical simulations of the shear displacement and bending angle can be regarded as satisfactory.

From the research teams' experience as well as other institutions dealing with numerical researches, it turns out that it is possible to carry out a proper computer simulation of the frontal protection system of a motor vehicle according to Directive 2005/66/EC (2006/368/EC) and latter amendments. Models used in the simulations are compatible with the ones described in the Directive. Identified parameters of the material models adopted for the calculations correspond to the actual material's strain-rates with due regard for the nonlinearities.

It has been established that simulation research test results can serve as an evaluation of frontal protection system of motor vehicles under the requirements defined in Directive 2005/66/EC of European Parliament and of the Council.

References

- [1] ARUP: *A new pedestrian lower legform model for LS-DYNA*, p. 1, ARUP, 2003.
- [2] Ballesteros M.F., Dischinger P.C., Langenberg P.: *Pedestrian injuries and vehicle type in Maryland, 1995–1999*, Accident Analysis & Prevention, Vol. 36, No. 1, 2004, pp. 73–81.
- [3] Commission Regulation (EC), No. 631/2009, Official journal of the EU, 2009.
- [4] European Enhanced Vehicle-safety Committee, WG 17 Report, *Improved test methods to evaluate pedestrian protection afforded by passenger cars*, Brussels, 2002.
- [5] Henary B.Y., Crandall J., Bhalla K., et al.: *Child and adult pedestrian impact: the influence of vehicle type on injury severity*, Ann. Proc. Assoc. Adv. Automot. Med. 47, 2003, pp. 105–126.
- [6] Lefler D.E., Gabler H.C.: *The fatality and injury risk of light truck impacts with pedestrians in the United States*, Accident Analysis and Prevention, Vol. 36, 2004, pp. 295–304.
- [7] Matsui Y., Wittek A. Konosu A.: *Comparison of pedestrian subsystem safety tests using impactors and full-scale dummy tests*, Japan Automobile Research Inst., 2002.
- [8] McLean A.J.: *Vehicle design for pedestrian protection*, Centre for Automototive Safety Research CASR037, The University of Adelaide, 2005.
- [9] Roudsari B.S., Mock C.N., Kaufman R., Grossman D., Henary B.Y., Crandall J.: *Pedestrian crashes: higher injury severity and mortality rate for light truck vehicles compared with passenger vehicles*, Injury Prevention, Vol. 10, 2004, pp. 154–158.
- [10] Rusiński E., Czmochoowski J., Smolnicki T.: *Advanced finite element method for load-carrying structures of machines*, Oficyna Wydawnicza PWR, Wrocław, 2000.
- [11] Rusiński E., Kopczyński A., Czmochoowski J.: *Tests of thin-walled beams joined by spot welding*, Journal of Materials Processing Technology, Vol. 157–158, 2004, pp. 45–409.
- [12] Simms C., Wood D.: *Pedestrian and cyclist impact: a biomechanical perspective*, London, New York: Springer, 2009.
- [13] World Health Organization: *Global status report on road safety*, Geneva, 2009.
- [14] World Health Organization: *World report on road traffic injury prevention*, Geneva, 2004.
- [15] Zienkiewicz O.C., Taylor R.L.: *The finite element method*, Fourth Edition, Vol. 1–2, McGraw-Hill, Berkshire England, 1991.

Wpływ przedniego układu zabezpieczającego na bezpieczeństwo bierne pieszego

W pracy przedstawiono studium badań nad zwiększeniem bezpieczeństwa biernego pieszego podczas potrącenia przez pojazd SUV. Wykorzystanie symulacji numerycznych opartych na Metodzie Elementów Skończonych (MES) znacząco przyspieszyło testy kolejnych wersji konstrukcyjnych przedniego układu zabezpieczającego. Podczas badań korzystano z certyfikowanego impaktora nogi człowieka – zarówno rzeczywistego jak i numerycznego. Przeprowadzone badania w akredytowanym laboratorium badawczym potwierdziły zgodność wyników symulacji z eksperymentem fizycznym. Zgodnie z Dyrektywą 2005/66/WE opracowana konstrukcja przedniego układu zabezpieczającego może być dopuszczona do użytku na określonym pojeździe typu SUV.

Love waves in initially deformed rubberlike Gent and Yeoh materials

A. KOSIŃSKA, S. KOSIŃSKI

Łódź University of Technology, al. Politechniki 6, 90-924 Łódź, Poland.

The purpose of this paper is to consider the effect of the initial deformation on the propagation of Love waves in nonlinear rubberlike materials with the representation of the strain energy function derived by Gent and Yeoh. A layer of finite thickness overlying a half space, both made of different and initially deformed rubberlike materials is taken. We assume that the initial deformation in both material regions is the same. The dependence of the strain energy function $W = W(I_1)$ on the first invariants I_1 of the deformation tensor generates in both of these materials essential qualitative differences between the linear and linearised approach to the Love waves.

Keywords: *Love waves, Gent and Yeoh materials, small motions superimposed on large static deformations*

1. Basic equations

We consider a layer and a half-space referred to a coordinate system as shown in Figure 1. Both the layer and the supporting half-space are made of different pre-stressed incompressible nonlinear rubberlike materials and they are rigidly coupled along the plane $X_2 = 0$. The initial static deformation in both material regions, the layer and the half-space are the same. Here and below all quantities with the mark “-“ are valid for the half-space $X_2 < 0$. The general motion to be discussed here is defined by (1). It is assumed that the material has been subjected to an initial static homogeneous deformation with constant principal stretches and to a different superimposed small motions $u_3 = u_3(X_1, X_2, t)$ and $\bar{u}_3 = \bar{u}_3(X_1, X_2, t)$ characterized by a small displacement field which is time dependent:

$$\begin{aligned} x_1 &= \lambda X_1, & x_2 &= \lambda^{-2} X_2, & x_3 &= \lambda X_3 + u_3(X_1, X_2, t), \\ \bar{x}_1 &= \lambda X_1, & \bar{x}_2 &= \lambda^{-2} X_2, & \bar{x}_3 &= \lambda X_3 + \bar{u}_3(X_1, X_2, t) \end{aligned} \quad (1)$$

and we determine the propagation conditions for the infinitesimal plane harmonic SH waves which are represented by the terms u_3 and \bar{u}_3 . The final and static deformations are very close. The components of the deformation gradient \mathbf{F}_0 and \mathbf{F} (for static and final deformation) and the components of the right Cauchy-Green tensor \mathbf{C} , are:

$$[\mathbf{F}_0] = \begin{bmatrix} \lambda & 0 & 0 \\ 0 & \lambda^{-2} & 0 \\ 0 & 0 & \lambda \end{bmatrix}, \quad [\mathbf{F}] = \begin{bmatrix} \lambda & 0 & 0 \\ 0 & \lambda^{-2} & 0 \\ u_{3,1} & u_{3,2} & \lambda \end{bmatrix}, \quad [\bar{\mathbf{F}}] = \begin{bmatrix} \lambda & 0 & 0 \\ 0 & \lambda^{-2} & 0 \\ \bar{u}_{3,1} & \bar{u}_{3,2} & \lambda \end{bmatrix}, \quad (2)$$

where:

$$u_3(X_1, X_2, t) = w(X_2)u(X_1, t),$$

$$\partial u_3 / \partial X_i = u_{3,i} \text{ for } i = 1, 2.$$

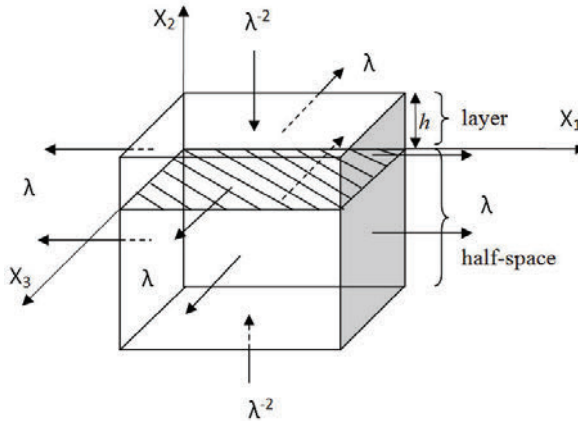


Fig. 1. The model of waveguide

For an incompressible isotropic hyperelastic material there exists a strain energy function denoted $W = W(\mathbf{F})$, defined on the space of deformation gradients such that, the nominal stress tensor \mathbf{S} (the transpose of the first Piola-Kirchhoff tensor) is defined as

$$\mathbf{S} = [\partial(W(\mathbf{F})) / \partial \mathbf{F}] = 2W_1 \mathbf{F}^T + 2W_2 (I_1 \mathbf{F}^T - \mathbf{C} \mathbf{F}^T) - \pi \mathbf{F}^{-1}, \quad (3)$$

where:

$$I_i \text{ are invariants of the deformation tensor } \mathbf{C} = \mathbf{F}^T \mathbf{F}, \quad W_i = \partial W / \partial I_i \text{ for } i = 1, 2,$$

π is the hydrostatic pressure. The linearization of the constitutive relations gives the following result

$$\tilde{\mathbf{S}} = \mathbf{S}^0 + \hat{\mathbf{S}}, \quad \tilde{\pi} = \pi^0 + \hat{\pi}, \quad (4)$$

where the first term in both equations is connected with the static deformation and the second one with the small wave motion $u_3 = u_3(X_1, X_2, t)$. The stress tensor components which we need to consider below are S_{13} and S_{23} . It follows from (2) and (3) that

$$S_{13}^0 = 0, \quad \hat{S}_{13} = 2(W_1 + W_2 \lambda^{-4})u_{3,2}, \quad S_{23}^0 = 0, \quad \hat{S}_{23} = 2(W_1 + W_2 \lambda^2)u_{3,2}. \quad (5)$$

$$\tilde{S}_{22} = S_{22}^0 = 2(W_1 \lambda^{-2} + 2W_2) - \pi^0 \lambda^2 \Rightarrow \hat{\pi} = 0.$$

Substitution of (4) into the differential equations of motion of finite elasticity, adequate for the analyzed case, i.e.

$$S_{ci,\alpha} = \rho_R \ddot{u}_3 \quad (i, \alpha = 1, 2, 3), \quad (6)$$

gives for the superimposed infinitesimal displacement two nontrivial systems of equations of motion in the layer and in the half-space

$$\begin{aligned} i = 1, 2 &\Rightarrow \hat{\pi}_{,1} = \hat{\pi}_{,2} = 0, & \hat{\pi}_{,1} = \hat{\pi}_{,2} = 0, \\ i = 3 &\Rightarrow A_{33}^{11}(\mathbf{F}_0)u_{3,11} + A_{33}^{22}(\mathbf{F}_0)u_{3,22} = \rho_R \ddot{u}_3, & \bar{A}_{33}^{11}(\bar{\mathbf{F}}_0)\bar{u}_{3,11} + \bar{A}_{33}^{22}(\bar{\mathbf{F}}_0)\bar{u}_{3,22} = \bar{\rho}_R \ddot{\bar{u}}_3. \end{aligned} \quad (7)$$

The nontrivial equation of motion in the layer takes the form

$$c_{T\parallel}^2 w(X_2)[u(X_1, t)]_{,11} + c_{T\perp}^2 u(X_1, t)[w(X_2)]_{,22} = w(X_2) \ddot{u}(X_1, t), \quad (8)$$

where $c_{T\parallel}^2 = 2(\bar{W}_1 + \bar{W}_2 \lambda_2^2)/\rho_R$ and $c_{T\perp}^2 = 2(\bar{W}_1 + \bar{W}_2 \lambda_1^2)/\rho_R$ can be interpreted as propagation speed of the shear plane waves in initially deformed layer in the direction parallel and normal to the interface $X_2 = 0$ (comp. Figure 1) and $\bar{W}_i = W_i(\mathbf{F}_0)$, $i = 1, 2$.

Suppose now that the displacements in the layer and in the half-space are given by

$$u_3 = w(X_2) \exp[i(k X_1 - \omega t)], \quad \bar{u}_3 = \bar{w}(X_2) \exp[i(\bar{k} X_1 - \bar{\omega} t)]. \quad (9)$$

Substituting of (10)_{1,2} into (9) gives two equations for two unknown functions $w(X_2)$, $\bar{w}(X_2)$

$$[w(X_2)]_{,22} + k^2 p^2 w(X_2) = 0, \quad [\bar{w}(X_2)]_{,22} + \bar{k}^2 \bar{p}^2 \bar{w}(X_2) = 0, \quad (10)$$

where: $p^2 = (\omega^2 / (k^2 c_{T\perp}^2) - (c_{T\parallel} / c_{T\perp})^2)$, $\bar{p}^2 = (\bar{\omega}^2 / (\bar{k}^2 \bar{c}_{T\perp}^2) - (\bar{c}_{T\parallel} / \bar{c}_{T\perp})^2)$, and the displacements (10) take the form

$$u_3 = \exp[i(k X_1 - \omega t \pm k p X_2)], \quad \bar{u}_3 = \exp[i(\bar{k} X_1 - \bar{\omega} t \pm \bar{k} \bar{p} X_2)]. \quad (11)$$

They are the four principal solutions essential for the propagation of the Love waves.

Where the initial deformation vanishes, then speeds $c_{T//} = c_{T\perp} = c_T = (\mu / \rho_R)^{1/2}$, functions p, \bar{p} and displacements (12) are identical as in the linear theory.

The initial static deformations λ_i and $\bar{\lambda}_i$ ($i = 1, 2, 3$) in the layer and half-space are identical. When the layer and the half-space are in rigid contact along the plane $X_2 = 0$, then the displacement vector and stress vector must be continuous at the interface i.e.

$$\tilde{S}_{2i}(\mathbf{F}) = \bar{\tilde{S}}_{2i}(\bar{\mathbf{F}}), \quad i = 1, 2, 3 \quad \text{and} \quad u_3(X_1, 0, t) = \bar{u}_3(X_1, 0, t). \tag{12}$$

The boundary conditions at the interface are satisfied if and only if $\omega = \bar{\omega}, k = \bar{k}$.

According to the continuity conditions at the interface, the small wave motion is dynamically admissible if and only if, the static deformations and small wave motions satisfy the following conditions:

$$\begin{aligned} \hat{S}_{23}(\mathbf{F}) = \hat{\bar{S}}_{23}(\bar{\mathbf{F}}) &\Rightarrow \rho_R c_{T\perp}^2 u_{3,2} = \bar{\rho}_R \bar{c}_{T\perp}^2 \bar{u}_{3,2} \\ \hat{S}_{21}(\mathbf{F}) = \hat{\bar{S}}_{21}(\bar{\mathbf{F}}) &= 0 \quad (\text{identity}) \end{aligned} \tag{13}$$

$$S_{22}^0(\mathbf{F}_0) = \bar{S}_{22}^0(\bar{\mathbf{F}}_0) \Rightarrow \pi^0 - \bar{\pi}^0 = 2\lambda^{-2} [(W_1 - \bar{W}_1) + 2(W_2 - \bar{W}_2)].$$

The last relationship gives the dependency between the hydrostatic pressures in the layer π^0 and in the half-space $\bar{\pi}^0$.

2. Love waves

Love waves are surface waves which result from the multiple interactions of SH waves. The simplest geometry (Figure 2) in which Love waves occurs is a layer of thickness h of material with velocity c_{Tn} underlain by a half-space of material with the higher velocity \bar{c}_{Tn} . Love waves require a velocity structure that varies with depth and so cannot exist in a half-space in contrast to Rayleigh waves. The particle motion of the Love waves is parallel to the surface but perpendicular to the direction of propagation. The SH wave incident on the free surface is fully reflected without phase change, but if it interacts with the boundary between the layer and the half-space the reflected and transmitted waves can occur. Denoting now by $M = c_{Tn} / \bar{c}_{Tn}$ the ratio of propagation speeds of SH waves and according to the Snell law we obtain the following relations:

$$c = c_{Tn} / \sin \Theta_I = \bar{c}_{Tn} / \sin \Theta_T, \sin \Theta_T = \frac{1}{M} \sin \Theta_I \Rightarrow \sin \Theta_I < M \tag{14}$$

where:

$c = \omega / k = \bar{\omega} / \bar{k}$ is the phase velocity of the Love waves.

In view of the above expressions we can always find waves transmitted to the half-space if $M > 1$ (Figure 2a). However, if $M < 1$, there will be a critical angle of incidence defined by

$$\sin \Theta_{cr} = M. \tag{15}$$

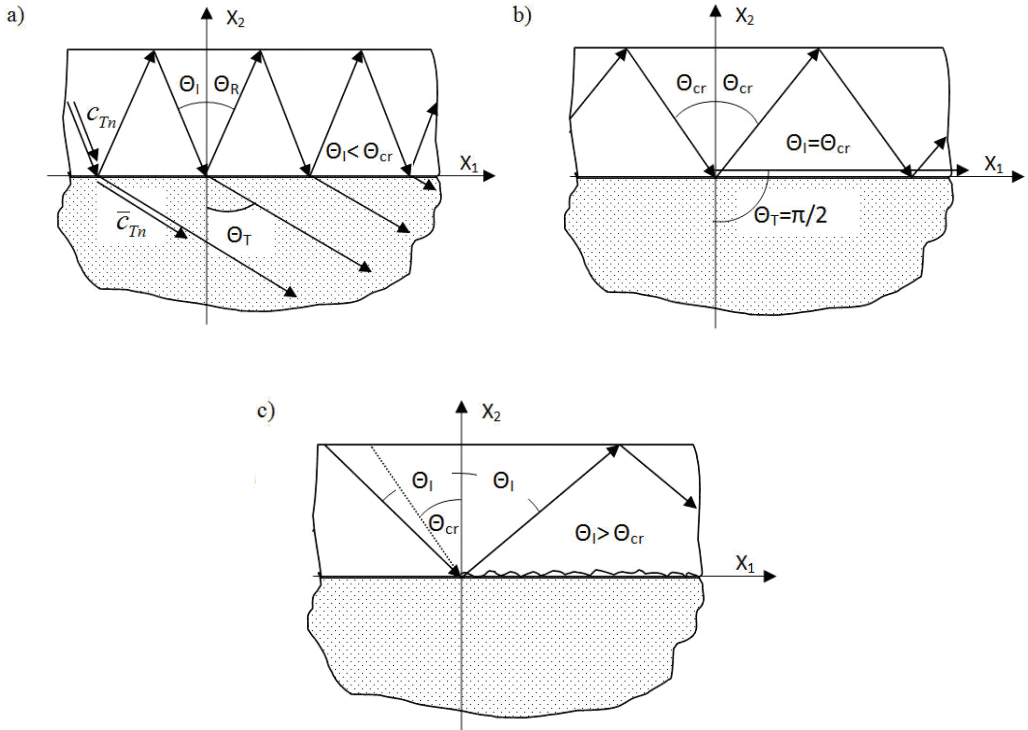


Fig. 2. Propagation of SH waves in the joined layer and half-space in the case when the critical angle occurs: a) $\Theta_I < \Theta_{cr}$, b) $\Theta_I = \Theta_{cr}$, c) $\Theta_I > \Theta_{cr}$

If $\Theta_I = \Theta_{cr}$, we have $\Theta_T = \pi/2$ and the transmitted wave propagates along the interface (Figure 2b). If $\Theta_I > \Theta_{cr}$ (Figure 2c) then \bar{p} (comp. (11)) becomes imaginary and there is no transmitted wave in half-space, always surface waves disturbances propagating along the interface and attenuating with vertical distance toward the half-space.

Combining the four basic solutions (9) obtained earlier, we are able to compose all wave configurations characteristics for the Love waves (Figure 2) in the form:

$$u_3 = A_1 \exp[ik(X_1 + pX_2 - ct)] + A_2 \exp[ik(X_1 - pX_2 - ct)] \quad (\text{layer})$$

$$\bar{u}_3 = \bar{A}_1 \exp[ik\bar{(X_1 + \bar{p}X_2 - ct)}] \quad (\text{half-space}) \quad (16)$$

It is easy to see that in the case when $c > (c_{2//}, \bar{c}_{2//})$, both p, \bar{p} are real. The wave motion characteristic for the Love waves is practically confined to the thin layer h adjacent to the boundary. The solution \bar{u}_3 in the half-space $X_2 \leq 0$ decreases rapidly with the distance from the interface $X_2 \rightarrow -\infty$. The last condition can be satisfied when we assume that \bar{p} is an imaginary number i.e.

$$c < \bar{c}_{2//} \Rightarrow \bar{p} = -i\bar{v}, \bar{v} = \left((\bar{c}_{T//} / \bar{c}_{T\perp})^2 - c^2 / \bar{c}_{T\perp}^2 \right)^{1/2}, \quad (17)$$

Finally after modifications the expressions for the displacements take the form

$$\text{layer:} \quad u_3 = (A_1 \exp[ik p X_2] + A_2 \exp[-ik p X_2]) \exp[ik(X_1 - ct)],$$

$$\text{half-space:} \quad \bar{u}_3 = \bar{A}_1 \exp(k\bar{v} X_2) \exp[ik(X_1 - ct)]. \quad (18)$$

The two solids are rigidly bounded, and both the half-space and the layer are made of different nonlinear materials. The linearised solution of the Love waves problem can be found immediately when the solutions (17) will become completed with boundary conditions at the interface $X_2 = 0$ and at the free surface $X_2 = h$ (Figure 2)

$$\hat{S}_{23}(X_1, 0, t) = \hat{\bar{S}}_{23}(X_1, 0, t),$$

$$u_3(X_1, 0, t) = \bar{u}_3(X_1, 0, t), \quad (19)$$

$$\hat{S}_{23}(X_1, h, t) = 0.$$

Figure 2a shows the typical configuration of SH waves in the low velocity layer and half-space ($c_T < \bar{c}_T$) before the total reflection, when the reflected plane SH wave exists. If the angle of incidence increases then for certain value $\theta_I = \theta_{cr}$ the angle $\theta_R = \pi/2$ and the refracted wave propagates along the interface. If $\theta_I > \theta_{cr}$ ($c < \bar{c}_{T//}$) there is no refracted wave, but only surface disturbances propagating along the interface and decreasing rapidly with the distance from the interface (Figure 2b). It follows from the boundary conditions (20) that

$$\begin{bmatrix} \exp(ikph) & -\exp(-ikph) & 0 \\ 1 & 1 & -1 \\ ip\rho_R c_{T\perp}^2 & -ip\rho_R c_{T\perp}^2 & \bar{\rho}_R \bar{c}_{T\perp}^2 \bar{v} \end{bmatrix} \begin{Bmatrix} A_1 \\ A_2 \\ \bar{A}_2 \end{Bmatrix} = \begin{Bmatrix} 0 \\ 0 \\ 0 \end{Bmatrix}. \quad (20)$$

Setting the determinant of these equations equal to zero we find the dispersion relation for Love waves (comp. [1])

$$\tan(kph) = \frac{\bar{\rho}_R \bar{c}_{T\perp}^2 \bar{v}}{\rho_R c_{T\perp}^2 p} = \frac{\bar{\rho}_R \bar{c}_{T\perp} \bar{c}_{T\parallel}}{\rho_R c_{T\perp} c_{T\parallel}} \left(\frac{1 - c^2 / \bar{c}_{T\parallel}^2}{c^2 / c_{T\parallel}^2 - 1} \right)^{1/2}. \quad (21)$$

It is easy to see that in the case when the initial deformations vanish i.e. for $\mathbf{F}_0 \rightarrow \mathbf{1}$ and $\bar{\mathbf{F}}_0 \rightarrow \mathbf{1}$, all speeds of propagation in the layer $\rho_R c_{T\parallel}^2 = \rho_R c_{T\perp}^2 = \mu$ and in the half-space $\bar{\rho}_R \bar{c}_{T\perp}^2 = \bar{\rho}_R \bar{c}_{T\perp}^2 = \bar{\mu}$ are constant, and the Equation (22) is the same as in the linear theory.

Taking now into account the expressions for the propagation speeds $c_{T\parallel}$, $c_{T\perp}$, $\bar{c}_{T\parallel}$, $\bar{c}_{T\perp}$ defined in Equation (9) we obtain for arbitrary nonlinear incompressible elastic material, which is described by the strain energy function $W = W(I_1, I_2)$ and for the assumed initial deformation (1)

$$\tan(kph) = \left(\frac{\bar{\bar{W}}_1 + \bar{\bar{W}}_2 \lambda^2}{\bar{\bar{W}}_1 + \bar{\bar{W}}_2 \lambda^2} \frac{\bar{\bar{W}}_1 + \bar{\bar{W}}_2 \lambda^{-4}}{\bar{\bar{W}}_1 + \bar{\bar{W}}_2 \lambda^{-4}} \right)^{1/2} \left(\frac{1 - c^2 / \bar{c}_{2\parallel}^2}{c^2 / c_{2\parallel}^2 - 1} \right)^{1/2}, \quad (22)$$

The strain energy function $W = W(I_1, I_2)$ for many models of nonlinear elastic incompressible materials is independent on the second strain invariant I_2 of the deformation tensor i.e. $W = W(I_1)$, $W_2 = \bar{W}_2 = 0$ and the expressions for both speeds of propagation (9) in the layer and in the half-space and the dispersion relation (23) take the forms

$$c_T^2 = c_{T\parallel}^2 = c_{T\perp}^2 = 2\bar{\bar{W}}_1 \rho_R^{-1}, \quad \bar{c}_T^2 = \bar{c}_{T\parallel}^2 = \bar{c}_{T\perp}^2 = 2\bar{\bar{W}}_1 \bar{\rho}_R^{-1}, \quad (23)$$

$$\tan(khp) = \frac{\bar{\bar{W}}_1}{\bar{\bar{W}}_1} \left(\frac{1 - c^2 / \bar{c}_T^2}{c^2 / c_T^2 - 1} \right)^{1/2}, \quad (24)$$

where the function p has now the form $p^2 = c^2 / c_T^2 - 1$. The right hand side of (23) must be real, there should be also satisfied the condition known from the linear theory i.e. $c_T^2 < \bar{c}_T^2$. Substitution of (24) into (25) simplify on the dispersion relation to the form

$$\tan(khp) = \frac{1}{M} \frac{\bar{\rho}_R}{\rho_R} \left(\frac{M^{-2} - 1}{p^2} - 1 \right)^{1/2}, \quad (25)$$

where:

$M = c_T / \bar{c}_T$ and μ is the shear modulus.

If $\lambda = 1$ the initial deformation vanishes, $q = \bar{\bar{W}}_1 / \bar{W} = \bar{\mu} / \mu$ and the dispersion relation takes the form known from the linear theory

$$\tan(khp) = \frac{\bar{\mu}}{\mu} \left(\frac{1}{p^2} \left(1 - (1 + p^2) \frac{\mu}{\bar{\mu}} \frac{\bar{\rho}_R}{\rho_R} \right) \right)^{1/2}, \quad \tan(khp) = qm \left(\left(\frac{p_0}{p} \right)^2 - 1 \right)^{1/2}, \quad (26)$$

where:

$$m = c_{0T} / \bar{c}_{0T},$$

$$c_{0T} = \sqrt{\mu / \rho_R},$$

$$\bar{c}_{0T} = \sqrt{\bar{\mu} / \bar{\rho}_R},$$

$$p_0^2 = m^{-2} - 1.$$

3. Constitutive relations

The constitutive modelling of incompressible hyperelastic materials such as vulcanised rubbers, carbon filled reinforced rubber, polymers and human arterial wall tissues involves strain energy functions W that depend on the first two invariants of the deformation tensor W . The most well known of these is the Mooney-Rivlin model and its special form the neo-Hookean. The function W can be determined from experimental results obtained in homogeneous strain, such as uniaxial tension, pure shear and equibiaxial tension. In recent years, several constitutive models that capture the effects of limiting chain extensibility and crystallization have been proposed. Here we confine attention to two such phenomenological models. The first one proposed by Gent depends only on the first invariant and involves just two material parameters. The second one Yeoh hyperelastic material is a cubic in I_1 and involves three material parameters. Conceptually, the strain energy function proposed Yeoh is a material model with a shear modulus that varies with deformation and for this reason the proposed model is applicable over a wide range of strain.

The neo-Hookean strain energy function is the simplest model for nonlinear behaviour of elastic incompressible materials. Useful at small stretches, the neo-Hookean model involves a single constant – the shear modulus μ and has a linear dependence on the first deformation invariant I_1 . A classic modification of this simple relationship

is the two constant Mooney–Rivlin model that adds an additional term linear in I_2 . The Mooney–Rivlin model extends the applicability range of the previous model to slightly larger stretches.

The Gent strain energy function

$$W(I_1) = -\frac{\mu}{2} J_m \ln \left(1 - \frac{I_1 - 3}{J_m} \right), \quad (27)$$

where

$$I_1 < J_m + 3, \quad (28)$$

was proposed by Gent (1996). This model is known to be much more effective than the classical hyperelastic models in describing the mechanical behaviour of rubberlike materials at large stretches. The two constant Gent model involves the shear modulus μ and a dimensionless parameter J_m that measures the extent of limiting chain extensibility at the molecular level. Note that $W = W(I_1)$ depends only on the first deformation-invariant. This model predicts a stress response that reflects the strain–stiffening and approaches an asymptote for a limiting value of stretch that depends on J_m . In the limit as $J_m \rightarrow \infty$ one recovers from (26) the neo-Hookean model. On recalling the constraint (29), we see that in simple extension the limiting measured stretch λ_{\max} must be such that

$$(I_1)_{\max} = \lambda_{\max}^2 + \frac{2}{\lambda_{\max}} = J_m + 3, \quad (29)$$

and the value of J_m corresponding to λ_{\max} can be determined.

It is known from the literature and from the simple stress–strain tests, that for rubberlike materials $\partial W / \partial I_1$ is generally much larger than $\partial W / \partial I_2$. The idea suggested by Yeoh resolve into neglecting $\partial W / \partial I_2$ and equating it to zero, because $\partial W / \partial I_2$ appears to be sufficiently small that neglecting it is not expected to give rise to very serious errors. Assuming that $\partial W / \partial I_2 = 0$ and that $\partial W / \partial I_1$ is independent on I_2 we obtain now leading terms of Rivlin strain energy function (comp. [5])

$$W(I_1) = C_{10}(I_1 - 3) + C_{20}(I_1 - 3)^2 + C_{30}(I_1 - 3)^3, \quad (30)$$

which is cubic equation in $(I_1 - 3)$ and C_{10} , C_{20} , C_{30} are material parameters.

The ratio $M = c_T / \bar{c}_T < 1$ (comp. (25), (26)) of the propagation speeds of transverse waves in the layer c_T and in the half-space \bar{c}_T (comp. (26)) is the basic variable parameter in our analysis. For the Yeoh material and for the assumed initial deformation

(1) which is identical in the layer and in the half-space we obtain the following condition for the parameter M

$$M = \frac{c_T}{\bar{c}_T} = m \left(\frac{1 + 2c_{20}c_{10}^{-1}(I_1 - 3) + 3c_{30}c_{10}^{-1}(I_1 - 3)^2}{1 + 2\bar{c}_{20}\bar{c}_{10}^{-1}(\bar{I}_1 - 3) + 3\bar{c}_{30}\bar{c}_{10}^{-1}(\bar{I}_1 - 3)^2} \right)^{1/2} < 1, \quad (31)$$

where:

$$m = c_{0T} / \bar{c}_{0T} = ((c_{10}\rho_R^{-1})(\bar{c}_{10}\bar{\rho}_R^{-1}))^{1/2},$$

if $\lambda = 1$ then $M = m$.

Analogous condition for the Gent material takes the form

$$M = \frac{c_T}{\bar{c}_T} = m \left(\frac{J_m \bar{J}_m - (\bar{I}_1 - 3)}{\bar{J}_m J_m - (I_1 - 3)} \right)^{1/2} < 1, \quad (32)$$

and also if $\lambda = 1$, then the result is $M = m$.

4. Numerical analysis

The dispersion relation for Love waves (26) discussed in the previous section is now examined numerically. The waveguide consists of a semi-infinite half-space covered with a layer of finite thickness h . We assume in the beginning that both, the half-space and the layer are made of different Yeoh materials (silicon rubber). Some experimental results for three kinds of silicon rubber (soft, medium, hard) by utilising Yeoh constitutive relation were presented in [4]. All values of Yeoh material parameters are listed in Table 1. It is assumed that the mass density has the same value. The calculations relating for Yeoh material base on the three material combinations selected from Table 1 for which the condition $c_T / \bar{c}_T < 1$ is satisfied.

Table 1. Yeoh material parameters

Silicone rubber	C_{10} [MPa]	C_{20} [MPa]	C_{30} [MPa]
Soft	0.0231	-0.0000314	0.000195
Medium	0.0335	-0.0019100	0.000937
Hard	0.0583	-0.0036600	0.001780

Similar calculations were made for Gent material but only for one pair of materials. All the necessary experimental data in Table 2 arise from [2] and [3].

Table 2. Gent material parameters

Rubber	μ [MPa]	J_m	ρ_R [kg/m ³]
Silicone	0.323	13	0.91×10^3
Natural vulcanised	0.610	97.2	1.1×10^3

Figure 3a presents the ratios of the propagation speeds $M(\lambda)$ in the layer and in the half-space as functions of the initial deformation parameter λ . For the three selected combinations of the Yeoh material the condition $M(\lambda) < 1$ is satisfied and the propagation of Love waves is possible. The function $M(\lambda)$ has one local minimum for the value $\lambda = 1$ and two local maximums and for $M(\lambda) < m$ there exists the real range of the values λ such, what a pair of values $\lambda < 1$ and $\lambda > 1$ for which the function $M(\lambda)$ has the same value (for example $\lambda = 0.608$ and $\lambda = 2$). The difference of the values of the function $M(\lambda)$ in the region $M(\lambda) > m$ is practically negligible small. The dispersion equation for the value $m = 0.630$ is solved graphically on Figure 3b. The right hand side of (26) depends only on the speeds ratio $M(\lambda)$ and on the mass density ratio. The solid bold lines on this Figure 3b describe the function on the right hand side of (26) for different values of the deformation parameter λ . The branches of the function

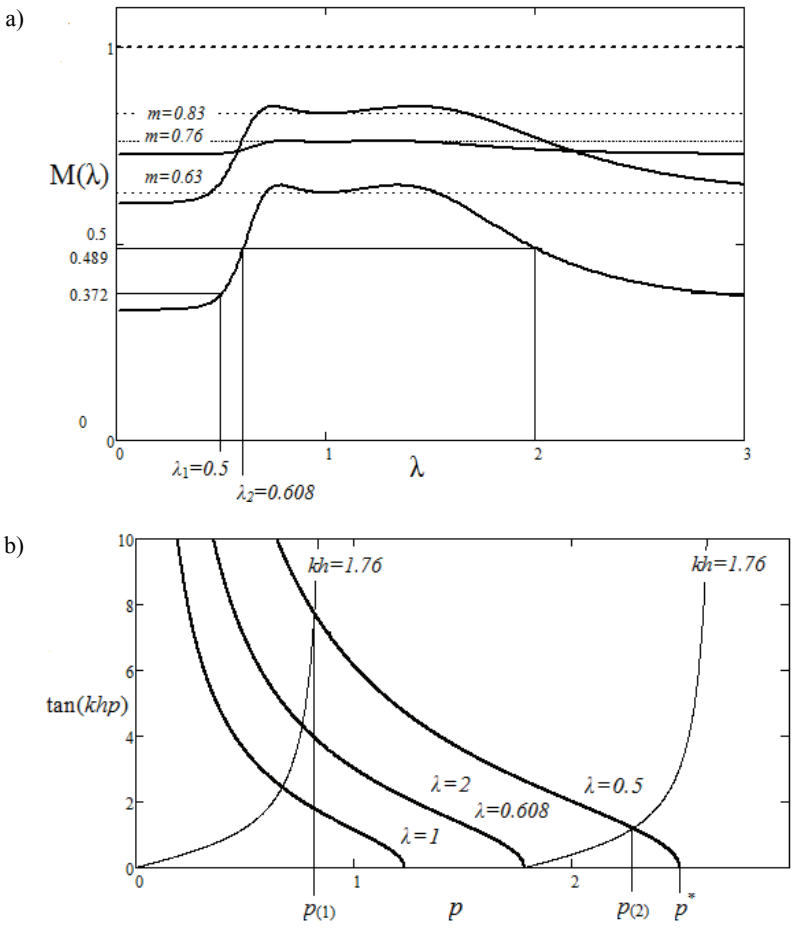


Fig. 3. Basic relations for Yeoh material

$\tan(khp)$ for the value $kh = 1.76$ are described with solid thin lines. The transcendental Equations (26) may have many real roots. The values of the function on the right hand side of (26) calculated for $\lambda = 0.5$ are positive in the interval $0 < p < p^*$. The function of the right hand side of (26) takes the value zero for $p = p^* = \sqrt{M^{-2} - 1} > 0$. All coordinates $p_{(i)}$ of the points of intersection of this curve with the n branches of the function $\tan(1.76p) > 0$ belong to the interval $0 < p_{(i)} < p^*$.

Assuming now that the wave number k can change and that the sequence of n values $p_{(i)}$ in the interval $(0, p^*)$ exists, then n particular modes of propagation of the waves in the layer to a given wave number are possible. On the Figure 3b the curve obtained for the value $\lambda = 0.5$ intersects the two branches of the tangent curve at the points $p_{(1)}$ and $p_{(2)}$. Figure 4 presents the analogous graphs for Gent material. In this case the function $M(\lambda)$ has the absolute minimum for $\lambda = 1$ and the condition $M(\lambda) < 1$ restricts the admissible values of λ to the segment $(0.607, 2.07)$, and as previous we can select pairs of values $\lambda < 1$ and $\lambda > 1$ for which the function $M(\lambda)$ has the same values.

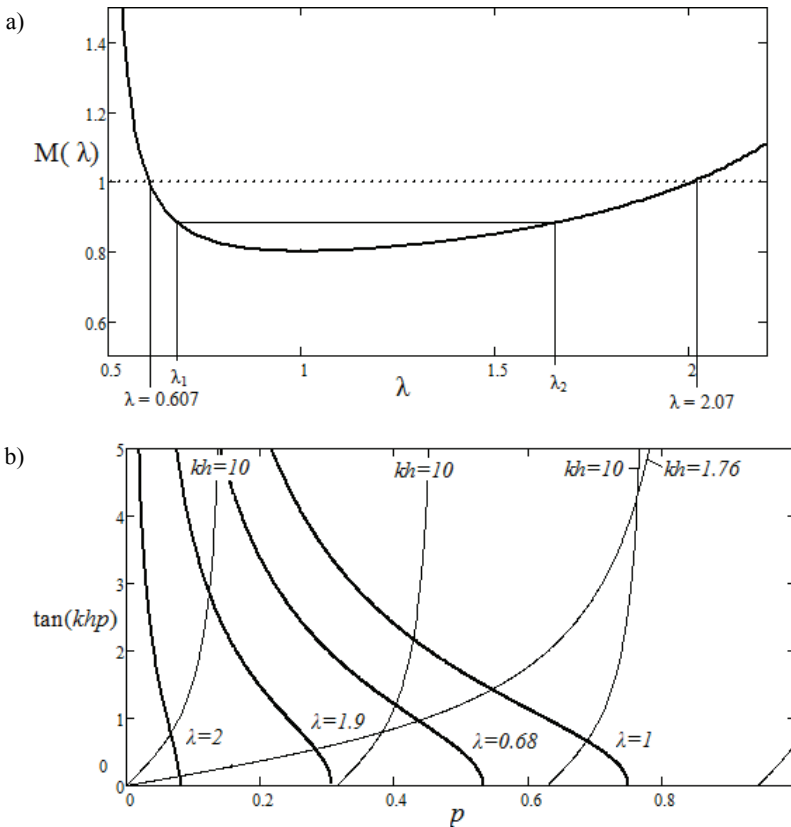


Fig. 4. Basic relations for Gent material

The branches of the function $\tan(khp)$ for two values of the parameter kh , i.e. $kh = 1.76$ and $kh = 10$ are presented on the Figure 4b. It is easy to see that the shape of the function $M(\lambda)$ has essential influence on the propagation of Love waves in materials with constitutive relationship $W = W(I_1)$. If the graph of the function is such as on the Figure 3a then in the range $M(\lambda) < M(1)$ it is possible the extension of the number of propagation modes with regard to the results known from the linear theory. The reduction of the number of propagation modes can follow in the range $M(\lambda) > M(1)$. Such kind of dependence is presented on the Figure 4a. It is to notice, that in the case of Gent material every initial deformation of the form (1) with parameter $\lambda \in (0.607, 2.07)$ reduces the number of propagation modes. Such reduction follows also for the Yeoh material but in the range $M(\lambda) > M(1)$ in which the value of the function $M(\lambda)$ is practically invariable i. e. $M(\lambda) \approx M(1) = m$. For this reason we cannot observe the effects of reduction on Figure 3b. Generally we can conclude that in the above problem the dynamical behaviour of the Yeoh and Gent materials subjected to specific deformation (1) is quite different.

References

- [1] Dowaikh M.A.: *On SH waves in a pre-stressed layered half-space for an incompressible elastic material*, Mech. Res. Comm., Vol. 26, No. 6, 1999, pp. 665–672.
- [2] Gent A.N.: *A new constitutive relation for rubber*, Rubber Chem. & Technol., Vol. 69, 1996, pp. 59–61.
- [3] Gent A.N.: *Surface instabilities in compressed or bent rubber blocks*, Rubber Chem. & Technol., Vol. 72, 1999, pp. 253–262.
- [4] Korochkina T.V.: *Experimental and numerical investigation into nonlinear deformation of silicone rubber pads during ink transfer process*, Polymer Testing, Vol. 27, 2008, pp. 778–791.
- [5] Yeoh O.H.: *Characterization of elastic properties of carbon-black-filled rubber*, Rubber Chem. & Technol., Vol. 63, 1990, pp. 792–805.

Fale Love'a we wstępnie odkształconych materiałach Genta i Yeoha

W pracy rozpatrzono zlinearyzowane zagadnienie brzegowe dla fal Love'a. Założono, że półprzestrzeń sprężysta i spoczywająca na niej cienka warstwa o grubości h wykonane są z różnych materiałów Genta lub Yeoha i poddane są jednorodnej statycznej deformacji wstępnej. Deformacja wstępna w obu obszarach falowodu jest taka sama. Linearyzację równań ruchu uzyskano przez nałożenie małego, zależnego od czasu ruchu falowego na duże skończone deformacje statyczne. Zależność funkcji energii odkształcenia $W = W(I_1)$ od pierwszego niezmiennika tensora deformacji o postaci charakterystycznej dla obu materiałów powoduje występowanie dużych różnic jakościowych między liniowym i zlinearyzowanym podejściem do propagacji fal Love'a w nieliniowych gumopodobnych materiałach sprężystych.



The synergistic effect of copper powder with PTFE in a grease lubricant under mixed friction conditions

S. KRAWIEC

Wrocław University of Technology, Wybrzeże Wyspiańskiego 27, 50-370 Wrocław, Poland.

This paper describes experimental work on the frictional performance of a lithium grease lubricant filled with a combination of polytetrafluoroethylene (PTFE) and copper powders. The tribological testing was carried out in agreement with the prescriptions of the Polish standard PN-76/C-04147 using a four-ball apparatus. The performance of the tested compositions was evaluated using three criteria: ball wear d , limiting wear load G , and seizure load F_z . Synergy between action of the powders of PTFE and copper in compositions with 6 wt.% of these fillers was found. Examinations of the chemical composition of the upper layer of the wear scars of the tested balls were carried out using an X-ray microanalysis method with dispersion of the radiation energy. The results of these analyses made it possible to confirm the author's notion that the synergy of PTFE with copper in the lithium grease tested was possible due to the thermal decomposition of PTFE and the consequent creation of new layers during a reaction of the decomposition products with the plating layer of copper. These new layers are, to a high degree of probability, complexes with copper, sulphur, and fluorine.

Keywords: *fillers, greases, synergism, mixed friction*

1. Introduction

The research that has been performed in the recent years points clearly to modification of greases with dedicated fillers as a most promising method for enhancing their anti-friction and anti-wear properties. A set of such fillers shall not only assist in the creation of plating layers on the mating surfaces but shall also modify these surfaces and improve their tribological performance with respect to these layers. These goals are met by, e.g. powders of copper with acetyl-acetone [9], copper powder and Schiff's aromatic base [10] or two-core complex of copper and nickel [11].

According to [5, 19] a mutual action that is more efficient than the sum of individual actions is termed as synergy, synergism or a synergistic effect. It should be noted, however, that in the tribology literature the notion of synergy is also used for another type of conjoint action that does not comply strictly with the definition given above. As a matter of an example, a synergistic effect produced by addition of dialkyldithiocarbonate of molybdenum (MoDTZ) and/or dialkyldithiophosphate of zinc (ZnDTP) to a mineral oil was described in [14]. In this case the minimum value of the coefficient of friction was assumed as a criterion of synergy. When using oil with the two additives (MoDTC + ZnDTP), the value of the coefficient of friction was equal

to 0.04, considerably less than the values obtained when lubricating with MoDTC or ZnDTP alone (approx. 0.06 and 0.09 respectively).

Similarly, a conjoint action of fillers that resulted in the minimum amount of wear was also termed as synergism by Morar et al. in [13]. The authors investigated the tribological characteristics of a grease lubricant filled with copper hydroxide ($\text{Cu}(\text{OH})_2$) and caprolactam ($\text{C}_6\text{H}_{11}\text{NO}$). As a proof of synergy, they reported relations in the diameter of the wear scar on the balls of a four-ball wear apparatus: under an axial load of 1500 N and a lubricant composition including either copper hydroxide or caprolactam this diameter was equal to 0.96 mm and 3.9 mm respectively. When testing a lubricant filled with a product of reaction between these two fillers, this diameter was a mere 0.52 mm. The definition of synergy as a conjoint action of fillers that results in the minimum values of a certain criterion (e.g. the coefficient of friction, wear etc.) may also be found in other research papers [1, 15–16, 18].

It shall also be stressed that researchers that have been dealing with friction corrosion in the recent years differentiate between synergistic and additive actions. By synergy they mean a process employed for the description of the influence of corrosion on wear. Gant *et al.* in [2] presented the results of the wear of hard materials (WC-Co) that were obtained on an ASTM G 65 tribometer when testing was carried out in the presence of a corroding agent (sulphuric acid solution), wear agent (quartz sand and water) and under an aggregated action of the two. The synergy of tribo-corrosion was calculated as:

$$S = T - W - C, \quad (1)$$

where:

W – the wear obtained when lubricating with a solution of deionised water and quartz sand,

C – the wear in the presence of a corrosion agent only (sulphuric acid),

T – the wear under a joint action of the two agents. Also Souza in [17], when analysing the influence of erosion and corrosion on degradation (wear) of WC-Co-Cr coatings (HVOF technology), calculated the total volume loss from the following formula:

$$TVL = E + C + S, \quad (2)$$

where:

E – the erosion wear,

C – the corrosion wear,

S – the synergy as an interaction between corrosion and erosion. Other research papers dealing with friction and corrosion define synergy in the same way, e.g. [4, 20–21].

In summary, in the author's opinion, in the area of research dealing with the modification of greases with fillers, a conjoint action of these fillers may be termed as synergy when one of the following conditions is met:

1) The effect of conjoint action is greater than the sum of the individual actions for those values for which a maximum value is sought, e.g. seizure value, limiting wear load index.

2) The effect of conjoint action is less than the sum of the individual actions for those values for which a minimum value is sought, e.g. the coefficient of friction or wear.

The author has been dealing with the modification of grease lubricants with powders of some solid lubricants like graphite, molybdenum disulphide, PTFE and copper for over 25 years now, e.g. [6–8, 12]. The frictional characteristics of these lubricants (wear, seizure load F_z , etc.) were identified based upon testing carried out on a four-ball apparatus. When observing the mating surfaces of the balls subject to a seizure test and lubricated with a PTFE filled grease lubricant, a certain regularity had been observed: whenever the silver colour of the ball in the close proximity of the wear scar on the rotating ball changed slightly to blue, then, at an elevated load in the next trial, the balls got welded. This change in colour, which is associated with high temperature at the point of contact, inspired further research. Considering the individual physical and chemical properties of PTFE and copper together with the mechanisms of their conjoint action as fillers in grease lubricants, the following hypothesis was set forth: Powders of PTFE and copper used as fillers in grease lubricants generate in the process of friction a synergetic anti-friction and anti-wear action giving thus a very effective grease lubrication mixture for sliding steel nodes operating under mixed friction conditions.

A premise for setting this hypothesis stems from the following reasoning: as copper filler to a grease lubricant has a capacity of plating the mating sliding surfaces, and a by-product of the thermal decomposition of PTFE is, among others, tetrafluoroethylene (C_2F_4), a gas that features a very high reactivity [3], then the probability of the synergistic effect is high. This gas (together with other products of the thermal decomposition of PTFE) reacts with a part of the lubrication layer made by copper and shall create fluorine compounds (common or complex, e.g. with copper) on the sliding surface. These compounds, by improving the tribological properties of the boundary layer, increase the lubrication efficiency of the grease composition.

The verification of this hypothesis will be based upon the results of tribological experiments made using steel-to-steel specimens with a concentrated contact together with the results of chemical examinations of the upper layer of the mating surfaces.

2. Experimental method, apparatus and test conditions

Testing was carried out in agreement with the prescriptions of the Polish standard PN-76/C-04147, “Testing of lubrication properties of oil and grease lubricants” using a standard four-ball apparatus. To evaluate the efficiency of the tested compositions in agreement with this standard, three indicators were employed: ball wear d , limiting wear load G_{0z} , and seizure load F_z . In some situations an additional indicator was also

used, which was the limiting load F_g defined as the maximum load that is still safe with respect to the balls' seizure. This load corresponds to the maximum pressure that a lubricating layer is still able to support. According to PN-76/C-0414, wear, seizure load and limiting load are found in 10 second tests carried out at a constant speed of the rotating ball (1450 r.p.m.) and at a constant load that is incrementally increased up to the seizure of the balls. Plots in Figure 1 show a wear/load relationship ($d = f(F)$) for the balls. The F_z value is represented by the starting point of a dashed line vector, and the F_g value, by the last point of the continuous line. The limiting load of wear G_{oz} is a specific load that defines pressure in a frictional nod at a constant load of $F = 150$ daN calculated from:

$$G_{oz} = \frac{78}{d^2}, [\text{MPa}] \quad (3)$$

where d , in mm, is the average diameter of scars on the stationary balls after $t = 60$ s.

Compounds with one filler (PTFE or Cu) and with two fillers (PTFE + Cu, 6 wt.% each) were analysed. The measurement of wear of the balls was carried out in directions parallel and perpendicular to the wear scar. Scars less than 1 mm were measured under a microscope with an accuracy of 0.01 mm; the remaining scars, using a magnifying glass with an accuracy of 0.1 mm. Trials were repeated always 6 times. The results were statistically processed at a level of confidence of 95% using Student's *t*-test.

3. Specification and characteristics of the materials tested

The following materials were used for the experiments:

- PTFE powder (suspensive Tarflen® with the granulation from 20 to 40 μm).
- Electrolytic copper powder with the granulation of 40 μm manufactured by cathodic electro-deposition in the process of electrolysis of water solutions of copper sulphate. The arrangement of powder particles is a dendritic one.
 - Bearing balls made of 100Cr6 steel, 62 HRC in hardness and 12.7 mm in diameter, 16th grade accuracy and in the $S = 0$ μm dimensional selection group. The other parameters were in agreement with the Polish standard PN-83/M-86452.
 - A lithium grease lubricant (brand name 1S) as the base grease (carrier) for the tested fillers. This grease features the worst lubrication properties of the three grease lubricants applicable for sliding bearings tested in [7].

4. Preparation of grease compositions for testing

Grease compositions were prepared with a mixer. Weighed portions of grease and filler were mixed for 30 minutes at a mixing-blade speed equal to 800 r.p.m. The mixing time $t = 30$ min had been established experimentally to ensure uniform distri-

bution of the filler particles in the grease carrier. The uniformity was assessed visually observing the prepared composition under a biological microscope after 10, 20, and 30 minutes of mixing.

5. Results of testing

A summary of experimental results is presented in the form of plots: ball wear versus load ($d = f(F)$) for the analysed compositions (1S + 6 wt.% Cu, 1S + 6 wt.% PTFE, and 1S + 6 wt.% Cu + 6 wt.% PTFE), are shown in Figure 1.

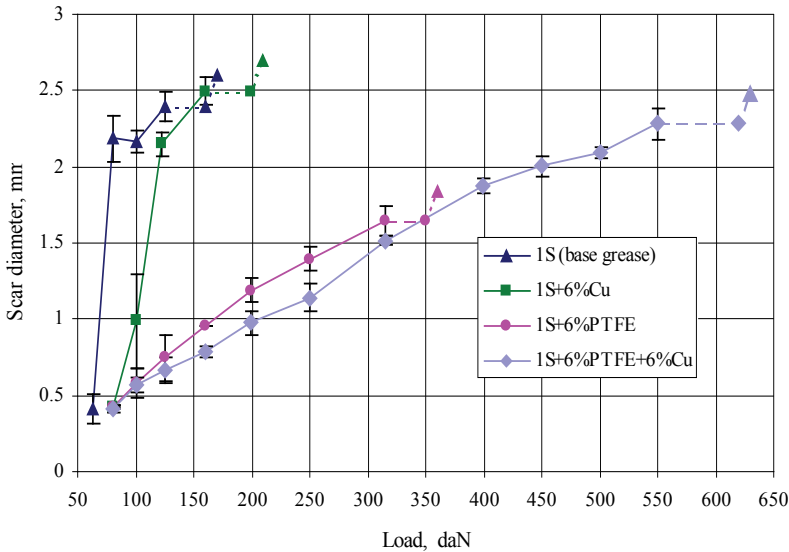


Fig. 1. Wear rate as a function of load for the tested grease compositions

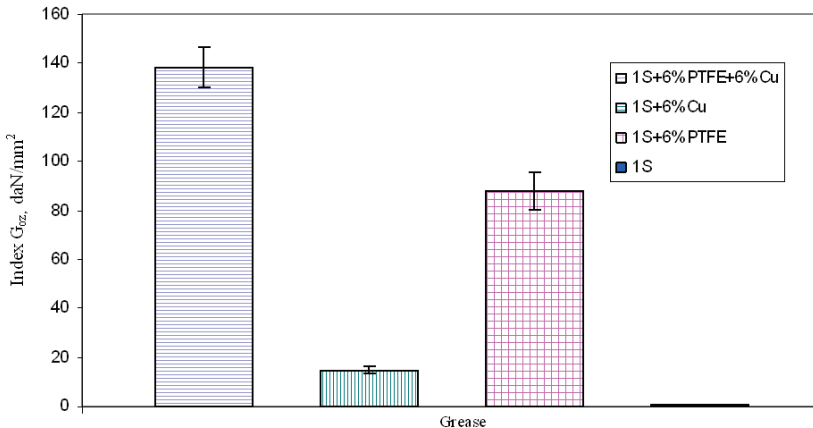


Fig. 2. Limit wear load index G_{oz} for the tested grease compositions

Additionally, for the sake of comparison, a tribological characteristic of $d = (F)$ when lubricating with the 1S grease was included. The value of the loading in Figure 1 that corresponds to the last point of the continuous line is the limiting load F_g , and the beginning of the vector traced with a dashed line represents the load of welding F_z . Calculated values of the limiting wear load G_{oz} for these greases are illustrated in Figure 2. A value of G_{oz} for the base grease is equal to zero as four of the six tests carried out resulted with the seizure of the balls. Table 1 shows numerical data of all criteria adopted for the evaluation of the frictional performance of the analysed lubrications compositions. Additionally, a theoretical sum of the criteria values is given that might have been expected after the application of a grease lubricant with two fillers if this merely resulted in the summation of the effects of the individual fillers.

Table 1. Comparison of wear d , index G_{oz} , and loads F_g and F_z for the analysed compositions

Grease lubricant	1S + 6% PTFE	1S + 6% Cu	Maximum value sought: G_{oz} , F_g , F_z (Σ of effects of individual fillers)	Minimum value sought: d (lesser of those given in column 2 and 3)	1S + 6% PTFE + 6% Cu
1	2	3	4	5	6
Index G_{oz} [daN/mm ²]	88.2	14.78	102.98	–	138.3
Limiting load F_g [daN]	315	160	475	–	550
Seizure load F_z [daN]	350	200	550	–	620
Wear d [mm] at a load of $F = 160$ [daN]	0.96	2.49	–	0.96	0.78

The presented results of G_{oz} , F_z , F_g and wear d confirm the presence of the synergistic effect of the tested fillers in the process of friction. As an example: the value of the limiting load F_g (Table 1) when lubricating with a composition made of copper filler alone is equal to 160 daN; when filling with PTFE alone, it is equal to 315 daN, and when filling with a composition of PTFE and copper, it is equal to 550 daN. It is obvious that an algebraic sum of the limiting loads for greases with one filler (475 daN) is less than the value obtained when testing a composition with both fillers (550 daN). A conjoint action of this type, in agreement with definitions given earlier (condition 1), is termed as synergy. This relation is also true when the seizure load F_z or limiting wear index G_{oz} is taken as a criterion.

This specific conjoint action of the tested fillers may also be shown by taking ball wear (scars) as an example. Wear is considered as a negative-value criterion, so in agreement with the definitions given in section 1, the fulfilment of the second condition is necessary. For the analysed compositions it is fulfilled. As an example (Table 1), the wear at a load of 160 daN is equal to 2.49 mm using a composition with copper, 0.96 mm using a PTFE-filled lubricant, and only 0.78 mm using copper and PTFE.

These results validate the hypothesis set forth in this paper regarding the beneficial effect of copper and PTFE fillers on the frictional performance of a lithium grease lubricant.

6. Supplementary testing

As the experimental study has proven unambiguously the presence of the synergistic effect in the 1S grease lubricant filled with powders of PTFE and copper, an attempt was made to explain its mechanism in this case. In the author's opinion, the underlying reason of this effect in the tested grease with the analysed fillers under mixed friction conditions is the thermal decomposition of PTFE. The mechanism of this effect may be explained in the following way: the increased values of pressure and slip velocity in a frictional node cause an increase in temperature in the area of contact of the two surfaces. At a certain temperature, the decomposition process of PTFE starts. As a result of the reaction of the decomposition products (to a high probability, tetrafluoroethylene) with the metal plating layer of copper, new layers are formed that are normal or complex compounds of fluorine and copper.

The objective of complementary testing was to verify this notion. The recognition of compounds of fluorine and copper on the surface of balls that were tested under loading close to the limiting load F_g will be, in the author's opinion, validation of this assertion. The limiting load for a composition with two fillers (1S + 6 wt.% PTFE + 6 wt.% Cu) shown in Figure 1 is 550 daN. These surfaces that were tested under a load slightly lower than the limiting one (500 daN) were analysed. This load guarantees that the compounds present on these surfaces are a result of a conjoint action of the two fillers, as an operational limit of a composition with PTFE alone is 315 daN, and that of a composition with copper powder alone is 160 daN (Figure 1).

It shall be made clear that X-ray examinations of the loaded ball surfaces made to identify the types of chemical compounds present failed to provide positive results. Equally unsuccessful were X-ray examinations made with a very small Bragg angle ($\theta = 1^\circ$) apparatus. The reason might be an insufficient sensitivity of the available X-ray apparatuses and some specific features of the analysed surfaces, i.e. their concave bowl form and a highly differentiated topography. Considering such circumstances, an attempt to identify the whole compound was limited to its main component, i.e. fluorine. A micro-examination X-ray method with dispersion of the radiation energy was used for this purpose. It is a very accurate method with an absolute value of element recognition equal to 10^{-14} g. The microanalysis was carried out using a SEM 515 Philips scanning microscope equipped with an EDAX 9800 micro analyser. A direct recognition of fluorine on the examined steel surfaces with this method was also difficult. The reason is a close energy affinity of fluorine and iron reflexes. An $F_{K\alpha}$ fluorine peak is present at a level of 0.675 keV and that of iron $Fe_{L\alpha}$, at a level of 0.705 keV. With a spectrometer used for this examination, it was impossible to recognise unambiguously fluorine on the examined surface. An indirect method was therefore employed.

The method consisted of a computer construction of theoretical peaks on the characteristic X-ray spectrum obtained: first for iron Fe_{La} , then for fluorine F_{ka} . Figure 3 shows a general view of a characteristic X-ray spectrum from the surface of a ball loaded with $F = 500$ daN and lubricated with a composition filled with powder of PTFE and copper.

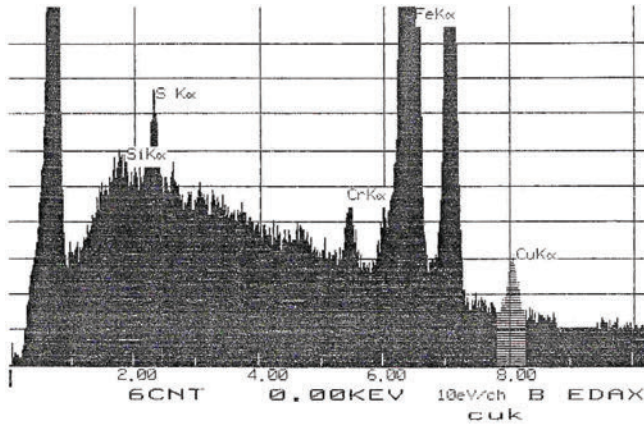


Fig. 3. Spectrum of characteristic radiation from the surface of a ball that is loaded with $F = 500$ daN and lubricated with a composition made of 6% PTFE + 6% Cu

Figure 4a, on the other hand, shows part of the spectrum obtained together with a theoretic peak for fluorine F_{ka} and Figure 4b, for iron Fe_{La} (a white envelope in both cases).

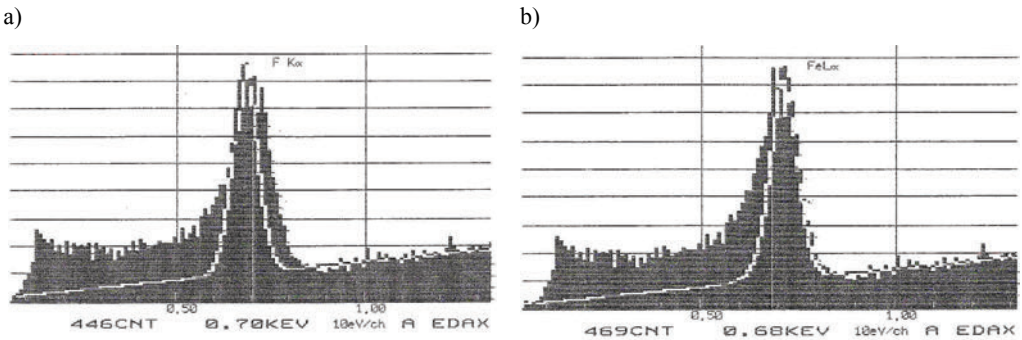


Fig. 4. Section of the spectrum from Figure 3 with the envelope showing the reflection of a) fluorine, b) iron

It is seen that the theoretical peaks do not include the whole spectrum but are limited to its part only. When the theoretical peak of fluorine $F_{K\alpha}$ was constructed, it did not include the part of the spectrum facing the iron reflex Fe_{La} (0.705 keV of voltage).

A similar situation exists with the theoretic peak of iron Fe_{La} (Figure 4b), which (the peak) did not include the part of the spectrum facing the fluorine reflex (0.675 kV of voltage). This proves that the actual peak obtained stems from fluorine and iron. As mentioned earlier, since the examined balls were loaded with 500 daN, i.e. with a load that is considerably higher than the limiting load for greases modified with PTFE (315 daN, see Figure 1), it may be concluded that the fluorine recognised on these surfaces originates not from PTFE powders but from fluorine containing compounds created in the course of the friction process.

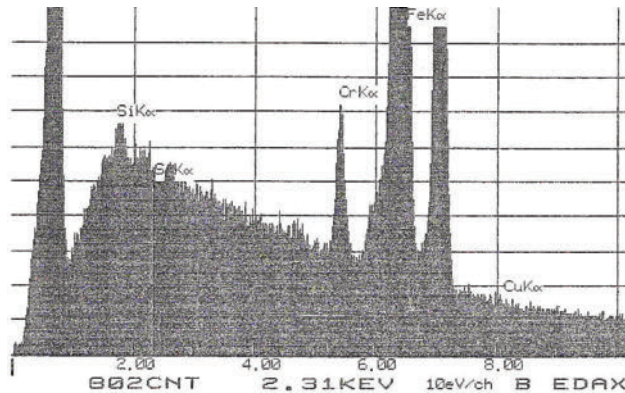


Fig. 5. Spectrum of characteristic radiation from the load-free surface of the ball (matrix)

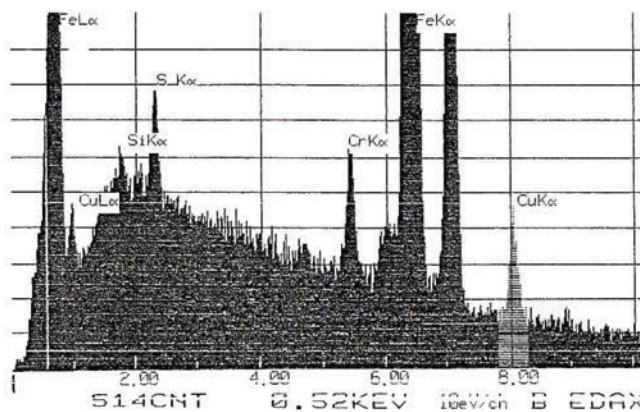


Fig. 6. Spectrum of characteristic radiation from the surface of a ball that is loaded with $F = 126$ daN and lubricated with a composition made of 6% Cu

An additional confirmation of this notion comes from the results of comparative examination of the chemical composition of the surfaces of the balls lubricated with a composition containing 6 wt.% of Cu and a composition with 6 wt.% of PTFE + 6 wt.% Cu. Figure 5 shows a spectrum of the characteristic radiation from the non-

loaded surface of the ball that served as a reference in this examination. As seen in Figure 5, the base surface, apart of fundamental elements (Fe, Cr, Si), contains only trace amounts of sulphur, which is indicated by a white cursor ($S_{Ka} = 2.307$ keV). The Polish standard PN/M-84041 permits the maximum amount of sulphur in 100Cr6 steel at a level of 0.02%. Figure 6 shows a characteristic spectrum of radiation from a ball loaded with 126 daN and lubricated with a composition containing 6 wt.% Cu.

If compared, the chemical composition of the two lubricated surfaces (Figures 3 and 6) is the same in terms of the number of elements. These surfaces, when compared to the base (non-lubricated ball, Figure 5), have additionally copper and a considerably larger amount of sulphur. The fact that the examined surfaces, irrespective of the filler employed in the grease (1S + 6 wt.% Cu or 1S + 6 wt.% Cu + 6 wt. % PTFE) contain the same elements and that the PTFE + Cu filled greases are approximately 3.5 times more efficient than those filled with copper only allows one to conclude that fluorine is the main source of the synergy of the fillers employed.

The results of the above examinations validate the notion that the synergistic effect of PTFE and copper in the tested grease lubricant (in the process of friction) stems from the thermal decomposition of PTFE, with the resulting reaction of the decomposition products with a plating layer of copper and the subsequent creation of new layers containing (most probably) complexes with copper, sulphur and fluorine. It shall be added that these compounds feature good tribological properties, which was proved in the previously reported experimental work.

7. Conclusions

This study has demonstrated the following:

- 1) Grease fillers like PTFE and copper powders produce a synergistic effect in the friction process. The source of this synergy is the thermal decomposition of PTFE.
- 2) The modification of lubrication properties of grease lubricants with synergistic fillers is an effective method for enhancing their lubrication properties. The welding load of a composition filled with PTFE and copper is 3 times higher than that for a composition filled with copper alone and nearly twice as high as that for a composition filled with PTFE only.

References

- [1] Cho M.H., Bahadur S.: *Study of the tribological synergistic effects in nano CuO-filled and fiber-reinforced polyphenylene sulfide composites*, Wear, Vol. 258, 2005, pp. 835–845.
- [2] Gant A.J., Gee M.G., May A.T.: *The evaluation of tribo-corrosion synergy for WC-Co hard metals in low stress abrasion*, Wear, Vol. 256, 2004, pp. 500–516.
- [3] Ishikawa N., Kobayashi Y.: *Fluorine compounds – chemistry and application*, Moskva, Mir, 1982.

- [4] Jilbert G., Field J.: *Synergistic effects of rain and sand erosion*, Wear, Vol. 243, 2000, pp. 6–17.
- [5] Kopaliński W.: *Vocabulary of foreign words and phrases* (in Polish), Warszawa, Wiedza Powszechna, 1988.
- [6] Krawiec S.: *Optimisation of PTFE content in a grease lubricant using the minimum volume of the wear function* (in Polish), Tribologia (Tribology), Vol. 185, No. 3, 2004, pp. 207–215.
- [7] Krawiec S.: *Influence of synergism of some selected fillers in a grease lubricant on the service life of sliding machine pairs* (in Polish), Monograph, Oficyna Wydawnicza PWR, Wrocław, 1998.
- [8] Krawiec S.: *Influence of MoS₂ content in a grease lubricant on the lubrication performance of a sliding bearing* (in Polish), Zagadnienia Eksploatacji Maszyn, PAN, Vol. 26, No. 1, 1991, pp. 47–58.
- [9] Kužarov A.S., Oniščuk N.Ju., Sukčov V.V.: *Influence of copper powder fillers on the tribological performance of a lithium grease* (in Russian), Trenie i iznos (Friction and wear), Vol. 10, No. 5, 1989, pp. 901–908.
- [10] Kužarov A.S., Oniščuk N.Ju.: *Influence of the aromatic Schiff's base on the tribological performance of copper powder filled grease lubricants in a steel/steel friction pair* (in Russian), Trenie i iznos (Friction and Wear), Vol. 8, No. 6, 1987, pp. 1105–1110.
- [11] Kužarov A.S., Fisenko O.V.: *Investigation of the terminological performance of metal-plating grease lubricants based upon the CIA TIM 201- grease with copper and nickel fillers*, Trenie i iznos (Friction and Wear), Vol. 13, No. 6, 1992, pp. 1057–1064.
- [12] Lawrowski Z., Krawiec S.: *Some aspects of the lubrication process using grease – polytetrafluoroethylene (ptfe) compositions*, Proc. VI Tribological Conference, Budapest, 1966, pp. 301–304.
- [13] Morar V.E., Kračun A., Kračun S.V., Čobany A.: *Investigation of the lubrication performance of some copper compounds* (in Russian), Trenie i iznos, Vol. 8, No. 2, 1987, pp. 274–280.
- [14] Muraki M., Yanagi Y., Sakaguchi K.: *Synergistic effect on frictional characteristics under rolling–sliding conditions due to a combination of molybdenum dialkylthiocarbamate and zinc dialkylthiophosphate*, Tribology International, Vol. 30, No. 1, 1997, pp. 69–75.
- [15] Nazarenko T.I., Lozniecova N.N., Ščegolev G.G., Toporov Ju.P.: *Investigation of lubrication properties of lubricants with copper complexes additives* (in Russian), Trenie i iznos, Vol. 13, No. 2, 1992, pp. 324–327.
- [16] Płaza S.: *Tribo-technical reactions of the surface of friction* (in Polish), Tribologia (Tribology), Vol. 4, 1995, pp. 335–348.
- [17] Souza V.A.D., Neville A.: *Corrosion and synergy in a WC-Co-Cr HVOF thermal spray coating – understanding their role in erosion – corrosion degradation*, Wear, Vol. 259, 2005, pp. 171–180.
- [18] Suzuki M., Prat P.: *Synergism of an MoS₂ sputtered film and a transfer film of a PTFE composite*, Wear, Vol. 225–229, 1999, pp. 995–1003.
- [19] *Vocabulary of foreign words* (in Polish), Warszawa, PWN, 1995.
- [20] Zhang D.He.T., Wu Y.: *Mechanisms responsible for synergy between fretting and corrosion for three biomaterials in saline solution*, Wear, Vol. 250, 2001, pp. 180–187.
- [21] Zheng Y., Yao Z., Wei X., Ke W.: *The synergistic effect between erosion and corrosion in acidic slurry medium*, Wear, Vol. 186–187, 1995, pp. 555–561.

Efekt synergetyczny proszku miedzi i PTFE w smarze plastycznym podczas tarcia mieszanego

W artykule opisano badania efektywności smarowania smaru plastycznego litowego napełnionego kombinacją proszku PTFE i miedzi. Badania tribologiczne prowadzono na aparacie czterokulowym, z zastosowaniem wytycznych normy PN-76/C-04147. Efektywność badanych kompozycji oceniano według trzech wielkości kryterialnych, tj. zużycia kulek d , granicznego obciążenia zużycia G_{oz} , oraz obciążenia zespawania F_z . Stwierdzono efekt synergistyczny proszku PTFE i miedzi w kompozycjach zawierających po 6% wagowych tych napełniaczy. Przeprowadzono badania składu chemicznego warstw wierzchnich śladu zużycia kulek wykorzystując metodę mikroanalizy rentgenowskiej z dyspersją energii promieniowania. Wyniki tych analiz pozwoliły potwierdzić słuszność poglądu, że synergizm PTFE i miedzi w smarze (w procesie tarcia) zachodzi dzięki termicznemu rozpadowi PTFE i utworzeniu podczas reakcji produktów tego rozpadu z warstewką platerującą miedzi nowych warstewek będących najprawdopodobniej kompleksami zawierającymi miedź, siarkę i fluor.



Topology optimisation as a tool for obtaining a multimaterial structure

R. KUTYŁOWSKI, B. RASIAK, M. SZWECHŁOWICZ

Wrocław University of Technology, Wybrzeże Wyspiańskiego 25, 50-370 Wrocław, Poland.

Topology optimisation problem solutions are generally presented in such a way that ultimately a material/void (1/0) distribution is obtained in the design domain. For this purpose, filtering techniques are usually used or post-processing is applied in the optimisation process. As a rule, the result is quasi-optimal since no minimum value of the objective functional is then obtained. In this study an optimal body topology is determined. Its characteristic feature is that besides normal material and voids there is a material with poorer and varied parameters in the design domain. The latter material is often distributed in the form of a layer around the axis of each member of the construction and gets weaker with the distance from the axis. This means that the construction is multimaterial and individual layers can be distinguished in its members. In this sense, the construction is a layered one. The compliance functional is minimized under constraints imposed on the body mass, which means that the initially available mass is kept constant throughout the optimisation process. Looking for the functional stationary point one gets the following dependence: material density in a particular material point for the considered iteration is proportional to the strain energy accumulated in this point. A discretely updated Young modulus is used in the successive steps in the construction of stiffness matrices. The update for the individual material points in the successive iterations is based on the strain energy distribution in the previous step. The problem was solved numerically using FEM and identifying body material points with finite elements.

Keywords: *topology optimisation, layered multimaterial construction*

1. Introduction

Topology optimisation in the mathematical sense leads to a problem solution characterized by a minimum objective functional value, whereas topology optimisation known from the literature and practical applications leads to a material/void solution for which the objective functional value is slightly higher than for the optimal solution. Such an approach is necessitated by the technologies currently used for manufacturing or building the considered constructions. The technologies are based on the use of a single material for a construction (i.e. after the optimisation process there is only material/void in the design domain). The characteristic feature of the material is that for an arbitrary representative volume, the material parameters in this volume and in the whole structure are the same. The material may be a laminate, i.e. a material with periodic properties or with a specified microstructure, but for each representative volume of the structure it is always the same. Thus the manufacturing process forces a situation in which a topology optimisation solution must be modified by techniques yielding a material-void distribution which is not

optimal but very close to the optimum. This means that until now one has had to do with the “almost optimal” but producible solution. It should be noted that the present analysis is done for a specified load and the deadweight is not taken into account. This approach is identical to the approaches found in the literature.

This paper presents a way of obtaining an optimal body topology characterized by variable material parameters. In most cases, this variability can be described as follows: in the particular members of the topology a distinct core located in the member’s axis can be distinguished. The core is surrounded by material which is increasingly weaker with the distance from the axis to the member’s edge. It was found that the weakening of the material always occurs but its intensity and direction each time can be different. The difference between the density of the core and that of the surrounding material is often very large. The obtained topology is characterized by a lower objective functional value than a similar topology consisting of members with uniformly identical material properties. In both cases the material (of a relatively high density) is identically distributed, which means that in both cases the material is in the same areas. In the proposed approach, in the topology there is relatively weak material surrounding the particular members. In a certain sense, the approach is similar to the FGM (Functionally Gradient Materials) design being under development [7], [9]. In FGM methods there are also two materials with a gentle transition from one material to the other. This applies to both a micro and macro scale [3]. It is obvious that such materials in many respects are better than homogeneous materials or laminated materials. From the material strength point of view, the most important is the fact that stress concentrations will appear at the interface when two different materials are combined. The stress concentrations are absent when FGMs are used. The production of FGMs is complicated, but progress in this field is fairly quick, as evidenced by [4], where details of the production technology are provided.

In the present paper an optimal topology is obtained not for two, but for one material whose parameters change in a gradient manner, or to put it in another way, for a larger number of materials with different material parameters. The essence of the proposed approach and of the FGM approach is the same: material properties change in a certain direction. However, in the proposed approach the gradient change in a specific direction is multimaterial.

In the topology optimisation process presented below the compliance functional will be minimized under constraints imposed on the mass of the body, which means that the mass available at the beginning will be kept constant throughout the process.

2. Topology optimisation problem formulation

Compliance can be written as Equation (1) in which it is expressed as the work of mass forces \mathbf{X} and external load \mathbf{t} , where \mathbf{v} is a displacement vector.

$$\Pi^E = \int_{\Omega} \mathbf{X} \mathbf{v} \, d\Omega + \int_{\partial\Omega_i} \mathbf{t} \mathbf{v} \, ds. \quad (1)$$

The internal energy accumulated in the structure can be expressed by the equation

$$\Pi^I = \frac{1}{2} \int_{\Omega} e^T C e \, d\Omega, \quad (2)$$

where:

C – an elasticity tensor,

e – a strain tensor.

Since compliance and elastic energy are equal, elastic energy (strain energy) is used in further analysis. It is subjected to minimization

$$\Pi^E = \Pi^I \rightarrow \min \Pi^I. \quad (3)$$

The topology optimisation problem is considered taking into account the constraints imposed on body mass, in the form

$$H(\rho) = \frac{m_j}{m_0} - 1 = 0. \quad (4)$$

During the optimisation process, body mass m_j (for each optimisation step j separately) should be equal to initial available mass m_0

$$m_0 = \alpha m, \quad 0 < \alpha < 1, \quad m = V\rho, \quad (5)$$

where:

V – the design domain volume,

ρ – denotes material density,

α – a mass reduction coefficient.

Considering the constraints imposed on body mass, the optimisation problem can be written using Lagrange multiplier λ :

$$F(\rho, \lambda) = \min \left\{ \int_{\Omega} e^T C e \, d\Omega + \lambda \left(\int_{\Omega} \rho_x \, d\Omega - m_0 \right) \right\}, \quad (6)$$

where ρ_x is the density of any material point within the design domain.

3. FEM algorithm

The problem was solved numerically using FEM. The provided numerical examples refer to cases known from the literature in order to make comparisons possible.

For this reason the problem was considered as two-dimensional. Flat rectangular finite elements with eight nodal parameters (two orthogonal displacements in each node) were adopted. Appropriate FE mesh density is employed, assuming mutual correspondence between each element and a material body point represented by a finitely small considered. In the FEM method this is expressed through the changing parameters of the particular finite elements.

In the FEM notation an important quantity is the strain energy accumulated in the i -th element for the j -th iteration, which is:

$$\Pi_i^j = \delta_i^T k_i \delta_i, \quad i = 1 \dots n, \quad (7)$$

where δ is a nodal parameter vector. The relative strain energy value for the i -th element is:

$$\overline{\Pi}_i^j = \frac{\Pi_i^j}{\Pi_{i \max}^j}. \quad (8)$$

Searching for a stationary point of functional (6) one gets the following dependence:

$$\rho_i^j = \overline{\Pi}_i^j \rho, \quad (9)$$

according to which the density in i -th element for the j -th step is proportional to the strain energy accumulated in the element. Young's modulus needs to be updated in the successive steps of the optimisation process. On the basis of Equation (9) a discrete update is performed as follows [1–2], [8]:

$$E = E_0 \left(\frac{\rho_j^i}{\rho} \right)^p, \quad (10)$$

where:

- ρ – material density in the current iteration,
- E_0 – the initial Young modulus proper for the material.

Figure 1 shows a selected fragment of the topology optimisation process block diagram with the parts used in the further analysis highlighted. The diagram is based on previous papers [5–6], in which effective topology optimisation algorithms were presented.

In each optimisation step, after the Young modulus is updated, the global vector of the nodal parameters and the strain energy (subsequently normalized) are calculated (Figure 1). Using Equation (9) one gets the mass density distribution for each element separately. Since constraints were imposed on body mass one must check whether

they are fulfilled, if not, an appropriate procedure will ensure (by scaling of the density values in the particular elements) that the mass stability condition is satisfied. As a result of the uniform scaling of all the elements, the value of 1 will be exceeded in some of them. Then the accumulated mass surplus should be uniformly redistributed among all the elements or only among those with appropriately high density. This stage of the process should be regarded as complete when the total mass in the design domain is equal to the available mass. The density distribution in the design domain at this stage contains, besides material with density ρ and voids (i.e. 1 and 0 in the normalized domain), densities in a range of 0–1, corresponding to the so-called “weakened” material, i.e. a material with relative density lower than ρ . Later in the paper the term “density” will be used as synonymous with the lower density.

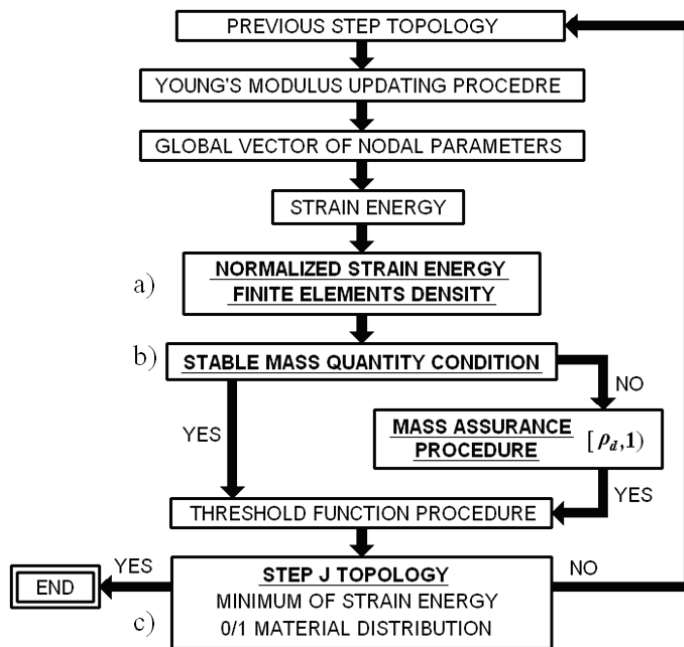


Fig. 1. Block diagram of selected part of topology optimisation process: normalized strain energy a), satisfying mass stability condition, b) topology of considered step c)

Since the aim is a 0/1 distribution, material from less strained areas (where it is practically useless) should be moved to areas of relatively higher strain. This translocation is performed using a threshold function referred to as TF (the applied function depends on the optimisation process step number). The function ensures a 0/1 type distribution.

In the proposed approach, the above algorithm is run to the penultimate iteration inclusive. In the last iteration, the normalized strain energy is analyzed in the whole design domain (Figure 1a). The analysis will yield an optimal topology.

4. Numerical examples

In this section a numerical analysis is carried out for a cantilever beam and an MBB beam (Figure 2) as the most typical topology optimisation cases. The calculations were performed for steel (density ρ and Young's modulus $E_0 = 2e5$ MPa) as the material.

In the analysis below, all dimensional quantities after proper transformations will be ultimately written as dimensionless quantities. Moreover, terms corresponding to the objective functional, i.e. compliance and equivalent strain energy, will be treated as synonymous.

The numerical analysis of the cases will include:

- an analysis of normalized strain energy and on this basis it will be possible to state that a particular distribution results in the optimal topology;
- a comparative analysis of the three stages distinguished in Figure 1, for which comparisons of the considered aspects can be made.

4.1. Layered multimaterial construction

The basic idea of constructing optimally designed layered structures is first demonstrated for the cantilever beam (Figure 2a) divided into 400 finite elements (FE mesh density: 20×20 elements). Design parameters helpful in the control of the optimisation process are: the exponent in the formula updating Young's modulus (10) and the form of the threshold function which helps to obtain a 0/1 type distribution. In addition, in the case of material redistribution during scaling with the mass quantity maintained stable, sometimes a lower limit of the density of the elements to which mass is redistributed (ρ_d) is introduced.

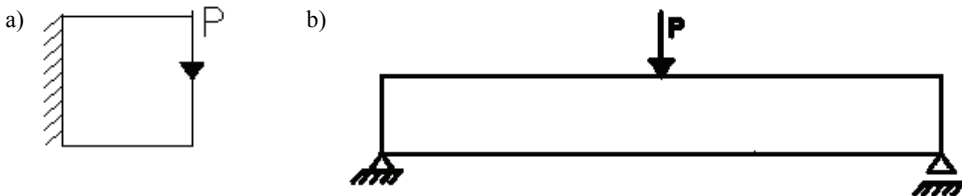


Fig. 2. a) Cantilever beam, b) simply supported beam (MBB beam)

The topology optimisation process yields solutions which are topologies showing the shape of the structure. This means that under given boundary conditions and load one obtains a material distribution in the initially defined domain. If the distribution is of the material/void type, the topology can be presented in the numerical notation (0/1) or by assigning the black colour to the material and white to the void. Black represents material with relative density equal to one, i.e. the material density assigned to the construction. However, if the topology optimisation process in the design domain re-

sults in, besides the latter material (e.g. steel), a “rarefied” material with 0–1 density, the obtained solution can be represented by shades of grey (from white to black) as equivalents of density numbers from the range of 0–1. Initially it was assumed that the range from 0 to 1 would be divided into 10 equal parts, represented by 10 constant shades of grey (Figure 3a). For example, the numerical interval of 0–0.1 was assigned the white colour while the interval of 0.9–1.0 was assigned black. This scale is sometimes rather ineffective in capturing local effects. Therefore it was decided to use another way of graphically presenting the results, particularly in cases when the material in the design domain is varied. In order to get a closer view of local changes in material density, the method shown in Figure 3b will be used. The same 10–interval grey scale was assigned to densities in a range of 0–0.5. For example, densities from 0 to 0.05 were assigned the white colour while densities in a range of 0.45–0.5 were assigned black. In this way, one can easily observe differences in density for relatively lower values. By assigning a single shade of grey to density values in a particular range, one obtains the effect of “homogenization” whereby it becomes possible to analyse how to obtain the desired material distribution through topology optimisation.

Consequently, the algorithm allows one to obtain an optimal design, which turns out to be a layered construction. The way of graphically presenting the results through the homogenization of density values, whereby the gradient layered distribution of material around the cores of the particular bars becomes clearly visible, is shown below. Since density distribution in the numerical notation is not very legible it is necessary to homogenize the density within the assumed range, which means that the values in this range (e.g. 0.2–0.3) are assigned a single average value represented by one shade of grey.

Using the scale shown in Figure 3 for assumed mass reduction coefficient $\alpha = 0.3$, power exponent in the Young modulus updating formula $p = 1$ and threshold function $TF = 0.02 \times nr$, where nr is the number of the iteration in the optimisation process and $\rho_d = 0.02$, for step 23 the normalized strain energy distribution (further referred to as density distribution) shown in Figure 4a was obtained. In this case, the strain energy for the whole structure amounts to 0.602. The 0/1 solution obtained for step 23 is shown in Figure 4b. The strain energy value in this case is slightly higher, amounting to 0.616. The fact that the strain energy for the topology shown in Figure 4a is smaller than for the topology shown in Figure 4b means that the topology (with varied densities) shown in Figure 4a is more optimal. In both figures (the presentation scale as in Figure 3a), relatively denser material is located in the same elements, but the material density is different. In Figure 4b the material density is equal to 1 (i.e. it is the assumed material density), whereas in Figure 4a the material density is varied, which is represented by shades of grey. Only directly under the applied force and near the support area the density of material is equal to 1 while the rest of the material is much weaker (the scale as in Figure 3a). As the strain energy distribution shown in Figure 4a indicates, the topology shown in Figure 4b seems to be a typical optimisation solution. However, it will become apparent that this is not the case. Figure 4a was intentionally

presented in such a way as to highlight the fact that in principle the two distributions are the same as regards the number of elements filled with material. But on further examination it will become clear that the two topologies differ from each other.

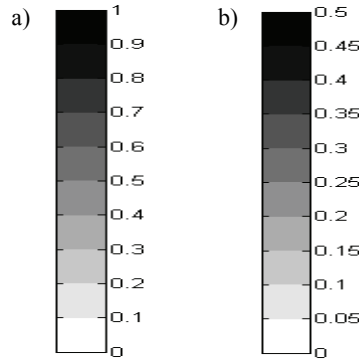


Fig. 3. Grey scale assigned to numerical intervals

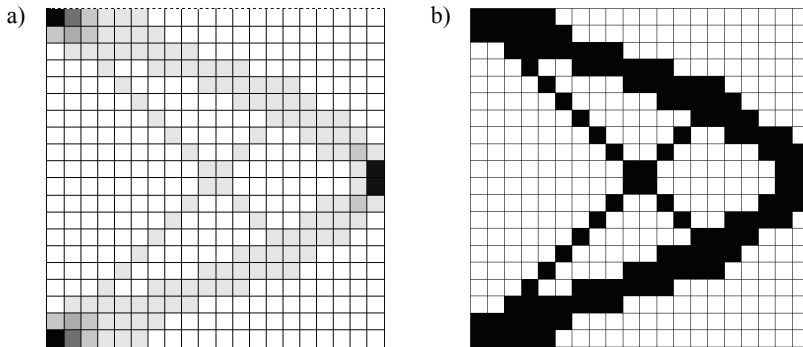


Fig. 4. a) Density distribution, b) 0/1 distribution topology

In order to find out what the real density distribution is, one should examine Figure 5a, where a fragment (marked in Figure 5b) of the topology from Figure 4a is shown in numerical notation. This is a real result yielded by the topology optimisation process. It turns out that the obtained optimal topology is characterized by highly varied distribution, but as it can be seen the material in the design domain is relatively weak (in a range from 0 to 0.1 – the white colour in Figure 4a), constituting a kind of membrane and participating in load carrying only to a small degree. Thus from the strength point of view, this material can be neglected, even though the strain energy increases as a result (as mentioned above). The elements filled with material in Figure 5a are represented by shades of gray in Figure 5b. It is apparent that for the scale of 0–1, it is difficult to show the varied material density distribution in the design domain using the grey scale.

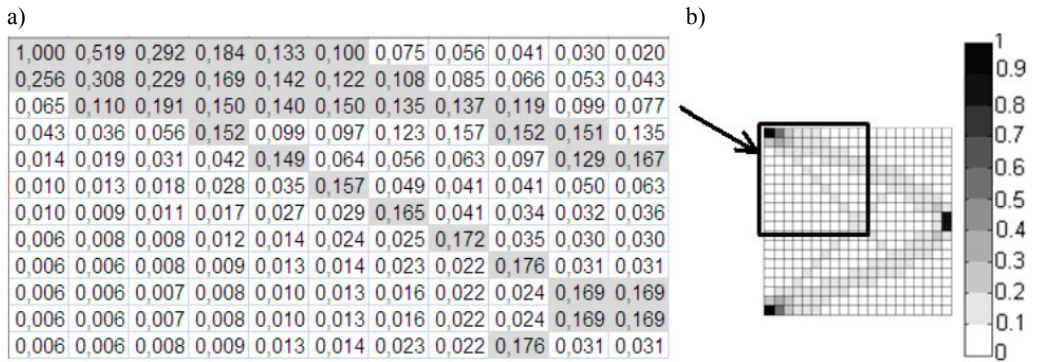


Fig. 5. a) Fragment of topology in initial numerical notation and b) the same fragment shown in topology figure

Figure 6 (Figure 6a–f) shows the density distribution topologies for step 23, corresponding to Figure 4a. The figures differ in their density scale ranges. Besides material and voids one can distinguish there more clearly areas with different shades of grey (material with weaker properties). Figure 6a is identical with Figure 4a and it is shown here to allow easy comparison with the other figures. The material density distribution topology for step 23rd in initial scale of 0–1 (Figure 6a) is poorly legible because a large number of elements were assigned a single shade of grey whereby it is difficult to perceive the actual gradient material distribution.

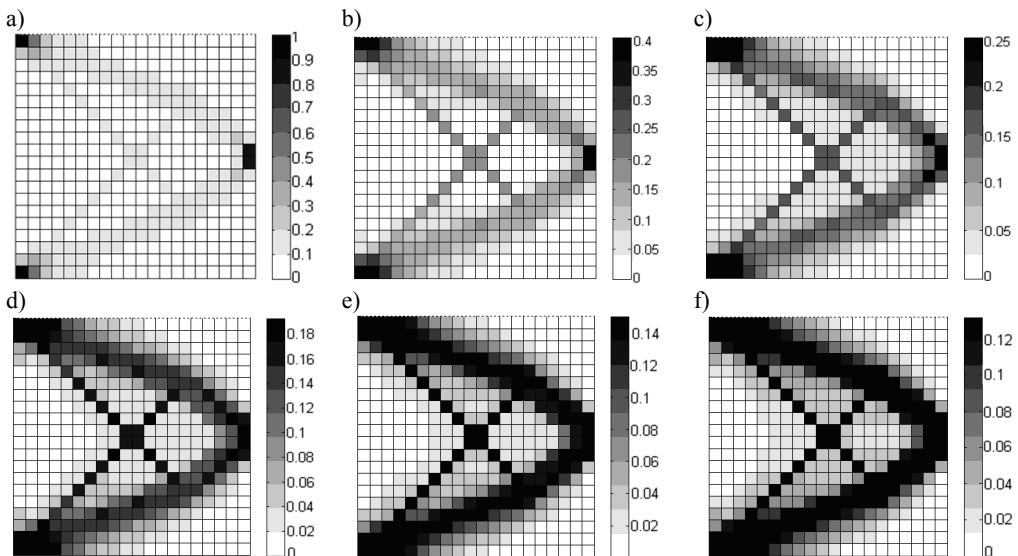


Fig. 6. Density distribution topology for step 23 with different grey scale ranges

Let us then apply the same 10-interval grey distribution to densities in a range of 0–0.4 and densities above 0.4 are assigned black. The next figures show the same topology for ranges from 0 to 0.25 (Figure 6c), from 0 to 0.18 (Figure 6d), from 0 to 0.15 (Figure 6e) and from 0 to 0.13 (Figure 6f). One can notice that the members shown in Figure 6a begin to expand in the next figures. One can distinguish an increasingly darker core which is identical in shape with the members shown in Figure 6a. The core is surrounded with relatively weaker material. Layers become visible at closeup as, for example, in Figure 7 which shows an enlarged fragment of Figure 6e. With an accuracy down to a finite element one can see how material density decreases perpendicularly to the core.

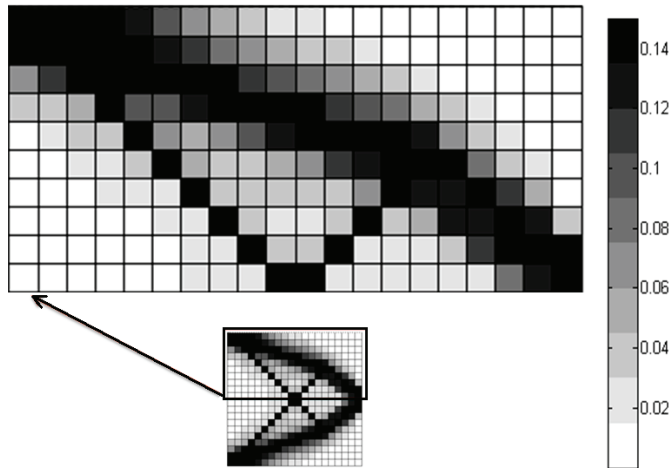


Fig. 7. Fragment of topology from Figure 6e

For the considered example Figure 8 shows the density distribution in the previous steps. The higher the iteration number, the sharper the core of each member. Also the layered structure of the members becomes visible.

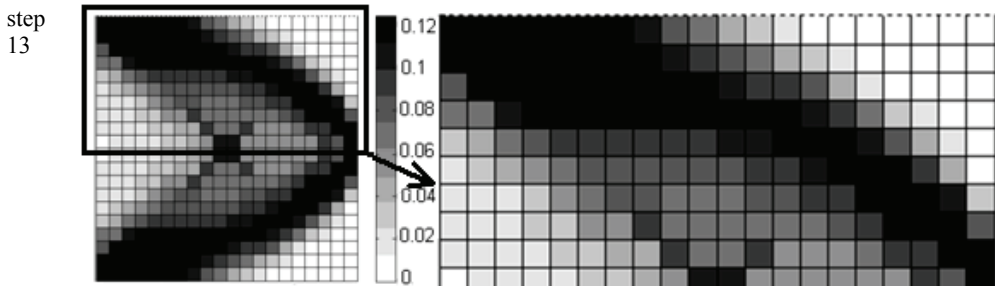


Fig. 8a. Density distribution topologies for step 13

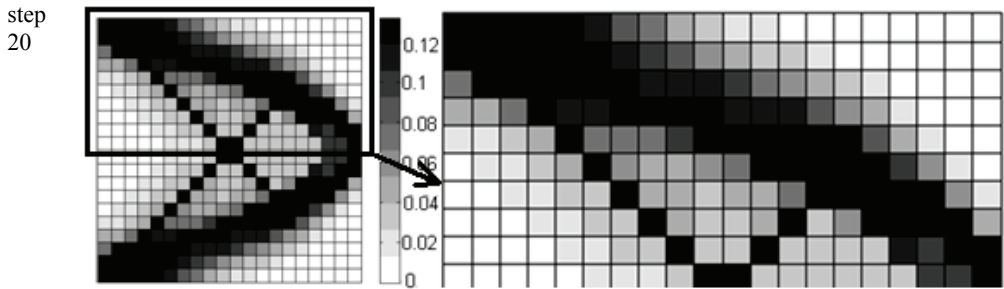


Fig. 8b. Density distribution topologies for step 20

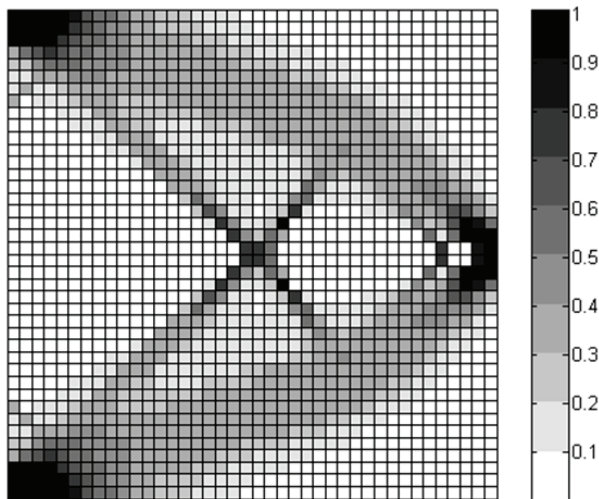


Fig. 9. Density distribution topology for 40×40 FE mesh

In order to obtain a clearer view of density distribution, the same example was calculated for a twice denser FE mesh (40×40 elements). All the control parameters remained the same as in the previous example. Also in this case, the solution for step 23, for which a 0/1 distribution and strain energy equal to 0.644 were obtained, is presented. The strain energy (0.599) density distribution for the density distribution is shown in Figure 9 where one can see the main structural areas (under the force, at the support and in the centre of the inner cross). Moreover, the outlines of the other members are distinguishable. Similarly as previously, in the initial scale of 0–1 the gradient character is poorly visible and the layered distribution of material around the core is hardly discernible. Therefore density distribution should be viewed in a “micro” scale. The scale of 0–0.04 was used to present the results (Figure 10).

In the enlarged fragment of the topology (Figure 10), one can clearly see the successive material layers with different densities arranged along the core of the structure.

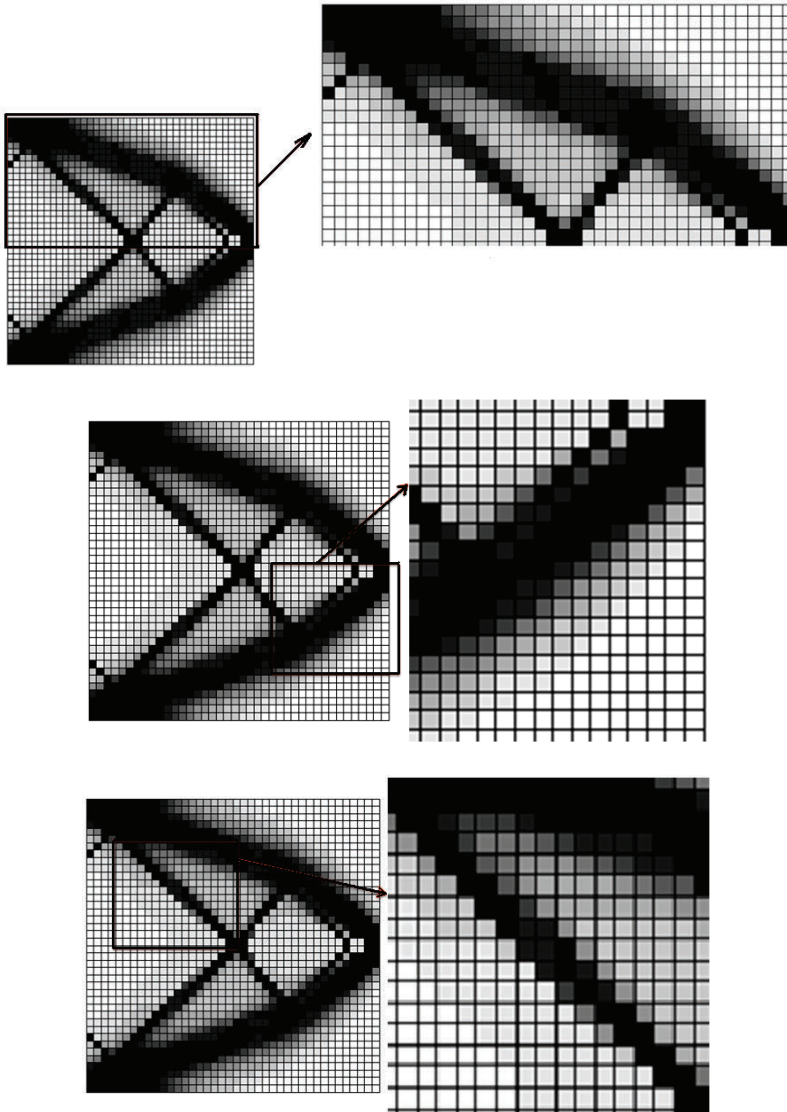


Fig. 10. Closeups of fragments of topology from Figure 9

Thanks to the denser mesh, the layer character is more visible. Moreover, smaller relative differences between the numerical density values in neighbouring elements are discernible, which proves that the homogenization applied within the particular intervals for the graphic presentation purposes is justified. Let us also consider a slightly different way of loading the cantilever beam (Figure 11a). For this loading scheme, the 0/1 topology shown in Figure 11b was obtained in step 90 at a strain energy of 0.7577. Mass coefficient $\alpha = 0.3$, exponent in the Young modulus updating

procedure $p = 2$, $\rho_d = 0.02$ and the variable threshold function for $nr < 35$, $TF = 0.00000015 \times nr$; $35 \leq nr < 57$, $TF = 0.0005 \times nr$; for $nr \geq 57$, $TF = 0.005 \times nr$ were assumed.

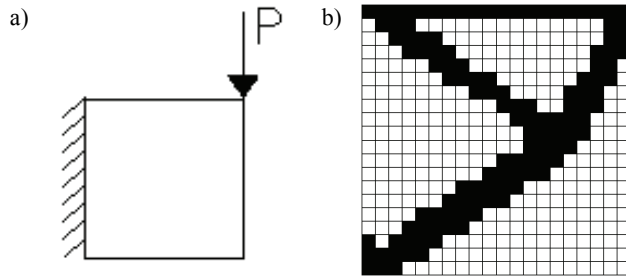


Fig. 11. a) Cantilever beam static loading scheme, b) 0/1 type solution

Below, the density distribution with the strain energy of 0.7562 for step 90 is shown. In the initially assumed scale of 0–1 (Figure 12a), the differentiation is indistinct and so in the next two figures (Figure 12b and Figure 12c) the same solution is presented in other scales of relative density. Similarly as in the previous example, the layered character of the structure is visible. There is a distinct core in the centre of each member and layers with decreasing (perpendicular to the core) relative density are situated parallel to it.

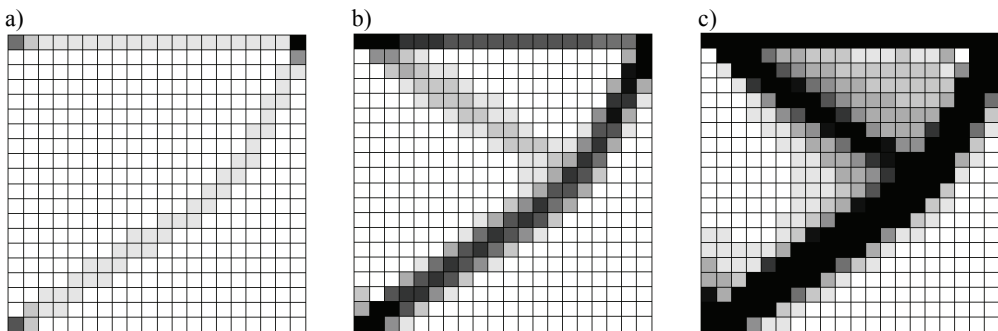


Fig. 12. Density distribution topology for scale a) from 0 to 1, b) from 0 to 0.2, c) from 0 to 0.05

In order to make the analysis complete, the same algorithm was applied to the MBB beam (Figure 2b). The results are presented in Figures 13 and 14. The calculations were done for mass reduction coefficient $\alpha = 0.5$ and exponent in the Young modulus updating procedure $p = 2$, using threshold function $TF = 0.02 \times nr$ and ρ_d as a function dependent on the mass quantity be redistributed. The design domain was divided into 864 finite elements (12×72 elements). A 0/1 solution was obtained in step 20 (Figure 13) with a strain energy of 2.622. For this step the strain energy distribution

identified with the density distribution is shown in Figure 14. The strain energy here amounts to 2.565, i.e. it is smaller than for the 0/1 topology. This means that this solution is “more optimal” than the material-void solution. In Figure 14 the values in the range of 0–0.07 were assigned shades of gray. In this case, the core is surrounded by very weak material. Details are visible in the closeup where one can see the layered material structure particularly around the core of the diagonal member extending from the support.

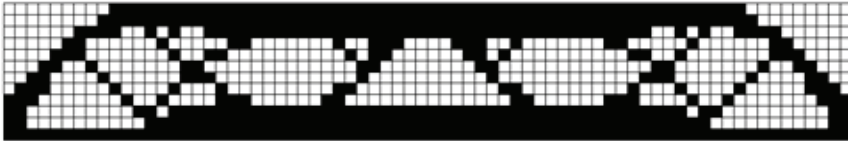


Fig. 13. 0/1 distribution topology for step 20

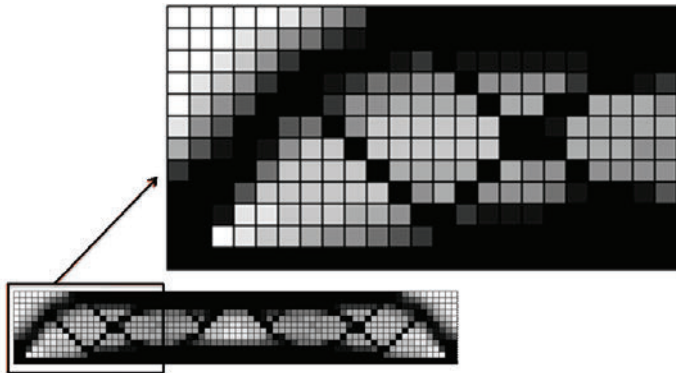


Fig. 14. Density distribution topology for step 20

4.2. Topologies for various stages of the optimisation procedure

In this section, topologies for selected stages of the optimisation process will be presented. The primary goal is to highlight the character of the topologies for the stages in order to show what differences there are between them and to define what is generally recognized as the optimal solution. For each selected optimisation process iteration, three different distributions directly relating to the algorithm shown in Figure 1 are presented:

- 1) “*Normalized energy*” (Figure 1a), i.e. the distribution of normalized strain energy;
- 2) “*Complement*” (Figure 1b), i.e. the distribution of normalized strain energy after the mass is made up to the amount specified by mass reduction coefficient α ;
- 3) “*Topology*” (Figure 1c), i.e. the final result for each iteration, obtained after the threshold function is applied.

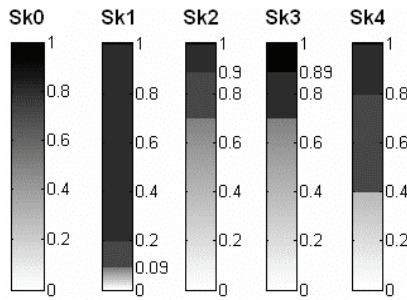


Fig. 15. Grey scale in presented examples: Sk0, Sk1, Sk2, Sk3 and Sk4

Different scales of grey were used (Figure 15) to improve the presentation of the results for the three distributions: *normalized energy*, *complement*, and *topology*. The first one (Sk0) is a continuous black-to-white scale.

Below, exemplary results for selected optimisation process steps (15, 20, 24–25, 30, 38) are presented in grey scale Sk0. A square design domain with its vertical edge rigidly supported, and loaded with a single force in the middle of the opposite edge (Figure 2a) was assumed. Coefficient α was equal to 0.44, power exponent $p = 1$, while threshold function $TF = 0.02 \times nr$ and $\rho_d = 0.01$ (for the topologies shown in Figures 16–18). In the preceding section, column “a” in Figure 16 was examined. Column “b” is scaled relative to column “a” (the core of each member is strengthened). The threshold function is used to move material from the less strained areas to more strained ones in order to obtain a 0/1 solution, i.e. the distributions shown in the third column. Figure 16 is included so that the reader can notice that the character of all the three topologies for a given iteration is similar, although different in details (often indiscernible without a proper magnification of the individual fragments of the topology). The topologies are similar in the fact that in all the cases the material is in almost exactly the same members.

One can see layered distributions in the particular iterations, as shown in the next figures. As previously, they are well visible. In order to better present the studied trends, shade-of-grey scales Sk1 and Sk2 (Figures 17–18) were used. It should be noted that in the case of the Sk0 scale for the *complement* and *topology* distributions there are almost black-and-white distributions in the last steps.

In the case of *normalized energy*, scale Sk1 (Figure 17a.) was used whereby one can distinguish a core made up of black (1.0), almost black [0.2; 1) and slightly lighter [0.09; 0.2) layers. The other areas with lower values are shown in lighter shades of grey. For example, for step 15 one can notice a certain gradation of shades of gray for the grey elements located outside the [0.09; 0.2) range (the arms of the cantilever) – darker, denser elements are located directly at the core while whiter, less dense (weaker) elements are situated closer to the edge of the members. Similarly one can interpret the results for the next steps in which a cross surrounded by a material with lower densities can be distinguished.

Cantilever beam scheme (20×20 elements with side length equal to 1.0 m, $p = 1$, $\alpha = 0.44$,

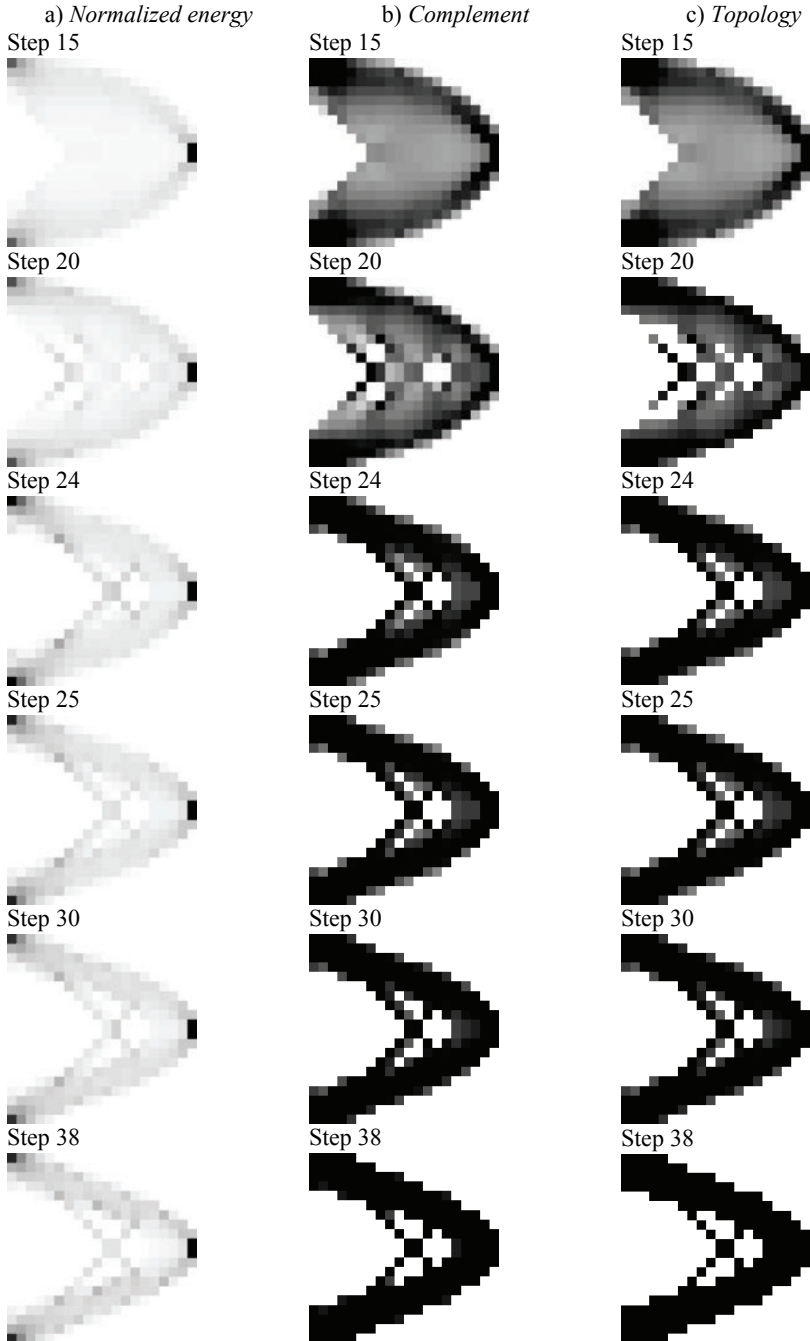


Fig. 16. Distributions obtained in selected iterations: a) normalized energy, b) complement, c) topology

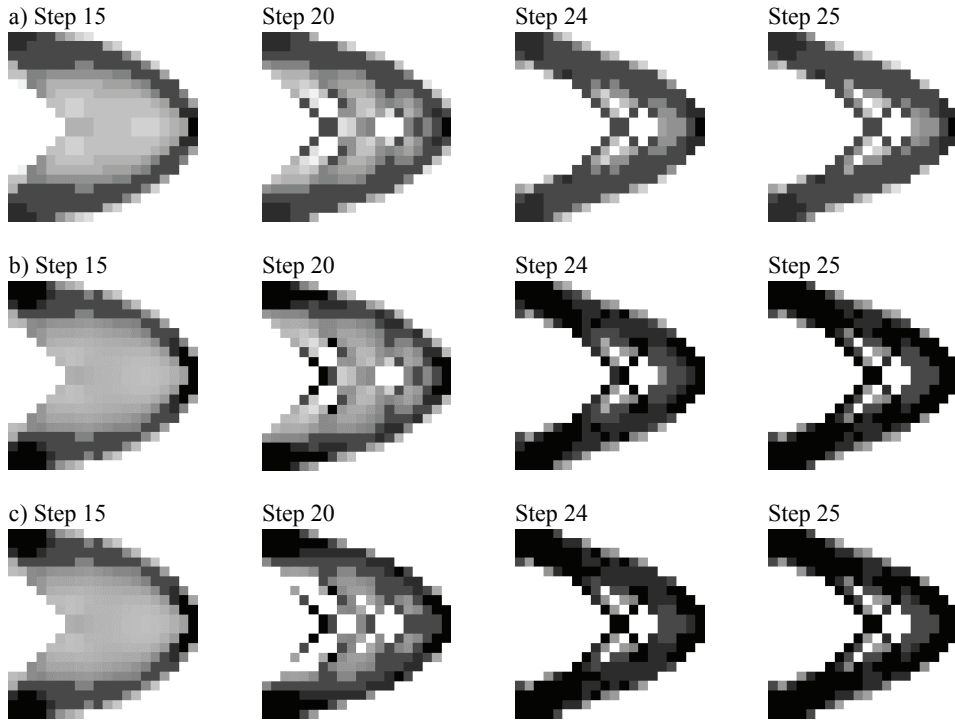


Fig. 17. Results obtained for cantilever beam scheme (20×20) in selected process iterations, presented in scales: a) normalized energy – scale Sk1, b) complement – scale Sk2, c) topology – scale Sk2

In the case of *complement*, a much larger total quantity of material than for *normalized energy* was used and the Sk2 scale was applied (Figure 17b). One can see a large area of black elements (1.0), which as the optimisation process advances begin to form the core of the structure. They are surrounded by almost black highly dense ($[0.9; 1)$) elements which in a way bond the black core, filling the areas in which it has not formed yet (e.g. in steps 24 and 25). The next outermost layer consists of elements with densities in a range of $[0.7; 0.9)$. The other elements, whose densities are the lowest (0; 0.7), are shown in shades of grey.

In the case of *topology*, which is the final distribution for each step, scale Sk2 was used. The differences between *topology* and *complement* are small. The distributions differ in details, e.g. for steps 20, 24 and 25. In step 20 of *complement* one can see larger areas of $[0.7; 0.9)$ elements while in step 25 of *topology* the break in the black core is smaller.

Figure 18a shows that the structure is made of multimaterial in which a core is distinguishable, but the latter is not homogenous, whereas in Figure 18b the material is more concentrated along the line of bars and it is more distinctly layered (each layer is represented by a different shade of grey).

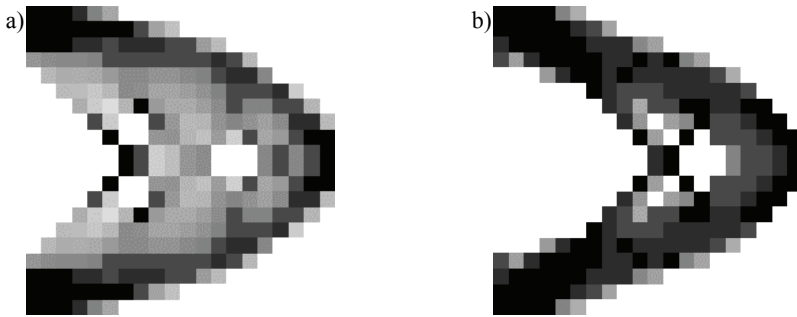


Fig. 18. Complement topologies from Figure 17 for a) step 20, b) step 24

5. Conclusion

The analysis shows the problem's complexity and highlights optimal solution identification. The optimal topology is considered to be a topology characterized by minimum strain energy, which is the case for a layered material distribution with material properties different for the different layers and constant or nearly constant for each individual layer.

In the structures a core forms and layers with decreasing relative density form parallel to it. This can be observed more closely using a denser FE mesh. The core material is usually surrounded by very weak material (practically negligible as regards load carrying).

On the basis of the strain energy analysis, optimal body topologies are obtained in the whole design domain. These are multimaterial topologies with densities equal to and lower than 1 (ρ).

References

- [1] Bendsøe M.P., Sigmund O.: *Material interpolation schemes in topology optimisation*, Archive of Applied Mechanics, Vol. 69, 1999, pp. 635–654.
- [2] Bendsøe M.P.: *Optimal shape design as a material distribution problem*, Struct. Optim., Vol. 1, 1989, pp. 193–202.
- [3] Glaucio H.P., Silva E.C.N., Chau H. Le.: *Optimal design of periodic functionally graded composites with prescribed properties*, Struct. Multidisc. Optim., Vol. 38, 2009, pp. 469–489.
- [4] Kieback B., Neubrand A., Riedel J.: *Processing techniques for functionally graded materials*, Mater. Sci. Eng., A362, 2003, pp. 81–105.
- [5] Kutylowski R., Rasiak B.: *Influence of various design parameters on the quality of optimal shape design in topology optimisation analysis*, Proceedings in Applied Mathematics and Mechanics, Vol. 8, 2008, pp. 10797–10798.
- [6] Kutylowski R., Szwechłowicz M.: *Analyse des Penalty-Faktors in SIMP-Methode in Bezug auf die Konvergenz der Lösung (The power law factor analysis in SIMP method from the convergence point of view)*, Proceedings in Applied Mathematics and Mechanics, Vol. 8, 2008, pp.10803–10804.

- [7] Miyamoto Y., Kaysser W.A., Rabin B.H., Kawasaki A., Ford R.G.: *Functionally graded materials: design, processing and applications*, Kluwer Academic, Dordrecht, 1999.
- [8] Ramm E., Bletzinger K.-U., Reitinger R., Maute K.: *The challenge of structural optimisation*, in: Topping B.H.V., Papadrakakis M. (ed) *Advanced in Structural Optimisation*, Int. Conf. on Computational Structures Technology held in Athen, 1994, pp. 27–52.
- [9] Suresh S., Mortensen A.: *Fundamentals of functionally graded materials*, Institute of Materials (IOM) Communications, Serie 698, London 1988.

Optimalizacja topologii narzędziem do uzyskania konstrukcji multimateriałowej

Rozwiązania problemu optymalizacji topologii są najczęściej przedstawiane w ten sposób, że ostatecznie w obszarze projektowym mamy do czynienia z rozkładem typu materiał – pustka. W pracy wykazano, że rzeczywista optymalna konstrukcja to konstrukcja warstwowa składająca się z różnych materiałów, w której twardy rdzeń pręta otoczony jest coraz słabszymi warstwami. Zastosowano podejście energetyczne minimalizując funkcjonal podatności przy więzach nałożonych na masę ciała. Implementację numeryczną wykonano przy wykorzystaniu metody elementów skończonych.



Wettability of hardmetal surfaces prepared for brazing with various methods

Z. MIRSKI, T. PIWOWARCZYK

Wrocław University of Technology, Wybrzeże Wyspiańskiego 27, 50-370 Wrocław, Poland.

Hardmetals belong to the materials hardly wettable by liquid brazing alloys, so they should not be brazed without removing the surface layer after sintering. In the paper, mechanical and chemical methods of preparing a hardmetal surface for brazing are discussed. Special attention is paid to the electrolytic etching method that gives very good energetic properties to surfaces of hardly wettable materials. Electrolytic etching of hardmetals consists in anodic dissolution of tungsten carbide grains in water solution of alkaline metal hydroxides. The α phase (WC) is removed from surfaces of carbide preforms, leaving the much better wettable β phase (Co-W-C). Cobalt does not show amphoteric properties, so it does not dissolve in bases. With regard to brazing, besides significant development of the surface, an especially profitable feature of this method is isolating the metallic cobalt phase, which allows easier wetting by brazing alloys. On the grounds of surface roughness measurements, parameters of electrolytic etching were determined to remove WC grains from surfaces of carbide preforms and to obtain much higher Co fraction on the brazed surface. The presented results are based on measurements of wetting angles on B40 hardmetal surfaces, isolated α and β phases and C45 steel, as well as on EDX cobalt analysis on hardmetal surfaces.

Keywords: *hardmetals, surface preparation, electrolytic etching, wetting measurements, EDX analysis*

1. Introduction

Hardmetals applied in tools manufacture are usually made in form of preforms joined with the body made of unalloyed or alloyed steels. Bonding hardmetals with steel is most often performed by hard and high-temperature soldering, or less frequently by brazing, resistance welding, fusion welding or gluing [3, 6, 8, 10–11, 15].

Hardmetals and steels used for tool bodies show diverse physicochemical and mechanical properties [3, 6, 8, 10–11, 15]. With respect to brazing, the most important are: two to three times smaller linear expansion coefficient, very low deformability and limited wettability of hardmetals, especially of carbide phases WC, TiC, TaC and NbC. In order to improve wettability of hardmetals by brazing alloys, it is necessary to choose their proper chemical composition and to prepare their surface properly for the bonding processes.

2. Methods of preparing hardmetal surface for brazing

Surface preparation of the materials to be joined has an essential effect on mechanical properties of brazed joints and thus their service reliability. Cleaning the

hardmetal surface, performed irrespective of the bonding method, is aimed at removing the skin formed during sintering, as well as oxides and other impurities [11]. It should be done directly before brazing, because effectiveness of surface preparation declines with time and is mostly influenced by storage conditions of the parts to be brazed [8, 13]. Their surface preparation is often complemented by applying (in chemical, physical or plasma process) metallic layers like nickel, cobalt, copper or silver [3, 11].

Various methods of preparation are applied in order to develop the surface and to ensure its coherence and wettability, namely mechanical, chemical, thermal (or combined like thermochemical) and electrochemical [3, 5, 8, 10–11, 13]. Surface preparation of the components to be joined includes two main stages [3, 5, 6, 8–13, 15]:

- modification of surface layer by various methods: mechanical, thermal, chemical or electrochemical,
- cleaning and degreasing to remove impurities.

Mechanical methods remove most of organic and inorganic impurities, influencing surface topography and reactivity. In addition, rough surfaces change nature of the alloy flow in the gap to turbulent and are better wettable [13]. In the case of hardmetals, the most often used mechanical methods are: grinding, abrasive blasting and abrasive tumbling [3, 6, 8, 11]. They develop real surfaces of the parts to be joined, that results in stronger intermolecular interactions. From the viewpoint of brazing, it is profitable to maintain roughness heights within 10 to 25 μm [10, 12]. The condition of effective mechanical surface cleaning is maintaining the assumed brazing gap, with respect to both its width and surface parallelism [10, 13]. When a cooling agent is used in the mechanical cleaning process, all its residues should be completely removed (it often contains silicones) [12–13].

Mechanical methods permit creating a geometrical structure of the surface layer that ensures its maximum development but does not guarantee good surface activation, so they should be complemented by later chemical treatment [11]. Chemical treatment consists in degreasing or pickling the parts in baths with suitable composition and temperature [8, 10–13]. The most frequently used chemical methods are pickling in solutions of acids (hydrochloric, sulphuric and nitric) or bases [11–13]. Due to high physicochemical activity they can remove organic impurities, significantly reduce thickness of the oxide layers and change their morphology. Choice of a cleaning chemical depends mainly on kind of the impurities, but also on surface condition and the joint structure [13].

Electrochemical methods of surface preparation ensure very advantageous energetic surface properties and are applied in the case of very high strength requirements. Electrochemical treatment consists in anodic dissolution by electrolysis [2, 11]. The chemical reactions are opposite to those occurring in electroplating at coating the products with metallic layers. Dissolving is enabled by the electrolyte, an electrically conducting liquid. During the process, dissolved ions pass to the electrolyte where the reaction products precipitate [2, 11].

3. Methodology of preparing hardmetals B40 and G20 for brazing

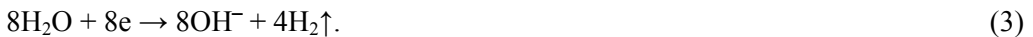
The hardmetals selected for testing were coarse-grained B40 and medium-grained G20 (designations acc. to PN-H-89500: 1988), sintered in a Tammann furnace at ca. 1380 °C for 1.5 h.

Hardmetals are poorly treatable by abrasive machining [1, 11]. Nevertheless, before brazing they are usually subject to mechanical grinding. Therefore, this method was selected as one of the ways of preparing the hardmetal preform surfaces. From the viewpoint of brazing, beside significant surface development related to the stereometric features, a particular advantage of this method is isolating the metallic cobalt phase that permits easier wetting with the brazing alloy. In this connection, electrolytic etching was chosen as the basic preparing method. It consists in anodic dissolving the tungsten carbide grains in aqueous solutions of base metals hydroxides. A presumption of this method is to remove the carbide phase α (WC) from surfaces of the preforms, leaving the much better wettable phase β (Co-W-C). Cobalt does not show amphoteric properties, so it does not undergo dissolving in bases. Electrolytic etching of a hardmetal results in obtaining a developed, spongy cobalt layer 0.1 to 10 μm thick on the joint surface [3, 7].

In the initial phase of anodic dissolving of the hardmetal by a reaction with sodium hydroxide, the external, porous layer of tungsten oxide WO_3 is decomposed according to the formula (1) [3]:



During electrolytic etching, the oxidation reaction (2) occurs on the anode and the reduction reaction occurs on the cathode (3):



In total, the ionic reaction of dissolving the WC grains is as follows (4):



Finally, the molecular reaction occurring during electrolytic etching of the hardmetal is (5):



The created sodium tungstate Na_2WO_4 goes to the solution and the volatile reaction products, i.e. carbon monoxide and hydrogen, for safety reasons should be disposed to the atmosphere.

In the own research, the electrolytes consisted of 4-mol solutions of NaOH and KOH in reagent grade. 160 g NaOH or 224 g KOH was dissolved in 1 dm³ of distilled water, as calculated on the grounds of molar masses of the bases. According to [3], the NaOH solution proved to be more active at dissolving the carbides than the analogical KOH solution. So, this more effective solution was finally chosen as the electrolyte in the surface preparation processes. The electrolytic etching parameters, i.e. electrode voltage U , time t and electrolyte temperature T , were selected in preliminary tests. Maximum roughness values were obtained by electrolytic etching at $U = 3500$ mV for $t = 10$ min and $T = 23$ °C. Comparative tests were also performed for the parameters $U = 1500$ mV and $t = 60$ min.

After the etching process, the outer carbide layer prepared by anodic dissolving of WC grains had to be cleaned from residues of the electrolyte and the reaction products. Cleaning was performed using the nitro solvent in an ultrasonic washer.

Table 1 gives cobalt concentration values on the hardmetal surfaces measured using a microscope SEM 515 Philips and an X-ray microanalyser 9800 EDAX.

Table 1. Concentration of cobalt on B40 hardmetal surfaces

Method of surface preparation	Concentration of cobalt in wt. %
As delivered, with no preparation	4.61
Grounding	9.69
Electrolytic etching	53.39

For comparison, the substrates composed of α phase (WC), β phase (Co-W-C) and C45 steel were also prepared for wetting angle measurements.

4. Laboratory stand for electrolytic etching

Electrolytic etching of the hardmetals B40 and G20 was performed using an electrolytic polisher Galvalab G7T made by SOJO with reversible magnetic stirrer. The most important parameters of the device were: electrode voltage $U = 2-12$ V, electrode current $I = 0.1-3.5$ A, time range $t = 1-20$ min and maximum etched area $S = 5$ cm². The electrolytic etching stand consists of a DC supply with a support, anode in form of a carbide preform connected to the positive pole, cathode in form of a nickel-coated copper disk dia. 36 mm, beaker with electrolyte and a magnetic stirrer.

5. Measurements of wetting angle θ on hardmetal surface

The wetting angle θ between the tangent to the liquid surface at the solid-liquid-air contact point and the solid surface characterises interaction on the solid-liquid phase boundary [11]. Measurement of the wetting angle allows preliminary determining brazeability of materials as well as predicting properties of brazed joints [11]. According to the guidelines on proper wetting angle measurement, the examined surfaces should be flat, horizontal and created of materials chemically homogeneous and neu-

tral with respect to the wetting liquids [14]. The wettability measurements should be made very carefully, because any impurity of the examined surface can be a source of significant errors.

Wettability of hardmetals by a liquid brazing alloy was determined on a stand for solder spreading tests using a high-temperature microscope Leitz Wetzlar under nitrogen protective atmosphere. Individual stages of melting and wetting by the liquid alloy were recorded every 10 °C. The substrates of hardmetals, isolated α and β phases and C45 steel were prepared as disks dia. 11.5 mm and 3 mm high. Chemical composition of the applied copper and brass brazing alloys and their melting points are settled in Table 2 (designations acc. to EN ISO 3677 include melting points in °C). They were prepared in form of cylinders dia. 3 mm and 3 mm high.

Table 2. Chemical composition and melting point of brazing alloys

Designation (acc. to EN ISO 17672)	Designation (acc. to EN ISO 3677)	Average chemical composition wt.%						
		Cu	Zn	Ni	Si	Mn	B	Sn
Cu 773	B-Cu48ZnNi(Si)–890/920	48	rem.	10	0.2	–	–	–
Cu 595	B-Cu84MnNi–965/1000	rem.	max. 1	3.25	–	12.5	–	max. 1
Cu 186	B-Cu97NiB–1085/1100	rem.	–	3	–	–	0.05	–
Cu 110	B-Cu100–1085	99.9	–	–	–	–	–	–

Because of long designations of the alloys acc. to EN ISO 3677, below are used much simplified designations: Cu48ZnNi, Cu84MnNi, Cu97NiB and Cu, respectively.

Wettability of hardmetal substrates is also decided by physicochemical properties of the applied brazing alloys. Measurements were started from evaluating wettability of B40 ground surface with brazing coppers within 1000 to 1250 °C, see Figure 1. Dynamics of wetting the hardmetal substrate is dependent on kind of the brazing alloy. The best wettability characterises the alloy Cu84MnNi that shows the wetting angle below 60° as early as at 1020 °C, and the angle is gradually reduced to a bit over 30° at 1180 °C. The alloy Cu97NiB and pure copper show temperature stops within 1100 to 1170 °C, where the angle changes are small. These results, as well as the results of the spreading tests [4], confirm rightness of adding manganese, nickel and boron, the elements improving wetting properties of brazing alloys.

Figure 2 shows measurement results of wetting angle for pure copper on various surfaces. The following substrates were chosen for testing: ground steel C45, ground hardmetal B40, electrolytically etched (3500 mV, 10 min) hardmetal B40, ground α phase and ground β phase. As was expected, ground surfaces of hardmetal and α phase (hardly wettable WC grains) show the poorest wetting properties. Even at 1150 °C, the wetting angle oscillates around high values between 120 and 130°. Significant overheating of the alloy to 1240 °C leads to its reduction for ground hardmetal only, but does not change it significantly for α phase. Ground steel is an exemplary material whose surface shows improved wetting properties even at small temperature changes.

In the analysed example, the wetting angle of 120° at 1100 °C decreases to 3° at the temperature elevated by 20 °C only. However, the electrolytically etched hardmetal and isolated β phase show very good wettability with brazing alloys. At 1120 °C, the wetting angles measured on their surfaces are 4° and 8°, respectively.

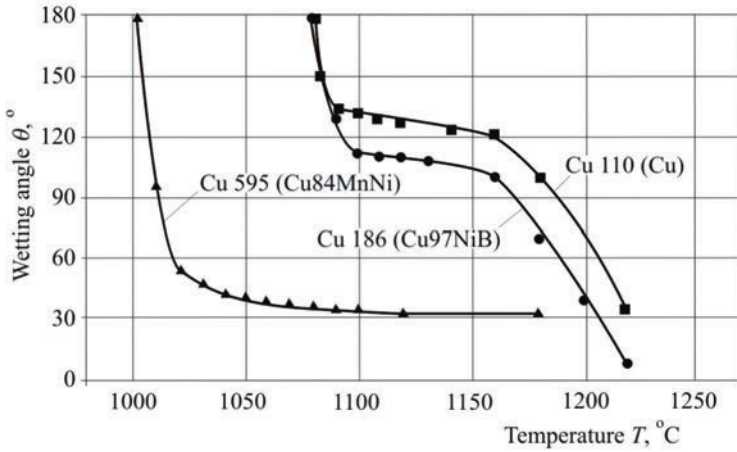


Fig. 1. Relationships between wetting angle and temperature for various brazing coppers on B40 hardmetal

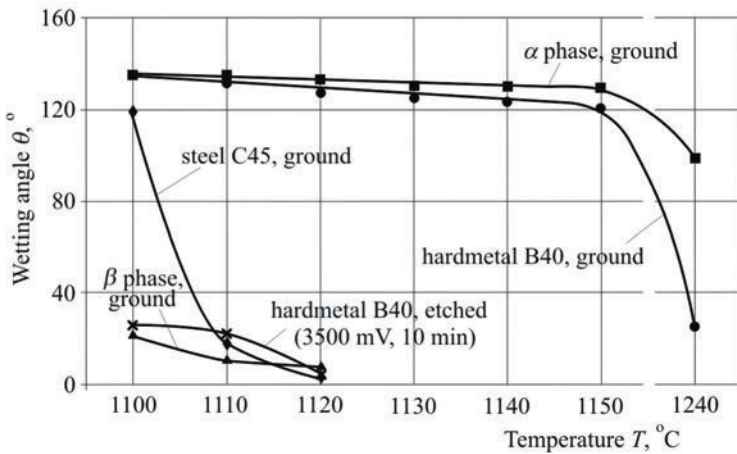


Fig. 2. Relationships between wetting angle and temperature for brazing copper (Cu) on various substrates

Analogous comparative tests were performed for the brazing alloy Cu97NiB. This time, the substrates were steel C45 and hardmetal B40 mechanically ground and electrolytically etched at two parameter sets: $U = 3500$ mV and $t = 10$ min or $U = 1500$ mV and $t = 60$ min (Figure 3). The poorest wettability showed the ground surface of hard-

metal B40. It is only after significant exceeding the melting point of the alloy, by even more than 200 °C, a decrease of the wetting angle is clearly visible, however this can lead to disadvantageous diffusion processes on the interface hardmetal-braze [3]. On the contrary, the hardmetal electrolytically etched at $U = 3500$ mV and $t = 10$ min, as well as steel C45 show well wettable surfaces as early as at 1110 °C, the temperature slightly higher than the melting point of the brazing alloy. Observed was also an influence of electrolytic etching on wetting properties of the surface. The wetting angle of ca. 5° for the surface etched at $U = 1500$ mV and $t = 60$ min was observed at 1180 °C only.

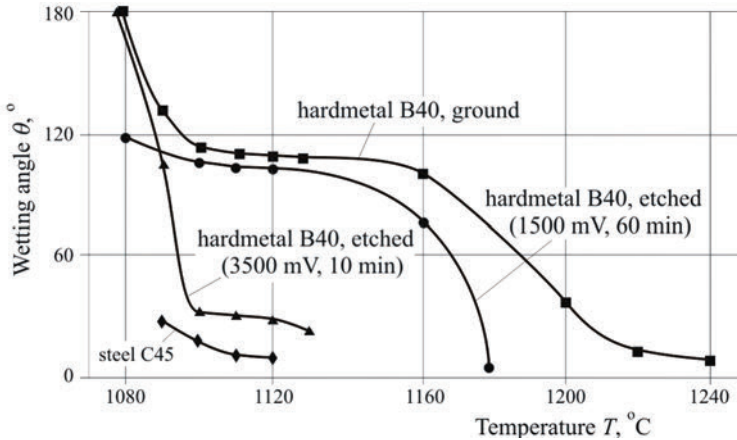


Fig. 3. Relationships between wetting angle and temperature for Cu97NiB on various substrates

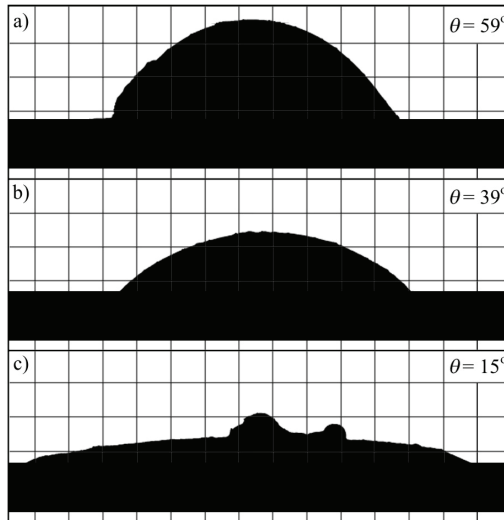


Fig. 4. a) Brazing alloy Cu48ZnNi on G20 hardmetal surfaces: as delivered, b) ground, c) electrolytically etched (3500 mV for 10 min, 4n solution of NaOH)

Figure 4 shows wetting behaviour of the brazing alloy Cu48ZnNi on the G20 hardmetal surfaces: as delivered (a), ground (b) and electrolytically etched (3500 mV for 10 min) (c), at 1110 °C. Graphic measurements of the wetting angle explicitly showed an improvement of the surface wettability due to dissolving tungsten carbides WC and leaving the easily wettable β phase on the surface. The wetting angle at 1110 °C was 15° for the hardmetal electrolytically etched, but as much as 59° for raw preforms and 39° for the ground ones. Therefore, raw hardmetal surface with omitted preparation stage is not properly wettable and not suitable for brazing.

6. Conclusions

Results of the research demonstrate that – from the viewpoint of wettability – electrolytic etching is an effective method of preparing hardmetal surfaces for brazing. It permits introducing new edges and gaps, increasing also fraction of the metallic surface. This confirms rightness of the argument indicating a dependence of wetting angle on roughness and homogeneity of the surface [14]. The following conclusions result from the performed examinations:

- Choosing a suitable method of preparing surfaces of the components to be brazed decisively influences their wettability by the brazing alloy and thus their brazability as well as quality of brazed joints of hardmetals with steel.
- The preparation method giving the best wettability of a hardmetal surface is selective electrolytic etching that ensures the smallest wetting angles and the largest spread factor values.
- Selecting proper parameters of electrolytic etching (voltage U and time t mainly) is a very important activity preceding the hardmetal surface preparation, significantly influencing its wettability by liquid brazing alloy.
- Mechanical grinding, being the commonly used method of preparing hardmetal surface for brazing, gives poor wettability by liquid brazing alloys, which is improved after significant overheating only, which is unacceptable from the technological point of view.

References

- [1] Cichosz P.: *Cutting tools* (in Polish), WNT Publ., Warsaw, 2006.
- [2] European Commission, Directorate-General Joint Research Center, Institute for Prospective Technological Studies, Draft reference document on best available techniques for the surface treatment metal and plastics, Sevilla, 2004.
- [3] Mirski Z.: *Control of the width of brazed joint clearance in the processes of joining dissimilar materials* (in Polish), The scientific works of Institute of Production Engineering and Automation of Wrocław University of Technology, Series: Monographs, No. 22, Wrocław University of Technology Publ., Wrocław, 2000.
- [4] Mirski Z.: *New silver-free filler metals for hardmetal brazing* (in Polish), National Scientific-Technical Conference „New welding materials and technologies”, Częstochowa, Edited by OW SIMP, 1989, pp. 147–157.

- [5] Mirski Z., Drzeniek H.: *Wettability of hardmetals at brazing* (in German), 5th International Conference on Brazing, High-temperature Brazing and Diffusion Welding, Aachen, 16–18 June 1998, DVS-Reports, DVS Verlag, Düsseldorf, Vol. 192, 1998, pp. 289–293.
- [6] Mirski Z., Granat K.: *Quality improvement of sintered joints of tools with sintered carbides* (in Polish), *Welding Technology Review*, No. 8–9, 2004, pp. 27–30.
- [7] Mirski Z., Szymkowski J., Piwowarczyk T.: *Gluing and brazing of electrolytic etched hardmetals* (in Polish) *Welding Technology Review*, No. 9–10, 2006, pp. 64–68.
- [8] Nowacki J., Chudziński M., Zmitrowicz P.: *Brazing in machine building* (in Polish), WNT Publ., Warsaw, 2007.
- [9] Nowacki J., Kawiak M.: *Loads, stresses and deformations in brazed joints* (in Polish), *Welding Technology Review*, No. 4, 2006, pp. 15–18.
- [10] Pilarczyk J.: *Engineer's guide – Welding* (in Polish), Part 2, WNT Publ., Warsaw, 2005.
- [11] Piwowarczyk T.: *Increase of adhesive and cohesive interaction in adhesive joints of hardmetals with steel C45* (in Polish), Doctoral Thesis, Institute of Production Engineering and Automation, Wrocław University of Technology, 2008.
- [12] Rangaswamy S.: *Brazing fundamentals. The Role of base metal surface condition in brazing*, Microbraz Technical Articles Library.
- [13] Schwartz M.: *Fundamentals of brazing and soldering, in welding, brazing, and soldering* (ASM Handbook), ASM International, Vol. 6, 1993.
- [14] Sobczak N., Singh M., Asthana R.: *High-temperature wettability measurements in metal/ceramic systems. Some methodological issues*, *Current Opinion in Solid State and Materials Science*, Vol. 9, No. 4–5, 2005, pp. 241–253.
- [15] Upadhyaya G.S.: *Cemented tungsten carbides production, properties, and testing*, Noyes Publ., New Jersey, 1998.

Zwilżalność powierzchni spieków węglkowych przygotowanych różnymi metodami do lutowania twardego

Węglik spiekane należą do materiałów trudno zwilżalnych ciekłym lutem, zatem nie powinny być lutowane bez usunięcia warstwy powierzchniowej po spiekaniu. W pracy omówiono mechaniczne i chemiczne metody przygotowania powierzchni węglków spiekanych do lutowania twardego. Szczególną uwagę poświęcono metodzie trawienia elektrolitycznego, oferującą bardzo dobre właściwości energetyczne powierzchni materiałom trudno zwilżalnym. Trawienie elektrolityczne węglków spiekanych polega na roztwarzaniu anodowym ziaren węgla wolframu w wodnym roztworze wodorotlenków metali alkalicznych. Założeniem tej metody jest usunięcie fazy α (WC) z powierzchni kształtek węglkowych pozostawiając znacznie lepiej zwilżalną fazę β – (Co-W-C). Kobalt nie wykazuje właściwości amfoterycznych w związku z czym nie ulega rozpuszczaniu się w zasadach. Z punktu widzenia lutowania, szczególnie korzystną zaletą tej metody, oprócz znacznego rozwinięcia powierzchni, jest wyodrębnienie metalicznej fazy kobaltowej umożliwiającej łatwiejsze zwilżanie lutem. Na podstawie pomiarów chropowości powierzchni określono parametry trawienia elektrolitycznego umożliwiające roztworzenie ziaren WC z powierzchni kształtek węglkowych, uzyskując znaczny wzrost udziału kobaltu na powierzchni lutowanej. Wyniki badań przedstawiono na podstawie pomiarów kąta zwilżania na powierzchni węglków spiekanych gat. B40, wyodrębnionych faz α i β stali C45 oraz analizy zawartości kobaltu na powierzchni węglków spiekanych metodą EDX.



Numerical study of the micro-formability of thin metallic materials: virtual micro-forming limit diagrams

N. SENE, P. BALLAND, R. ARRIEUX

Université de Savoie, Laboratoire SYMME, Polytech Annecy-Chambéry,
BP 80439, 74944, Annecy le Vieux Cedex, France.

This paper presents the determination of virtual micro-forming limit diagrams from two types of numerical simulations based on the finite element method: one with modelling of the full tool for micro-deep drawing and a thin blank with geometric imperfections, based on a defined roughness; and a second called “reduced simulation” where different deformation paths were simulated with appropriate boundary conditions by introducing the same type of geometric imperfections on aluminium 1050A (99.5%). A new test for detecting the onset of necking, called the “change of slope” criterion has been defined. Several methods based on histograms to represent the distributions of major and minor strains, have been used to determine the strain at the onset of necking. The numerical micro-forming limit diagrams (MFLD) were then compared to one obtained experimentally.

Keywords: *micro-forming limit diagrams, necking criteria, finite elements, reduced simulation, aluminium*

1. Introduction

The numerical simulation of deep drawing by the finite element method is a robust and beneficial means of developing various drawing operations. Information on the success of a part can be obtained by numerical simulation, by combining the finite element method and criteria for the detection of early necking. Much work has been carried out on the determination of numerical forming limit diagrams for materials of conventional thicknesses (about 1 mm) with common stamping tools. Moreover, various methods for the numerical determination of forming limit diagrams, based on the analysis of results from modelling tests by Marciniak [5] and Nakazima [6] have been proposed in the literature. By using the test by Nakazima, Brun et al. [2] studied the evolution of deformation in the thickness of sheets to detect the onset of necking and obtain the forming limit diagrams. Geiger and Merklein [3] have also used this test to analyze the gradient of major strains. The authors speculated that this gradient changes rapidly when localized necking occurs. To detect the onset of necking, Petek et al. [7] have used the first and second time derivatives of the thickness, with the Marciniak test. A new approach to identify the onset of localized necking by experimental and numerical methods has been proposed by Volk [9].

The aim of this paper was to study the forming limit diagrams of a thin aluminium sheet (0.2 mm) with a specific tool for small dimensions (9-mm punch), obtained from

numerical simulations of the micro-stamping. The idea was to employ a new detection criterion for the necking coupled with various methods for determining the deformations at the onset of necking. These curves are called micro-forming limit diagrams (MFLD). A simulation of blanks of various geometries with a micro-stamping tool of the type Marciniak, taking into account the state of the surface, was first performed to determine the micro-forming limit diagrams. The determination of the strain at the onset of necking was carried out using several methods related to histograms representing the distribution of major and minor strains. A comparison of the virtual micro-forming limit diagrams with those obtained experimentally rendered it possible to make a choice amongst these methods.

The chosen method was then used for the operation of a numerical simulation designated “reduced”. This signified that only a square area that was 0.1 mm thick was simulated by imposing adequate boundary conditions of symmetry and displacement. This restriction rendered it possible to eliminate the tools by boundary conditions that were difficult to identify, and to avoid contact modelling by determining the coefficient of friction, which is difficult to obtain during drawing while reducing the computation time. It was then possible to simulate paths of deformation in tensile, plane strain tensile and biaxial tensile. The ultimate goal was to be able to very quickly determine the micro-forming limit diagrams. This simulation was carried out by introducing geometric imperfections in the form of surface roughness. Indeed, given the thinness of the sheets, these defects can have a significant influence on the onset of necking.

This paper first presents the numerical simulation of the micro-stamping process, which also describes the modelling of the tool and the blank, the determination of geometric surface characteristics and the determination of virtual micro-forming limit diagrams. Subsequently, a simulation designated “reduced” is introduced and the numerical micro-forming limit diagrams are determined and compared to a curve obtained experimentally.

2. Numerical simulation of the micro-stamping process

The numerical simulation was performed with the finite element code Abaqus/Explicite [4] using a double precision calculation method. The contact conditions are complex when it comes to stamping and need to be controlled, which motivated us to choose the explicit version since the management of contact between the parts was strong. This simulation reproduced the experimental protocol developed in the laboratory to determine the micro-forming limit diagrams [8].

2.1. Presentation of the numerical simulation of the micro-stamping

The equipment, consisting of a punch with a diameter of 9 mm, a die and a round blank holder with an inside diameter of 10 mm, was described by analytical rigid sur-

faces (Figure 1) while the blank was modelled with 3D elements. The blanks had a thickness of 0.2 mm and a sub-thickness of 0.1 mm in an area with a diameter of 3 mm at the centre of the sheets, thus rendering it unnecessary to use a spacer. Different geometries of the blanks ($L = 24$ mm, $L = 10$ mm and $L = 6$ mm) (Table 1) were modelled, corresponding respectively to the following three strains paths: biaxial tensile, plane strain tensile and uniaxial tensile.

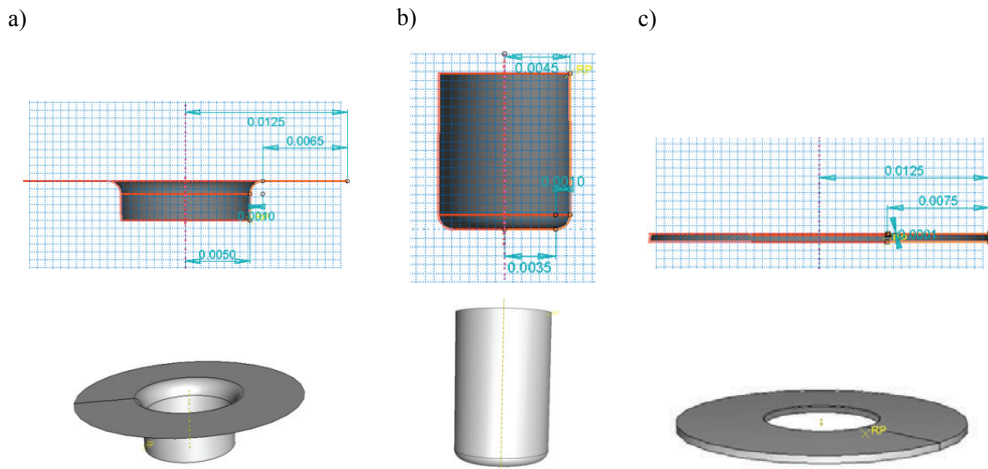


Fig. 1. Fabrication of parts for the micro-stamping tool: a) die, b) punch, c) blank holder

Table 1. Different blank dimensions

Blank no.	L (mm)	R (mm)	R_c (mm)	r (mm)
1	6	12	14	1.5
2	10			
3	24			

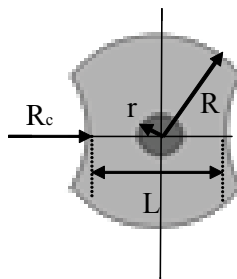


Fig. 2. Blank geometry

For reasons of symmetry and computation time, one quarter of the blank was discretized. Regarding the modelling of the blank, a diameter of 18 mm, which corresponds to

the diameter of the ring clamp that secures the blank between the die and blank holder, was employed. The blanks (Figure 3) were meshed with hexahedral elements of type C3D8R involving an element in the central sub-thickness and two in the thickness. The sub-thickness will in the following be referred to as the central zone.

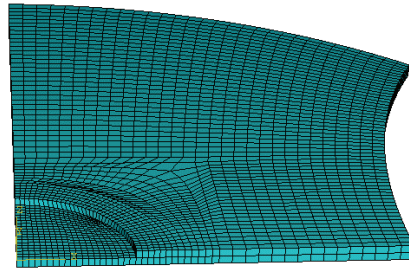


Fig. 3. Example of the meshing of a quarter of the blank with a width of 10 mm

The mechanical parameters of the material were identified through tensile tests on specimens with a thickness of 0.2 mm. A constitutive law for elasto-plastic anisotropy was introduced in Abaqus, as were a Young modulus of 60 GPa, a Poisson ratio of 0.3, a density of 2700 kg/m³ and a reference curve of 0 degree for a sample thickness of 0.2 mm (Figure 4) corresponding to the parameters obtained by a tensile test on Al 1050A annealing at 600 °C for 2 hours. The Hill yield criterion was used, and its parameters (Table 1) were also identified and introduced into Abaqus.

Table 1. Hill parameters

R_{11}	R_{13}	R_{32}	R_{22}	R_{33}	R_{12}
1	1	1	1.288	0.994	1.258

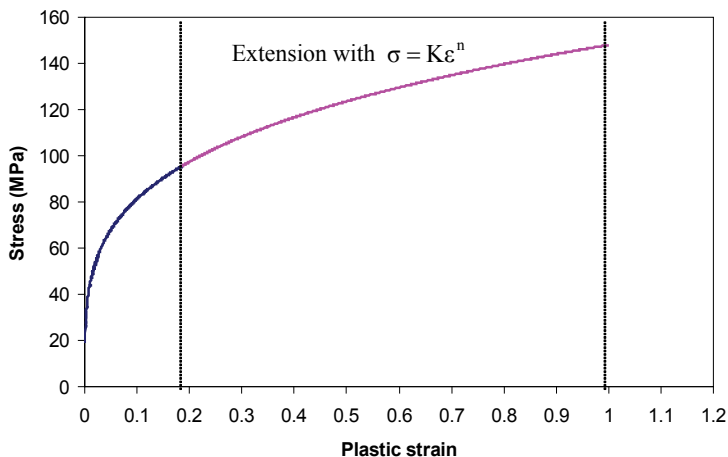


Fig. 4. Reference curve for the behaviour law

Symmetry conditions were imposed on the blanks and a condition of end restraint was used to represent the rod clamp. A speed equal to 3.3×10^{-5} m/s, corresponding to that used experimentally, was applied to the punch. All the degrees of freedom of the die were blocked (end restraint). The blank holder was set to have a concentrated force of 200 N along the axis of motion of the punch, representing the only degree of freedom. For our simulations, the Coulomb law was used to model the contact between the tool and the blank. The friction coefficient was set to 0.2, which corresponds to what is generally utilized between steel and aluminium. The displacement of the punch was progressive (smooth step), and this choice was made in order not to cause any acceleration and thus to avoid effects of inertia in the simulation.

2.2. Determination of the geometric surface characteristics

Given the thinness of the sheet, the surface roughness appeared to be an important parameter at the onset of necking. It was thus utilized to numerically cause heterogeneities. In the experimental trials, the central sub-thickness was achieved with an EDM machine [8]. To verify the roughness caused by machining and with the aim of obtaining the same conditions as in the experimental tests, the surface of the central area of the sample – experimentally obtained by EDM – was measured with an Altisurf optical metrology apparatus. This device can measure surfaces in 3D and thus extract information regarding the roughness. Data processing was performed with the analysis software Altimap (Mountains, Digital Surf). The surface state of our samples is shown in Figure 5.

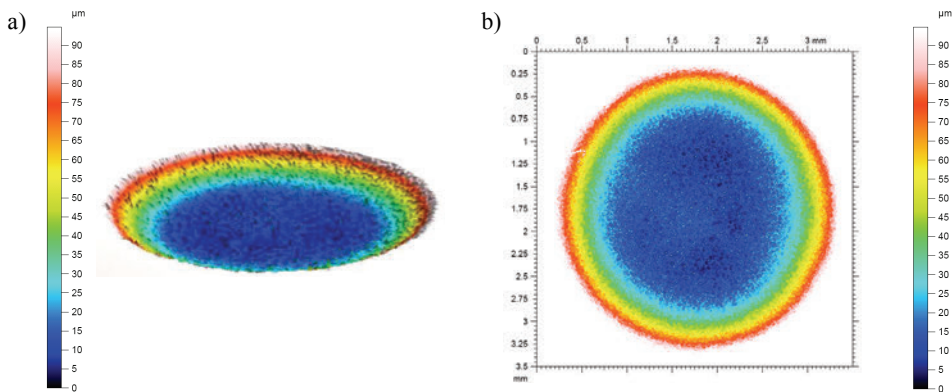


Fig. 5. View of the central zone of the specimen: a) 3D view, b) 2D view

Different roughness profiles i.e. horizontal (Figure 6), vertical and oblique, were extracted to allow us to determine the roughness parameters (Table 2).

According to the three roughness profiles, the maximum depth of the grooves, i.e., of the defects, was given by the value R_V which was approximately equal to 7 μm. The per-

centage of the defect depth was 7% compared to the depth of the central zone (0.1 mm). Subsequently, the depth distribution of defects in the central area could be directly obtained with the software Altimap, by introducing their depth. Defect depths of less than or equal to 7 μm represented 14% of the surface of the central zone (Figure 7). We thus introduced thickness defects with a depth of 7 μm (7% of the sub-thickness) randomly to 14% of the elements of the central part of the blanks. An algorithm was programmed on Matlab to reduce the thickness of certain randomly selected elements. The algorithm carried out a random sorting of the elements to be reduced (the number of defects), and then decreased the height of the nodes (defect depth) to perform.

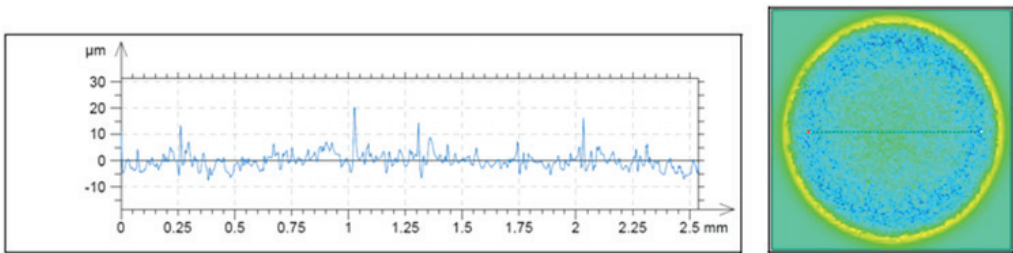


Fig. 6. Horizontal roughness profile

Table 2. Roughness parameters of the horizontal profile

ISO 4287		
Amplitude parameters		
R_a (μm)	1.85	R_a : Arithmetic mean deviation of the roughness profile
R_v (μm)	6.92	R_v : Maximum depth of the grooves in the roughness profile
Parameters related to the peaks		
PPc (1/mm)	20.9	PPc : Number of peaks in the rough profile
Spacing parameters		
RSm (mm)	0.0427	RSm : Average width of roughness profile elements

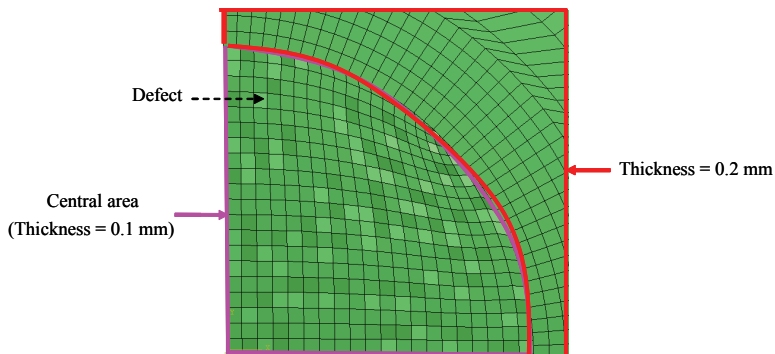


Fig. 7. Introduction of defects in the central zone (lighter colour)

2.3. Numerical micro-forming limit diagrams

The virtual micro-forming limit diagrams were determined by analyzing the results from the numerical simulation. The literature proposes various methods for a numerical determination of forming limit diagrams, based on analysis of the results of modelling of mechanical tests [5–7]. To detect the onset of the localization, a new criterion called “change of slope” was used.

2.3.1. Criteria for the onset of necking: change of slope

The first step was to find the most and least deformed meshing elements at the time when the force started to drop. For this, we extracted the main strains and the numbers of the corresponding elements. The strain of the element with the most significant strain was then plotted as a function of the major strain for the element with the least significant strain. Subsequently, we traced the major strain of the most deformed element versus the major strain of the less deformed element, obtained throughout the simulation (Figure 8). It was assumed that the localization occurred where there was a change of slope in the curve (Figure 8).

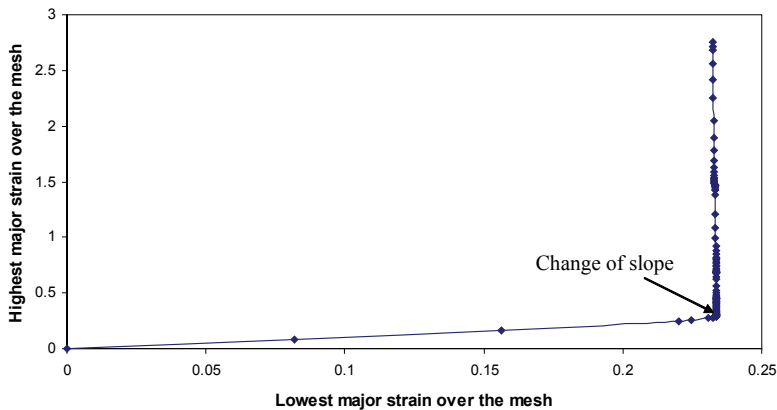


Fig. 8. Major strain of the most deformed element as a function of the major strain of the least deformed element

This method was applied to the three blank geometries. To obtain the micro-forming limit diagrams, it was necessary to extract the major and minor strains at the time of localization, i.e., at the time when necking appeared. Several methods are proposed below for obtaining these strains.

2.3.2. Determination of the strains at the onset of necking

To determine the strains at the onset of necking, i.e., at the time of the localization, various methods were used. We first extracted, for the each test geometry, the major

and minor strains obtained at the time of the localization according to the “change of slope” criterion. Subsequently, a histogram was drawn rendering it possible to represent the distribution of the major strains on the entire surface of the central zone (Figure 9a). Furthermore, another histogram was created, representing the distribution of minor strains (Figure 9b).

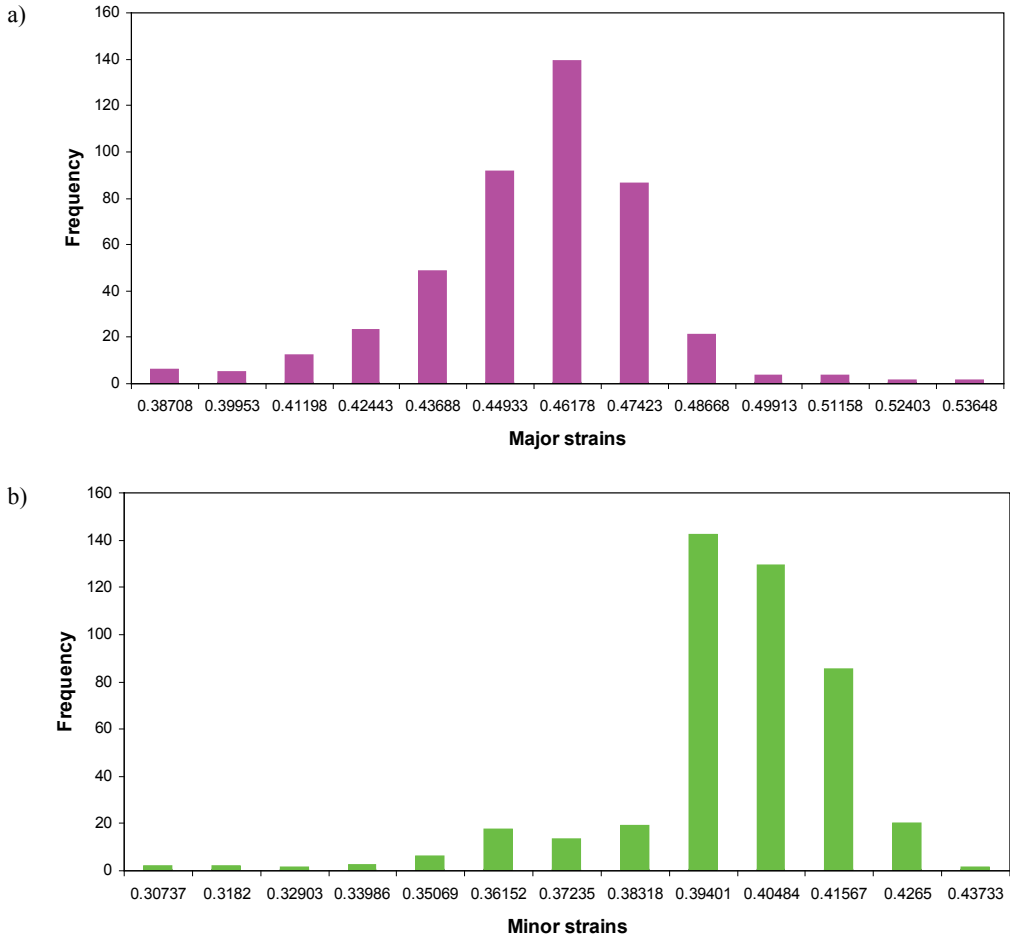


Fig. 9. Histograms obtained in biaxial tensile mode with the «change of slope» criterion: a) major strains, b) minor strains

From the two histograms of the major and minor strains, it was possible to determine the associated normal distributions, respectively portrayed in Figure 10a and Figure 10b.

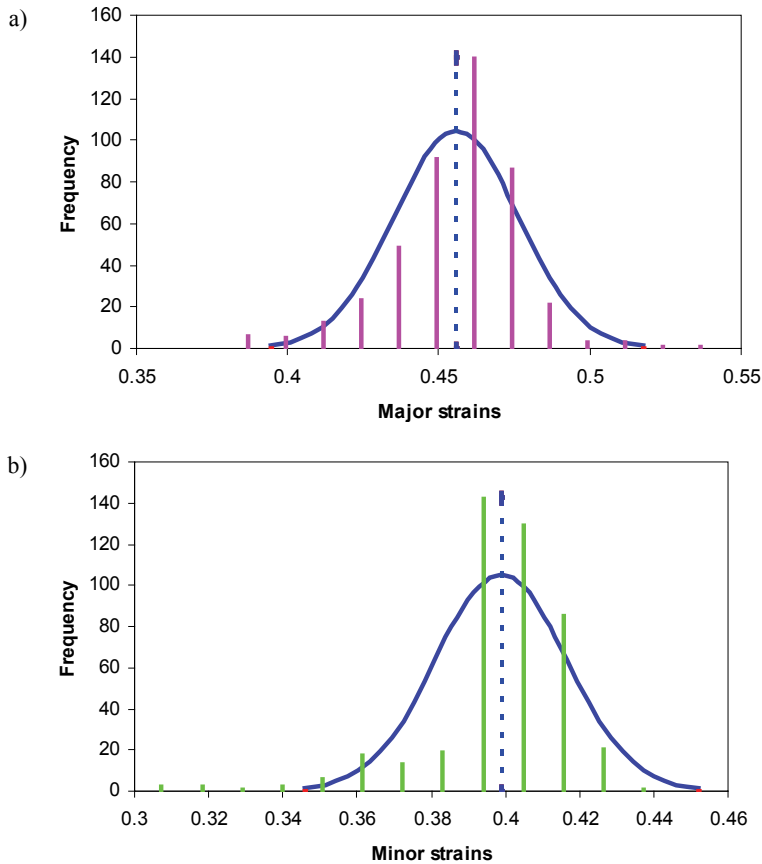


Fig. 10. Comparison of the histograms with a normal distribution profile:
 a) Major strains, b) minor strains

Hereafter, the average is denoted μ , the standard deviation σ and the maximum value \max . The profile of the normal distribution presents the following strains: $|\mu|$, $|\mu + \sigma|$, $|\mu - \sigma|$ and $|\max|$ (Figure 11).

In order to obtain values of major and minor strain at the onset of necking, several methods were studied. The first method considered the maximum value $|\max|$ obtained by the profile of the normal distribution of the major and minor strains. The second method consisted in using the value $|\mu|$ obtained with the profiles of the normal distributions of the major and minor strains. The third method considered the value $|\mu + \sigma|$, the fourth method consisted in averaging the values beyond $|\mu + \sigma|$, and the last method employed the value $|\mu - \sigma|$.

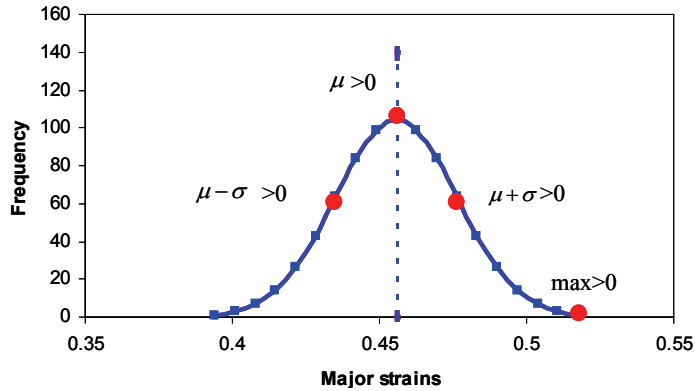


Fig. 11. A representation of the normal distribution profile

The above-mentioned methods were applied to calculate the major and minor strains at the time of localization of the different geometries. Thus, micro-forming limit diagrams were obtained by representing the major strains as a function of the corresponding minor strains. Figure 12 presents all the micro-forming limit diagrams obtained for the “change of slope” criterion based on the various methods for determining the strains at the onset of necking.

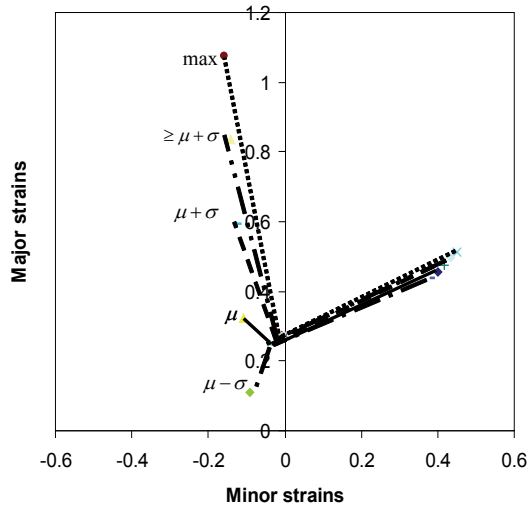


Fig. 12. Comparison of the MFLD obtained for the «change of slope» criterion

The results show that the points provided during biaxial tensile and plane strain tensile were similar for all the methods for determining the strain at the onset of necking. On the other hand, during tensile, there were significant discrepancies. Certain of the thus-obtained curves demonstrated forms differing significantly from those

commonly observed. In order to choose the best suited method, the experimentally obtained MFLDs were compared to their numerically obtained counterparts.

2.3.3. Comparison between experimental and numerical results

Micro-stamping trials were performed on a system based on the principle of Marciniak-type tests [5]. The device consisted of a flat-bottomed 9-mm punch, a die and a round blank holder with an inside diameter of 10 mm. This equipment was coupled to a system for measuring strains based on digital image processing [8], [1]. Different geometries of aluminium 1050 A (99.5%) blanks with a thickness of 0.2 mm were cut with a die sinking EDM machine. At the same time, a sub-thickness of 0.1 mm, which replaced the use of a spacer, was machined in the central area of the blanks. The samples were then annealed at a temperature of 600 °C for 2 h. The micro-forming limit diagrams provided by the numerical simulation of the micro-stamping were compared to one obtained experimentally (Figure 13).

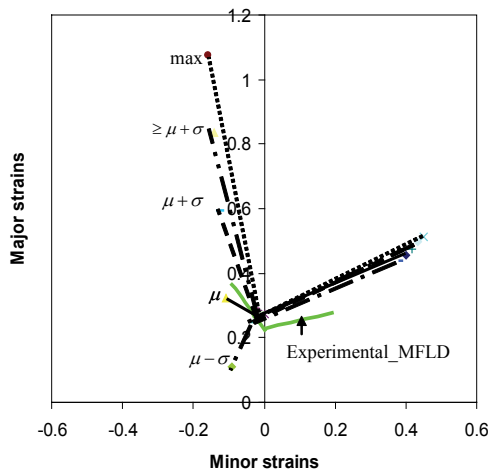


Fig. 13. Comparison of MFLD obtained with the «change of slope» criterion

The results from Figure 13 show that the points obtained during biaxial tensile and pull off were quite similar to the experimental results for all methods determining the necking. However, in tensile mode, the mean value method was the one that most resembled the experimental trials. Consequently, the mean value method was selected for determining the strains at the onset of necking. In order to avoid taking into account parameters such as the friction and boundary conditions that are difficult to manage, as well as to reduce the computation time and to obtain an MFLD as similar as possible to its experimental counterpart, the following paragraph presents a reduced numerical simulation not taking into account the full tool.

3. Development of a reduced numerical simulation

In order to obtain the three key points of a forming limit diagram, three types of forces were simulated: biaxial tensile, pull off and tensile.

3.1. Definition of a reduced simulation

For the reduced numerical simulation, only a square area of the central zone of the sample was simulated by using appropriate boundary conditions on one quarter of the blank (Figure 14a–c). The blank was meshed with 3D hexahedral elements of type C3D8R. The simulation was performed with the Abaqus finite element code with implicit double precision as there is no contact to manage and since the computation time is lower with this version. The same mechanical parameters as in the numerical simulation of the micro-stamping were used.

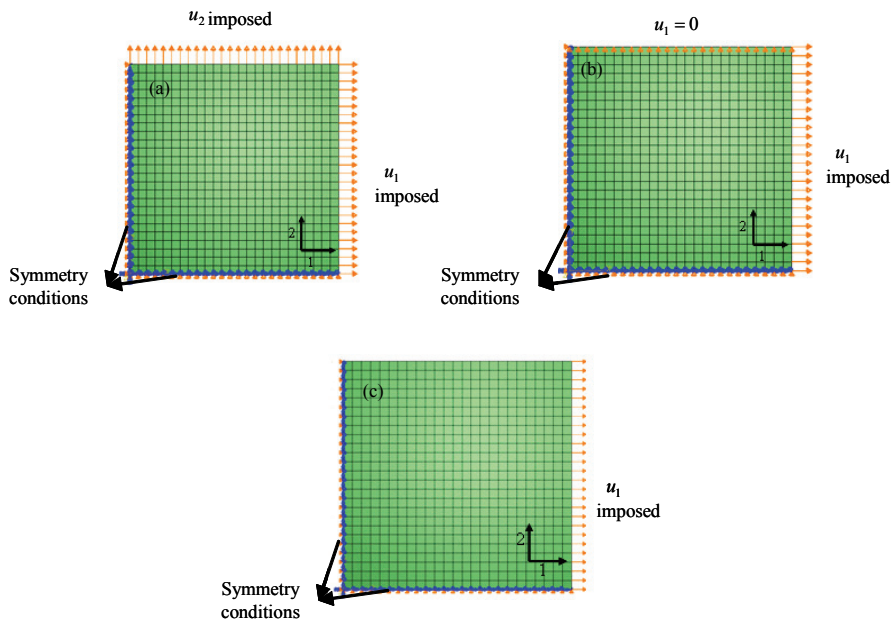


Fig. 14. Boundary conditions: a) biaxial tensile, b) plane strain tensile, c) tensile

Biaxial tensile, tensile and plane strain tensile stresses were simulated in order to quickly obtain the numerical micro-forming limit diagrams. Homogeneous strains were obtained during biaxial tensile and pull off without localization. In order to induce the localization, we then randomly introduced defects in the thickness with a certain percentage of reduced elements to the blank. For the distribution of the defects, the same algorithm was employed as the one for the distribution of elements in the central zone in the numerical micro-stamping simulation.

A reduced numerical simulation was carried out for the 3 solicitations, with a defect depth percentage equal to 7% and a percentage of the number of defects equal to 14%. This corresponded to the data used when performing the numerical simulation of the micro-deep drawing. The conditions were thus equivalent and it was possible to compare the resultant micro-forming limit diagrams.

3.2. Determination of the MFLDs with the reduced simulation

To determine the virtual micro-forming limit diagram, we applied the “change of slope” criterion coupled with the mean value method to biaxial tensile, pull off and tensile stresses. Figure 15 shows a comparison of the results obtained by the reduced simulation to those provided by the full tool simulation as well as to the experimental results.

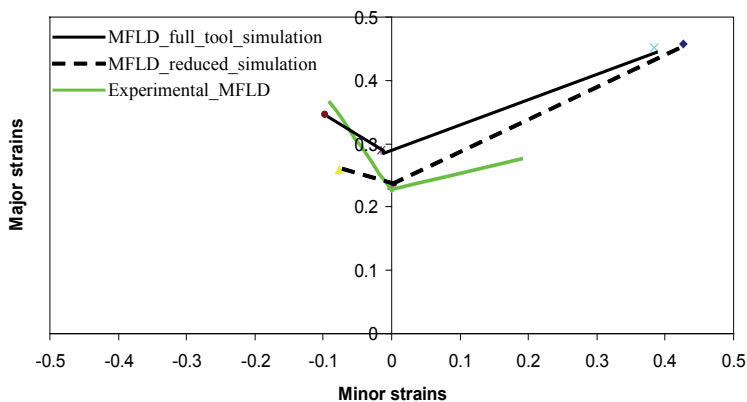


Fig. 15. Comparison of MFLDs obtained by reduced simulation, the full tool simulation and experimental results

When visualizing these diagrams, one can see that the micro-forming limit diagram obtained by the reduced simulation was close to the experimental results. Thus, the reduced numerical simulation provided better results as opposed to the full-tool simulation. The reduced simulation also rendered it possible to more rapidly obtain the forming limit diagrams as it used the implicit Abaqus version, simulating merely the central area (fewer elements) and thus decreasing the computation time. With this simulation method, one can also avoid taking into account the parameters of the simulation that are difficult to manage (friction and boundary conditions of the tool).

Besides, the influence of the defect depth, their amount and their random distribution was studied on the micro-forming limit diagrams. As expected, the level of the micro-forming limit diagram decreased when the defect depth and the number of defects increased. On the other hand, it has been checked that the choice of the random distribution of the defects had no influence on the micro-forming limit diagram.

However, they notice a small gap between virtual and real forming limit diagrams. This discrepancy may be related to various parameters of the numerical simulation, such as:

- the finite element method, i.e., the method of computation (explicit or implicit) and the choice of finite elements,
- the number of mesh elements in the thickness,
- the choice of the yield criterion (the Hill criterion is for instance not necessarily the most suitable – one might instead employ that of Barlat).

To improve the relevance of micro-forming limit diagrams, one would need to optimize the parameters of the numerical simulation.

4. Conclusions

This paper presents two types of numerical simulations by the finite element method: one with the full tool for micro-stamping and a blank with geometric imperfections in the central zone, and a second denoted “reduced simulation” where different strain paths were simulated with the introduction of geometric defects.

To obtain micro-forming limit diagrams with the full tool, a detection criterion of the onset of the localization was used: the “change of slope” criterion. Several methods for determining the strain at the onset of necking, based on the histograms representing the distribution of major and minor strains, were treated. The comparison of numerical micro-forming limit diagrams provided by the “change of slope” criterion coupled with methods for determining strains at the onset of necking with the micro-forming limit diagram from the experimental test showed that the “change of slope” criterion in association with the mean value method gave the best results. Therefore, this methodology was used to determine the micro-forming limit diagrams by reduced numerical simulation.

When comparing the results from the reduced numerical simulation to those of the full tool and to experimental data, the former demonstrated an improvement in tensile mode. Based on this work, the potential of reduced numerical simulation has been emphasized: this methodology provides significant time savings for obtained MFLDs that are close to reality. In addition, the reduced numerical simulation renders it possible to be even closer to the distribution of surface defects and simulate a surface corresponding to that of for instance a rolled sheet.

References

- [1] Balland P., Dumoulin S., Milkansen C., Arrieux R., Sergent A., Barathay S.: *Détermination des courbes limites de formage sur des matériaux nanostructurés*, 18^{ème} Congrès Français de Mécanique, Grenoble, France, 2007.
- [2] Brun R., Chambard A.: *Actual and virtual testing techniques for a numerical definition of materials*, Proc. NUMISHEET'99, Besançon, France, 1999.

- [3] Geiger M., Merklein M.: *Determination of forming limit Diagrams-a new analysis method for characterization of materials formability*, Annals of the CIRP 52, 2003, pp. 213–216.
- [4] Hibbit, Karlson, Sorensen: Abaqus Inc. (Ed.). Abaqus Theory Manual, Version 6.5, U.S.A, 2005.
- [5] Marciniak Z., Kuczynski K.: *Limit strain in the process of stretch forming sheet metal*, International Journal of Mechanical Science, Vol. 9, 1967, pp. 609–620.
- [6] Nakazima K., Kikuma T., Hazuka K.: *Study on the formability of steel sheets*, Yawata Tech. Rep., No. 284, 1971, pp. 678–680.
- [7] Petek A., Pepelnjak T., Kuzman K.: *An improved method for determining forming limit diagram in the digital environment*, Journal of Mechanical Engineering, Vol. 51, 2005, pp. 330–345.
- [8] Sène N. A., Balland P., Arrieux R.: *About necking detection to determine forming limit diagrams for mini stamping*, 17th International Scientific and Technical Conference Design and Technology of Drawpieces and Die Stampings, Poznan, September, 2008.
- [9] Volk W.: *New experimental and numerical approach in the evaluation of the FLD with the FE-method*, in: *Proceedings of the FLC-Zurich 06*, Zurich, Switzerland, 2006.

Numeryczne badania mikro-odkształcalności materiałów metalicznych; wirtualna krzywa odkształceń granicznych dla mikroformowania

W pracy przedstawiono wyznaczenie wirtualnej krzywej odkształceń granicznych dla mikroformowania blach aluminiowych 11050A (99,5%), na podstawie dwóch rodzajów numerycznych symulacji opartych o metodę elementów skończonych. Pierwszy to modelowanie, z geometrycznymi modelami narzędzi procesu mikro wytłaczania cienkiego półfabrykatu z geometryczną niejednorodnością wprowadzoną za pomocą zdefiniowanej chropowatości. Drugi, nazwany „uproszczoną symulacją”, w którym różne drogi odkształcania były symulowane za pomocą odpowiednich warunków brzegowych wprowadzając tego samego typu niejednorodność geometryczną. Dla wykrywania początku utraty stateczności został zaproponowany nowy test nazwany kryterium zmiany nachylenia. Dla wyznaczenia odkształceń początku utraty stateczności zastosowano różne metody oparte o reprezentację rozkładu odkształceń głównych za pomocą histogramów. Wyznaczona numerycznie krzywa odkształceń granicznych dla mikroformowania (MFLD) została porównana z krzywą doświadczalną.



Modelling of thermal phenomena in electric arc during surfacing

J. SŁOMA, I. SZCZYGIEŁ, A. SACHAJDAK

Institute of Thermal Technology, Silesian University of Technology, 44-100 Gliwice, Poland.

Despite very rapid development of science in the recent years, the issues occurring in the electric arc have not been fully recognized. The main reason for this situation is the complexity of phenomena which occur in the arc as well as very high temperatures. The paper presents results of numerical calculations of phenomena which occur in the welding arc. The CFD Fluent package was used for modelling the following phenomena in the electric arc: melting, solidifying, generation of heat and multiphase flows. The 3D Model of a 50×30×6 metal plate cutaway padded with the use of the GMA method with a wire of 1.2 mm diameter was developed. The paper focuses on presenting the distribution of temperatures in time, the process of melting and later solidifying of the material, as well as the transport of the material from the arc to the padding weld. It also shows the initial verification of the model by comparing the results with a picture recorded by 1000 frames/second fast camera.

Nomenclature

ρ – density

t – time

\vec{v} – velocity

α_q – volume fraction phase q

ρ_q – density phase q

\vec{v}_q – velocity vector phase q

\dot{m}_{pq} – mass transfer from phase p to phase q

\dot{m}_{qp} – mass transfer from phase q to phase p

p – pressure

\vec{g} – gravitational acceleration [m/s^2]

μ – dynamic viscosity

Q – volumetric energy source

E – energy

k – thermal conductivity

T – temperature

H_q – for each phase is based on the specific heat of that phase and the shared temperature

H – enthalpy

h – sensible enthalpy

h_{ref} – reference enthalpy

T_{ref} – reference temperature

C_p – specific heat at constant pressure

ΔH – latent heat,

T_{solidus} – solidus temperature

T_{liquidus} – liquidus temperature

β – liquid fraction

S – source term

A_{mush} – mushy zone constant

\bar{v}_p – solid velocity due to the pulling of solidified material out of the domain

1. Introduction

Surfacing is the process of renovation of worn machine parts. The surface of the part, which is damaged due to operation, is covered by a layer of new material. The material is provided to the surface in molten form. During surfacing, the base material is partially melted, so the added layer (deposit) is mixed with the base one. The participation of the base material in the deposit can be up to 60%, but high values of this participation are not desired.

There are a number of surfacing techniques: gas surfacing, arc surfacing, submerged arc surfacing, electroslag surfacing, GTA (gas tungsten arc), TIG (tungsten inert gas), GMA (gas metal arc), SSA (self shielded arc), PTA (plasma transferred arc), laser surfacing and the others [3–5]. In the paper, the GMA technology is considered.

In GMA method, the deposit is delivered to the base material in the inert gas shield. The melting of the wire is accomplished by the electric arc acting between two electrodes. One of them is the base material while the wire constitutes the second one. The wire is provided by the feeding system through the inert gas nozzle. The gas is used to separate melted material from the external environment [6]. The scheme of GMA surfacing is presented in Figure 1.

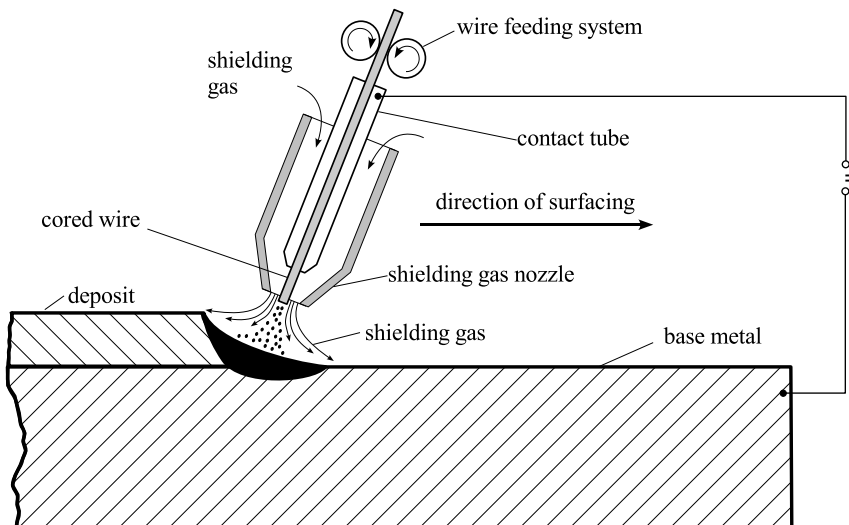


Fig. 1. Scheme of GMA surfacing

The surfacing head moves in a plane motion. The electrical arc which is created between the wire and the surfaced material causes the wire to melt, and electromagnetic forces accelerate the motion of metal drops towards the surfaced metal plate, where a moving liquid puddle of the surfacing weld is created. This puddle cools down and partially floods the surfaced metal plate. This is necessary for the surfacing weld to be bound with the surfaced metal plate efficiently and permanently. On the other hand, it is not desired from the perspective of the properties of the surfacing weld to mix the surfacing weld material with the surfaced metal plate excessively. The quality of the surfacing weld also depends on the speed of its crystallization – generally, the quicker crystallization occurs, the higher the quality of the surfacing weld is. These processes depend on the motion advance of the surfer head, the power of the arc and the capacity of retracting heat from the system. From the economic point of view, the motion of the head which requires increasing the power of the electrical arc should be as fast as possible. This, however, may lead to excessive flooding and heating of the surfaced metal plate, which in extreme cases may even lead to a total local flooding or plate damaging. As was mentioned, this depends on the heat transfer conditions of the system [2].

2. Governing equations [1]

In this case, the following set of equations were solved

- **Conservation of mass**

$$\frac{\partial \rho}{\partial t} + \nabla \cdot (\rho \vec{v}) = 0, \quad (1)$$

where:

- ρ – density,
- t – time,
- \vec{v} – velocity vector.

- **Volume fraction equation**

$$\frac{1}{\rho_q} \left[\frac{\partial}{\partial t} (\alpha_q \rho_q) + \nabla \cdot (\alpha_q \rho_q \vec{v}_q) = \sum_{p=1}^n (\dot{m}_{pq} - \dot{m}_{qp}) \right], \quad (2)$$

where:

- \dot{m}_{qp} – the mass transfer from phase q to phase p ,
- \dot{m}_{pq} – the mass transfer from phase p to phase q ,
- α_q – volume fraction phase q ,
- ρ_q – density phase q ,
- \vec{v}_q – velocity vector phase q ,

- **Material properties**

$$\rho = \alpha_q \rho_q + (1 - \alpha_q) \rho_p, \quad (3)$$

where:

- α_p – volume fraction phase q ,
- ρ_q – density phase q ,
- ρ_p – density phase p .

- **Momentum equation**

A single momentum equation is solved throughout the domain, and the resulting velocity field is shared among the phases. The momentum equation, shown below, is dependent on the volume fractions of all phases through the properties ρ and μ

$$\frac{\partial}{\partial t}(\rho \bar{v}) + \nabla(\rho \bar{v} \bar{v}) = \nabla p + \nabla[\mu(\nabla \bar{v} + \nabla \bar{v}^T)] + \rho \bar{g} + S, \quad (4)$$

where:

- p – pressure
- \bar{g} – gravitational acceleration [m/s^2]
- μ – dynamic viscosity

The enthalpy–porosity technique treats the mushy region (partially solidified region) as a porous medium. The porosity in each cell is set equal to the liquid fraction in that cell. In fully solidified regions, the porosity is equal to zero, which extinguishes the velocities in these regions. The momentum sinks due to the reduced porosity in the mushy zone takes the following form:

$$S = \frac{(1 - \beta)^2}{\beta^3 + \varepsilon} A_{mush}(\bar{v} - \bar{v}_p), \quad (5)$$

where:

- β – the liquid volume fraction,
- ε – a small number (0.001) to prevent division by zero,
- A_{mush} – the mushy zone constant,
- \bar{v}_p – the solid velocity due to the pulling of solidified material out of the domain.

- **Energy equation**

For solidification/melting problems, the energy equation is written as

$$\frac{\partial}{\partial t}(\rho H) + \nabla(\rho \bar{v} H) = \nabla(k \nabla T) + Q. \quad (6)$$

The VOF model treats enthalpy H , and temperature T , as mass-averaged variables:

$$H = \frac{\sum_{q=1}^n \alpha_q \rho_q H_q}{\sum_{q=1}^n \alpha_q \rho_q}, \quad (7)$$

where H_q for each phase is based on the specific heat of that phase and the shared temperature. The properties ρ and k (thermal conductivity) are shared by the phases. The sources term Q contains contributions from radiation solved using discrete ordinate method, as well as any other volumetric heat sources as energy of electric arc:

$$Q = Q^R + Q^{EA}, \quad (8)$$

where:

$$Q^{EA} = \frac{I^{EA} U^{EA}}{V^{EA}}, \quad (9)$$

I^{EA} – amperage electric arc,

U^{EA} – voltage electric arc,

V^{EA} – volume of electric arc.

The enthalpy of the material is computed as the sum of the sensible enthalpy h and the latent heat ΔH :

$$H = h + \Delta H, \quad (10)$$

where:

$$h = h_{\text{ref}} + \int_{T_{\text{ref}}}^T c_p dT, \quad (11)$$

h_{ref} – reference enthalpy,

T_{ref} – reference temperature,

C_p – specific heat at constant pressure.

The liquid fraction β can be defined as:

$$\beta = 0 \text{ if } T < T_{\text{solidus}}, \quad (12)$$

$$\beta = 1 \text{ if } T > T_{\text{liquidus}}, \quad (13)$$

$$\beta = \frac{T - T_{\text{solidus}}}{T_{\text{liquidus}} - T_{\text{solidus}}} \quad \text{if } T_{\text{solidus}} < T < T_{\text{liquidus}}. \quad (14)$$

The latent heat content can now be written in terms of the latent heat of the material, L

$$\Delta H = \beta L. \quad (15)$$

The latent heat content can vary between zero (for a solid) and L (for a liquid)

- **Turbulence**

In the case of turbulence quantities, a single set of transport equations is solved, and the turbulence variables (e.g., k and ϵ or the Reynolds stresses) are shared by the phases throughout the field.

3. Basic assumptions

The shown 3D case covered a fragment of 50 mm × 30 mm of steel sheet 6 mm thick with following features:

- density 7850 kg/m³,
- liquidus temperature 1520 °C,
- solidus temperature 1350 °C,
- specific heat 460 J/kg × K,
- melting heat 272 KJ/kg.

The diameter of the wire for surfacing was 1.2 mm as shown in the picture. Surfacing was conducted by the GMA method (electric arc in argon shield).

The scheme is shown in the Figure 2.

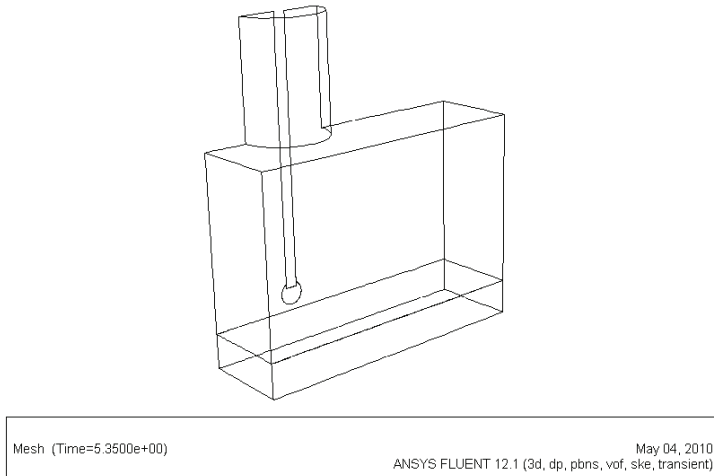


Fig. 2. Model's view in section

The area was divided into 2 million cells using a symmetric system in order to reduce the number of cells. The electrode moves parallel to the plate at the speed of 0.0026 m/s.

At the same time the process of melting is taking place together with the movement of the electrode wire at the speed of 0.02 m/s. Argon comes through the nozzles of shield gas at the volume flux of 12 litres/min. These values reflect the standard values of surfacing.

Additionally, the area of electric arc between the electrode and surfacing plate was sectioned. In this area some functions describing the emission of thermal energy from the electric arc were used. The rest of the area was limited by the boundary conditions of the type of pressure-outlet which should reflect the interaction of the welding area with the environment.

Boundary conditions were assumed as follows:

- velocity of inert gas at boundary 0.5 m/s, normal to inlet, uniform distribution, temperature equal to ambient 25 °C (Dirichlet boundary condition),
- velocity of electrode wire 0.02 m/s, assumed as velocity of liquid metal at the end of wire, normal to boundary, uniform distribution, temperature at 2000 °C (Dirichlet boundary condition),
- ambient temperature $t_{am} = 25$ °C and ambient gauge pressure $p_{am} = 0$ Pa assumed as pressure outlet boundary condition at the boundary of calculation region (Dirichlet boundary condition),
- the convective heat transfer coefficient 15 W/m²K and free stream temperature 25 °C were assumed at the bottom of welding plate (Robin boundary condition),
- the movement of the welding plate was assumed at 0.0026 m/s, it was simulated by moving reference frame method in CFD software.

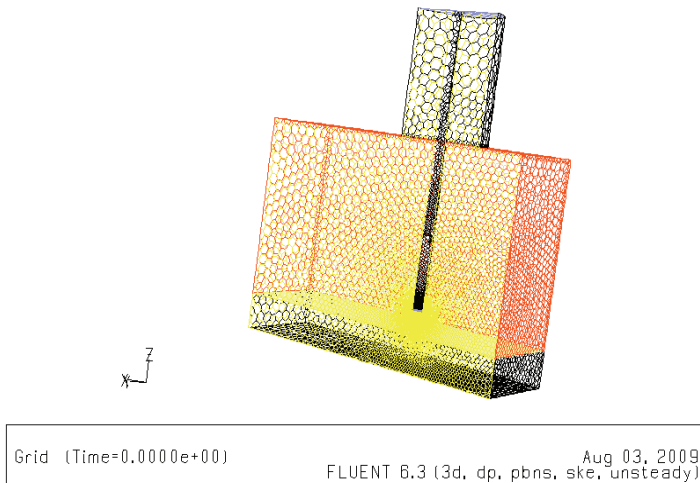


Fig. 3. Model mesh

A multifaced non-structural grid was used for calculations, as shown in the Figure above. Due to the fact that modelling the phenomena of melting and solidifying along with multiphase flows is still a complicated matter, within limits of commercial capacity of CFD packages, such as Fluent, the calculations were conducted in stages from the simplest phenomena to the most complex model, according to the following cases:

- only gas flows,
- gas flows and wire melts,
- gas flows, wire melts and heat generates in electric arc.

The heat generation was simulated in a sphere with a diameter of 2 mm.

For the solution to be stable, it was necessary to use a very short time step of 0.001 second.

4. Results of numerical calculations

The Figures below (4–6) show graphic results of calculations for quantities of flowing material and temperature, as well as the process of solidifying after 5 second.

5. Imaging by means of fast camera

Imaging of models by filming of a real process by means of a fast camera was conducted on S500MC metal sheet 6 mm thick.

Surfacing wire by ESAB OK.Autrod 13.91 diameter 1.2 was used for the research (solid wire).

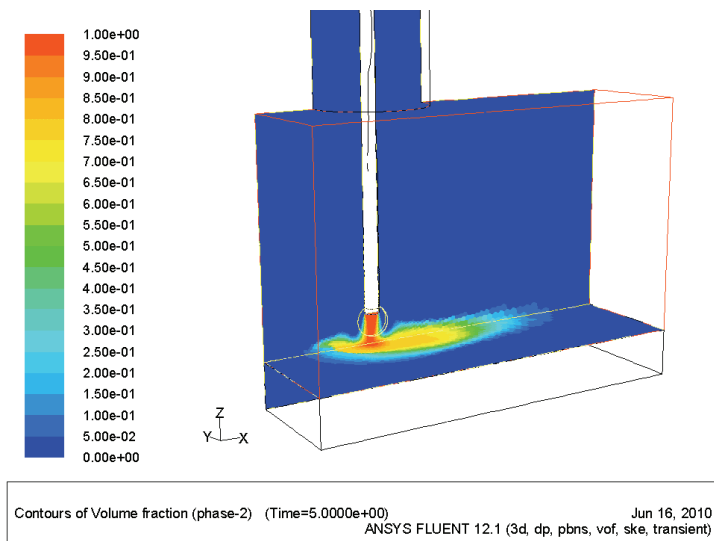
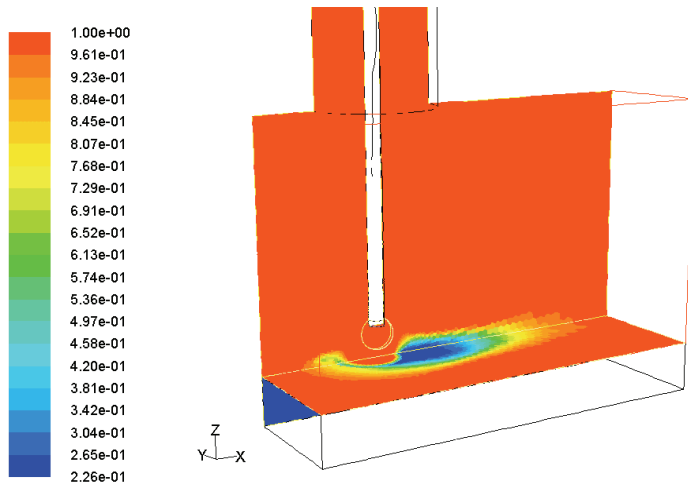
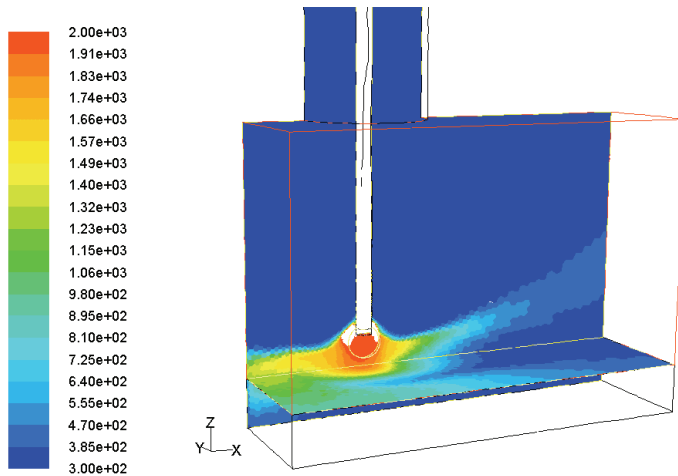


Fig. 4. Arrangement of material after 5 seconds



Contours of Liquid Fraction (mixture) (Time=5.0000e+00) Jun 16, 2010
ANSYS FLUENT 12.1 (3d, dp, pbns, vof, ske, transient)

Fig. 5. Solidifying process after 5 seconds



Contours of Static Temperature (mixture) (k) (Time=5.0000e+00) Jun 16, 2010
ANSYS FLUENT 12.1 (3d, dp, pbns, vof, ske, transient)

Fig. 6. Temperature schedule after 5 seconds

Two surfacing techniques were tested

- impulse,
- standard.

Surfacing parameters are shown in Table 1.

Table 1

	Welding machine's settings				Fast camera settings		
	Intensity [A]	Voltage [V]	Wire's feed [m/min]	Welding type [impulse/standard]	Remarks	fps	Shutter's time [s]
Case 1	230	26	6.8	standard	wire Autrod 13.91		1/20000
Case 2	230	26.3	8.4	impuls	wire Autrod 13.91		1/10000

The images in Table 2 show the process of the surfacing frame by frame.

Table 2. Sequence [solid wire Autrod 13.91] case 1 column A (standard) and case 2 column B (impulse)



The differences between the two kinds of the welding arc are easy to be perceived. In the short circuit arc, shown on the left we can see that the stream of the melted metal is continuous. Whereas in the case of the impulse arc, we can see the process of emerging of a globe, we can also see so called bridge and next we can see the burning of the arc.

6. The comparison of the results

The comparison of the images produced by means of fast camera and the numerical calculation results is shown in Figure 7. Some regularities can be discerned despite the obvious limitations of the imaging technique. Comparison with the analytical results shows that the shape of the welding pool and the face of the crystallising weld are depicted in proper way. We can also observe the flow of the molten metal extending from the electrode to the welding pool. The above observations can certify the rightness of the assumptions accepted in the model. On the basis of the analysis of the images of the surfaced area, we can draw a few conclusions that can be used to increase the effectiveness of the model in the future, such as those concerning the shape and boundaries of the electric arc, or those referring to the distance between the electrode and the surfaced material.

7. Conclusions

The numerical model of surfacing in the 3D geometry was presented. It is based on the partial models of melting and solidification, multiphase flow, heat transfer with radiation and energy occurring in electric arc.

Preliminary calculations showed that it is possible to model the presented phenomena by means of currently available equipment and software, however, only in very short time steps which significantly extend the period of the calculations.

The research with the use of a fast camera showed that it is a tool enabling the recording of the phenomena of substance flow in the electric arc.

Two technologies of welding were observed: continuous arc welding and impulse arc welding.

During the research the differences between those two methods could be observed. In the standard method it can be seen that the stream of the melted metal is unbroken (it flows). In the impulse method drops are formed and arc burning occurs. The camera is appropriate for filming those phenomena. It was possible to catch arc's area.

The following phenomena can be observed

- the arc,
- transport of mass,
- arc's area where energy is emitted.

It is a useful material for verification of numerical models.

The photos taken can be a basic for primary verification of numerical models.

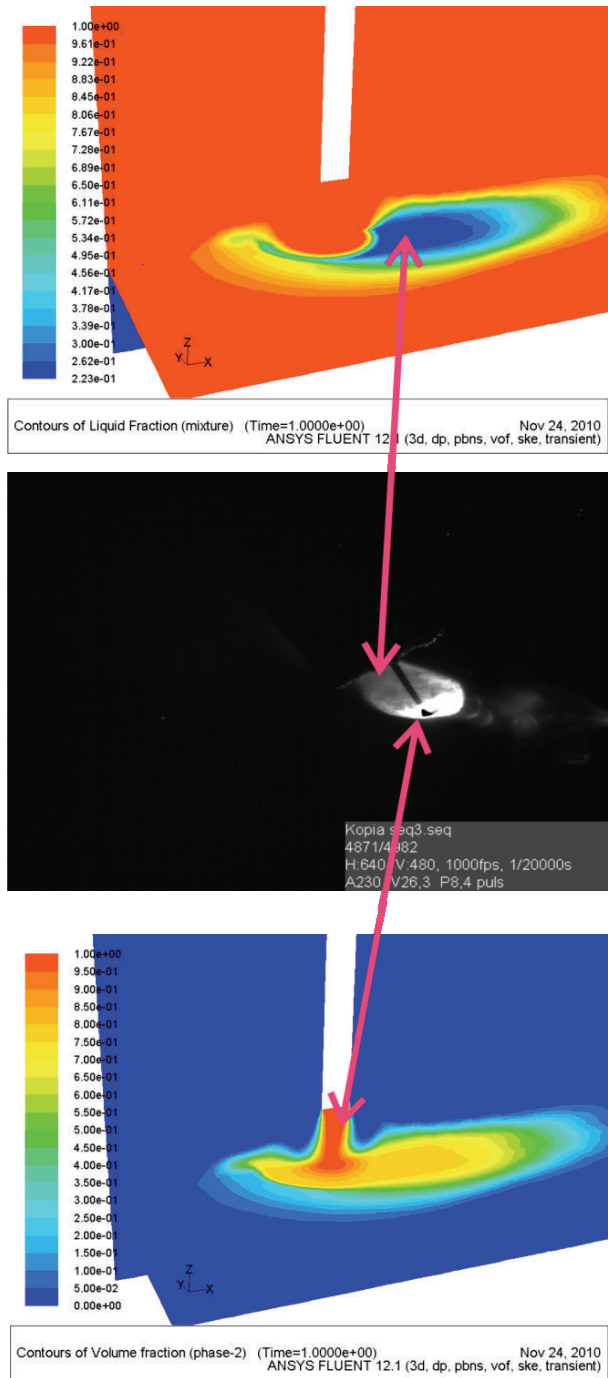


Fig. 7. The comparison of the image produced by means of a Fast camera with the numerical calculations

References

- [1] Ansys Fluent 12.0 Theory Guide.
- [2] Fic A, Szczygieł I., Sachajdak A.: *Analiza wrażliwości temperatury względem oporu kontaktowego w układzie do napawania powierzchni*, XIII Sympozjum Wymiany ciepła i masy, Darłówek, 2007.
- [3] Klimpel A. et al.: *Abrasion resistance of GMA metal cord wires surfaced deposits*, Journal of Materials Processing Technology, Vol. 164–165, 2005, pp. 1056–1061.
- [4] Klimpel A., Mazur M.: *Podręcznik spawalnictwa* (in Polish), Wyd. Pol. Sl., 2004.
- [5] Pilarczyk J. et al.: *Welding technology* (in Polish), WNT Warszawa, 2003.
- [6] Szczygieł I., Fic A., Sachajdak A.: *Inverse analysis of thermal phenomena during surfacing by welding*, Computer Methods in Mechanics, June 19–22, 2007, Łódź–Spała, Poland.

Modelowanie zjawisk cieplnych w łuku elektrycznym podczas napawania

Pomimo bardzo szybkiego rozwoju nauki w ostatnich latach zagadnienia zachodzące w łuku elektrycznym ciągle nie zostały rozpoznane do końca. Główną przyczyną takiego stanu rzeczy jest złożoność zjawisk występujących w łuku oraz bardzo wysokie temperatury. W artykule przedstawiono wyniki obliczeń numerycznych zjawisk występujących w łuku spawalniczym. W celu modelowania zjawisk w łuku elektrycznym: topnienia, krzepnięcia, generacji ciepła oraz przepływów wielofazowych użyto pakietu CFD Fluent. Opracowano model 3D wycinka blachy 50×30×6 napawanej metoda GMA drutem o średnicy 1,2 mm. Skupiono się głównie na zaprezentowaniu rozkładu temperatur w czasie, pokazano jak zachodzi proces topnienia a następnie krzepnięcia materiału oraz przedstawiono transport materiału z łuku do napoiny. Przeprowadzono również wstępną weryfikację modelu porównując wyniki z obrazem zarejestrowanym przez szybka kamerę 1000 klatek/s.

Rheological model of Cu based alloys accounting for the preheating prior to deformation

D. SZELIGA, M. PIETRZYK

Akademia Gorniczo-Hutnicza, Kraków, Poland.

R. KUZIAK, V. PIDVYSOTSKYY

Instytut Metalurgii Żelaza, Gliwice, Poland.

Development of the rheological model of copper based alloys, accounting for the state of the solid solution prior to deformation, is the objective of the paper. Two alloys are considered, Cu-1%Cr and Cu-0.7%Cr-1%Si-2%Ni. Plastometric tests were performed at various temperatures and various strain rates. Different preheating conditions before the tests were applied aimed at investigation of the effect of the initial microstructure on the flow stress. Three different rheological models for the investigated alloys were developed using inverse analysis of the tests results. Accuracy of the inverse analysis for various models was compared and the best model was selected. This model allowed comparison of the flow stress for various preheating schedules at different temperatures and strain rates, including also those which were not applied in the plastometric tests. Developed models were implemented into the finite element code FORGE based on the Norton-Hoff visco-plastic flow rule and simulations of forging of the alloys were performed.

Keywords: copper based alloys, plastometric tests, rheological model, identification, inverse analysis, finite element modelling

1. Introduction

Due to its high density and low strength, copper is not competitive to other constructional materials. There are, however, several applications of materials, in which other beyond strength properties are important, such as electrical and thermal or corrosion resistance. Elements of electric circuits or heat exchangers are examples of applications, in which copper is an excellent material. On the other hand, several thermal or electrical applications of metals require certain reasonably high level of strength, which cannot be reached by pure copper. This is the reason that some small quantities of other elements are added to copper to increase the strength, while high thermal and electrical properties are maintained. Properties of these alloys, accounting for precipitation hardening, are widely investigated [2, 5–6, 10]. Process of manufacturing of parts made of Cu based alloys has been also widely investigated by the Authors [14, 16, 18, 20–22]. These works were focused mainly on analysis of various manufacturing cycles in order to select the best technological parameters. The idea of simulation of manufacturing chain is presented in [18, 21]. Evaluation of various technological variants based on hot and cold forging is de-

scribed in [20]. Finally, microstructure evolution analysis and modelling for the investigated alloy is presented in [16]. The preheating schedule prior to deformation is one of the stages of the manufacturing cycle. In the case of copper alloys, this stage can be performed in few alternative ways and with different state of the batch material. Thus, the objective of the present work is determination of the rheological models for the Cu-based alloys, accounting for the preheating schedule and resulting microstructure prior to deformation. Application of these models to FE simulations of the manufacturing chains and predictions of the die wear recapitulate this work.

2. Experiment

Two copper based alloys were investigated, Cu-1%Cr and, for comparison, Cu-0.7%Cr-1%Si-2%Ni. Main properties and applications of these alloys are described in [14, 20]. The chemical composition of the alloys is given in Table 1.

Table 1. Chemical composition of the investigated alloys, wt.%

Alloy	Cu	Cr	Ni	Si	Fe	As	Bi
CuCr	balance	0.81	<0.001	<0.001	0.026	<0.001	<5 ppm
CuCrNiSi	balance	~0.7	~2	~1			

The material for experiments was cast in the form of cylinder (\varnothing 200 mm), hot extruded to the diameter of 60–70 mm followed by cooling in air. The average grain size (mean linear intercept) after cooling was 15.6 μm . All the tests were conducted on the Gleeble 3800 simulator at the Institute for Ferrous Metallurgy in Gliwice, Poland. The cylindrical samples measuring ϕ 10 \times 12 mm were compressed at temperatures in the range 500–1000 $^{\circ}\text{C}$ and strain rates 0.1–50 s^{-1} to the total strain of 1. Temperatures and load-displacement data were recorded.

Four preheating schedules before the tests, described in Table 3, were applied for the CuCr samples. It allowed investigation of the effect of the initial microstructure on the flow stress. Notation in Table 2: T_d – deformation temperature, T_w – preheating temperature, H_r – heating rate, t_w – time at the temperature T_w , C_r – cooling rate to the deformation temperature, t_p – time at the deformation temperature before the test. Alloy CuCrSiNi was tested for comparison only and it was subjected to the preheating schedule B.

Table 2. Preheating schedules for the tested CuCr samples

Schedule	T_w , $^{\circ}\text{C}$	H_r , $^{\circ}\text{C/s}$	t_w , s	C_r , $^{\circ}\text{C/s}$	t_p , s
A	T_d	3	120	–	–
B	950	3	300	5	60
C	T_d	3	30	–	–
D	1000	3	300	5	3

Samples A after extrusion were subject to super saturation annealing at 1000 $^{\circ}\text{C}$ for 1 hour. Remaining samples B, C and D were in the extruded state. Two schedules (A and C) comprise of heating directly to the deformation temperature and

holding at this temperature for the time t_p . In the remaining two cases, the samples are heated to the temperatures of 950 °C or 1000 °C, held at this temperature for time t_w and cooled to the test temperature. All samples were cooled with water to ambient temperature after the deformation and the microstructure was investigated. Time elapsing from the end of deformation to the start of water cooling was around 0.3 s. Measurements of the grain size are shown in Figure 1. For pictures of microstructures see publications [16, 20].

In the deformation temperature range 800–900 °C, the microstructure of the samples is partly recrystallised. Only recrystallised grains are considered in the quantitative analysis, which is summarised in Figure 1. Thus, smaller grains are observed for super saturated samples than for the extruded ones. The recrystallised volume fraction increases with increasing temperature, at which the deformation is conducted. For constant temperature, the grain size decreases slightly with increasing strain rate (schedules B, C, D). It is a characteristic feature of both dynamically and statically recrystallised microstructures. However, dynamic recrystallisation was detected when the samples were deformed at low rates. Influence of temperature and strain rate on grain size is small for lower temperatures 700–800 °C. For samples deformed at temperature 900 °C and strain rate 10 and 50 s⁻¹, the recrystallised volume fraction is close to one. Samples deformed at 1000 °C are fully recrystallised. It is assumed that deformation at high rates at 900 °C allows the static recrystallisation in the time elapsing from the end of deformation and start of water cooling. In these samples, grain size after saturation annealing was larger than after extrusion. It is expected that character of relationship between grain size and process parameters shown in Figure 1 is controlled by chromium that can be either in solid solution or in the form of large precipitates. Figure 1 shows that the deformation of the samples after saturation annealing develops finer grain size compared to as-extruded state.

Plastometric tests were also performed in the temperature range 20–200 °C to determine the rheological model for simulations of forging at room temperature, accounting for the deformation heating. Beyond this, the stress relaxation tests were performed to identify the microstructure evolution model. These results are presented in [16] and are not repeated here.

Temperatures and loads were monitored as a function of die displacement in all tests. Examples of measured temperatures are presented in Figure 2a, while measured loads are shown in Figure 2b. It is seen that temperatures vary during the tests. It is worth mentioning that the resistance heating is applied in Gleeble simulators to heat the samples prior to deformation. The heating is maintained during deformation tests at low strain rates and switched off during deformation at high rates. Due to high conductivity of copper alloys, it is extremely difficult to maintain constant temperature during deformation. Beyond this, due to the effect of friction strain and stress distributions in the sample are not uniform. Therefore, inverse analysis was applied to the interpretation of the results of the tests. Recorded temperatures and loads were used as input data for the inverse analysis.

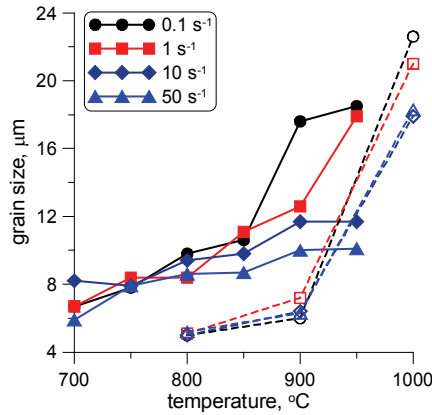


Fig. 1. Measured grain size after compression for samples from extruded material (filled symbols and solid lines – schedules B, C and D) and from the material after saturation annealing (open symbols and dashed lines – schedule A). Shape of symbols corresponds to the strain rate, see legend for reference

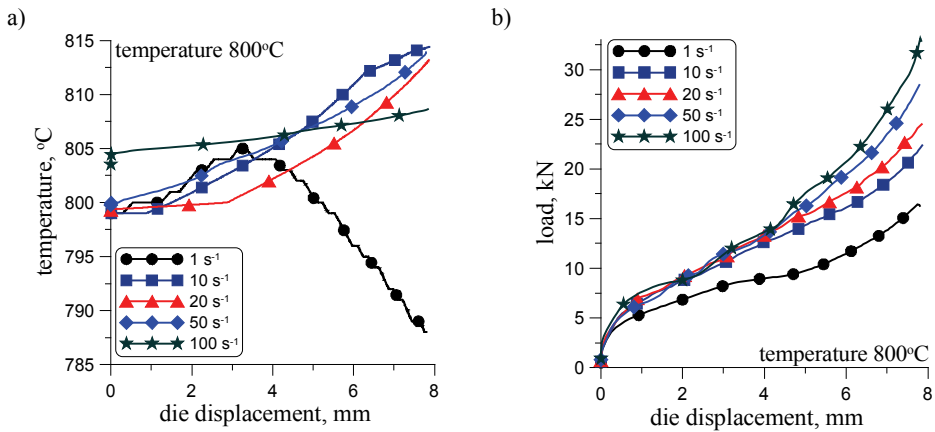


Fig. 2. Selected examples of temperatures a) and loads b) recorded during the tests, nominal temperature 800 °C, preheating schedule D

3. Rheological models

The plastometric tests were performed at various projects and the tests conditions are not identical for all the material states resulting from the preheating schedules. The objective of the present work is to compare the response of the CuCr alloys subject to various heat treatments prior to deformation. This comparison should be done for a wide range of temperatures and strain rates, including also those which were not applied in the plastometric tests. The comparison become possible only when the inverse analysis was performed for all the tests and mathematical formulae describing flow stress as function of temperature and strain rate were identified.

3.1. Inverse analysis

Results of plastometric tests were used to identify rheological models of alloys. Due to disturbances mentioned above (effect of friction, deformation heating etc.), the plastometric tests involve inhomogeneity of deformation and temperature. Thus, direct interpretation of results is difficult. It is shown [8–9, 22] that application of the inverse analysis to the interpretation of the tests minimizes the influence of these disturbances and allows to determine the flow stress independent of the method of testing. The inverse approach is applied in the present work to interpret the results of the axisymmetrical compression tests performed for the Cu based alloys. The inverse algorithm developed by the Authors [23] is used in the analysis. The flow stress model is identified by searching for the minimum of the objective function, which is defined as a square root error between measured and calculated loads:

$$\Phi = \sqrt{\frac{1}{Npt} \sum_{i=1}^{Npt} \left[\frac{1}{Nps} \sum_{j=1}^{Nps} \left(\frac{F_{cji}(\mathbf{x}, \mathbf{p}_i) - F_{mji}}{F_{mji}} \right)^2 \right]} \quad (1)$$

where:

- F_{mij}, F_{cij} – measured and calculated loads,
- Npt – number of tests,
- Nps – number of load measurements in one test,
- \mathbf{p} – vector of process parameters (strain rates, temperatures),
- \mathbf{x} – vector of coefficients in the flow stress model.

The direct problem model is based on the thermal-mechanical finite element program described in [19] and is defined as simulation of the axisymmetrical compression tests. The mechanical part of the FE code is based on the Levy-Misses flow rule and Huber-Misses yield criterion. This part is coupled with the FE solution of the Fourier heat transfer equation with relevant boundary conditions.

Inverse analysis of the tests results yielded the flow stress vs. strain relations independent of the influence of such disturbances as friction or deformation heating. Comparison of selected stress-strain curves obtained for different preheating conditions is shown in Figure 3. Since schedules B and C gave similar results, the latter case was not repeated for all investigated temperatures and strain rates. Letter E in Figure 3 refers to the CuCrNiSi alloy preheated according to the schedule B.

It is seen that super saturation annealing (state A) gives larger flow stress comparing to the three remaining preheating schedules. At low temperatures (800 °C) the flow stress of the CuCr in the state A is comparable with the CuCrNiSi in the state B. On the other hand, oscillations are observed for lower values of the Zener-Hollomon parameter B and C states. Flow stress for the CuCrNiSi alloy is larger than for the CuCr alloy.

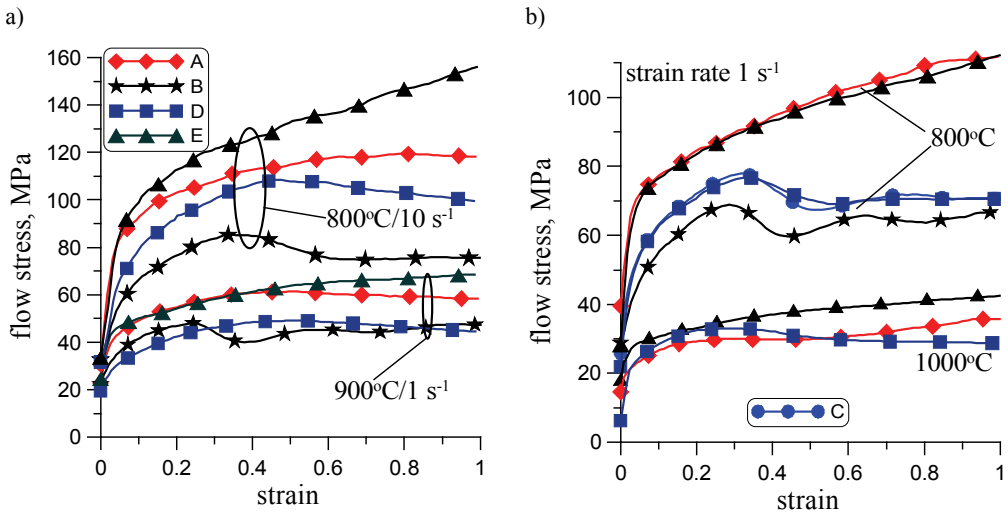


Fig. 3. Comparison of selected stress-strain curves obtained for different preheating conditions. Letter E refers to the CuCrNiSi alloy preheated according to the schedule B

At low strain rates the flow stress of the CuCrNiSi alloy in the extruded state (B) is comparable to that of the CuCr alloy in the super saturation annealing state (A). At higher strain rates the flow stress of the CuCrNiSi exceeds that of the CuCr alloy in all considered states.

3.2. Flow stress models

As it has been mentioned, the comparison between various preheating schedules has to be done for a wide range of temperatures and strain rates, including also those which were not applied in the plastometric tests. To achieve this objective, as well as to enable implementation of the models into the FE codes, the mathematical form of the flow stress relations has to be developed. On the basis of analysis of all the results the following flow stress equations are selected:

Hansel and Spittel Equation [12]

$$\sigma = A\varepsilon^n \exp(-q\varepsilon)\dot{\varepsilon}^m \exp(-\beta T). \quad (2)$$

Equation proposed in [7]

$$\sigma_p = \sqrt{3} \left[kqW\varepsilon^n + (1-W)k_{sat}q_{sat} \right] (\sqrt{3}\dot{\varepsilon})^m \quad (3)$$

$$W = \exp(-w\varepsilon), \quad q = \exp\left(\frac{Q}{RT}\right), \quad q_{sat} = \exp\left(\frac{Q_{sat}}{RT}\right).$$

Equation developed in the University of Sheffield [4], published also in [11]

$$\sigma_p = \sigma_0 + (\sigma_{ss(e)} - \sigma_0) \left[1 - \exp\left(-\frac{\varepsilon}{\varepsilon_r}\right) \right]^{\frac{1}{2}} - R, \quad (4)$$

where ε_c is critical strain for dynamic recrystallisation, and:

$$R = \begin{cases} 0 & \varepsilon \leq \varepsilon_c \\ (\sigma_{ss(e)} - \sigma_{ss}) \left[1 - \exp\left(-\left[\frac{\varepsilon - \varepsilon_c}{\varepsilon_{xr} - \varepsilon_c}\right]^2\right) \right] & \varepsilon > \varepsilon_c \end{cases},$$

$$\sigma_0 = \frac{1}{\alpha_0} \sinh^{-1} \left(\frac{Z}{A_0} \right)^{\frac{1}{n_0}},$$

$$\sigma_{ss} = \frac{1}{\alpha_{ss}} \sinh^{-1} \left(\frac{Z}{A_{ss}} \right)^{\frac{1}{n_{ss}}},$$

$$\sigma_{sse} = \frac{1}{\alpha_{sse}} \sinh^{-1} \left(\frac{Z}{A_{sse}} \right)^{\frac{1}{n_{sse}}},$$

$$Z = \dot{\varepsilon} \exp\left(\frac{Q_{def}}{RT_{def}}\right),$$

$$\varepsilon_r = \frac{1}{3.23} [q_1 + q_2 (\sigma_{ss(e)})^2],$$

$$\varepsilon_{xr} - \varepsilon_c = \frac{\varepsilon_{xs} - \varepsilon_c}{1.98},$$

$$\varepsilon_c = C_c \left(\frac{Z}{\sigma_{ss(e)}^2} \right)^{N_c},$$

$$\varepsilon_{xs} - \varepsilon_c = C_x \left(\frac{Z}{\sigma_{ss(e)}^2} \right)^{N_x}.$$

There are 16 coefficients in Equation (2): α_0 , α_{sse} , α_{ss} , n_0 , n_{sse} , n_{ss} , A_0 , A_{sse} , A_{ss} , q_1 , q_2 , C_c , N_c , C_x , N_x and activation energy Q_{def} . These coefficients were determined using inverse. Remaining parameters there are T – temperature in K, R – universal gas constant.

Table 2. Coefficients in Equation (2) obtained from the inverse analysis

Schedule	A	n	m	q	β	Φ
A	7640.6	0.2357	0.082	0.413	4.992	0.0914
B	1244.5	0.217	0.115	0.4862	3.1533	0.07552
C	123918	0.4142	0.0648	0.757	2.5023	0.16044
D	1889.5	0.2921	0.1498	0.4751	3.5716	0.0826
E	3927.6	0.2585	0.147	0.242	4.2576	0.0391

Table 3. Coefficients in Equation (3) obtained from the inverse analysis

Schedule	k	Q	n	m	k_{sat}	Q_{sat}	w	Φ
A	0.26893	5942.2	0.2255	0.0831	0.0379	7720.9	1.613	0.09518
B	1.7296	3613.2	0.2118	0.117	0.74115	4013.4	2.203	0.07149
C	39.001	759.4	0.333	0.0547	2.1787	3129.6	2.67	0.1353
D	1.2698	388.4	0.2704	0.15	0.01687	5763.1	1.868	0.8175
E	0.42625	4794.4	0.0657	0.1467	0.1768	6257.2	2.147	0.0397

Table 3. Coefficients in Equation (4) obtained from the inverse analysis

Schedule	α_0	α_{sse}	α_{ss}	n_0	n_{sse}	n_{ss}	A_0	A_{sse}
A	0.336×10^{22}	0.1558	2.318	0.924×10^{17}	0.6537	0.228	0.142×10^{14}	0.2666
B	0.2205×10^8	11.64	0.08767	0.393×10^{22}	6.0464	0.0173	0.236×10^{12}	5.0
C	0.947×10^9	898.77	0.06046	0.455×10^{13}	11.469	0.0112	0.255×10^{12}	4.9337
D	0.192×10^8	10.932	0.13218	0.175×10^{13}	4.5397	0.0174	0.291×10^{12}	4.3175
E	0.13×10^{10}	0.27114	1.3882	0.473×10^{14}	4.2865	0.0129	0.267×10^{10}	0.9553
A_{ss}	q_1	q_2	C_c	N_c	C_x	N_x	Q_{def}	Φ
1.3995	3.8985	0.115×10^{-10}	0.239×10^{-4}	0.195×10^{-3}	0.977×10^{-3}	0.152	556160	0.0865
0.031	0.48844	0.115×10^{-10}	0.00227	0.00537	0.0088	0.1986	287900	0.0625
0.03688	1.1532	0.115×10^{-10}	0.00132	0.05488	0.00358	0.1967	328530	0.0957
0.03038	0.69229	0.115×10^{-10}	0.256×10^{-2}	0.006	0.0088	0.2535	278840	0.0499
0.00469	1.1038	0.115×10^{-10}	0.57732	0.11785	0.716×10^{-3}	0.0632	305390	0.0386

Coefficients in the flow stress equations obtained from the inverse analysis of the plastometric tests for all the preheating schedules (A–D) and additionally for the alloy

CuCrSiNi (E) are given in Tables 2–4. The final value of the objective function (1) is given in this table, as well.

Although cold forming is not a subject of the present work, the flow stress model for cold forming is given below for completeness, see also [20]. Further tests were performed at the room temperature, accounting for the deformation heating. The following flow stress model was obtained for the temperatures 20–50 °C:

$$\sigma_p = A \exp(m_1 T) \varepsilon^{m_2} \dot{\varepsilon}^{m_3} \exp\left(\frac{m_4}{\varepsilon}\right). \tag{5}$$

The values of the coefficients in this model were determined using inverse analysis: $m_1 = -2.504 \times 10^{-3} \text{ K}^{-1}$, $m_2 = 0.362$, $m_3 = 0.098$, $m_4 = 1.3338 \times 10^{-4}$ and $A = 468 \text{ MPa} \times \text{S}^{m_3}$.

3.3. Comparison of models

Three equations describing flow stress are investigated in the present work. The coefficients in these equations obtained from the inverse analysis are given in Tables 2–4. The last column in these tables contains the final value of the objective function (1) at the end of the optimisation. This value is a measure of the accuracy of the inverse analysis. It should be pointed out, however, that this accuracy depends solely on the capability of the selected function to describe flow stress in a wide range of strains, strain rates and temperatures, accounting for a softening due to dynamic recrystallisation. The inverse algorithm does not distinguish between the equations and is equally efficient for all three identified models. Values of the objective function Φ for various models and for various states of the alloys are gathered in Figure 4.

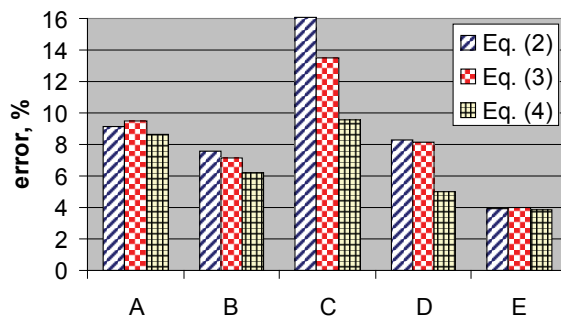


Fig. 4. Accuracy of the inverse solution (final value of function (1)) for various preheating schedules and for various equations

It is seen that in general the best accuracy is obtained for Equation (4), slightly lower accuracy is observed for Equation (3) and Equation (2) gives the largest values

of the function Φ . This is connected to the fact that dynamic recrystallisation model is included in Equation (4).

4. Effect of the preheating schedule on the flow stress.

Comparison of flow curves for various preheating schedules

Looking at the thermal treatment of alloys it can be concluded that alloy CuCrSiNi after preheating schedule B in Table 1 exhibit the most regular behaviour, which can be reasonably well described by all three models. This alloy does not recrystallise dynamically even at low Zener-Hollomon parameters. The largest error of the inverse analysis is obtained for the preheating schedule C. The effect of the dynamic recrystallisation is the strongest for this alloy. Considered functions have problems with reproducing the oscillations, which are observed in the material response. Functions (2) and (3) cannot even reproduce the inflection point, which is properly reproduced by Equation (4) only.

On the basis of the evaluation of the error of the inverse analysis, Equation (4) was selected for comparison of the flow stress of alloys after different preheating schedules. This equation gives the error below 10% for all investigated preheating schedules, even for the schedule C, which leads to strong influence of dynamic recrystallisation. Selected examples of the comparison of the flow stress calculated for various preheating schedules at various deformation conditions are shown in Figure 5. Results obtained for the CuCrNiSi alloy preheated according to the schedule B are also presented in this figure. The value of the Zener-Hollomon parameter is given for each plot.

Although only few selected representative plots are presented in Figure 5, the discussion presented below is based on analysis of all obtained results. Application of Equations (2–4) with optimised coefficients allowed comparison for all preheating schedules in the full range of the investigated temperatures and strain rates.

When silicon is added to the alloy, the hardening dominates over recovery and the flow stress is higher than for the remaining samples. This effect is particularly strong for high values of the Zener-Hollomon parameter Z . Behaviour of the CuCr alloy subject to preheating schedules B, C and D is similar, except the tendency to the oscillatory response. Effect of dynamic recrystallisation at low values of Z is observed for these three materials, however, only preheating schedule C results in strong oscillations. It is well seen in Figure 5c, where different stress scale is used.

The state of the solid solution influences the stacking-fault energy. During super saturation annealing Cr is introduced into the solution and causes an increase of the stacking-fault energy. In consequence a possibility of dynamic recrystallisation is limited and flow stress increases. This effect is observed in lower temperatures, see for example Figures 5a and b.

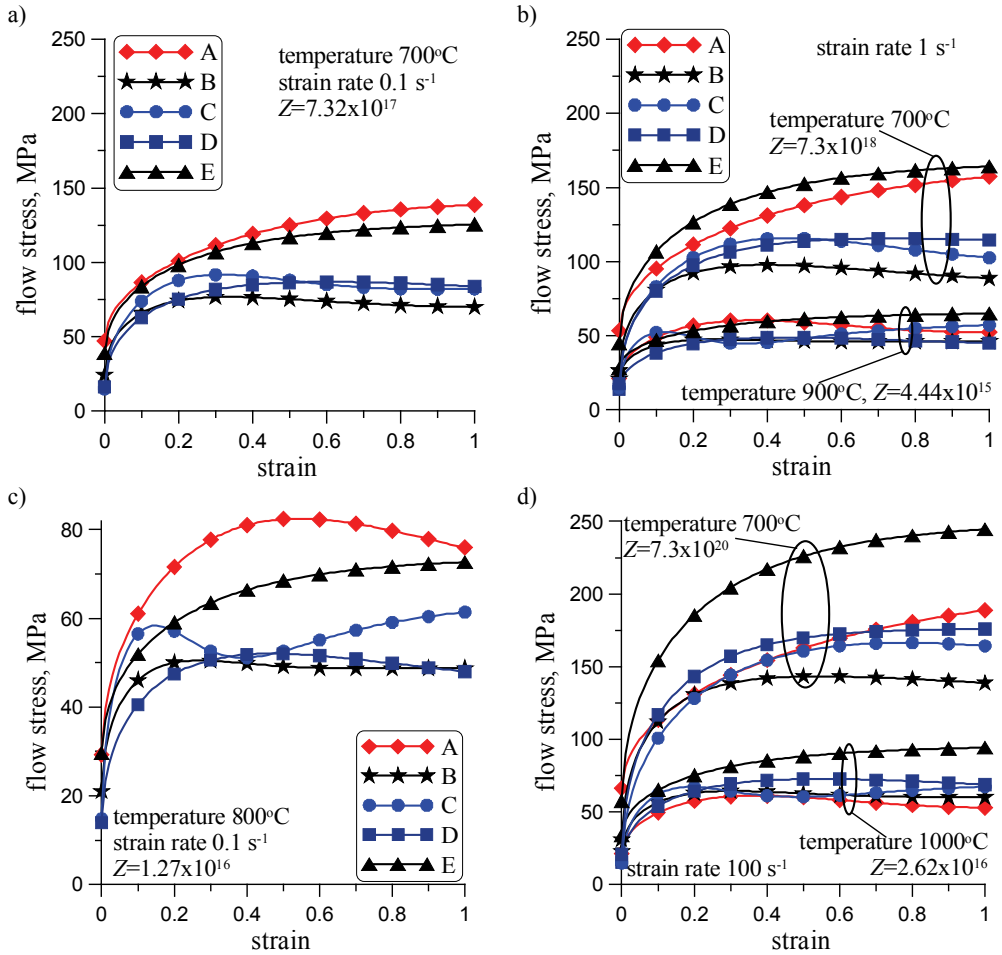


Fig. 5. Selected stress-strain curves obtained for different preheating conditions, calculated using Equation (4) with optimal coefficients

5. Simulations of forging

Analysis of the influence of the preheating schedule on the strains and stresses in the industrial forging process is the objective of this part of the work.

5.1. Finite element model

Finite element (FE) code Forge based on the Norton-Hoff visco-plastic flow rule [13, 17] is used in simulations. The constitutive law in Forge is [3]:

$$\boldsymbol{\sigma} = 2K\left(\sqrt{3}\dot{\boldsymbol{\varepsilon}}_i\right)^{m-1}\dot{\boldsymbol{\varepsilon}}, \quad (5)$$

where:

- $K(T, \varepsilon, \dot{\boldsymbol{\varepsilon}})$ – consistency, which is material parameter dependent on the flow stress,
- $\boldsymbol{\sigma}$ – Cauchy stress tensor,
- $\dot{\boldsymbol{\varepsilon}}$ – strain rate tensor.

The visco-plastic mechanical formulation is coupled with the finite element solution of the Fourier heat transfer equation with relevant boundary conditions. Forge software was selected due to its good remeshing, which is indispensable for simulations of the closed die forging. Microstructure evolution model is implemented to the Forge software, as shown in [15]. More details on the thermal-mechanical-microstructural FE modelling of the CuCr alloys can be found in [20] and the microstructural aspects are not addressed in the present work. The die wear model is considered in [20], as well. Simulations of forging of materials after different preheating schedules are shown below.

5.2. FE simulations of forging of CuCr alloys after different preheating schedules

3D forging presented in Figure 6 is considered. Two preheating schedules, A and B, were selected for the analysis. Remaining schedules yield the flow stress, which does not differ noticeably from B and are not considered. In all considered cases closed die forging is preceded by upsetting with the reduction of 15 mm. This upsetting allows obtaining proper filling of the die [20]. Cross section, at which the results are presented, is shown in Figure 7. Temperature distribution on the surface of the forging is shown in this figure, as well. Distribution of temperature at the investigated cross section for the preheating schedules A and B is shown in Figure 8. Temperatures are slightly lower for the schedule B. The temperature drop due to air cooling and the heat transfer to the dies is, in general, compensated by the temperature increase due to deformation heating. In the whole volume of the forging the temperature is above the initial 700 °C. The largest temperatures are observed in the area of the flange.

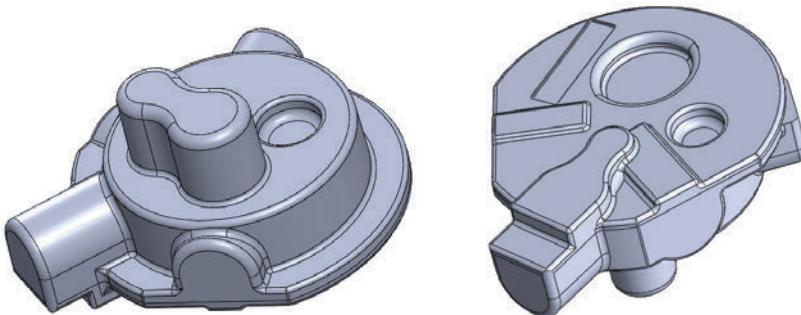


Fig. 6. 3D forging investigated in the present work

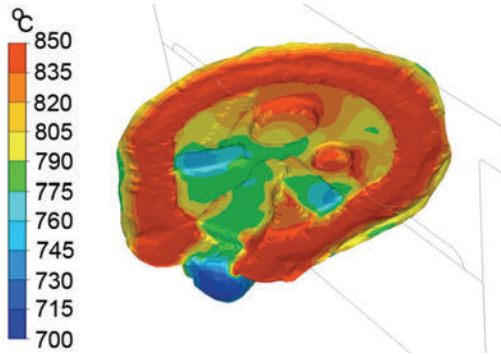


Fig. 7. Temperature distribution on the surface of the forging and cross section, at which remaining results are presented

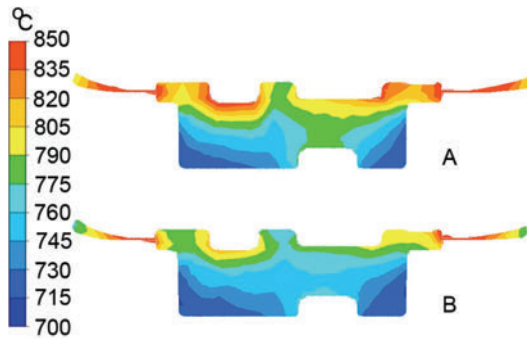


Fig. 8. Temperature distribution in the forging preheated according to the schedule A and B forged at 700 °C

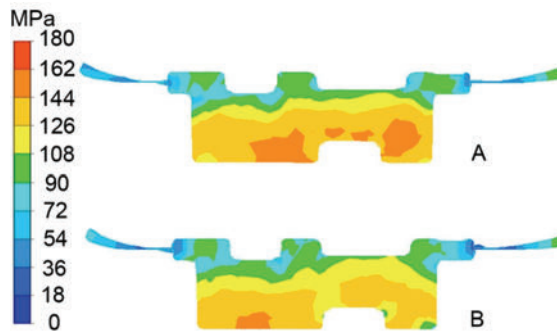


Fig. 9. Distribution of the effective stress in the forging preheated according to the schedule A and B forged at 700 °C

Calculated distribution of the effective stress at the considered cross section is shown in Figure 9. As expected, slightly larger stresses occur for the schedule A. Cal-

culated distribution of the effective strain at the considered cross section is shown in Figure 10. It is seen that the effect of preheating on the strain distribution is negligible.

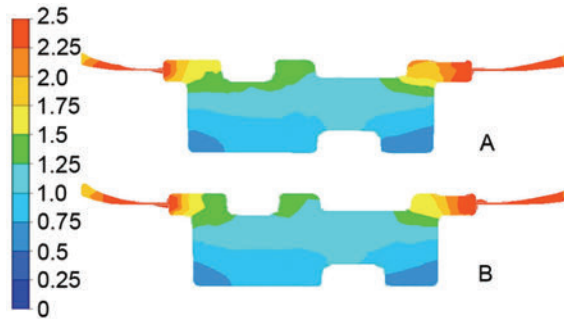


Fig. 10. Distribution of the effective strain in the forging preheated according to the schedule A and B forged at 700 °C

Analysis of results of simulations for forging presented in Figure 6 has shown that 15 mm upsetting allows obtaining proper shape of products for all preheating schedules. Preheating schedules influence temperatures and stresses during forging, both are slightly larger for the schedule A comparing to the remaining schedules. Strains are not sensitive to the preheating schedule.

5.3. Tool wear

An increased tool life is required for an economic production with high process reliability. Therefore, estimation of the tool life for different preheating prior to forging is investigated. Depending on the temperature of the process and the tool velocity, various mechanisms of the tool failure are possible, see [20] for more details for the CuCr alloys. The tool wear model based on the fundamental work of Archard [1] only is considered in the present work. The volume of the worn off material is proportional to the sliding distance:

$$V = \frac{C_s}{H} \int_0^t \mu p \Delta v dt, \quad (6)$$

where:

C_s – constant,

H – hardness of the tool material,

p – normal pressure,

μ – friction coefficient, which in the present work is 0.15 in the Coulomb model,

Δv – slip velocity between the die and the deformed material.

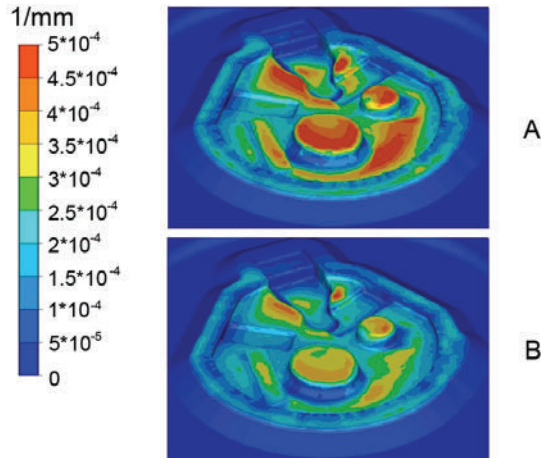


Fig. 11. Die wear for the preheating schedules A and B

This tool life model is implemented in the FE code and simulations were performed. Results of calculations of the tool wear due to sliding during hot forging of the part shown in Figure 6 made of CuCr alloy after two preheating schedules A and B are presented in Figure 11. It is seen that the largest die wear due to sliding during hot forging occurs in the area of convexities on the surface of the forging. Comparison of the different preheating schedules shows that die wear is noticeably larger for the schedule A. Thus, in general, application of the preheating schedule B or C should be advised.

6. Conclusions

The effect of the preheating prior to deformation on the behaviour of the CuCr alloy during deformation was investigated. CuCrNiSi alloy was additionally tested as a reference material. Rheological models were developed for four different preheating schedules. Comparison of material behaviour during deformation depending on the preheating schedule and process conditions was made and the following conclusions are drawn:

- Super saturation annealing before deformation gives higher flow stress of the CuCr alloys.
- The material at the extruded state has lower flow stress. The response of the material is oscillatory. Oscillations are larger for the samples preheated at the temperature of 950 °C or 1000 °C before deformation.
- The samples preheated before deformation at the temperature of 950 °C have the lowest flow stress.
- CuCrNiSi alloy involves larger resistance to deformation comparing to the CuCr alloys and is not advised for industrial applications.

Recapitulating, the preheating schedule B composed of preheating at 950 °C for 300 s, cooling to the test temperature with the rate of 5 °C/s, maintaining at this temperature for 5 s followed by deformation is suggested as the best for hot forging processes for the CuCr alloy. It gives low resistance to deformation while reasonably low oscillations of the response of the material are maintained.

Acknowledgements

Financial assistance of the MNiSzW, project R07 005 02, is acknowledged.

References

- [1] Archard J.F.: *Contact and rubbing of flat surfaces*, J. Appl. Phys., Vol. 24, 1953, pp. 981–988.
- [2] Blaz L., Korbel A., Bochniak W., Rdzawski Z.: *Dynamic precipitation in copper alloys*, Proc. 7th JIM Int. Symp., eds., Hosoi H., Yoshinaga H., Oikawa H., Maruyama K., Nagoya, 1993, pp. 286–294.
- [3] Chenot J.-L., Bellet M.: *The viscoplastic approach for the finite-element modelling of metal forming processes*, Numerical modelling of material deformation processes, eds. P. Hartley, I. Pillinger, C.E.N. Sturges, Springer-Verlag, London, Berlin, 1992, pp. 179–224.
- [4] Davenport S.B., Silk N.J., Sparks C.N., Sellars C.M.: *Development of constitutive equations for the modelling of hot rolling*, Materials Science and Technology, Vol. 16, 1999, pp. 1–8.
- [5] Dybiec H., Rdzawski Z., Richert M.: *Flow stress and structure of age-hardened Cu-0.4%Cr alloy after large deformation*, Materials Science and Engineering, Vol. A108, 1989, pp. 97–104.
- [6] Fernee H., Nairn J., Atrons A.: *Precipitation hardening of Cu-Fe-Cr alloys. Part I. Mechanical and electrical properties*, Journal of Materials Science, Vol. 36, 2001, pp. 2711–2719.
- [7] Gavrus A., Massoni E., Chenot J.-L.: *An inverse analysis using a finite element model for identification of rheological parameters*, Journal of Materials Processing Technology, Vol. 60, 1996, pp. 447–454.
- [8] Gavrus A., Massoni E., Chenot J.-L.: *Constitutive parameter identification using a computer aided rheology*, Proc. NUMIFORM '95, eds. S.-F. Shen, P.R. Dawson, A. Balkema, Ithaca, 1995, pp. 563–568.
- [9] Gelin J.C., Ghouati O.: *Inverse identification methods for material parameters estimation in large plastic deformations*, Proc. COMPLAS 4, eds. D.R.J. Owen, E. Onate, E. Hinton, Pineridge Press, Barcelona, 1995, pp. 767–778.
- [10] Groza J.: *Heat-resistant dispersion-strengthened copper alloys*, Journal of Materials Engineering and Performance, Vol. 1, 1992, pp. 113–121.
- [11] Hadasik E., Kuziak R., Kawalla R., Adamczyk M., Pietrzyk M.: *Rheological model for simulation of hot rolling of new generation steel strips for automotive industry*, Steel research international, Vol. 77, 2006, pp. 927–933.
- [12] Hansel A., Spittel T.: *Kraft- und Arbeitsbedarf Bildsamer Formgebungs-verfahren*, VEB Deutscher Verlag für Grundstoffindustrie, Leipzig, 1979.
- [13] Hoff N.J.: *Approximate analysis of structures in the presence of moderately large steps deformation*, Quart., Appl. Mech., Vol. 2, 1954, p. 49.

- [14] Kumar S., Singh T.P.: *A comparative study of the performance of different EDM electrode materials in two dielectric media*, IE(I) Journal-PR, Vol. 87, 2007, pp. 3–8.
- [15] Kuziak R., Pidvysots'kyy V., Drozdowski K.: *Validation of the thermo-mechanical-microstructural model of hot forging process*, Computer Methods in Materials Science, Vol. 9, 2009, pp. 424–434.
- [16] Kuziak R., Pidvysotskyy V., Pietrzyk M.: *Selection of the best thermomechanical processing parameters during manufacturing of forgings made of the CuCr alloys*, Computer Methods in Materials Science, Vol. 10, 2010, pp. 181–189.
- [17] Norton F.H.: *Creep of steel at high temperature*, McGraw Hill, New York, 1929.
- [18] Pidvysotskyy V., Kuziak R., Pietrzyk M.: *Modelling of production chain based on forming of copper-chromium alloy*, Steel Research Int., Vol. 79, No. 2, 2008, Spec. Edit. Metal Forming Conf., pp. 826–833.
- [19] Pietrzyk M.: *Journal of Materials Processing Technology*, Vol. 125–126, 2002, pp. 53–62.
- [20] Pietrzyk M., Kuziak R., Pidvysotskyy V., Nowak J., Węglarczyk S., Drozdowski K.: *Computer aided technology design for forging of CuCr alloys*, Metalurgia 2010, eds. K. Swiatkowski et al., Kraków, 2010, pp. 147–169.
- [21] Pietrzyk M., Madej Ł., Kuziak R.: *Optimal design of manufacturing chain based on forging for copper alloys, with product properties being the objective function*, Annals of the CIRP, Vol. 55, 2010, pp. 319–322.
- [22] Stobrawa J., Rdzawski Z., Gluchowski W., Malec W.: *Ultrafine grained strips of precipitation hardened copper alloys*, Archives of Metallurgy and Materials, Vol. 56, 2011, pp. 171–179.
- [23] Szeliga D., Gawąd J., Pietrzyk M.: *Inverse analysis for identification of rheological and friction models in metal forming*, Computer Methods in Applied Mechanical Engineering, Vol. 195, 2006, pp. 6778–6798.

Model reologiczny stopu miedzi uwzględniający schemat nagrzewania wstępnego przed odkształcaniem

Celem pracy było opracowanie modelu reologicznego dla stopów miedzi uwzględniającego stan początkowy materiału przed odkształcaniem. W ramach pracy dokonano analizy dwóch stopów: Cu-1%Cr i Cu-0.7%Cr-1%Si-2%Ni, dla których wykonano próby plastometryczne w szerokim zakresie temperatur i prędkości odkształcania. Wpływ początkowej mikrostruktury materiału na wartość naprężenia uplastyczniającego badano na podstawie różnych schematów nagrzewania zastosowanych przed odkształcaniem. Wybrano trzy równania opisujące naprężenie uplastyczniające dla stopów miedzi oraz przeprowadzono obliczenia metodą odwrotną dla identyfikacji parametrów tych równań. Ostatecznie wybrano model, dla którego zaobserwowano najmniejszy błąd pomiędzy danymi doświadczalnymi a obliczonymi na podstawie równania. Przyjęty model pozwolił na ocenę zachowania się materiału przy zastosowaniu różnych schematów nagrzewania i poddanym odkształcaniu w szerokim zakresie temperatur i prędkości odkształcania, uwzględniając również te warunki, które nie były stosowane w próbach plastometrycznych. Opracowany model został zaimplementowany w programie elementów skończonych FORGE i wykonano symulacje procesu.



Effect of Boron on the structure and mechanical properties of PM Fe-Si compacts after through vacuum carburising

K. WIDANKA

Wroclaw University of Technology, Institute of Materials Science and Applied Mechanics,
Materials Science Division, Wroclaw, Poland.

The work was aimed at determining the influence of boron on the structure and mechanical properties of sintered steels obtained by through vacuum carburising of Fe-Si compacts.

Vacuum carburising with immediate sintering of the compacts made of a mixture of iron ASC100.29, silicon and ferrobore powders was carried out at 1050 and 1150 °C in a laboratory vacuum furnace.

The structures of surface layer and core, as well as selected mechanical properties of the obtained sintered alloys were studied. It was found that the boron addition up to 0.015% improved the strength characteristic of the examined steels.

Keywords: *vacuum carburising, iron-silicon-boron compacts, microstructure, mechanical properties, sintered steels*

1. Introduction

Both boron and silicon are rarely added to PM steels as alloying elements.

Silicon has a relatively high solubility in Fe_{α} , decreasing with temperature from 18.5% for the temperature range within 1020 to 1200 °C down to 15% at ambient temperature. Maximum solubility of silicon in Fe_{γ} is ca. 2% [11].

Boron dissolves in ferrite and also in austenite in very low amounts. Maximum solubility of boron in Fe_{γ} is ca. 0.02% at the temperature range within 1100 to 1200 °C [9]. Boron is introduced to wrought structural steels mainly to improve their hardenability. In sintered steels, boron mostly plays another role: it intensifies the sintering process by creating a liquid phase at the sintering temperature as a result of the eutectic reaction (ferrite with iron boride Fe_2B). Thereby, it increases density of the sintered compacts and, as a consequence, improves their mechanical properties [4], [7], [10], [15].

Both silicon and boron decrease the solubility of carbon in austenite.

The vacuum carburising may be used for sintered materials due to better control of carburising depth in comparison with conventional gas carburising. This allows obtaining the required thickness of carburised layer in more predictable way. The method ensures faster carburising course, mainly thanks to higher temperature and lower hydrocarbon gas pressure during the process [5–6], [8], [13], [16].

The carburising depth depends on carbon diffusion rate into the material, which depends on process parameters and also on the carburised material.

Carbon diffusion rate in iron and iron alloys is decided by its diffusion coefficient, which for carburising processes carried out at high temperatures (above 1000 °C) is more than twice larger than for traditional gas carburising [3]. An addition of silicon in these alloys increases the carbon diffusion coefficient. Experimental data related to the effect of boron on carbon diffusion parameters in steels are limited due to very low solubility of boron both in ferrite and in austenite. All the available data [2], [12], [14] confirm that boron addition increases carbon activity in the Fe-C-B alloys. This allows assuming that an additive of boron increases the carbon diffusion coefficient like silicon.

In this paper, analysis of boron effect on structure and selected mechanical properties of through-carburised Fe-Si compacts is presented. Compacts with 1% of silicon, without and with boron addition from 0.005 to 0.015% were pressed to lowest density of 7.2 g/cm³ in order to minimise the interconnected porosity.

Carburising of the compacts carried out in a vacuum furnace was accompanied by the sintering process. This way, sintered steels were obtained, with variable carbon content on their cross-sections. Such obtained sinters were subjected to structural examination of the surface layer and core, hardness measurements and tensile test to determine their basic mechanical properties.

2. Material and experimental procedure

Standard flat specimens for mechanical testing with shape and dimensions: 5.85 × 6.05 mm (in gage section) according to ISO 2740 were prepared of a mixture of iron powder ASC100.29 (by Höganäs AB), ferrobore FeB16 powder and silicon powder Si AX0.5 (by H.C. Starck) with average particle size equal to 3.5 µm. Double-sided compacting under pressure within 750 to 800 MPa was applied to obtain compacts with the lowest density of 7.2 g/cm³. Four series of specimens, one without and three with boron additive (with its different content), were performed. Their chemical composition and green density, which was measured by means of Archimedes method, are given in Table 1.

Table 1. Chemical composition and density of compacts

Specimen	Chemical composition			"Green" density [g/cm ³]
	wt % Si	wt % B	wt % Fe	
Fe-Si-0.005B	1.0	0.005	remainder	7.27
Fe-Si-0.010B		0.010	remainder	7.25
Fe-Si-0.015B		0.015	remainder	7.25
Fe-1.0Si		–	remainder	7.24

The vacuum carburising process was carried out in a laboratory vacuum furnace (made by Seco/Warwick). Parameters of the process were based on the results of the own research, to obtain surface carbon content within the range 0.7% to 0.8%. The selected parameters are given in Table 2.

Table 2. Parameters of vacuum carburising

Carburising temperature [°C]	Carburising time [min.]	Diffusion temperature [°C]	Diffusion time [min]	Total carburising time [min]
1050	60	1150	120	180

The carburising atmosphere consisted of propane diluted with nitrogen. Working pressure in the furnace chamber was 2 kPa. Stable working pressure in the chamber during carburising was maintained by cyclic dosing the gas with constant flow rate of 110 dm³/h. Cooling rate in nitrogen was 7 °C/s. Diagram of the vacuum carburising process is shown in Figure 1.

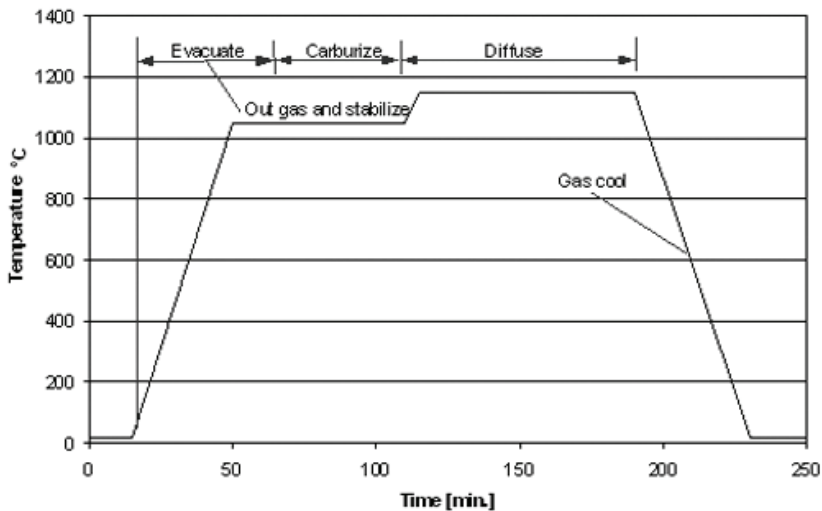


Fig. 1. Schematic diagram of vacuum carburising process

The specimens for structural examinations were taken from the specimens for mechanical tests after carburising, by cutting fragments of their measurement parts. Metallographic cross-sections were made on transverse cross-sections of the specimens.

Microscopic examination of the specimens was performed using a light microscope Neophot 32 (by Zeiss) at magnification within 100 to 500 times.

Quantitative parameters of the microstructure were evaluated using a computerised image-analysis system "Multiscan" made by the Polish company Computer Scanning Systems. For each specimen the minimum of five (5) images of microstructure were analysed.

Hardness measurements were taken using a hardness tester Zwick by the Vickers method at the load within 9.81 to 49.05 N.

Tensile tests of three specimens for the each silicon content were performed on a hydraulic pulsator MTS 810.

3. Results and discussion

In unetched condition, porosity degree of the carburised samples was determined by microscopic method using a computerised image analyser. For each sample the minimum of ten (10) images of pores from whole cross-section were analysed. The porosity level observed in core and surface layer was similar. The obtained results and evaluated on their grounds densities of the specimens are presented in Table 3. Figure 2 shows a representative view of pores in the specimen Fe-Si-0.010 B (0.01% B).

Table 3. Porosity and density of specimens

Specimen	Porosity [%]	Density [g/cm ³]
Fe-Si-0.005B	7.0	7.32
Fe-Si-0.010B	7.1	7.31
Fe-Si-0.015B	7.2	7.30
Fe-1.0Si	7.0	7.32

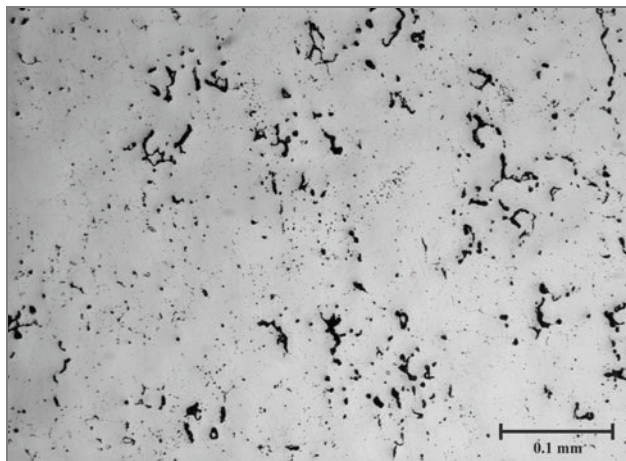


Fig. 2. Representative picture of pores in the specimen Fe-Si-0.010B (with 0.01% B)

Hardness was measured in two zones: in surface layer and in core. To determine the hardness profile, measurements were also taken on the cross-section along the centre line from the surface to the core every 0.25 mm.

The obtained hardness measurements permitted determining thickness of the carburised layers. It was assumed that carburisation depth corresponds to mean hardness (HV5) calculated as arithmetic average of the values for surface layer and core. The so calculated carburisation depth values for all the specimens are presented in Table 4. The average thickness of carburised layer of ca. 2.4 mm is comparable for all the examined specimens with boron. A slightly larger value (by ca. 0.2 mm) was found for the specimens Fe-Si-0.010B (0.01%B). In comparison to the specimens Fe-Si (without boron) this carburisation depth (2.6 mm) is larger about 18%.

Hardness values for surface layers and cores of the specimens are given in Table 4 and representative hardness profile for the specimen Fe-Si-0.005 (0.005%B) is shown in Figure 3. The measured average values for the surface layer are within 184 to 195 HV5 and the values for the core are within 109 to 138 HV5. Larger differences between individual specimens occur in the core than on the surface. The course of hardness profiles is characterised by wide and round transition from the surface layer to the core, which evidences smooth drop of carbon content in the carburised layer.

Table 4. Hardness and thickness of carburised layer of the specimens

Specimen	Hardness		Thickness of carburised layer [mm]
	of carburised layer HV5	of core HV5	
Fe-Si-0.005B	190 ± 4	125 ± 1	2.4 ± 0.1
Fe-Si-0.010B	195 ± 3	138 ± 2	2.6 ± 0.1
Fe-Si-0.015B	191 ± 3	130 ± 1	2.5 ± 0.1
Fe-1.0Si	184 ± 4	109 ± 2	2.2 ± 0.1

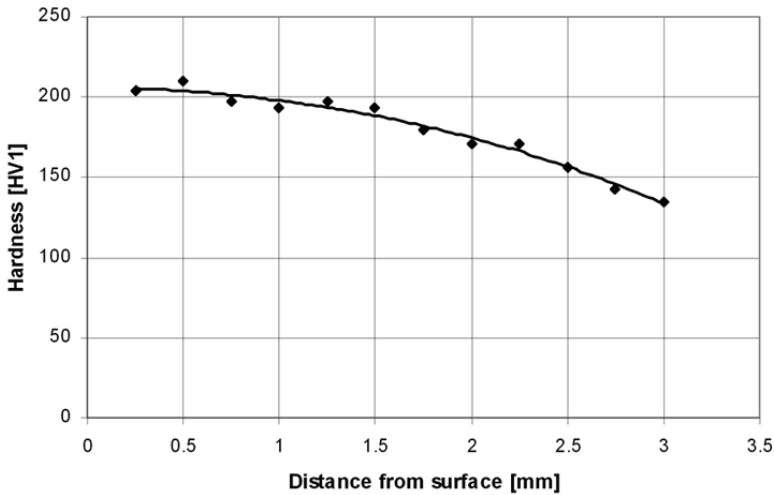


Fig. 3. Representative hardness profile for specimen Fe-Si-0.005B

After etching with 3% nital, material microstructure of the specimens was revealed. Representative microstructures of carburised layers and cores of the specimens Fe-Si-0.005B and Fe-1.0Si are shown sequentially in Figures 4–7. Microstructure of surface layer of the examined Fe-Si-B specimens consists of pearlite and a small amount of precipitates, probably of boro-cementite $\text{Fe}_3(\text{C}, \text{B})$, iron boride Fe_2B and carboborides $\text{Fe}_{23}(\text{C}, \text{B})_6$ [1]. The carboborides, unlike borocementite and iron boride which were formed in the layer structure during heating at the carburizing temperature, could produce during cooling the specimens from the carburizing temperature only. The observed content of borocementite and iron boride in the carburized layer increases with increasing boron content.

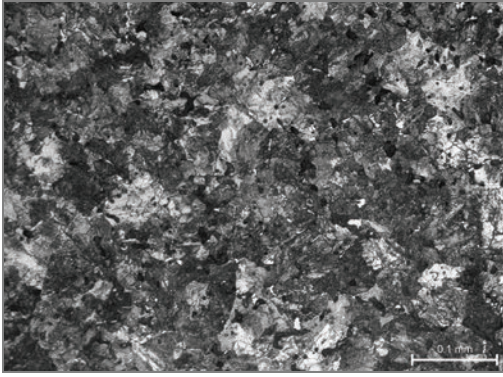


Fig. 4. Carburised layer microstructure of the specimen Fe-Si-0.010B (0.01%B)

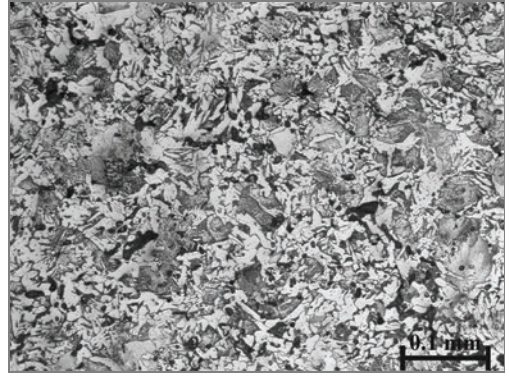


Fig. 5. Core microstructure of the specimen Fe-Si-0.010B (0.01%B)

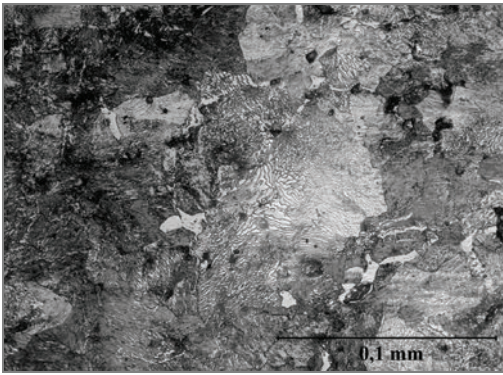


Fig. 6. Carburised layer microstructure of the specimen Fe-1.0Si (1.0% Si)

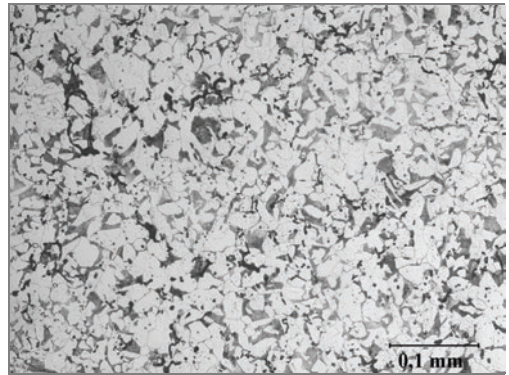


Fig. 7. Core microstructure of the specimen Fe-1.0Si (1.0% Si)

In the microstructure of surface layer of the Fe-1.0Si specimens a pearlite with small amount of cementite Fe_3C in form of isolated particles, placed on the grains boundaries of prior austenite, was observed.

Microstructure of transition zone in all the specimens consists of pearlite and ferrite that fraction increases with increasing distance from the surface layer.

Core microstructure of all the specimens consist mainly of ferrite with pearlite that fraction changes depending on boron content from the highest 45% for the specimen Fe-Si-0.010B to the smallest 22% for the specimen Fe-Si-0.005B.

Fractions of pearlite and the calculated on their grounds carbon concentrations in the core structure are presented in Table 5. The carbon concentrations were calculated accepting 0.77% C in the eutectoidal point and omitting silicon effect that shifts it to the left, towards lower carbon concentration. With this effect considered, the calculated carbon concentrations would be slightly lower.

Table 5. Estimated fractions of pearlite and corresponding carbon contents in cores of the specimens

Specimen	Pearlite fraction [%]	Carbon content [wt %]
Fe-Si-0.005B	22	0.17
Fe-Si-0.010B	45	0.36
Fe-Si-0.015B	33	0.25
Fe-1.0Si	20	0.15

Size of pearlite and ferrite grains in the surface layer and core is similar in all the examined specimens. The grains in the layer are larger than those in the core. The pearlite grain size evaluated by comparative method corresponds to the reference standard No. 7 according to ASTM and the ferrite grain size to the standard No. 9.

Basic mechanical properties of the specimens after vacuum carburising were determined in a static tensile test. The results are presented in Table 6.

Table 6. Results of tensile test of the examined specimens (*Average value for three tests (three specimens))

Specimen	UTS* [MPa]	YS* [MPa]	Elongation* [%]
Fe-Si-0.005B	634 ± 6	396 ± 2	3.2 ± 0.2
Fe-Si-0.010B	712 ± 5	431 ± 2	3.6 ± 0.1
Fe-Si-0.015B	665 ± 6	401 ± 3	3.4 ± 0.1
Fe-1.0Si	620 ± 5	380 ± 2	3.7 ± 0.1

The highest ultimate tensile strength and yield stress was obtained for the specimens Fe-Si-0.010B and the lowest for the specimens Fe-1.0Si. The elongation is similar in all specimens.

The higher tensile strength of the specimens with boron, in comparison to the specimens without it, is a direct consequence of the larger pearlite fraction in the core structure (Table 5). In turn, larger pearlite fraction in the core results from deeper diffusion of carbon into the material (larger carburising depth – Table 4). Thus, by the same pearlitic microstructure of surface layer, the strength of the examined specimens depends mainly on their core strength and exactly on its microstructure. Beneficial to core strength in this case, besides pearlite fraction, is also the presence of silicon and its well-know effect on solid solution strengthening of ferrite. According to the database CASIP 5.1 (by Höganäs) the hardness of sintered steels with carbon content within the range 0.2% to 0.4%, produced by the traditional method (of mixtures of iron and graphite powders) based on the ASC100.29 powder of similar density, corresponds to values ranging from 105 to 118 HV, respectively.

Silicon addition in amount of 1% to iron compacts was aimed at accelerating the carbon diffusion process and also improving the core strength of the sintered steels obtained by through vacuum carburising.

4. Conclusions

The vacuum carburising method used to iron compacts allows combining the carburising and sintering operations in one process. By proper selection of process pa-

rameters, carbon was introduced to the whole volume of the Fe-Si and Fe-Si-B compacts.

The advantageous effect of high temperature of process on increasing the carbon diffusion coefficient resulted in accelerated diffusion of carbon deep into the material, and in carburising the compacts through in a relatively short time. This permitted obtaining specimens of sintered steels with variable carbon content on their cross-section and thus with variable structure.

Boron addition to Fe-Si compacts intensifies carbon flow from the carburised layer to the core. In this way the sintered steels with 1% of silicon and micro-additive of boron obtained by the vacuum carburising method reach the better strength characteristic due to deeper carburising.

The addition of 0.01% boron provides an optimum set of properties for the examined sintered steels.

References

- [1] Brewer L., Chang S.G.: *Metallography, structures and phase diagrams*, Metals Handbook, 8th Edition, ASM International, Vol. 8, 1973.
- [2] Eckstein H.J.: *Technologie der Wärmebehandlung von Stahl*, Leipzig, 1976, pp. 60–67.
- [3] Gary G. Tibbetts: *Diffusivity of carbon in iron and steels at high temperatures*, Journal of Applied Physics, Vol. 51, No. 9, 1980, pp. 4813–4816.
- [4] German R.M., Rabin B.H.: *Enhanced sintering through second phase additions*, Powder Metallurgy, Vol. 28, No. 1, 1985, pp. 7–12.
- [5] Herring D.H., Hansen P.T.: *Heat treating ferrous P/M parts*, Advanced Materials & Processes, Vol. 153, No. 4, 1998, pp. 44CC–44GG.
- [6] Herring D.H.: *Pros and cons of atmosphere and vacuum carburizing*, Industrial Heating Magazine, January, 2002, pp. 45–48.
- [7] Karwan-Baczewska J., Rosso M.: *Effect of boron on microstructure and mechanical properties of PM sintered and nitrided steels*, Powder Metallurgy, Vol. 44, No. 3, 2001, pp. 221–227.
- [8] Kula P., Pietrasik R., Dybowski K.: *Vacuum carburizing-process optimisation*, Journal of Materials Processing Technology, Vol. 164–165, 1995, pp. 876–881.
- [9] Kunst H., Schaaber O.: *Remarks of boriding of steel*, HTM Härtereitechn. Mitt., Vol. 22, No. 1, 1967, pp. 1–25.
- [10] Madan D.S., German R.M., James W.B.: *Iron–boron enhanced sintering*, Progress in Powder Metallurgy, Vol. 42, No. 1, 1986, pp. 267–283.
- [11] Massalski T.B., Okamoto H.: *Binary alloy phase diagrams*, 2nd Edition, Materials Park, Ohio, ASM International, 1990.
- [12] Neumann F., Schenck H.: *Die durch Zusatzelemente bewirkte Aktivitätsänderungen von Kohlenstoff in flüssigen Eisenlösungen nahe der Kohlenstoffsättigung*, Arch. für Eisenhütten, Vol. 30, 1959, pp. 477.
- [13] Preisser F., Seemann R., Zenker W.R.: *Update on vacuum-based carburizing*, Advanced Materials & Processes, Vol. 153, No. 6, 1998, pp. 84II–84LL.

- [14] Schenck H.: *Chemische Aktivitäten vom Bohr und Stickstoff in flüssigen Bereich des Systems Eisen-Bohr-Stickstoff bei 1600 C*, Arch. für Eisenhütten, Vol. 39, 1968, pp. 255.
- [15] Selecka M., Salak A., Danninger H.: *The effect of boron liquid phase sintering on properties of Ni-, Mo- and Cr-alloyed structural steels*, Journal of Materials Processing Technology, Vol. 143–144, 2003, pp. 910–915.
- [16] Weber R.G.: *Vacuum carburizing and carbonitriding of P/M ferrous alloys*, International Journal of Powder Metallurgy, Vol. 15, No. 2, 1983, pp. 383–391.

Wpływ boru na strukturę i własności mechaniczne wyprasek Fe-Si nawęglanych próżniowo na wskroś

Celem pracy było określenie wpływu boru na strukturę i wybrane własności mechaniczne wyprasek żelaznych z 1% dodatkiem krzemu poddanych nawęglaniu próżniowemu na wskroś.

Proces nawęglania połączony z jednoczesnym spiekaniem wyprasek wykonanych z proszków żelaza ASC100.29, krzemu i żelazoboru przeprowadzono w laboratoryjnym piecu próżniowym, w temperaturach 1050 °C i 1150 °C.

Badano i analizowano strukturę warstwy wierzchniej i rdzenia stali spiekanych o zmiennej na przekroju zawartości węgla, otrzymanych w wyniku zastosowanej metody. Wykazano, że mikrododatek boru w ilości do 0.015% poprawia charakterystykę wytrzymałościową badanych stali spiekanych z krzemem.



The idea of the model of evaluation of logistics warehouse systems with taking their energy consumption under consideration

P. ZAJĄC

Wrocław University of Technology, Wybrzeże Wyspiańskiego 25, 50-370 Wrocław, Poland.

Increasingly, the energy consumption is the factor, which has to be taken into consideration at the evaluation of logistics systems. Meanwhile, it is hard to find the intelligible and universal way of counting the energy consumption in the literature or in valid norms. This paper is the presentation of the conception of counting the energy consumption. It was made on the basis of a driving characteristic, with the use of potential energy formula and also with the mathematical dependence which was formulated by the author. This dependence concerns the kinetic energy. Here is being also discussed the mathematical model, which allows us to count the energy consumption of the logistics warehouse system. In addition, here is also demonstrated the way of determining the index number of the energy consumption of this system. Moreover, in this paper are also presented exemplary calculations, final conclusions and courses of action of successive research works.

Keywords: *logistics, energy, transport*

1. Preface

Nowadays, many requirements which were established to the logistics warehouse systems have changed. Energy consumption is very often one of the most important elements in the processes of the planning, the estimation of efficiency or the revitalization. Energy is defined as a balance of energy that was delivered to the logistics system. This energy can be for example connected with the rotation of unit loads. It is worth to emphasize, that there is no universal index, thanks to which it would be possible to evaluate logistics warehouse systems, with taking the energy consumption under consideration. In the literature there are some attempts of creating this kind of index, for example: Directive of the European Parliament and of the Council 2006/32/WE of April 5, 2006 on energy end-use efficiency and energy services and repealing Council Directive 93/76/EEC; renewed Lisbon Strategy and National Cohesion Strategy (2007–2013). There are two ways of measurement of increasing energetic efficiency (energy savings): “top down” method; “bottom up” method. In the “top down” method there is a use of aggregate data and, that is the reason why this method is called the “method of energy efficiency indexes”. Thanks to this method it is possible to establish correct indexes, but they are only indexes of development of situations. However, this method doesn’t generate detailed measurements. Most

often objects of estimation in this method are sectors, branches and groups of economy, groups of devices, types of transport. Estimated values of energy consumption have to be corrected, because of external factors, such as degree days during the heating season, structural changes, structure of production and so on. "Bottom up" method is more precise way of calculating savings of energy, which result from the increase of energetic efficiency. First of all it is necessary to count the energy consumption of the single ultimate receiver, to achieve the basic size (for example, the energy consumption of the fridge in the fixed time interval – it has to be done before the introduction of the activity that is meant to increase the energetic efficiency). The next step is the comparison of the given level of energy consumption with the level of energy consumption which was recorded in the same time interval, after the introduction of the activity that is meant to increase energetic efficiency. The difference between these two results is the measure of improvement energetic efficiency. If this calculation is made for all receivers and results are summed up, it will create quite exact measurement of increase of energetic efficiency. During calculations it is also necessary to take weather conditions and other factors under consideration, just like in the "top down" method [5].

Energy savings can be caused not only by the introduction of activities, which are meant to increase the energetic efficiency, but they also can be the result of changes in the behaviour or in the life style (which means the change of the level of supply of services), changes in weather conditions that can't be controlled and structural changes (for example the reduction of manufacture because of energy consuming branches of industry). If there is no correction, these types of structural changes will influence the improvement of energetic efficiency [4].

The development of methods of monitoring the energetic efficiency and methods of evaluation of activities for improvement of energetic efficiency is the project of European Commission entitled "Evaluation and Monitoring of Energy Efficiency in the New EU Member Countries and the EU-25" (acronym EEE-NMC), which was execute within the framework of the program called Intelligent Energy Europe.

ODEX index is the aggregate energy efficiency index. It was worked out for the purposes of monitoring energetic efficiency and also in order to achieve the index that will be intelligible and simple to work out. This index is also illustrating the progress connected with the energy efficiency in countries of European Union. This index was obtained by aggregating of changes in single energy consumption, which was observed during the particular time and on the fixed levels of end-using. By the use of relevant physical parameters, ODEX index is in very correct way illustrating the progress which concerns energy efficiency. ODEX is a kind of alternative to the monetary index of energetic intensity. These indexes depend on many factors which are not directly connected with the energetic efficiency. ODEX index doesn't show the current level of energetic intensity. It shows only the progress in relation to the base year. ODEX indexes are very useful to monitor the realization of the indicative purpose within the sphere of energetic efficiency (2006/32/WE directive).

Methodology of calculating ODEX indexes is currently working out within the framework of European Commission programs, which are called ODYSSEE. Now there are two ways of calculating the ODEX index. Both methods give the same results. The first method (the aggregation method, which is based in a single consumption) connects the progress in energetic efficiency that was achieved in all subsectors, on the basis of the quantity of the energy that was saved (for example Mtoe). It is based on the "effect of single consumption". The second method (the method of weighted index) consists in considering separated indexes of single consumption of each subsector, on the basis of his participation in energy consumption of the sector.

ODEX is calculated for each year, as a quotient of actual energy consumption E_t and the theoretical energy consumption without taking a single consumption into consideration (without energy savings obtained by the reduction of single consumption of energy as a result of activities in aid of improvement of energetic efficiency of manufacturing process of given product). If the energetic efficiency index amounted to 82 in 2000, it means that in the comparison to energetic technologies and practices that were used in 1990, the energetic efficiency was improved by 15%.

This way of calculation rely on the method which was described in the "United Nations Framework Convention", colloquially called The Kyoto Protocol (from December, 1997 and it has been in force since the 16 February, 2005). As a result of agreements, there was made a decision according to which, the "Index EEI" was established as a system of classification of energetic efficiency. This index describes the efficiency of devices. Within the index there is a scale (from A to G), where "A" is the best class and it means that efficiency of the device is the highest and "G" is the poorest class, and it means that the efficiency of the device is the lowest. There are also some subclasses, for example A+ or A++. These classes are calculated from the proportion of a year-long consumption of energy of given device, to the standard consumption of energy of the device, which is definite by specific regulations. The difference between the energy consumption of the devices that are a part of adjacent class amount to about 22%. During the renovation or periodical servicing, and when there is necessity of replacement of the elements of machines, Kyoto Protocol encourages replacing old elements with the new, more energy-saving elements. That is why, there is also the necessity of study and establishing of this type of activities, setting in motion of adaptation processes for manufacturers of devices and spare parts.

There is also another transport index (energetic), which is well known in Germany. The value of this index is the information about the energy, which has to be delivered to do generate required work.

In the paper there is a worked out method of evaluation transport warehouse systems, with the use of energy index. To count this index it is necessary to sum up energies: energy that was delivered to the isolated system, recover energy and the energy that was wasted. This method let us evaluate an existing transport warehouse system. It can be done at the project stage or during the process of revitalization in a way of optimization of energy consumption, which is needed to move one unit load through

the warehouse system. If the warehouse is equipped with “A” class elements, it doesn’t mean that the operating of the system will be optimal [1–2].

Information connected with this subject-matter, were collected on the basis of reviews of the base of researches: EBSCO, COMPENDEX, PROQUEST, Baztech, e-Journals.

In this paper was presented the conception of model of evaluation of logistics warehouse system, with taking above-cited demands under consideration.

2. The rules of calculating the energy, in the model of evaluation of warehouse system

The level of the terminal floor, in the front of the entrance to the warehouse (where the reloading is taking place) was assumed to be the reference level – energy of the pallet that is received to the warehouse amount to 0 (in warehouses without temperature regimes – this problem is going to be touched on), so every movement of the pallet with the material generates energy changes. There is an assumption, that the energy is equal to the work that has to be done to move the pallet [6], [8].

$$E_E = E_P + E_S + E_Z + E_C + E_W. \quad (1)$$

where:

E_P – energy, which is necessary to lift the pallet,

E_S – energy, which is necessary to lift empty forks,

E_Z – energy which is necessary to transport the pallet,

E_C – energy which is necessary for travelling of the truck without a load,

E_W – energy which is necessary to execute tasks connected with the use forks.

Potential energy can be calculated from the well known formula $E = mgh$, but the kinetic energy has to be calculated on the basis of driving characteristic of conveyors and vehicles. Here is an example of characteristic of forklift truck, on the picture below.

There is no formula in the literature that would be able to calculate the energy of forklift truck. So for the purposes of this research, the formula was created on the basis of the simplest case [8].

$$F = m \cdot a + m \cdot g \cdot \mu, \quad (2)$$

where $\mu = f(mat1, mat2)$.

The equation of the movement of the truck can be presented by means of dependence (3):

$$F(V) = m \cdot a + W_t, \quad (3)$$

where:

$m \cdot a$ – inertial force,

$W_t = f_t \cdot Q$ – resistances to motion,
 f_t – rolling resistance coefficient,
 $F(V)$ – driving forces.

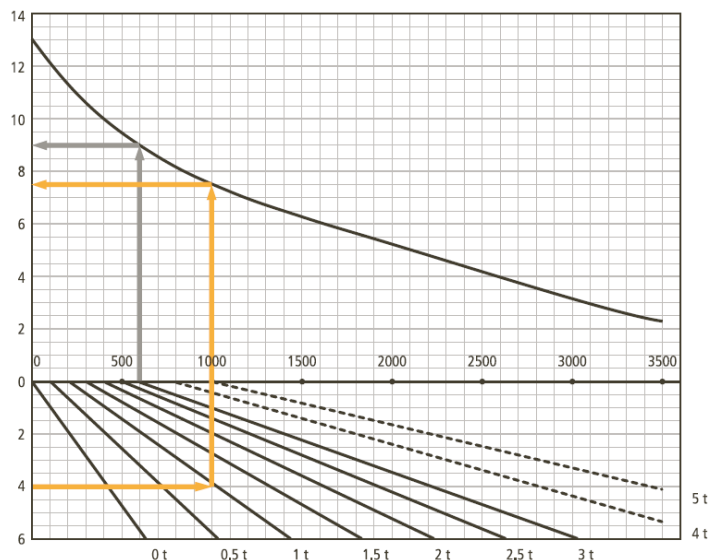


Fig. 1. Exemplary driving characteristic of the forklift truck EZS350, made by Jungheinrich

Resistances to motion can be divided into: basic and additional. Rolling resistance, suspension dumping, toe-in resistance and aerodynamic drag are rated among the first group. Grade resistance, and resistances connected with the drawbar pull, the start-up and with the turn are rated among the second group. Equation of movement has a form:

$$\xi \cdot m \cdot \frac{dV}{dt} + W_{r.coal} = F_N(V), \quad (4)$$

where ξ – ratio of rotor.

Possibilities of energy recovery, short time of storing this energy and the converting of this energy into different forms – all these factors are taken into consideration in this method.

The organization of the transport warehouse system: organization of the warehouse, organization of the work, organization of devices.

Here is an assumption that there are:

- 1, 2, ..., m devices,
- docks (receiving docks and shipping docks),
- storage areas (row of racks/intermediate storage area) 1, 2, 3, ..., k .

Process of warehousing consists of: the process of receiving, storing, picking and giving the loads out. In this model is the assumption that in the picking process there are going to be used pallet unit loads. Here are stages that can be singled out in the process of moving unit load, started with setting the unit load ext to the receiving dock, through the process of storing and giving it out:

- receiving a pallet (i),
- transport of the pallet (j),
- put the pallet back on the chosen place in the intermediate storage area (l).

In some cases during the process, there are changes of devices between the stages i , j , l . Each stage is realized by the device, so the storing of pallet (movement of the unit load in transport-warehouse system) can be presented as a three numbers (i, j, l), that present the number of the device, which is realizing the warehousing.

The process of storing can be divided into single operations:

- o_1 – travelling of the empty forklift truck to the place, where the unit load is placed,
- o_2 – executing the task which is connected with the use of forks,
- o_3 – delivering the pallet to the PP_1 ,
- o_4 – return of the empty forklift truck to the M point (readiness point),
- o_5 – reloading,
- o_6 – transport from the PP_1 to the PP_2 ,
- o_7 – reloading,
- o_8 – taking the pallet to the rack,
- o_9 – executing the task which is connected with the use of forks,
- o_{10} – return of the empty forklift truck to the M point (readiness point).

Here is also a data that characterizes each device:

- single energetic demand in the horizontal direction,
- single energetic demand in the vertical direction.

Data is written as a matrix ZE . The matrix ZE measures $m \times 2$.

$$ZE_{i1} = \begin{cases} > 0 \text{ there is an elementary } ZE_i \text{ in hotizontal direction,} \\ 0 \text{ then the device is not realizing the dislocation,} \end{cases}$$

$$ZE_{i2} = \begin{cases} > 0 \text{ there is an elementary } ZE_i \text{ in vertical direction,} \\ 0 \text{ then the device is not realizing the dislocation,} \end{cases}$$

$$ZE = \begin{matrix} 1 \\ 2 \\ \cdot \\ \cdot \\ m \end{matrix} \begin{bmatrix} ze_{11} & ze_{12} \\ ze_{21} & ze_{22} \\ \cdot & \cdot \\ \cdot & \cdot \\ ze_{m1} & ze_{m2} \end{bmatrix} \quad (5)$$

3. Unloading, introduction of the unit load to the warehouse

Here is a set of n pallets, which are located in the particular dock. There is also information about these pallets:

- the mass of the pallet,
- the address of storing place within the warehouse.

Next step is the creation of the matrix transport parameters PT . The matrix measures $n \times 5$, where:

- PT_{i1} – the mass of the pallet i ,
- PT_{i2} – the track of the unloading stage of the pallet i ,
- PT_{i3} – the track of the transport stage of the pallet i ,
- PT_{i4} – the track of the locating stage of pallet i ,
- PT_{i5} – the height of the storing of pallet i ,

$$PT = \begin{matrix} 1 \\ 2 \\ 3 \\ \cdot \\ n \end{matrix} \begin{bmatrix} pt_{11} & pt_{12} & pt_{13} & pt_{14} & pt_{15} \\ pt_{21} & \dots & \dots & \cdot & pt_{25} \\ \cdot & \cdot & \cdot & \cdot & \cdot \\ \cdot & \cdot & \cdot & \cdot & \cdot \\ pt_{n1} & \cdot & \cdot & \cdot & pt_{n5} \end{bmatrix}. \quad (6)$$

It is necessary to define the technology of unloading for each pallet (unit load). Because of the fact that there is a possibility of reloading from one device to the material handling device between some stages of the process, it is necessary to determine single energy consumption for these operations. The dimension of matrix amount to $m \times m$ and there are three numbers (i, j, k) , and each number is realizing a given stage of unloading. For example, the compositions of numbers $(3, 5, 1)$ means that the first stage of the process is realized by the device number 3, the second stage is realized by the device number 5 and the third stage is realized by the device number 1. The collection of these technologies for all pallets is creating a matrix T , where:

t_{ij} – indicate the number of the device which is realizing the j stage of the unloading process of the pallet i ,

$$i = 1, 2, 3, \dots, m,$$

$$j = 1, 2, 3,$$

$$T = \begin{matrix} & t_{11} & t_{12} & t_{13} \\ t_{21} & t_{22} & t_{23} \\ & t_{n1} & t_{n2} & t_{n3} \end{matrix}. \quad (7)$$

The matrix Z , is defined in the following way:

$Z_{ij} \geq 0$ when the reloading from the one device i to the second device j is possible and is equal to the single energy consumption of this operation there is no reloading,

$$Z_{ij} = \begin{cases} > 0 \text{ when the reloading from the one device } i \text{ to the second device } j \text{ is possible and} \\ \text{is equal to the single energy consumption of this operation,} \\ 0 \text{ there is no reloading,} \end{cases}$$

$$Z = \begin{bmatrix} Z_{11} & Z_{12} & \cdots & Z_{1M} \\ Z_{21} & Z_{22} & \cdots & Z_{2M} \\ \cdots & \cdots & \cdots & \cdots \\ Z_{M1} & \cdots & \cdots & Z_{MM} \end{bmatrix}. \quad (8)$$

For each pallet and with the taking into the consideration (T) technology, it is easy to determine elementary energy consumption. This energy consumption is going to be indicated as a matrix O with the dimension $n \times 10$. Elements of this matrix are defined below:

$$O_{ij} = \begin{cases} 1 \text{ single energy consumption which is need to carry out an operation of } j \text{ detail,} \\ 0 \text{ if the operations } j \text{ is not realized,} \end{cases}$$

This matrix is determined on the basis of matrix ZE , Z and T .

$$O_{i1} = ZE(T(i, 1), 1),$$

$$O_{i2} = ZE(T(i, 1), 2),$$

$$O_{i3} = 0_{i1},$$

$$O_{i4} = 0_{i1},$$

$$O_{i5} = ZE(T(i, 1), T(i, 1)),$$

$$O_{i6} = ZE(T(i, 2), 1),$$

$$O_{i7} = Z(T(i, 2), T(i, 3)),$$

$$O_{i8} = ZE(T(i, 3), 1),$$

$$O_{i9} = ZE(T(i, 3), 2),$$

$$O_{i10} = 0_{i8}.$$

To obtain energy consumption for each operation, it is necessary to correct elements of matrix, with taking the track, the load and the height into consideration. Coefficients of corrections are determined on the basis of the PT matrix. We are obtaining a matrix WK ($n \times 10$), which is defined as a matrix of the coefficients of correction of energy consumption for each operation and for each pallet.

After the operation of matrix multiplication the matrix WK and matrix O , we are going to obtain the matrix E , where the elements of this matrix correspond to the energy consumption for each operation and for each pallet.

Matrix multiplication is defined as a:

$$WK_{n \times 10} \otimes O_{n \times 10} = E_{n \times 10}, \quad (9)$$

where:

$$e_{ij} = WK_{ij} \cdot O_{ij}. \quad (10)$$

The total consumption of energy amount to:

$$E_C = \sum_{i=1}^n \sum_{j=1}^{10} e_{ij}. \quad (11)$$

Thermal energy is taken into consideration in a case of analysis of warehouse systems with the temperature regime. In these cases it is important to take the heat exchange into consideration – the heat that penetrates walls, the ceiling and the floor of the warehouse chamber; the heat that was abstracted from cooled loads on the pallet; the heat which was given back by the air, which was unintentionally introduced to the chamber; the heat connected with the work of ventilator of the radiator; the heat which is generated by people; and other kinds of heat, according to the equation.

Modern devices in warehouses are very often equipped with technical systems, which allow to energy recovery, energy storing and converting it into different forms (by using heat accumulators, storage cells, pressure accumulator). What is more, there is also a possibility of analyzing the utilization of solar (water heating, generation of electric energy). The model wasn't tested in regard to taking geothermal source of energy into consideration.

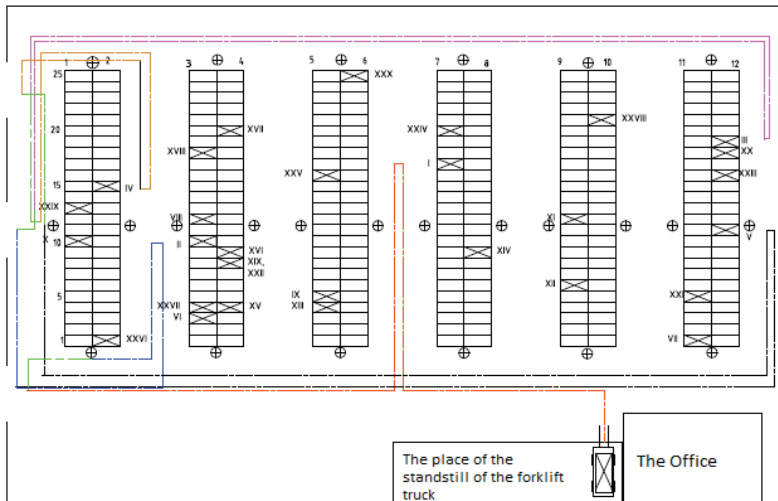


Fig. 2. Variants of information interchange, in the relation “office” – forklift truck:
a) paper-variant, b) terminal with the dock station, c) radio terminal

The flow of information in logistics system is described by the quantity and the cost of equipment which is needed to guarantee the flow of information. The energy which is necessary to the information interchange on the accurate level to guarantee the required warehouse rotation was also taken into consideration. The energy of the system of the information interchange in the logistics warehouse system can be divided into: the energy of identification of elements and the energy of information transfer (in some cases the data transfer) [3].

Figure 2 is illustrating the dependence of the working track of forklift truck and the technology of information interchange.

Functionality of RFID marks which relies on the affiliation both to the first and to the second group was taken into consideration. These marks can be used to recording of actual positions of elements of the logistics system, in the context of minimization simple cycles of their work. On the basis of index [1] and [3] it is possible to calculate the index of usability of electronic data interchange (the bigger value, the more justified the application of *EDI* [7]). The index can be described in this way $W_{edi} = (0-1)$.

This index can be calculated in following way:

$$W_{edi} = \sum_{i=1}^n w_i \times W_j, \quad (12)$$

where:

W_{edi} – global index which characterizes the usability of *EDI* in the organization,

w_i – weight of the partial index i ,

W_j – the value of partial *EDI* usability of index j .

Here is going to be illustrated the problem presented on the Figure 2. There were made calculations of energy consumption of logistics warehouse systems, where systems of information interchange was being changed: paper-version, version with making the use of dock station and version with making the use of radio terminal. Results of the calculations are presents in the Table 1 (Where W_x – energy consumption of the logistics warehouse system). The calculation shows that the optional electronic method of information interchange (column 2, 3) is more profitable than the paper-one (Table 2, column 1). The difference between variants amount to about 20% to 30%, but the results of calculation for the variants 2 and 3 don't differ a lot, when the rotation in the warehouse is small (not more than 2% – 3%).

Table 1. Example of statement of results during the selection of the information exchange system

	Statement		
	Warehouse 1	Warehouse 2	Warehouse 3
Index W_{EDI}	$0.1364 + \Sigma(W_x * W_x)$	$0.0884 + \Sigma(W_x * W_x)$	$0.0524 + \Sigma(W_x * W_x)$
Energy-consumption	17.26	13.45	12.75

4. Verification of the model of estimation of logistics systems

Minimal energy that is necessary to realize the flow of on pallet through the warehouse, which is equal to the cost of this flow, should take the minimization of the operation costs, heighten safety and reliability into consideration. So it is a kind of reconciliation of technical issues, economical issues and social issues (ergology, ecology, safety).

Below there were chosen model-and-statistic logistic warehouse systems. It was done on the basis of the analysis of logistics warehouse systems and they were adjusted to the shape and to the equipment of the warehouse.

Figure 3 is a kind of verification of the calculated example.

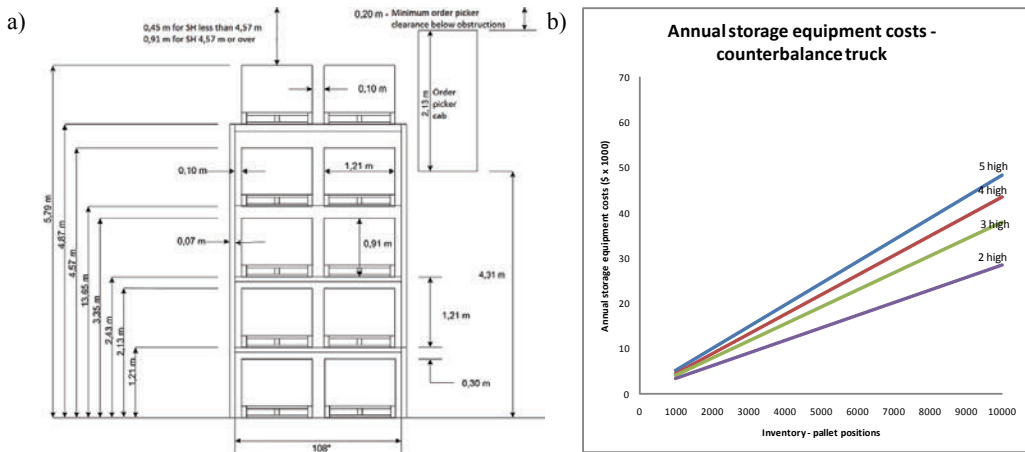


Fig. 3. Energy consumption of the logistics warehouse system that is serviced by the counterbalance truck with the restriction of the storage height to the 6 m

A simple test case

In the following test case, we will show that it is possible to achieve energy saving by applying a single change in the order of points obtained by well-known order picking heuristic algorithms.

Example

In a small warehouse consisted of a rectangular rack of dimension Length (5 units) and Height (4 units), where both start and end are located at the zero point, the unit of performing the order picking is programmed so that the order picking device has to visit the points (1, 3), (3, 4), (5, 3), (4, 1), (3, 2) and (2, 1), as shown in the Figure 4. If the route programming is performed according to, for example, the method1, then the path will be: 0-6-5-4-3-2-1-0. A small change in aforementioned path, for example, 0-6-4-5-3-2-1-0, may constitute a more energy economical solution. In Figure 4 one can notice: a) the six points obtained through the well-known method1 and b) the more energy economical solution achieved by changing the series 6-5-4 to 6-4-5.

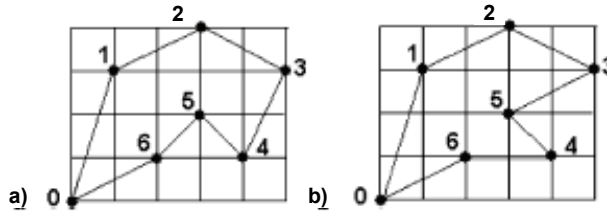


Fig. 4. Order picking by applying a) method1, b) energy saving

By recording the paths of horizontal as well as up and down movement, for each of the two methods the following remarks are made.

Again under the simplistic assumption that work performed in up and down movement is the same and does not depend on the friction, while the friction coefficient, μ , contributes in the horizontal movement, in the general case the energy consumption can be approximated by:

$$E = n_x s_x \mu W + n_y s_y W, \tag{13}$$

where s_x and s_y denote the spacing (step) of horizontal and vertical movements, respectively. Also, n_x and n_y denote the number of steps per direction. By setting $s_x = s_y = S$, the method1, applied to the present example, consists of 10 vertical and 10 horizontal steps, while the proposed energy saving path consists of 8 vertical and 12 horizontal ones. Therefore, the corresponding works of the above example are written as:

$$\text{method 1: } E1 = SW(10\mu + 10). \tag{14}$$

$$\text{Energy saving method: } E_{\text{ENERGY}} = SW(12\mu + 8). \tag{15}$$

And the energy gained in (%) becomes

$$G = \frac{E1 - E_{\text{ENERGY}}}{E1} \times 100(\%). \tag{16}$$

By substituting Equation (14) and (15) in Equation (16), one obtains:

$$\frac{(1 - \mu)}{(1 + \mu)} \cdot 5 \times 100(\%) \tag{17}$$

In the unrealistic case of no friction, the gain factor becomes 20%. For a typical coefficient of friction such as $\mu = 0.1$ the gain is calculated equal to 16.4%, while for $\mu = 0.05$ it becomes 18.1%. Obviously, in all cases the achieved gain is not negligible.

For the above example, the lengths of the paths found in the two methods have been calculated to be equal. If the velocities of the horizontal and vertical motion are equal, then the duration of both paths are equal. Usually the horizontal motion is performed with a greater velocity than the vertical one.

5. Conclusions

Suggested model of the estimation of warehouse system is producing good, comparable and repetitive results. This model can be used to the estimation of logistics warehouse systems in practice.

After the analysis of application the method of estimation of logistics warehouse systems, it is necessary to state that the practical application of these methods has a very important and wide aspect in economy. The knowledge about the energy consumption of warehouse systems can be used among different contexts. Here are three examples of this use:

1) Selection of right forklift truck to the given warehouse

According to this report, the delivered energy has to turn into the effective work, with taking loses of a drive during the travelling into consideration. Before the sale of the device, producers of these forklift trucks should collect following type of information:

- precise shape of the track (vertical shape – access roads and horizontal shape – the number of turning radius within the warehouse),
- the weight of the load,
- the length of the line segments (stability of the velocity, for example on the level of 5–6 km/h).

2) Warehouse management

Manager of the warehouse can coordinate the work of the forklift truck, because of the knowledge concerning the conditions of given warehouse. Taking into the consideration the fact that there is no restrictions connected with the time of the load service (because the time window can be a kind of criterion in this context), the work is optimal in the point of view of

- costs,
- time,
- profits.

3) Warehouse design

There are several postulates connected with the warehouse systems design that also results from this analysis. These postulates are:

- Modification of the direction of travel of the forklift truck by an angle of 90° , it is connected with the increase of the velocity before the turn and decrease of the velocity after the turn. That is why there are so many premises connected with the “straightening” of the warehouses.

- Minimization of changes of the aisles for the purposes of equipment.
- Appropriate organization of places, where the change of the equipment (that services loads) is taking place. Very often at the terminal, there is a one type of forklift truck that services the load. Then, there is taking place a change of equipment and the interception of the load by the conveyor. After that, the stacker crane or the reach truck is intercepting the load. On the average, two changes of equipment are taking place. These changes have to be planned carefully, to not waste the energy on the change of the height of unit load.

References

- [1] Bartoldi J.J., Platzman L.K.: *An $O(n \log n)$ planar travelling salesman heuristic based on spacefilling curves*, Operations Research Letters, 1983, Vol. 1, No. 4, pp. 121–125.
- [2] Gudehus T.: *Principles of order picking: operations in distribution and warehousing systems*, Essen, Germany: W. Girardet, 1973.
- [3] Kwasniowski S. (Ed.), Zajac P. (Ed.): *The automatic identification in logistics systems*, Publishing house of Wrocław University of Technology, Wrocław, 2004.
- [4] Kwasniowski S., Nowakowski T., Zajac M.: *Intermodal transport in logistics networks*, Publishing house of Wrocław University of Technology, Wrocław, 2008.
- [5] Makris P.A., Makri A.P., Provatidis C.G.: *Energy-saving methodology for material handling applications*, Applied Energy, Vol. 83, 2006, pp. 1116–1124.
- [6] Zajac P.: *Concept of model of estimate of – store house system transport*, Total Logistic Management, Gliwice, 2009, CD added to the “Logistics” magazine.
- [7] Zajac P.: *Electronic data interchange in logistics systems*, Publishing house of Wrocław University of Technology, Wrocław, 2010.
- [8] Zajac P.: *Transport and storage system optimization in terms of energy*, Research brochures of the Warsaw University of Technology, Warsaw, 2010.

Koncepcja modelu oceny logistycznych systemów magazynowych z uwzględnieniem ich energochłonności

Kryteria oceny logistycznych systemów magazynowych muszą coraz częściej uwzględniać energochłonność systemu magazynowego. Tymczasem w literaturze przedmiotu i normach powszechnie przyjętych za obowiązujące nie uzgodniono precyzyjnej i uniwersalnej metody jego obliczania. W pracy przedstawiono taką koncepcję wykorzystującą do tego celu wzory na energię potencjalną oraz wyprowadzonej zależności przez autora – dotyczącej energii kinetycznej, na podstawie charakterystyki napędowej. Omówiono model matematyczny pozwalający obliczać energochłonność oraz zaproponowano sposób określenia wskaźnika energochłonności magazynowego systemu logistycznego. Przedstawiono przykładowe obliczenia oraz sformułowano wnioski końcowe oraz kierunki dalszych prac.